– Transport Phenomena in Novel Energy Materials –

Pits and Traps in the Impedance Analysis of Ionic Conductors

Inauguraldissertation zur Erlangung des Doktorgrades der Naturwissenschaftlichen Fachbereiche im Fachgebiet Theoretische Physik (Fachbereich 07) an der Justus-Liebig-Universität Gießen

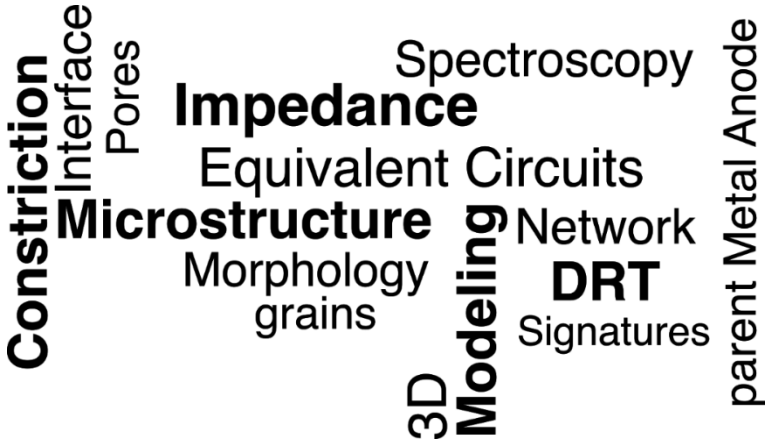

vorgelegt von

Janis Kevin Eckhardt

aus Sellnrod

angefertigt im Zeitraum von Oktober 2019 bis Dezember 2022

am Institut für Theoretische Physik

der Justus-Liebig-Universität Gießen

Betreuer: Prof. Dr. Christian Heiliger

Prof. Dr. Peter J. Klar

Eidesstattliche Erklärung

Hiermit versichere ich, die vorgelegte Dissertation selbstständig und ohne unerlaubte fremde Hilfe und nur mit den Hilfen angefertigt zu haben, die ich in der Dissertation angegeben habe. Alle Textstellen, die wörtlich oder sinngemäß aus veröffentlichten Schriften entnommen sind, und alle Angaben, die auf mündlichen Auskünften beruhen, sind als solche kenntlich gemacht.

Bei den von mir durchgeführten und in der Dissertation erwähnten Untersuchungen habe ich die Grundsätze guter wissenschaftlicher Praxis, wie in der „Satzung der Justus-Liebig-Universität zur Sicherung guter wissenschaftlicher Praxis“ niedergelegt sind, eingehalten.

_____ _____

Ort, Datum Unterschrift

Dekan: Prof. Dr. Stefan B. Hennemann

Erstgutachter: Prof. Dr. Christian Heiliger

Zweitgutachter: Prof. Dr. Peter J. Klar

Disputation: 21.07.2023

„*The task is not to see what has never been seen before, but to think what has never been thought before about what you see everyday*.“

– Erwin Schrödinger (1887 – 1961)

List of Abbreviations

IS	impedance spectroscopy
EU	European Union
LIB	lithium-ion battery
SSB	solid-state battery
OLE	organic liquid electrolyte
CAM	cathode active material
KPI	key performance indicator
EV	electric vehicle
DIC	dual-ion conductor
Me	metal
SE	solid electrolyte
SEI	solid electrolyte interphase
SPE	solid polymer electrolyte
ISE	inorganic solid electrolyte
SIC	single-ion conductor
WE	working electrode
CE	counter electrode
KK	Kramers-Kroning
ECM	equivalent circuit model
R	resistor
C	capacitor
BLM	brick layer model
MIEC	mixed ionic-electronic conductor
TLM	transmission line model
DRT	distribution of relaxation times
DDT	distribution of diffusion times
SOFC	solid oxide fuel cell
CNN	convolutional neural network
RF	random forest

Zusammenfassung

Die Eindämmung der globalen Folgen des Klimawandels wird als eine der größten Herausforderungen unserer Zeit angesehen. Der Umstieg von fossilen auf erneuerbare Energieträger ist ein wichtiger Meilenstein auf dem Weg zu Klimaneutralität und mehr Nachhaltigkeit. Speichertechnologien wie zum Beispiel Sekundärbatterien sind in diesem Zusammenhang von großer Bedeutung. Dies gilt zum einen für die Transformation des Automobilsektors, in dem Verbrennungsmotoren zunehmend durch Elektromotoren ersetzt werden, zum anderen aber auch, wenn es darum geht, überschüssige Energie aus regenerativen Energiequellen zu speichern. Dabei wird der Realisierung neuartiger elektrochemischer Speicher eine Schlüsselrolle zugeschrieben. Ein interessanter Ansatz sind beispielsweise Feststoffbatterien mit reversiblen Metallanoden, die theoretisch ein Vielfaches der Energiespeicherkapazität herkömmlicher Lithium-Ionen-Batterien bereitstellen können. Bis zur Marktreife sind jedoch noch diverse Herausforderungen zu bewältigen.

Die elektrochemische Impedanzspektroskopie ist ein leistungsfähiges Werkzeug, um neuartige Materialien zu charakterisieren und Systeme im Betrieb zu überwachen. Sie ist daher eine wichtige Analysemethode bei der Untersuchung von aktuellen und zukünftigen Energiespeichersystemen. Methodisch wird ein elektrisches Wechselfeld an das zu untersuchende System angelegt und das Antwortsignal als Funktion der Frequenz gemessen. Die Interpretation der Messergebnisse erfolgt zumeist über Mustererkennung und eindimensionale elektrische Ersatzschaltbilder. Diese Methode hat sich als Standardverfahren zur Untersuchung homogener Systeme wie Flüssigkeiten oder Einkristalle etabliert. Die Analyse von inhomogenen Festkörpersystemen wie polykristallinen Elektrokeramiken, porösen Materialien oder Verbundwerkstoffen aus mehreren Komponenten ist im Vergleich dazu jedoch wesentlich komplexer. Ihr mikrostruktureller Aufbau führt zu zusätzlichen geometrischen Freiheitsgraden im System. Dadurch kann das Transportverhalten durch reale Strukturen nicht adäquat durch ein eindimensionales Modell angenähert werden. Dies wird allerdings bei der Impedanzanalyse von Festkörpersystemen im Hinblick auf die Materialeigenschaften und die auftretenden Transportprozesse häufig außer Acht gelassen. Die Aussagekraft der gezogenen Schlussfolgerungen ist daher eingeschränkt und der Erkenntnisgewinn über das untersuchte System *a priori* begrenzt.

Die Art und Weise, wie geometrische Effekte die Korrelation zwischen dem Impedanzsignal und den Transport- oder Struktureigenschaften beeinflussen, ist bis heute nicht vollständig geklärt. Im Rahmen des Dissertationsprojektes wurden diese Fragestellungen im Zusammenhang mit aktuellen Herausforderungen in der Entwicklung von Feststoffbatterien intensiv untersucht. Dazu gehören insbesondere der Einfluss der Mikrostruktur des Festelektrolytseparators auf den Ionentransport und dessen Auswirkung auf die aus der Impedanz abgeleiteten Materialparameter. Darüber hinaus wurde der Einfluss der elektrochemischen und morphologischen Stabilität der Grenzfläche zwischen Metallanode und Festelektrolytseparator auf die Systemeigenschaften analysiert. Zu diesem Zweck wurde ein progressiver Arbeitsablauf entwickelt, der die Generierung realitätsnaher Modellsysteme, die Modellierung des Ionentransports auf der mikroskopischen und mesoskopischen Längenskala über ein mehrdimensionales elektrische Netzwerkmodell und die automatisierte Auswertung von Impedanzen über eindimensionale Ersatzschaltbilder umfasst.

Die in den verschiedenen Studien gewonnenen neuen Einblicke leisten einen wichtigen Beitrag zum besseren Verständnis der systeminternen Prozesse in Feststoffbatterien. Eine wichtige Erkenntnis ist dabei, dass die mit eindimensionalen Modellen abgeleiteten materialspezifischen Transportgrößen teilweise Ungenauigkeiten von mehreren Größenordnungen aufweisen. Darüber hinaus wurde gezeigt, dass das Impedanzsignal Signaturen der geometrischen Struktur der Probe und des Systems enthält, die in eindimensionalen Modellen oft nicht ausreichend abgebildet werden können und daher zu Fehlinterpretationen führen. Besonders deutlich wurde dies am Beispiel der Lithiummetallanode-

Festelektrolyt Grenzfläche: Stromeinschnürungseffekte durch morphologische Veränderungen während des Betriebs verschlechtern dramatisch die Leistungsfähigkeit des Systems, was lange Zeit irrtümlich dem Ladungstransferschritt zugeschrieben wurde. Dies führte zu der falschen Annahme, dass ein inhärent hoher Transferwiderstand die Realisierung des Konzepts der reversiblen Metallanode verhindere, und verzögerte dadurch dessen Weiterentwicklung. Auf der Grundlage detaillierter theoretischer Untersuchungen konnten die strukturbedingten Ungenauigkeiten der über Standardverfahren ermittelten Transportgrößen abgeschätzt und ein Leitfaden für die Interpretation experimenteller Impedanzdaten von Grundmetallanoden entwickelt werden. Das Dissertationsprojekt als Ganzes unterstreicht damit die Bedeutung einer umfassenden Strukturanalyse bei der Betrachtung und Interpretation von Festkörpersystemen.

Abstract

Mitigating the global consequences of climate change is one of the biggest challenges of our time. The transition from fossil fuels to renewable energy sources seems to be an important milestone on the road to climate neutrality and sustainability. In this context, energy storage technologies such as secondary batteries are of great interest. This applies not only to the transformation of the automotive sector, where internal combustion engines are gradually being replaced by electric ones, but also to the storage of excess energy from renewable sources. The realization of novel electrochemical storage systems appears to be essential in this regard. Solid-state batteries with reversible metal anodes, for example, theoretically enable a much higher energy storage capacity than conventional lithium-ion batteries. However, there are still a number of challenges to overcome before this technology is ready for the market.

Electrochemical impedance spectroscopy is a powerful tool for characterizing the electric transport properties of novel materials and monitoring systems in operation. It is therefore an important analysis method in the study of current and future energy storage systems. The analysis of impedance data mostly involves pattern recognition and fitting with a simple electric equivalent circuit model. This has become the standard for studying homogeneous systems such as liquids or single crystals. The analysis of inhomogeneous solid-state systems, such as polycrystalline electroceramics, porous materials, or multi-component composites, is much more complex. This is due to the microstructure of the sample and the morphology of interfaces, which introduce additional degrees of freedom into the system. As a result, the transport behavior through real structures cannot be adequately described by one-dimensional models. However, this is usually overlooked in impedance analysis in terms of material-specific properties and the transport processes taking place in the system. Therefore, the possible gain of knowledge about the system under study is limited *a priori*, as is the validity of the conclusions that can be drawn.

The extent to which geometric effects affect the correlation between the macroscopic impedance response signal and microscopic transport or structural properties is not yet fully understood. The dissertation project explores these open questions in the context of current challenges in the development of solid-state batteries. This includes studying the effect of the solid electrolyte separator microstructure on ion transport and its effect on the material-specific transport parameters derived using the standard impedance analysis procedure. In addition, the consequences of the electrochemical and morphological (in)stability of the interface between parent metal anode and solid electrolyte separator (during operation) on the properties of the system have been analyzed in detail. To this end, a comprehensive modeling workflow has been developed that includes the generation of realistic model structures, the modeling of ion transport on the microscopic and mesoscopic scale using a multidimensional electrical network model, and automated impedance analysis.

The insights gained in various studies are a significant contribution to a better understanding of the internal processes in solid-state batteries. An important finding is that the material-specific transport quantities derived with one-dimensional models sometimes exhibit inaccuracies of several orders of magnitude. It has also been shown that the impedance response of the system contains signatures of the sample geometry, such as microstructure or interface morphology, that cannot be adequately represented in one-dimensional models, leading to misinterpretations. This has been particularly evident when studying the interface behavior between lithium metal anode and garnet-type solid electrolyte: Geometric constriction effects due to morphological instabilities dramatically degrade system performance. For a long time, this has been mistakenly attributed to the charge transfer reaction, leading to the misconception that an inherently high transfer resistance prevents the realization of the reversible metal anode concept. Overall, detailed theoretical investigations have allowed to estimate structural inaccuracies of the determined transport quantities and to develop a guideline for the interpretation of experimental impedance data of parent metal

anodes. The dissertation as a whole emphasizes the importance of comprehensive structural analysis when considering and interpreting solid-state systems.

Table of Contents

1. Introduction

Addressing the global ramifications of climate change stands as a paramount challenge in our time. The shift from reliance on fossil fuels to the use of embracing renewable energy sources is a pivotal milestone on the road to climate neutrality and more sustainability. Thus, the exploration of energy storage technologies such as secondary batteries is attracting immense interest and attention. The significance of these advancements extends not only to the ongoing transformation of the automotive sector, where the gradual replacement of internal combustion engines with their electric counterparts is steadily underway, but also to the crucial task of efficiently storing the surplus energy generated from renewable sources. The development of innovative electrochemical storage systems is therefore a crucial endeavor. For instance, solid-state batteries featuring reversible metal anodes holds tremendous potential, theoretically offering a substantially higher capacity for energy storage compared to conventional lithium-ion batteries. Before this technology can be considered ready for widespread adoption and commercialization, however, several formidable challenges require careful consideration, with particular focus on enhancing the stability and reliability of the system's interfaces.

In this respect, impedance spectroscopy (IS) is a powerful analysis tool in materials research and development. The method is non-destructive, non-invasive, and, depending on the frequency range considered, requires relatively short measurement times. Important historical milestones for this method include the invention of potentiostats in the 1940s and the introduction of frequency response analyzers in the 1970s, which significantly simplified the process of impedance measurements.[1] IS has become increasingly popular in recent years since it is a rather simple automated electrical characterization tool whose results complement those of other electrochemical methods. This is also reflected in the number of annual publications with contributions from IS, which has increased by about a factor of 20 since the beginning of the millennium.[2] However, there are only a few studies that have addressed the challenges of IS and uncertainty analysis of microscopic material-specific transport parameters derived from IS measurements. Most of them focus exclusively on the experimental side, although it is well known that, for example, the microstructure of a solid has a major influence on the evolving transport paths through the system. In particular, the interpretation of the measurement results with respect to the characterization of the electric and electrochemical properties of the sample under investigation is only rarely questioned.

The goal of this Ph.D. thesis is to highlight the challenges of correlating the macroscopic impedance response signal of the system with transport effects and properties occurring at the microscopic level. To this end, a modeling workflow has been developed to compute synthetic impedance data from three-dimensional solid-state systems. This includes automated image recognition for segmentation of the microstructure, transport computations with an electric network model, and analysis tools such as distribution of relaxation times and equivalent circuit model fitting for data analysis. Such an approach allows direct comparison of geometric system parameters and microscopic transport quantities with the results of commonly used standard IS analysis methods. The conclusions derived are general in nature, but the following discussion focuses solely on electric energy storage systems, as their societal role is becoming increasingly important in light of climate concerns.

1.1 The Role of Energy Management Systems in Combating Climate Change

The worldwide total demand for energy constantly increases in the course of the advancing industrialization, increasing health in developing countries, and growth of world population. Global electricity consumption is projected to increase by almost 80%, from around 24.8 PWh in 2021 to 44.5 PWh in 2050.[3-4] Depending on the forecast, Germany’s demand for electric energy is even expected to more than

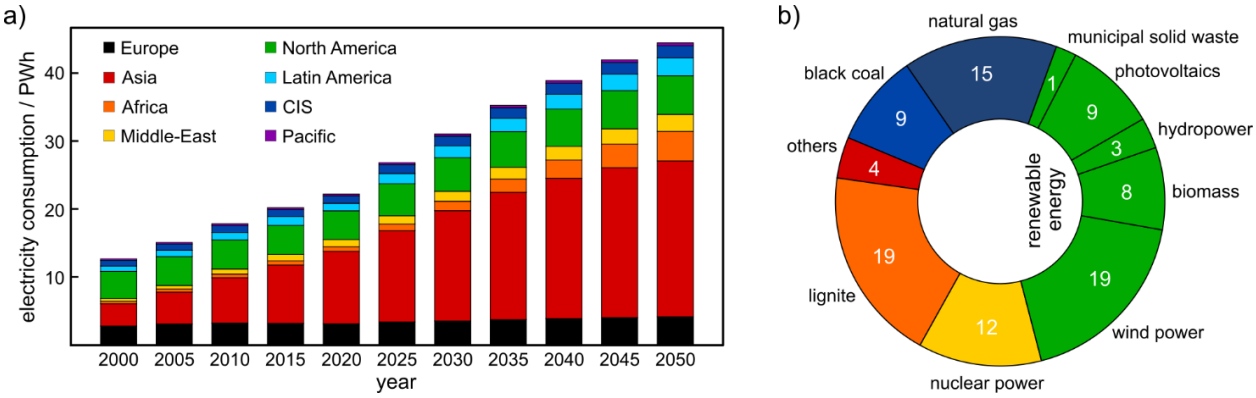

Figure 1. *Overview of (a) the worldwide electricity consumption and (b) shares of gross electricity production for Germany (583 TWh) in 2021.*[4-5] *Global demand for electricity is expected to double by 2050, driven by increased activity and efforts to electrify end-users. Germany aims to boost its share of renewable energy from 40% today to 100% during this period.*

triple, from 0.58 PWh now to more than 2.1 PWh in 2050.[5-6] Today, most electricity is generated centrally in a small number of power plants scattered across national territories, from where it is distributed to each region of the country. For this purpose, nuclear power plants are often used, where nuclear fission releases a large amount of energy that is converted into heat or electric energy.[7-8]

Other conventional power plants burn fossil fuels such as coal, natural gas or crude oil. The redox reaction during combustion, however, releases large amounts of CO_2 into the atmosphere. Greenhouse gases such as NO_x or CO_2 in the atmosphere prevent the direct heat transfer from Earth to space, resulting in steady warming of the planet over the next decades, centuries or even millennia. The consequences of the human-made climate change[9-10] are becoming more and more omnipresent, as extreme weather events (e.g., droughts and floods) have also occurred heavier and more frequently in Germany in recent years.[11-12] To combat global warming and mitigate further climate change effects, 195 parties signed the Paris Agreement in 2015 to reduce their amount of annual CO_2 and greenhouse gas emissions.[13] However, the trade-off between climate goals, on the one hand, and economic interests such as international competitiveness, on the other, is a balancing act. In recent years, many parties have prioritized economic success over climate protection despite the Paris Agreement.

There is a broad consensus among experts that the phase-out of fossil fuel power generation is necessary to achieve the Paris climate targets. Therefore, the European Union (EU) Commission recently approved the Complementary Climate Delegated Act, which adds specific nuclear and gas energy activities to the list of economic activities covered by the EU taxonomy.[14-15] In particular, the classification of nuclear energy as climate-friendly has been criticized by activists in light of the Chernobyl accident (1986), the natural disaster in Fukushima (2011), and open questions about the long-term storage of hazardous or radioactive waste.[16-18] Japan has recently decided to reactivate old reactors and to start planning new nuclear power plants in order to reconcile ever-increasing energy demand with the Paris Agreement.[19-20] Japan's changing attitude toward nuclear energy shows that it is challenging to simultaneous phase out both coal and nuclear power within just a few years without jeopardizing economic success.

The agenda of the EU indicates that phasing out coal-fired power generation is a higher priority than phasing out nuclear power, which does not emit greenhouse gases. Germany is playing a pioneering role worldwide with its decision in 2011 to exit nuclear energy by the end of 2022 and to phase-out of coal-fired power generation by 2030.[21-22] It corresponds to a complete transformation of the energy sector in just two decades, which will require an enormous national effort. This ambitious goal is based on the fact that the energy supply from renewable, climate-friendly energy sources exceeds the current and future global energy

demand by several times. However, one of the biggest challenges in this context is that energy production from renewable sources such as wind, water, and sun light cannot be readily adjusted to current energy demand. Instead, it depends on environmental conditions and on location. This uncertainty poses a significant risk not only to industrial manufacturing companies, but also to healthcare organizations such as hospitals.[23] Strategies to overcome these issues include transporting excess energy to regions with increased energy demand (e.g., transporting wind power from northern to southern Germany), decentralized and mobile storage of excess energy so that it can be used again when it is needed (smart grid), and rebalancing with energy-friendly power plants such as natural gas. This is a powerful reminder that the so-called *energy transition* is not just about energy generation, but also about energy storage, grids, and infrastructure in general.

Sustainability is at the forefront of all measures, i.e., not only in terms of *energy generation*, but also in terms of the carbon footprint of the value chain, the environmental impact of mining raw materials, recycling, waste management, or the abundance of resources and materials for applications.[24-25] The importance of the latter, in particular, is currently highlighted by the shortage of natural gas available on the international market due to Russia's aggression against Ukraine.[26] This in turn emphasizes the central role of *energy efficiency*. There is a need to improve and develop technologies and concepts in terms of energy consumption and the use of resources. One of multiple interesting approaches, for example, is the use of smart windows to regulate the flow of solar radiation through the glazing. This could be a promising way to reduce the energy consumption for temperature control in buildings.[27-30]

Altogether, a great deal of fundamental research, breakthrough discoveries, and innovation is needed to make the energy transition a success. Up to now, there is no alternative to sustainable, resource-conserving and efficient electrical energy storage. This is also evident from the decision of the Nobel Prize Committee in 2019 to award John B. Goodenough, M. Stanley Whittingham, and Akira Yoshino with the Nobel Prize in Chemistry for their pioneering work on lithium-ion batteries (LIB).[31-32] LIBs have a significant impact on our daily lives through their use, for example, in mobile phones, computers, tablets, and toothbrushes. However, the successful transformation of the entire power generation sector, as well as the mobility sector with the phase-out of the internal combustion engine in vehicles, cannot be achieved with LIB as a storage system alone. Solid-state batteries (SSB) with reversible metal anodes are a promising alternative. Theoretically, they can provide significantly better performance than conventional LIBs due to their higher energy storage capacity. However, there are still many challenges to overcome prior to the market launch as a commercial product. Therefore, in the following chapter, we will briefly review the fundamentals and challenges associated with SSBs in more detail.

1.2 The Elusive Holy Grail: The Challenge for Solid-State Batteries

The storage of electrical energy in form of chemical energy relies on the basic principle of separating electronic and ionic charge available in one material and recombining both charges in a second material. This happens in every electrochemical storage device during operation, including batteries. These in turn are classified into primary and secondary systems according to the reversibility of the electrochemical reactions taking place inside the cell, i.e., the ability to recharge.[33] In an absolute minimalistic cell design, a LIB contains three components, a negative electrode (anode), a positive electrode (cathode) and an electrolyte. The intercalation anode is usually made of graphite, whose layered structure allows lithium to be incorporated and stored during the charging process.[34] The ionically but not electronically conductive organic liquid electrolyte (OLE) ensures charge separation and prevents spontaneous self-discharge through a mechanical contact of both electrodes. If this cannot be achieved by a spatial distance of the electrodes, a so-called separator is used between them. It is a permeable polyolefin membrane impregnated with the

OLE, which allows fast transport of Li^+ ions but not electrons. The cathode is often a porous composite composed of cathode active material (CAM) particles, binder, and conductive additives, which is impregnated with the OLE. The ionic percolation paths through the OLE, and the electronic percolation paths through the network of CAM and conductive additives allow delithiation and lithiation of the CAM particles during charge and discharge, respectively, when the external circuit is closed and electrons can flow through the consumer load. Typical CAMs are layered transition metal oxides, spinel oxides, or polyanionic compounds.[35-40]

The electrochemistry of the battery, more specifically the choice of materials and the electrochemical reactions that take place, has a major impact on the key performance indicators (KPI). These include energy density, power density, specific capacity, coulomb efficiency, capacity retention, operating conditions, safety, price, or cycle life.[41] Today's state-of-the-art commercial rechargeable LIBs,[42-44] such as Tesla's 4680-type battery cell,[45] can be operated for several thousand charge and discharge cycles and offer a specific reversible capacity of 73 $mAh \cdot kg^{-1}$, and a specific energy density in the range of 290 $Wh \cdot kg^{-1}$. However, the fields of application for batteries are becoming increasingly diverse. At the same time, the requirements are becoming more and more demanding and difficult to meet with the conventional LIB concept. This is evident, for example, in the automotive sector. Batteries in electric vehicles (EV) must meet several criteria to make EVs ready for large-scale production. These include low production costs, fast charging, light weight to reduce the energy consumption of the EV during operation, high energy densities to enable long ranges, high reversibility to ensure a long service life, and high safety standards, especially in the event of accidents.

A major challenge in this context is that the LIB concept will soon reach its physicochemical limit with a maximum energy density of about 400 $Wh \cdot kg^{-1}$.[46-48] To exceed this boundary and achieve higher energy densities, the electrochemistry of the cell on the anode or cathode side must be changed, for example, by substituting individual materials. Another possibility leading to similar effects is to increase the amount of active material in the cathode by using thick electrodes.[49] The implementation of thick electrodes, however, is challenging since OLE are dual-ion conductors (DIC) with cationic transference numbers in the range of 0.27 (e.g., for $LiPF_6$). A large difference in the anionic and cationic partial conductivity of OLE leads to the formation of a concentration gradient within the electrolyte, which in turn limits the charge and discharge rates of the battery.[50-51] One of the most promising approaches on the anode side to significantly increase the energy density is to replace the intercalation electrode with a metal electrode.[52] The basic idea of this concept is to dissolve and rebuild the metal anode during the discharging and charging process, instead of reversibly incorporating and extracting metal (Me) ions into/from the host structure during discharging and charging. In other words, the charge transfer reaction at the anode interface involves crystal dissolution or growth ($Me = Me^+ + e^-$) rather than (de)intercalation. In most studies, lithium metal is considered as reversible anode material, since it may provide the highest possible increase in theoretical volumetric (2.061 $mAh \cdot cm^{-3}$) and gravimetric (3.860 $mAh \cdot g^{-1}$) capacity compared to graphite (760 $mAh \cdot cm^{-3}$ and 350 $mAh \cdot g^{-1}$, respectively).[53] Alternative anode materials such as sodium are discussed in only a small number of reports.[54-58]

The high interest in reversible parent metal anodes is due to the expected increase in the gravimetric energy density by 50% and in the volumetric energy density by 80% at the cell level compared to a conventional LIB.[44, 53] However, the implementation of this concept, especially the formation of the metal anode during charging, is a major challenge.[59] Inhomogeneous metal deposition leads to the growth of dendrites, which can easily penetrate conventional separators impregnated with OLEs. The resulting short-circuit causes thermal runaway of the battery, leading quickly to fire and thus poses a major safety concern.[60-61] Another challenge is the high reactivity of lithium, or alkali metals in general, when they come into contact with OLE in particular. Ongoing undesired side reactions consume electroactive species and thus lower the Coulomb efficiency and cycle life.[62-66] To control the reversible metal anode in secondary batteries and to

overcome the challenges described, much research is being conducted on SSBs. This is also evident at the industrial level, for example, in companies such as Toyota, Samsung, Panasonic, or Volkswagen.[67-69]

In an SSB system, a dense solid electrolyte (SE) separator takes the role of the permeable polyolefin membrane and the OLE. There are several good reasons to use an SE instead of an OLE. These include suppression of dendrite growth due to their mechanical properties, higher safety due to their non-flammable character, and increased Coulomb efficiency due to their lower sensitivity to side reactions. Suitable SE materials must meet various demands in terms of transport properties, thermal and chemical stability, and mechanical properties. The ionic conductivity of the SE should be as high as possible to minimize the internal cell resistance. This allows for thick electrode configurations and enables fast charging and discharging. The range of 10 $mS \cdot cm^{-1}$ and higher serves as reference value for the required effective SE ionic conductivity.[49, 70-72] In addition, the SE needs to be thermally stable under varying operating temperatures, for example, between −60 °C and 70 °C in the case of batteries in EVs.[73] A wide electrochemical stability window[74] is desirable to allow high operating voltages without decomposing the SE and to avoid the formation of an (insulating) solid electrolyte interphase (SEI). The requirements for the mechanical properties of the SE are even more diverse. SEs should be mechanically soft to compensate for electrochemically induced stresses, for example, in case of volume changes of CAM particles due to (de)intercalation of lithium. Here, the ability for reversible deformation helps to maintain physical contact with the CAM during cycling, reducing capacity fading.[75-76] At the same time, SE materials should exhibit high resistance to electrochemical-mechanical induced fracture, for example, due to dendrite or filament growth.

SEs can be classified into organic solid polymer electrolytes (SPE) and inorganic solid electrolytes (ISE). There are also hybrid concepts, which aim to combine the advantages of both components.[77-80] The mechanical properties of SPEs ensure easy processing (e.g., cold pressing) and battery cell manufacturing. The materials are inexpensive and exhibit a low density. The disadvantages of SPE , on the other hand, include the need for higher temperatures to achieve proper rate capabilities due to typically lower ion conductivities as well as the occurrence of a high interfacial resistance with the anode material.[81-82] The low ionic conductivity of SPEs is related to their character as DICs, which in turn causes concentration polarization effects similar to OLEs. ISEs, in contrast, are single-ion conductors (SIC) with an immobile anion framework and a transference number close to unity. This prevents concentration polarization across the electrolyte and enables higher ionic conductivities as well as better rate performance.[83] The thermal stability and non-flammability of ISE also ensure a high level of safety with regard to the safety tests designed for LIBs with liquid electrolytes.[83-84] Their mechanical properties, however, make manufacturing considerably more challenging. Hard ISEs often require energy-intensive hot-sintering steps to achieve a proper contact between grains and with CAM particles. Albeit, a temperature treatment of the CAM in contact with the SE may in turn harm the constitution of the CAM, affecting the battery performance.[85] The most promising ISE candidates can be divided into oxides and sulfides, which have different electrochemical and mechanical properties. Sulfides such as thiophosphates are characterized by high ionic conductivity and malleability at room temperature. Though, they show a rather narrow electrochemical window. Oxides, such as garnet ceramics, are chemically and thermally more stable, but their mechanical properties make them more difficult to process and manufacture.

Consequently, replacing a liquid electrolyte with a solid one poses many challenges, especially with respect to changing interfacial properties and requirements. A major benefit of liquids is that they can more efficiently compensate for stresses in the system (e.g., CAM breathing) and thus do not affect the mechanical stability of physical contacts.[86-91] Another important aspect is the (de)intercalation of lithium into the CAM. This requires both electronic and ionic percolation pathways to ensure the supply and removal of both types of charge carriers.[86-87, 92-95] Unlike OLEs, the mechanical properties of ISEs prevent infiltration of the pore space within the cathode. This often results in residual porosity and reduced wetting

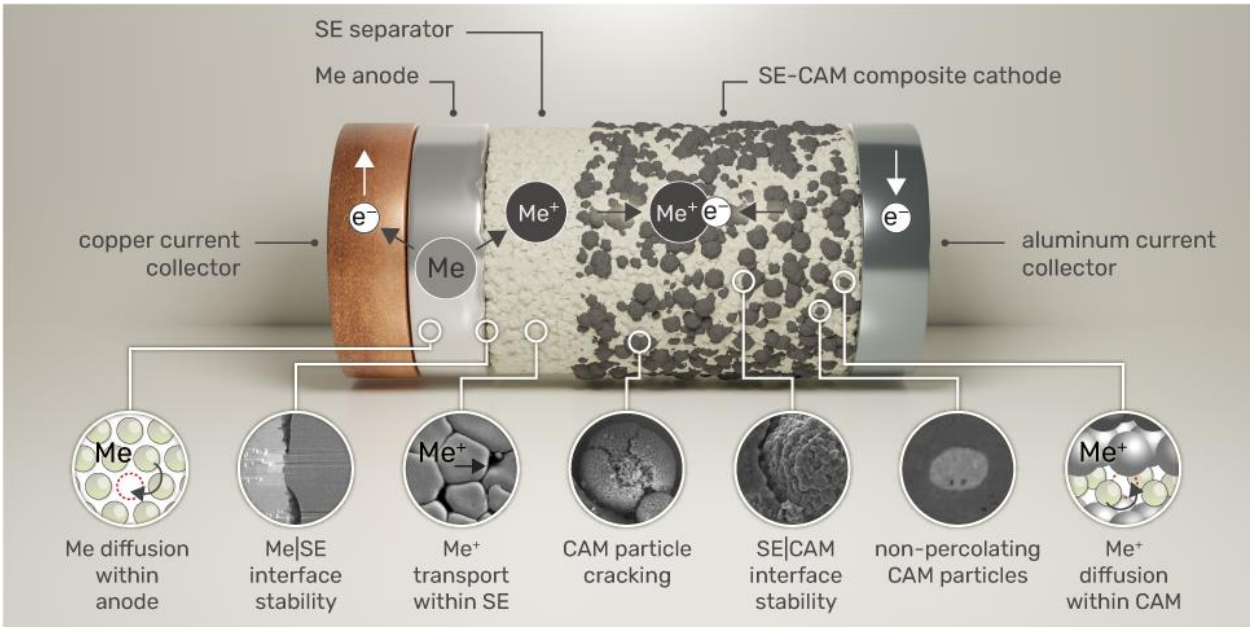

Figure 2. *Schematic architecture of an alkaline metal solid-state battery. It consists of a copper current collector, a parent metal anode, an SE separator, an SE-CAM composite and an aluminum current collector. The close-ups highlight certain critical kinetic aspects that determine the KPI of the SSB cell. Credit: Elisa Monte/JLU Giessen.*

of the CAM surface. Therefore, the microstructural configuration of the composite cathode appears to be of great significance. It is essential to ensure sufficient percolation paths and physical contact between CAM and ISE already during the manufacturing process.[96] On the anode side, the (electro)chemical, mechanical, and morphological stability of the interface between the alkali metal and the SE separator poses an additional challenge.[90, 97-99] The metal anode needs to be reversibly dissolved and deposited during discharging and charging, respectively. This requires compensation for the stresses introduced by volume changes, as well as homogeneous metal dissolution (i.e., stripping) and deposition (i.e., plating) to prevent various failure mechanisms of the system. These include dendrite or filament growth within the SE separator and contact loss due to pore or void formation at the alkali metal|SE separator interface.[97, 100-104] The stripping and plating behavior also depends on the micro- and mesostructure of the SE separator and the diffusive transport of atoms and interstitials in the metal anode.[101, 105-108]

In conclusion, the interface characteristics are decisively for the battery performance. SSBs require an optimized electronic and ionic percolation network in the composite cathode, fast charge transfer across all interfaces, fast ion diffusion in the CAM, fast ion transport in the SE, and morphologically, chemically and mechanically stable interfaces during operation. Degradation of physical contacts due to morphological changes is one of the major challenges on the road to commercialized SSBs. There are several strategies to overcome these issues, starting with the development of novel concepts to avoid degradation effects at the electrode|electrolyte interfaces, such as the deposition of protective coatings, and ending with the synthesis of improved separator or CAM materials.[109-115] In this context, combinatorial approaches from theory and experiment are becoming increasingly important. They aim to make research as resource and energy efficient, cost effective and sustainable as possible, while achieving scientific progress as fast as possible. Statistical approaches, such as design of experiments to systematically render the parameter space, the build-up of ontologies and the application of machine learning algorithms to identify hidden patterns in the data, are slowly complementing the spectrum of traditional methods, such as density functional theory, molecular dynamics, or kinetic Monte Carlo.

In recent years, an autonomous and rapidly growing research field for modeling whole battery cells has emerged, based on the early work of the Newman group in 1994. These models aim to account for all interactions between the cathode, anode and all kinds of interfaces.[116-124] Such modeling requires a variety of input parameters for charge transport, diffusion processes, reaction kinetics at the interfaces, and the microstructural composition of the system. Describing all these chemical processes often results in more than twenty parameters including multiple diffusivities, conductivities, rate constants, and geometric parameters such as particle size, separator thickness, or porosity.[125-127] Most of them can be determined by experimental measurements, leaving only a few unknowns. A detailed review of the literature, however, often reveals a huge variance in the experimentally determined parameters. Sometimes the published values of the same parameter span several orders of magnitude. This may be due to differences in sample preparation, measurement uncertainties, or even misinterpretation of experimental data.[128-130] John von Neumann (1903 – 1957) once famously said about complex models: "*With four parameters I can fit an elephant, and with five I can make him wiggle his trunk*." This indicates that the uncertainty in the input parameters makes the predictive power of such global models questionable. Thus, the findings from battery modeling are closely related to the quality and interpretation of the experimental data. This motivates studies on the determination of microscopic material-specific transport quantities such as conductivities and diffusion coefficients from experimental data obtained with well-established electrochemical methods such as IS.

1.3 Transport Characterization by Impedance Spectroscopy

Impedance spectroscopy is an electrochemical measurement technique where the system under investigation is excited by an external alternating electric field and the response signal is measured as a function of frequency. The origins of IS can be traced back to the 19th century when Kohlrausch experimented with alternating currents to determine electrolyte conductivities, Heaviside worked on linear system theory and Warburg worked on the impedance of electrochemical systems and diffusion processes.[131-134] For a long period of times, almost 100 years until the middle of the 20th century, technical circumstances allowed impedance measurements only for excitation frequencies above 100 Hz. This hampered its application, for example, for the study of corrosion and electro-dissolution mechanisms, since the experimentally accessible frequency range did not reach down to the slow relaxation times of reaction intermediates. Thus, IS has mostly been used to investigate the polarization behavior of interfaces of biological membranes,[135-136] or liquid electrolytes.[137-144] The development of the first frequency response analyzers in the 1970s, combined with the introduction of potentiostats about two decades earlier provided access to frequencies down to 0.1 Hz and enabled automation of data acquisition.[145-148] This led to increased interest and application of the method.[149-150] The study by Bauerle on the conductivity of ionically conducting electrolytes from 1969 represents a milestone in the research field of batteries and fuel cells.[151] It demonstrated for the first time that IS is a useful tool for the characterization of ceramics and motivated further theoretical and experimental investigations in the following years.

IS has become one of the most popular and powerful electrochemical tools for studying battery cells, reaction mechanisms, and corrosion processes. As a result, the number of publications containing IS data has increased exponentially over the past two decades. The findings obtained complement other electrochemical measurement methods such as chronopotentiometry, chronoamperometry cyclic voltammetry, and scanning electrochemical microscopy.[152-153] In this context, IS provides an understanding and quantitative information about transport mechanisms in complex electrochemical systems with comparatively little effort and in rather short measurement times. This includes physical and chemical details about transport effects taking place, dynamics of bound or mobile charge carriers, microscopic transport quantities such as chemical reaction rates, dielectric properties, diffusivities or conductivities, and

(micro-)structural changes in the sample during operation. The direct correlation between impedance features and reaction or failure mechanisms makes IS interesting for in situ and operando system diagnostics. It is suitable for predicting performance aspects of fuel cells, chemical sensors, and biosensors, or for understanding the state-of-health of batteries in EVs by estimating the internal temperature of the cell. Another field of application is process characterization in the form of empirical quality control procedures, for example, to evaluate the mechanical performance of engines or the quality of paints, emulsions, electropaintings, thin-film technologies, and material fabrications.[1, 154]

1.3.1 Fundamentals and Standard Data Analysis

IS relies on the fact that various microscopic transport processes in the system occur at different rates. The deviating kinetic behavior on the time scale is related to, for example, the type of charge carrier, the microstructure of the sample, or the nature and type of an electrode. Diffusion processes are quite slow, with typical relaxation times in the range of seconds. Ion migration through SEs is several orders of magnitude faster, with relaxation times in the range of milli- or microseconds. This in turn is much slower than electron migration in doped semiconductors with relaxation times of picoseconds or even less.[155-156] To deconvolute processes occurring on different time scales, an external alternating electric field of fixed (angular) frequency $\omega = 2\pi \cdot f$ is applied to excite the system under investigation either potentiostatically (i.e., applied voltage U) or galvanostatically (i.e., applied current I). The response signal is measured in terms of amplitude and phase shift φ. The impedance can be calculated using Ohm's law ($Z = U/I$).[157] This procedure is repeated over an extended frequency range, typically between a few millihertz and megahertz, resulting in a discrete complex-valued function $Z(\omega)$ known as the impedance spectrum. In an ideal scenario, each process dominates the transport characteristics in a certain frequency range, revealing impedance characteristics and signatures in the spectrum that allow a separation. This provides, for example, access to material-specific parameters such as polarization resistance, double layer capacitance, or bulk conductivity, instead of only effective transport quantities as in the case of a direct current measurement.

The macroscopic impedance response signal reflects a superposition of all effects within the system between the working electrode (WE) and the counter electrode (CE) in the case of a two-electrode setup. These include the microscopic transport processes under study, but also unwanted measurement artifacts due to stochastic noise, interfering electric fields (e.g., 50 Hz mains frequency), varying environmental conditions (e.g., temperature or humidity fluctuations, and vibrations), and the measurement setup itself. Several disturbing effects can be suppressed by simple experimental measures, such as using a Faraday cage to shield electric fields or by twisting the cables to reduce inductance contributions.[154] The Kramers-Kronig (KK) relations can assist in revealing the error structure in the measured data due to instrumental artifacts or non-stationary behavior of the system. The KK relations are Hilbert integral transformations that holistically link real and imaginary parts of any complex function that is analytic in the upper half-plane.[158-161] This means that the measured real or imaginary part alone is suitable to predict the corresponding counterpart, which can then be compared with the measurement result to check the quality of the recorded data.

The KK relations rely on the assumption that the system is linear, stable and causal. These are the three basic requirements that a system should meet when examined using IS.[154] The constraint of *linearity* addresses the response signal to an applied perturbation. The current-voltage characteristic of an electrochemical system is generally a non-linear function. It can be expressed mathematically as a Taylor series, whose linear term has to dominate the global behavior in the case of an IS measurement. This requires small perturbation amplitudes, typically in the range of tens to hundreds of millivolts for potentiostatic and milliamperes for galvanostatic experiments, respectively. The exact choice of the applied

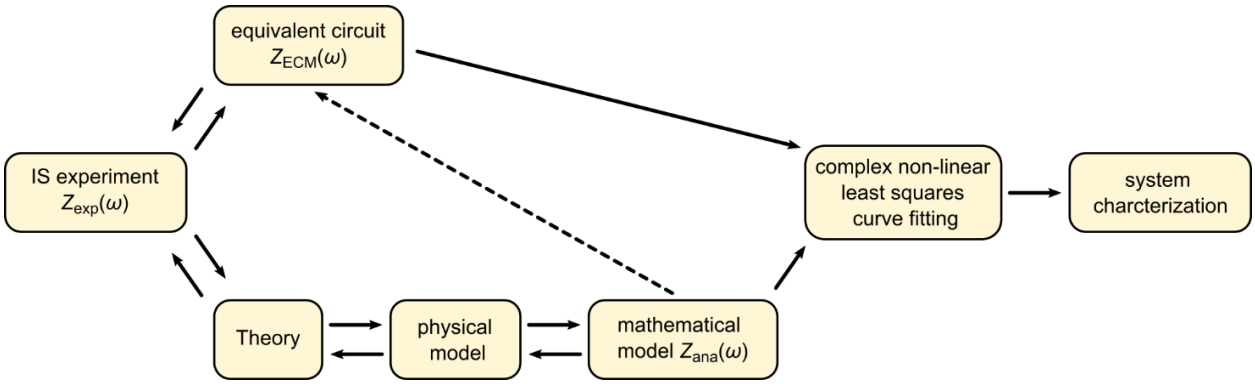

Figure 3. *Flow diagram for the standard analysis of experimental IS measurements. Adapted with permission.*[1] *Copyright © 2018, Wiley.*

amplitude is a compromise between achieving a sufficient signal-to-noise ratio and simultaneously satisfying the linearity condition. The *stability* constraint focuses on ensuring that the excitation does not alter the system in any way. This is particularly challenging for battery systems, as both potentiostatic and galvanostatic IS involve charging and discharging steps.[162] Research efforts in this direction have led, for example, to time correction methods in the investigation of rechargeable LIBs or to criteria for determining an optimal excitation amplitude.[163-165] The *causality* condition targets the time scale of the response signal to the perturbation, i.e., the reaction should not precede the perturbation. This ensures that the measured signal is only due to the applied excitation. Undesirable non-stationary or drifting behavior is often encountered at low frequencies due to the long measurement times ($t \sim 2\pi/\omega$).

The first step in analyzing an impedance spectrum is to check the validity of the measurement using the KK relations and, if necessary, to remove corrupt records from the dataset. The analysis aimed at distinguishing individual transport effects is usually performed in the frequency domain. Thereby, the impedance spectrum is typically visualized in the Argand diagram, i.e., the so-called Nyquist plot. This is a frequency implicit data representation, where the negative imaginary part of the impedance $-Z''$ is plotted versus the real part of the impedance Z'. It is complemented by less common explicitly frequency-dependent representations, the group of Bode diagrams that consider negative imaginary $-Z''$ and real part Z' of the impedance, or absolute impedance $|Z|$ and phase angle φ versus angular frequency ω. All data representation forms also apply to transformed impedance functions such as the admittance $Y(\omega) = Z^{-1}(\omega)$, the modulus $M(\omega) = \mathrm{i}\cdot\omega\cdot C_{geo}\cdot Z(\omega)$, and the dielectric permittivity $\varepsilon(\omega) = M^{-1}(\omega)$ functions. The geometric capacitance $C_{geo} = \varepsilon_0\cdot A/L$ corresponds to the empty measurement cell, i.e., ε_0 describes the vacuum permittivity and A/L the cell constant of the setup. Each of these functions emphasizes different aspects of polarization and charge transport in a material and has been or is still being used in different research areas.[156]

The visualization of the impedance function gives an initial idea of the number of transport processes taking place in the underlying system. A rule of thumb often used in the literature suggests that each semicircle in the Nyquist representation corresponds to an electrical transport process. The corresponding macroscopic transport parameters are usually derived using physically based equivalent circuit models (ECM). This requires detailed knowledge of the system under investigation in terms of the migration and reaction processes taking place and the type of charge carriers involved. The basic concept is to assign different circuit elements to these microscopic processes and then assemble them into a single equivalent circuit model. The resulting ECM in turn is designed to describe the impedance response of the macroscopic sample. In consequence, all elements in the macroscopic picture have an analogue at the microscopic level. Capacitive behavior (i.e., polarization effects) can be described by capacitors, inductive behavior by coils and resistive behavior by electric resistors. An electric migration process combines capacitive and resistive

behavior and is typically modeled by a parallel circuit of a resistor (R) with a capacitor (C) forming an RC-element.

For solid (ceramic) single ion or electron conductors, the ECM approach leads to boundary layer models such as the *brick layer model* (BLM). The classical BLM, originally proposed by Bauerle in 1969, consists of two RC-elements connected in series that represent bulk transport through grains and transport across grain boundaries, respectively.[166-170] On this basis, extensions have been developed in the following years, for example, to consider conduction along grain boundaries.[171-172] In contrast, mixed ionic-electronic conductors (MIEC) or DICs are typically described by a variant of a transmission line model (TLM). TLMs consider the interaction between the serial paths of different charge carrier types, for example, by a chemical capacitance.[173-175] In each case, the respective electric ECM is used to model the experimental spectrum through complex non-linear least squares curve-fitting usually applying Levenberg-Marquardt strategies or linear regression.[176] This gives access to the macroscopic transport parameters (R_i, C_i) of the individual transport effects within the system.

A major drawback of the ECM analysis approach is that it is not free of assumptions about transport mechanisms in the system. Several different equivalent circuit models, even physically untenable ones, can lead to the same result.[177-179] Consequently, the conclusions derived from the measurement are ambiguous, and the screening of possible equivalent circuits already requires a lot of information about the system. In addition, the analysis becomes more complicated when several transport effects contribute to the impedance in similar frequency ranges. This leads to overlapping signals in the spectrum, which prevent visual identification of different impedance contributions by pattern recognition. Therefore, it is useful to consider not only the impedance function $Z(\omega)$, but also those of the transformed admittance $Y(\omega)$, modulus $M(\omega)$, and dielectric permittivity $\varepsilon(\omega)$ functions. Another approach is the transition from the frequency domain to the time domain, since the resolution in the latter is much higher than in the Nyquist or Bode diagrams. Such distribution function-based analysis methods have, at first glance, distinct advantages over ECM analysis. They do not rely on any *a priori* assumptions about the system, making them a valuable alternative for interpreting impedance data. In addition, they can also assist in equivalent circuit analysis, for example, in finding and constructing a suitable model.[180-183]

The distribution function $\gamma(\tau)$ underlying an impedance function $Z(\omega)$ can be determined by performing a distribution of relaxation times (DRT)[184-188] or distribution of diffusion times (DDT)[189-191] analysis. The basic concept relies on the fact that any model function can be expressed by a series connection of an infinite number of RC-elements (i.e., a Voigt circuit).[192] Therefore, the distribution function $\gamma(\tau)$ can be expressed as a weighted sum of Dirac distributions $\gamma(\tau) = \Sigma_i\, r_i \cdot \delta(\tau - \tau_i)$. The singularity τ_i corresponds to the time constant and the weight r_i to the resistance of the respective RC-element. The determination of the expansion coefficients r_i requires the solution of an ill-posed inverse problem in the form of a linear Fredholm integral of the first kind.[193] This means that the solution of the problem is not unique and several distribution functions $\gamma(\tau)$ can lead to the same result within the experimental uncertainty.[194-195] This is particularly challenging for discrete functions such as the measured impedance $Z(\omega)$, where only a finite number of frequency points are sampled (typically about 10 points per decade). Therefore, intense research has been conducted in recent years on special solution methods and algorithms to deal with the ambiguity and to avoid false or non-physical signals and artificial oscillations. These include Fourier transform methods,[196-198] evolutionary programming,[199-200] maximum entropy,[201-202] Tikhonov or ridge regression,[192, 194, 203-207] hierarchical Bayesian regression,[178, 208-209] elastic net regression,[210] Gaussian process regression,[211] and neural networks.[212]

Many of the methods listed are quite sophisticated and time consuming to apply. They require interpolation, extrapolation, data preprocessing with filters, and fine tuning of settings and hyperparameters. Regression methods are one of the more simple but robust approaches that allow reliable calculation of a DRT with

limited error sources and good stability to noise in experimental data. The Tikhonov regularization approach is well suited for automatization, especially for synthetic data. It depends only on a single regularization hyperparameter λ, which determines the smoothness of the calculated DRT. The solution process involves the discretization of the Fredholm-type integral equation and the expansion of $\gamma(\tau)$ into basis functions. Dirac distributions are a suitable basis only in the case of continuous analytic functions, since they do not overlap. For discrete functions, however, this is a necessary property to ensure that the full range of relaxation times can be modeled, i.e., also for time steps $1/\omega$ which have not been sampled. The focus is therefore usually on positive-definite radial basis functions such as Gaussian or differentiable Matérn functions. As a side effect, however, the coefficients in the expansion formula no longer correspond directly to the resistance, as it is the case with Dirac basis functions. The full width at half maximum of the radial basis functions correlates with the number of discrete frequency data points. Thus, it determines the resolution and precession of the DRT analysis.

The application of the discretized integral equation to all sampled data points leads to a linear system of equations with the coefficients of the radial basis functions as unknown parameters. The resulting matrix equation is slightly modified by adding an additional regularization term to account for the effect of noise and errors in the impedance data. This penalty term is proportional to the first or second derivative of the distribution function $\gamma(\tau)$ itself. Simply speaking, it introduces a threshold value at which fluctuations in $Z(\omega)$ are due to actual transport effects. This allows to suppress artificial signals, but at the cost of a reduced resolution power of the method. Therefore, the regularization parameter should be chosen as small as possible to achieve high resolution, but also as large as necessary to avoid artificial signals. This shows the importance of high-quality measurement data to achieve valuable DRT results. In general, the linear system can be solved strictly mathematically, but this can lead to negative coefficients and thus to a non-physical solution. The physical solution can be calculated by quadratic programming under the constraint that the minimum value of the coefficients is equal to zero. The resulting distribution function $\gamma(\tau)$, which is obtained by inserting the expansion coefficients into the decomposition formula, is visualized as a function of the relaxation time τ. A signal in the DRT is typically related to a transport effect in the system. Its center position corresponds to the time constant τ_i, the area under the signal represents the resistance value R_i, and the corresponding capacitance can be calculated by $C_i = \tau_i/R_i$. In general, the DRT approach shows superior performance compared to the ECM approach in identifying the number, size, and average timescale of physical processes within the system.

1.3.2 Methods for Multidimensional Transport Modeling

Obtaining high quality impedance data requires significant experimental effort. This concerns, among others, compliance with the KK relations and reproducibility of measurements. It is noteworthy that the uncertainty analysis of derived microscopic material-specific transport parameters such as conductivities mostly focuses on the measurement of structural quantities such as sample thickness or electrode area.[154, 213] The assignment and interpretation of contributions in the impedance or distribution function is usually not considered in this process. A semicircle in the Nyquist diagram and a signal in the DRT is usually attributed to an electric migration process within the system. This approach has led to great success in the past, especially for systems involving liquids. However, it is not obvious whether every contribution in the impedance and every signal in the distribution function is always due to electric migration processes. The uncertainty results from the mapping of the macroscopic response signal of a multidimensional sample to a highly simplified, lower-dimensional ECM. Such an ECM cannot describe the formation of percolation paths due to the microstructure of a solid-state system.[214-222] This poses a major challenge for the derivation of quantitative values for the material-specific parameters, as well as for the qualitative interpretation of the individual contributions in the impedance spectrum. The arising difficulties are commonly not

considered, but they highlight the need for a deeper theoretical treatment of the problem and the incorporation of additional experimental evidence about the structure of the sample into the modeling approach.

Impedance modeling techniques can be categorized into physicochemical and electrical models based on the underlying concepts. The former describes the elementary kinetics of chemical reactions and diffusion processes in terms of rate equations in the time domain. This results in a sophisticated system of ordinary differential equations, which can be solved using transient numerical simulation approaches.[223-228] Thereby, a periodic (sinusoidal) potential $\varphi(t)$ at fixed frequency is applied to the system as an excitation signal and the current response signal $I(t)$ is measured until a periodic steady state is reached. The corresponding impedance value can then be calculated from the transient traces by Laplace transformation. Repeating this procedure for discrete values in the frequency range of interest will yield the impedance spectrum $Z(\omega)$.[224] Another similar but less time-consuming approach is to consider a single fast non-periodic steplike perturbation signal $\varphi(t)$ and the measure of the resulting relaxation of the current signal $I(t)$. The time-dependent potential and current functions can then be transferred to the frequency domain by computing the Fourier transform. This allows the calculation of impedance by dividing $\varphi(\omega)$ and $I(\omega)$.[225] In general, physicochemical models can be very complex and messy, requiring long computation times, multiple variable parameters, and often requiring approximations with respect to the structural setup of the system.

Electrical models such as ECMs can be a more intuitive way to interpret the physical and chemical processes taking place in the system. They are usually solved in the frequency domain and are particularly suitable for the phenomenological description of electrochemical systems. A major limitation of ECM analysis is that commercial software only allows data fitting for simplistic electric circuits that do not properly reflect the structure of the system. In consequence, the global nature of the impedance signal hinders the interpretation of IS data in terms of fundamental microscopic material-specific parameters. A more suitable electric model description requires methodologies and software that allow for transport modeling through real system structures. One way is to apply the finite element method to discretize the sample volume and then to use Poisson's equation for the transport description considering Dirichlet and Neuman boundary conditions for the electrodes and the sample surface.[229-240] Another possibility for transport modeling is to perform a nodal analysis.[241-245] This concept is based on Kirchhoff's current law, which states that the algebraic sum of currents in a network of conductors is zero at each node.[246] Voxelization of the model structure leads to a node network in which different local equivalent circuit diagrams can be inserted according to the structural conditions. Solving Poisson's equation or nodal analysis gives the potential distribution within the system. This allows the calculation of the total current flowing through the structure. It can be used in combination with the applied potential difference between the electrodes to determine the impedance at a fixed ω using Ohm's law. This process can be repeated several times at different frequencies to map the full impedance spectrum $Z(\omega)$.

1.4 Challenges and Difficulties in Impedance Analysis of Solid-State Systems

Joachim Maier and Jürgen Fleig were among the first at the end of the 20th century to develop a simulation tool based on Poisson's equation to investigate the impedance of solid systems in more detail.[229-240] Most of their studies are motivated by the application of ceramics in solid oxide fuel cells (SOFC). Their results showed qualitatively that the microstructure of the sample and the physical contact area at the electrode interfaces have a major influence on the shape and magnitude of the impedance. In the following years, there were only a few more isolated upcoming reports dealing with structural influences on derived microscopic transport quantities.[247-248] This shows that the early findings in the field of SOFCs and the importance of geometric effects in IS analysis have not reached a wider scientific audience. They are rarely

considered in data interpretation even today, more than twenty-five years after the first reports. The reasons are multifaceted, starting with the fact that most of these papers[229-240] appeared at a time when the IS method was not yet popular and the role of solid-state systems, for example, in battery research, was not yet as important. In addition, the analysis approach using simple one-dimensional ECMs in commercial software is simple, fast, and can be applied by anyone without major barriers, yielding a set of numerical values for the transport parameters (although not necessarily the correct ones). In contrast, a multidimensional IS analysis is less accessible and requires more effort, for example, in the form of a prior comprehensive structural analysis.

However, the importance of reliable IS analysis cannot be underestimated. The consequences of insufficiently determined material-specific transport parameters and misinterpretation are tremendous. They range from the propagation of uncertainty through their subsequent application in (battery) modeling to falsely assumed electric migration processes in the system. Therefore, the goal of this Ph.D. thesis is to develop an automated modeling workflow to gain further insight into the influence of geometric effects on both the impedance and the distribution function. This includes gaining detailed knowledge of the quantitative and qualitative effects that may occur when the impedance response signal is projected from a multidimensional to a lower dimensional picture. In a broader context, assigning and understanding the behavior of structurally induced impedance signatures in the frequency or time domain can significantly expand the scope of IS in the field of early failure detection in applications.

1.4.1 Realization of a Computational Modeling Workflow

The established workflow for systematic impedance studies consists of three pillars, namely model system and structure generation, the actual impedance modeling, and automated data screening of computational results. The type of model systems considered depends on the question to be answered. Here, in particular, the influence of structural effects on the 100 nm to 100 µm scale on the macroscopic transport quantities and their relation to material-specific parameters is investigated. To this end, many synthetic structures have been generated as voxel representations using simple algorithms that are easy to implement. More complex model structures and grain geometries have been accessible using open source or commercial software such as *MicroStructPy* or *GeoDict*. They allow the simulation of micro- and mesostructures with defined grain geometries, grain size distributions and volume porosities.[249-251] The input parameters required to generate statistical twin structures are typically obtained from focused ion beam scanning electron microscopy images. To this end, an automated segmentation pipeline has been implemented to determine grain and pore size distributions.[252] The applied transfer learning approach consists of feature extraction using two pre-trained layers of a convolutional neural network (CNN), binary segmentation using a random forest (RF) classifier, and instance segmentation using built-in functionalities of the scikit-image library. This process involves manual segmentation of small sub-regions of about two training images and extraction of feature maps based on the pre-trained CNN in order to train the RF classifier. A detailed description of this approach can be found elsewhere.[252-253] Having such a segmentation routine is particularly valuable when dealing with experimental structural data. This applies not only to the derivation of size distributions, but also to the automated generation of true digital twin structures.

The second pillar is the transport description through the generated model structures. There are several ways to do this, ranging from a physicochemical or purely electrical transport description, to the use of commercial or in-house software. In this Ph.D. thesis, an electrical system description is used in a self-implemented code. Several reports in the literature indicate that different electrode configurations are realized in experimental measurements. This includes symmetrical arrangements of two identical physical contacts, asymmetrical considerations of electrode sizes and arrangements, and microelectrode geometries.[94, 105, 180, 254-255] Typically, the effect of electrode geometry can only be considered with great

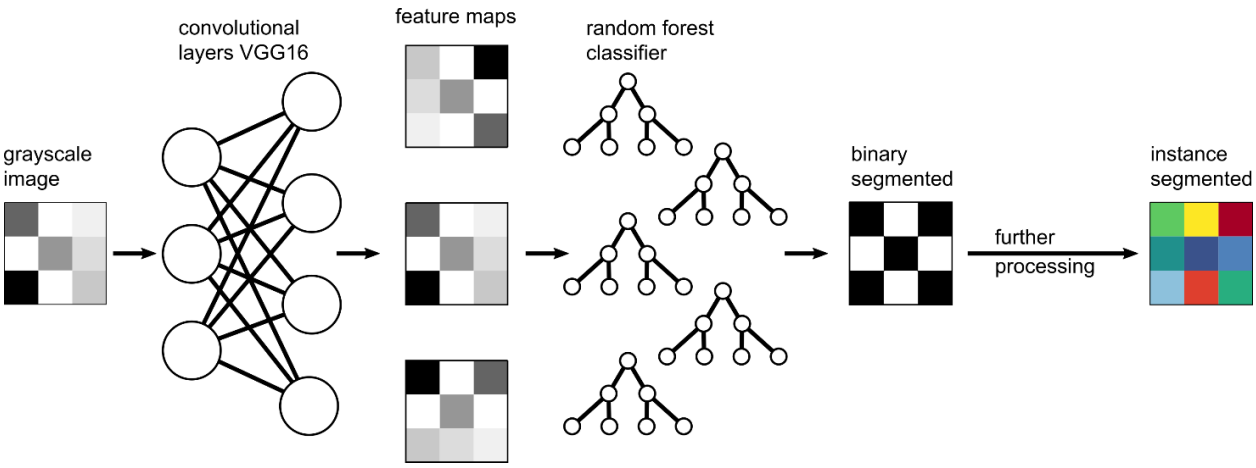

Figure 4. *Overview of the segmentation workflow implemented to determine digital twins, and grain or pore size distributions from scanning electron microscopy images. Adapted with permission.*[252] *Copyright © 2022, Sascha Kremer.*

effort and detailed knowledge of commercial software (code) such as *COMSOL*. Instead, an internal implementation offers great flexibility with respect to different contact situations and also the extension of models, e.g., in terms of additional microscopic processes etc.

An essential criterion in the selection and development of models in general is to focus on *what we want to learn and what can be learned*. Thereby, it is often not necessary to consider every little detail or every small local effect. History shows that the best experimental or theoretical research results are only as good as they are presented in a general and understandable manner. Physicochemical models can undoubtedly provide deep insights into the dynamics of the system under study, but they are often very complex and hard to follow by (experimental) scientists. Electric models, on the other hand, are much more descriptive at first glance. They merely extend the standard impedance analysis procedure used by experimentalists to a more complex model geometry. They rely on only a few microscopic material-specific transport quantities, but are sufficient, for example, to study the impact of structural effects on the impedance response. This ensures high visibility in the scientific community.

The motivation of the studies conducted addresses challenges in SSB research due to today's massive interest regarding improvement and innovations in electrical energy storage systems. Nonetheless, the conclusions derived are general in nature when considering solid-state systems. The ultimate goal is to understand the impedance behavior of the entire battery cell by correlating the impact of microscopic transport effects and micro- or mesoscopic structure in the system with signatures in the macroscopic impedance and distribution function. Understanding these correlations will allow one to use IS as a monitoring tool for structural changes in the system even in operando measurements. However, an SSB is such a complex compound with various overlapping transport and structural effects that *trying to look at an entire battery at once is like running before you can walk*. In other words, the behavior of individual parts (e.g., anode, SE separator, cathode) must first be identified and clarified, before the behavior of the entire cell can be fully understood. Therefore, the focus of this work was solely on the anode side by considering a ceramic (ISE separator) between two alkali metal anodes as a model system, representing a symmetric half-cell electrode configuration. The conducted studies target the influence of the micro- and mesostructure of the ISE separator and the effect of the interface morphology at the electrodes on the impedance and distribution function.

The transport computations were performed using an electric network model, based on nodal analysis. This is a three-step process consisting of setting up the node network, defining the local transport description, and solving the linear system of equations. First, the generated model structures are discretized using a voxelization routine, and the node network is built by assigning a node to the center of each voxel. The next

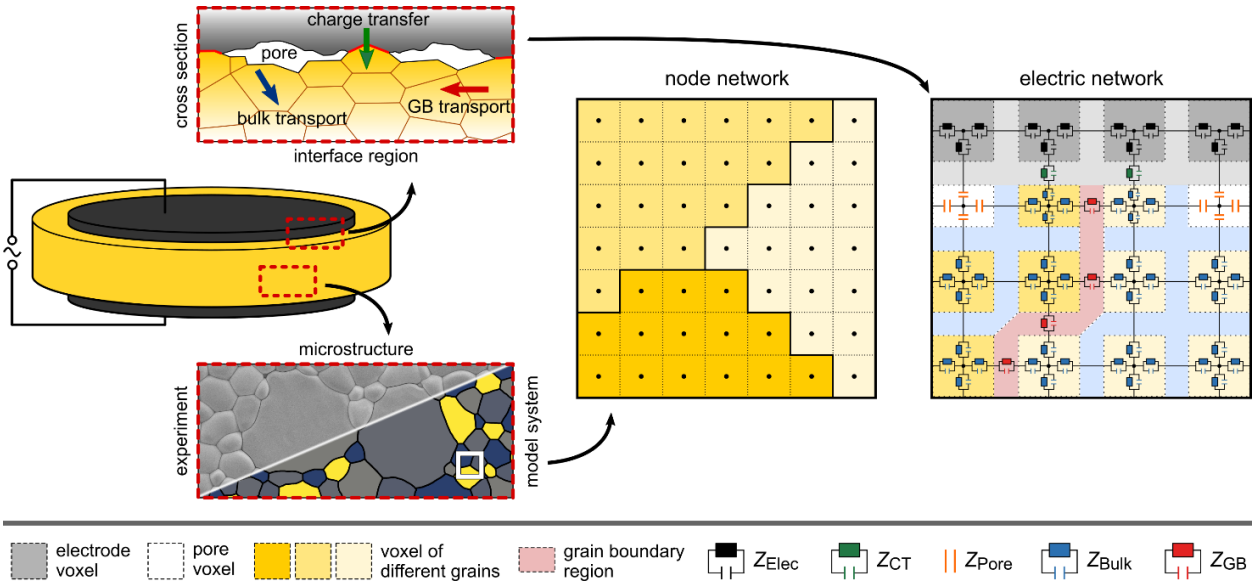

Figure 5. *Schematic representation of the modeling workflow implemented to compute the transport through realistic multidimensional systems. It consists of setting up a node network, defining the local transport description in the electric network, and computing the transport by nodal analysis.*

step is to identify the local transport processes that occur between two nodes and to define an appropriate electrical transport description. The ceramic ISE materials considered are SICs, i.e., the modeling focuses solely on ion transport. The systems studied show a grain structure and include crystal growth or dissolution at the electrode interface. Thereby, morphological instabilities at the interface between the metal electrode and the ISE separator have been considered, in particular the formation of pores or the formation of material phases with properties different from those of the bulk material. Ionic transport or charge transfer processes are described by *RC*-elements. The local capacitive behavior of pores is modeled by capacitors in the multidimensional electric network. The resistances and capacitances of the local circuit elements are calculated according to the rules for conductors and plate capacitors based on conductivity and permittivity, respectively. Local variations in these material-specific parameters were not considered in the computations in order to keep the number of variable quantities to a minimum. In the final step, the electric network is transformed into a linear system using Kirchhoff's current law. This in turn is solved using a variant of the conjugate gradient method.[246, 256] A detailed description how to implement this procedure can be found elsewhere.[245, 257]

Note that this type of transport modeling is a continuum description, i.e., local material-specific parameters such as conductivities or permittivities are assigned to structural elements. Quantum effects are not explicitly considered, i.e., the charge carriers (electrons and ions) are treated as classical particles.[258-260] However, quantum mechanical features may be implicitly contained in some of the microscopic material-specific parameters, e.g., quantum tunneling effects may contribute to the conductivity associated with grain boundaries. In that sense, the treatment of the microscopic transport here implies that the de Broglie wavelength λ_{dB} of the charge carrier is smaller than the voxel resolution d_i, i.e., the smallest characteristic length scale used to digitalize the micro- or mesoscopic structure of the sample. The condition $\lambda_{dB} < d_i$ is always fulfilled in the case of ions as the corresponding λ_{dB} are on the scale of atomic bond length, and usually also for electrons as long as d_i is of the order of several tens of nanometers.

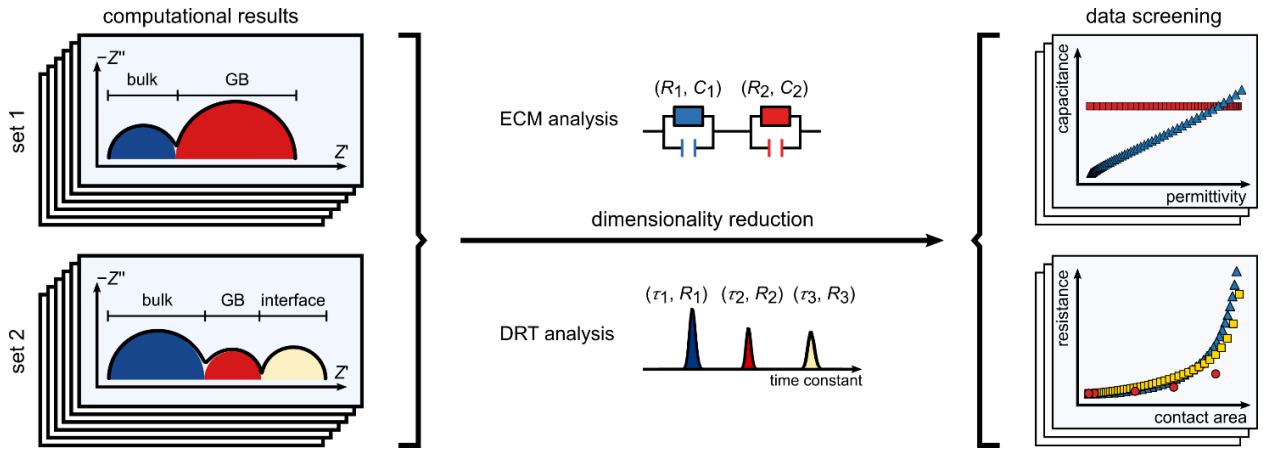

Figure 6. *Schematic representation of the data screening workflow. The computational results are mapped to a lower dimensional space using ECM analysis. Here, the developed DRT tool supports the automatic determination of the initial parameter estimate for the minimization step.*

The third pillar deals with IS data analysis. The investigation of individual structural effects and the influence of certain material-specific parameters on the impedance results in a large amount of data in the form of several thousand computed impedance spectra. Therefore, it is reasonable, at first instance, to map the single impedances to a few characteristic parameters using ECM analysis in order to accelerate data screening. Third-party analysis software such as *RelaxIS 3* is only suitable for small datasets, since the calculation time increases exponentially for more complex ECMs and large amounts of data. This motivated the implementation of a custom fitting routine based on complex non-linear least squares minimization. As a result, multiple impedance spectra can be fitted in parallel on high performance computers, which drastically reduces the calculation time. Apparently, the quality of the fitting result when searching for the global minimum, depends strongly on the choice of the initial parameter guess. The initial parameters were first calculated automatically by a generic algorithm. After the successful implementation of a custom DRT software based on Tikhonov regularization, it was replaced by the analysis result of the distribution function $\gamma(\tau)$. A detailed description of the realization of the in-house DRT software can be found elsewhere.[261] The visualization of the derived fitting parameters allows fast identification of trends and records that are of particular interest, which can then be studied in more detail.

1.4.2 The Effect of Microstructure and Interface Morphology

The application of the developed modeling software has resulted in six published papers up to now. The first publication, "*Understanding the Impact of Microstructure on Charge Transport in Polycrystalline Materials Through Impedance Modelling*", addresses the effects of the microstructure of a ceramic sample on the impedance (see chapter 2.1).[245] The structural data considered reflect parts of dense ceria thin films visually examined by scanning electron microscopy.[254] The computations performed assume ideally-reversible electrodes at conform interfaces and account for a single mobile charge carrier species only. It is demonstrated that the formation of percolation paths leads to structural signatures in the impedance and distribution function. These are visually observed in the computed impedances and the corresponding DRT. In addition, such signals are also derived analytically based on a simple two-path model. This highlights the inherent problem with IS standard analysis using pattern recognition. It is a misconception that every impedance contribution can be assigned to an electric migration process. Another effect of microstructure and resulting percolation are quantitative constraints on the derived material parameters. These are usually calculated using a classical BLM approach. This includes a fitting step of the impedance with two *RC*-elements connected in series, where the circuit elements describe transport through the bulk of grains and

across grain boundaries. The corresponding macroscopic parameter pairs (R_i, C_i) are then transformed into material parameters (σ_i, ε_i) by assuming a homogeneous structure consisting of a three-dimensional arrangement of face-sharing cubic grains with a constant edge length and grain boundary layers with a constant thickness in between. The resulting quasi-one-dimensional transport in the system ensures the formulation of analytical equations linking the macroscopic and the microscopic levels. The application of this procedure to synthetic IS data considering real microstructures shows that, in particular, the calculated grain boundary material parameters yield deviations in the order of 100% from the actual microscopic material-specific quantities. This is significantly larger than the influence of inaccuracies in the determination of structural parameters (e.g., sample thickness) or the macroscopic transport quantities in the ECM fitting process.[213] The estimate of the error band improves comparability between different studies on the same material published in the literature and provides useful information about realistic parameter ranges.

The follow-up study, "*Influence of Microstructure on the Material Properties of LLZO Ceramics Derived by Impedance Spectroscopy and Brick Layer Model Analysis*", explicitly investigates garnet-type ceramics, which are considered as promising candidates for the solid electrolyte separator in SSBs (see chapter 2.2).[253] Interlaboratory comparability of reported results on garnet materials is not necessarily guaranteed, since their polycrystalline microstructure (e.g., porosity and grain size distribution) is highly dependent on the sintering protocol. Based on machine learning assisted microstructural analysis of garnet-type ceramics synthesized with different sintering protocols, 3D transport computations through multiple statistical twin structures are performed to revise the commonly used 1D brick layer model analysis for interpreting experimental impedance data. The computations performed are based on ideally-reversible electrodes with conform interfaces, and the model structures take into account different grain size and pore size distributions. It is emphasized that the microstructure-induced (in)accuracy of the derived transport parameters includes not only the conductivity and permittivity of the bulk or grain boundary transport, but also their activation energies and the estimation of the grain boundary thickness in the structure. In particular, the interplay between the grain structure and the pore structure determines the quantitative deviation between the true material-specific transport parameters and those derived from the 1D BLM analysis. The grain structure alone can result in inaccuracies of up to 150% in the grain boundary conductivity. The effect of porosity on both bulk and grain boundary quantities can be even more severe. The consideration of these effects in the analysis of the experimental impedance results indicates that the variation of the BLM-derived transport parameters is mainly due to sintering-induced structural changes on the mesoscale rather than material alteration. Overall, the findings in this study will improve interlaboratory comparability of reported results by providing a guide to the true range of transport quantities, helping experimentalists distinguishing between structural effects and real changes of the material-specific transport properties.

The previous study has shown that the effect of pores in the micro- and mesostructure on the electrochemical transport properties of the system is enormous. The quantitative effect depends on the total number of pores in the structure (i.e., the porosity), but also on their spatial distribution. Therefore, it is difficult to quantify in general terms the resulting inaccuracy of the transport quantities derived from 1D models. Ordered mesoporous metal oxides, which are currently attracting increasing attention for energy applications, are well suited to provide an educated estimate of the magnitude of pore effects. Surfactant-templating methods and evaporation-induced self-assembly processes lead to highly ordered open pore–solid architectures with volumetric porosities of over 60%.[262-264] Thereby, the mesopores form a face-centered cubic structure with (111) orientation relative to the plane of the substrate.[265-266] The preservation of symmetry in these microstructures provides the unique opportunity to systematically investigate the influence of porosity on the transport properties. Thus, the third study, "*Understanding the Impedance of Mesoporous Oxides – Reliable Determination of the Material-Specific Conductivity*", explores the effect of

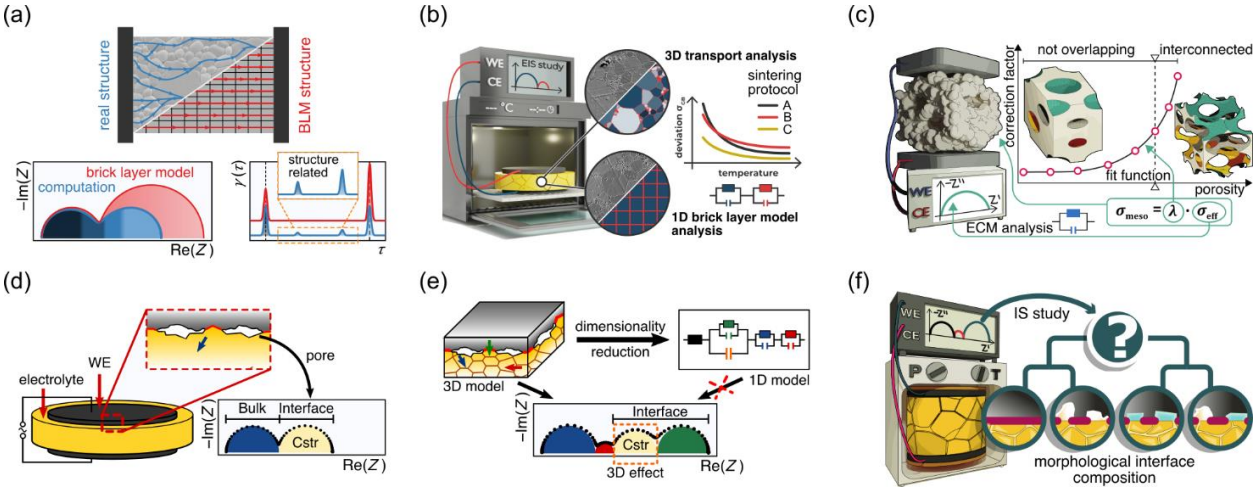

Figure 7. *Artwork summary of the contents of the different studies in this Ph.D. thesis with focus on (a) elucidating the effect of micro- and mesostructure on the impedance, (b) estimating the inaccuracy in BLM derived transport properties of garnet SEs, (c) reliably determining the material-specific conductivity of mesoporous oxides, (d) revealing the effect of interface morphology on the impedance of parent metal anodes, (e) understanding the geometric nature of current constriction, and (f) deriving a guideline for the impedance analysis of solid-state systems. Credit: Elisa Monte/JLU Giessen.*

pore size in these ordered nanocrystalline mesoporous thin films on the impedance (see chapter 2.3).[267] It is demonstrated that the impedance is determined solely by a geometric current constriction signal, which arises due to the regular pore arrangement. Contributions from transport within nanocrystallites or across grain boundaries cannot be resolved, even in the distribution function. As a result, ECM analysis of the impedance allows only the derivation of effective transport quantities using the total resistance and capacitance together with the cell constant of the measurement setup. Detailed theoretical analysis has revealed that the systematic impedance changes with increasing pore size can be directly related to the increase in volumetric porosity of the mesoporous thin films. This allows one to derive an empirical correction formula for the effective conductivity to reliably determine the material-specific electric conductivity. The effective conductivity underestimates the true material-specific conductivity by more than an order of magnitude in the case of high porosity and strong current constriction effects within the structure. For a homogeneous spatial distribution of pores in the structure with no major current constriction effects, the deviation increases almost linearly with porosity and is in the range of 100%. Altogether, the study emphasizes the importance of structural analysis on the micro- and mesoscale for a proper interpretation of macroscopic (impedance) measurements to derive microscopic material-specific parameters.

Pores are not only found in the bulk of a sample, but also in well-defined arrangements at solid-solid interfaces. Therefore, the other articles address the influence of the interface morphology between electrode and sample on the impedance response. The unique challenges of interfaces and surfaces are well known, as already Wolfgang Pauli (1900 – 1958) used to say, "*God made the bulk; the surface was invented by the devil.*". The electrode surface in liquid or hybrid systems is usually fully wetted and there is an ideal contact between the two components from a structural point of view. This is not guaranteed for solid-state systems due to different mechanical properties. Such situations are observed, for example, in SSB research on the anode side between the alkali metal and the ISE separator. Contamination or passivation layers on the metal surface, pore formation during cell assembly or operation, and chemical instabilities resulting in SEI formation reduce the physical contact area between the metal and the SE separator, leading to non-conformal interfaces. This in turn results in an increase in resistance, which can significantly compromise

the performance of an SSB cell. For a long time, the origin of the resistance was falsely attributed solely to the charge transfer reaction at the interface. Recently, Krauskopf et al. showed in an experimental IS study that the increase in impedance is not necessarily an intrinsic material property, but also the result of a forming current constriction effect.[98] This phenomenon is a well-established concept in the physics of electric contacts.[268-270] But up to now, it has not received much attention in SSB research, despite its tremendous impact on the commercialization of reversible metal anodes. A quote from Prof. Matthew McDowell during his talk at the symposium on *Lithium Metal Anodes and Their Application in Batteries* in 2022 shows that the concept is starting to get more attention in the SSB community: "… *constriction resistance … you cannot understand the interface without it*".[271] It emphasizes the need for a fundamental understanding of this phenomenon and its dependence on geometric and material parameters.

The fourth study, "*Interplay of Dynamic Constriction and Interface Morphology between Reversible Metal Anode and Solid Electrolyte in Solid State Batteries*", addresses the origin of the constriction effect in the impedance and its dependence on interface morphology (see chapter 2.4).[272] Thereby, the simplest possible model system is considered, consisting of a single-crystalline SE separator sandwiched between two homogenous metal electrodes. The degradation of the interface at the working electrode is described by a separate layer consisting of a cubic contact spot of variable size surrounded by a pore phase. The material parameters are assumed to be similar to those of a garnet-type SE and the metal|SE interface is considered to be highly conductive with zero polarization resistance. The findings highlight the need for a semantic distinction between *contact* and *electrode area* in a macroscopic transport description, in addition to the necessity to categorize the constriction effect into a *static* and a *dynamic* case. The former is the well-known situation encountered for a conformal contact when the electrode area is smaller than that of the sample.[268-270] This leads to a bottleneck at the interface and current penetration into the bulk, ensuring that the sample volume under the non-contacted surface also contributes to the overall transport. The static concept is extended with the introduction of the *dynamic constriction* notation, which refers to non-conformal interface contacts. This is required when considering alternating electric fields, since the conductive behavior of pores, for example, changes with frequency from dielectrically conductive at high frequencies to electrically insulating in the direct current range. This can give rise to a separate semicircle in the Nyquist representation of the impedance, resulting in a fingerprint that resembles a microscopic electric migration process. However, this is not a self-contained type of transport process in the strict sense. It is rather a global geometric effect, which basically involves all the different microscopic migration processes that occur at the interface and adjacent regions. Finally, the effect of different interface morphologies is investigated. It shows that the constriction resistance decreases with a finer contact area distribution and that the constriction capacitance is strongly influenced by the pore depth and permittivity. The study as a whole demonstrates the importance of dielectric transport behavior in the interpretation of IS results, but also that impedance data bear valuable information, for example, on pore formation and dynamics at the metal anode interface.

In the follow-up study, "*3D Impedance Modeling of Metal Anodes in Solid-State Batteries – Incompatibility of Pore Formation and Constriction Effect in Physical-Based 1D Circuit Models*", the previous work is extended to realistic cases typical for anodes in SSBs (see chapter 2.5).[273] The model system considered consists of an SE separator with a layered grain-structure sandwiched between two metal electrodes. The interface morphology at the working electrode is again described by a single cubic contact spot surrounded by a pore phase. The study addresses the interplay between the dynamic constriction effect, resistive charge transfer at porous interfaces, and transport across grain boundaries in polycrystalline SEs. The comparison of results of the multidimensional electric network modeling with the predictions of a *physical-based* one-dimensional electric circuit model explicitly shows that the standard impedance analysis procedure fails in the case of porous interface morphologies. The usually successful approach of correlating components of ECMs with single microscopic transport processes cannot fully grab the non-locality of the dynamic

constriction effect. Therefore, a *fit circuit model* is proposed and the dependencies of the macroscopic transport parameters on the microscopic material parameters, and the contact area between metal electrode and SE separator are studied. It is demonstrated that the shape of the impedance spectrum, the size of the fitting parameters, and thus the interpretation of the measured data depends to a large extent on the magnitude of the constriction time constant. The latter serves as a descriptor for the switch between dielectric and insulating behavior of the pores at the interface, indicating a significant change in transport pathways through the SE separator. The overall discussion reveals that the analysis and interpretation of IS data is challenging without an explicit theoretical model that accounts for structural properties on the microscopic and mesoscopic scale.

The two previous studies considered only simplified model systems in terms of SE separator microstructure and interface morphology, which in turn is sufficient to point out the fundamentals of the constriction effect. The sixth study, "*Guidelines for Impedance Analysis of Parent Metal Anodes in Solid-State Batteries and the Role of Current Constriction at Interface Voids, Heterogeneities and SEI*", bridges the gap and demonstrates the validity of the prior conclusions also for disordered microstructures of the SE separator and inhomogeneous interface morphologies (see chapter 2.6).[274] These are based on a Voronoi algorithm and a multi-scale, time-dependent, 3D contact model, respectively.[275] It is shown that not only a pore depth distribution but also an inhomogeneous interface morphology with a broad pore size distribution leads to a distorted constriction impedance contribution. This has also recently been observed in experimental IS data on reversible metal anodes.[276-277] Another challenge in interpreting the interface impedance is that various processes, such as charge transfer, morphological and chemical instabilities due to pores or SEI formation, and passivation layers can contribute to the signal. The identification of the dominant effect, however, is crucial for the development of strategies to improve the performance of an SSB. Therefore, this study provides a universal recipe in the form of a hierarchical scheme to assign the characteristics of interface signals to chemical and structural properties, and microscopic or mesoscopic transport processes across the interface. It is based on a thorough theoretical analysis of the dependence of the interface impedance contributions as a function of the physical contact area and temperature. Its applicability is demonstrated in an experimental case study considering the impedance data of a Li|$Li_{6.25}Al_{0.25}La_3Zr_2O_{12}$|Li symmetric half-cell. It clearly demonstrates that the interface properties are dominated by geometric current constriction. Therefore, charge transfer driven morphological instabilities during cycling hinder the successful commercialization of reversible metal anodes and need to be overcome.

1.5 Conclusions and Outlook

Impedance spectroscopy is undeniably a powerful tool for material characterization and system control. However, the discussions in this Ph.D. thesis demonstrate that the analysis and interpretation of IS data is challenging without an explicit theoretical model, which accounts for structural properties at the micro- or mesoscopic scale. The successful approach for liquids using pattern recognition and assuming a one-to-one correlation between individual circuit elements in simple ECMs with microscopic transport processes may fail in the case of solid-state systems. IS analysis considering solid-state systems requires additional degrees of freedom to account for effects such as microstructure and interface morphology. Geometry induced signals in the impedance and distribution function exhibit signatures comparable to those of electric migration processes. This is not yet widely known among scientists, although there have been initial studies on the subject for more than twenty years. The danger of misinterpretation of IS data was recently demonstrated in the development of reversible parent (lithium) metal anodes for SSBs. It was believed for many years that an inherently high charge transfer resistance at the interface between alkali metal and SE prevents a successful implementation of this concept. However, this was wrong. Instead, morphological instabilities during operation dominate the interface behavior between lithium and garnet-type SEs. This

makes a big difference in the required optimization strategies and highlights the need for reliable identification of the actual underlying interface effects. Therefore, it is necessary to establish careful correlations of impedance with the actual sample structure to avoid false conclusions from the IS analysis.

Wolfgang Pauli (1900 – 1958) once said of the efforts and results of scientific research, "*The best that most of us can hope to achieve in physics is simply to understand at a deeper level*". This Ph.D. project has certainly improved the understanding of the impedance response of solid-state systems, and the view of interfaces and microstructural effects. It should be emphasized, however, that the developed modeling workflow offers many additional possibilities to perform even more advanced and in-depth studies. Nonetheless, theory alone can only point out qualitative trends arising from changes of material parameters or certain morphological changes. A combined analysis with experiment, in contrast, will provide more valuable information, for example, on the correlation between pore formation and dynamics at the metal anode interface of SSBs or the identification of failure and degradation effects within a solid. This approach may have the potential for targeted monitoring of hidden morphological or microstructural changes at the micro- or mesoscopic level and, thus for a *state-of-health* control system in applications. The development of such a tool, however, requires more systematic combined experimental and theoretical studies on model systems with a high degree of control over the interface morphology and microstructure.

The conducted investigations are just a few of numerous cases that could have been studied in more detail. There are many other possible applications for the modeling concept and its extension. A detailed discussion, however, would go far beyond the scope of this chapter. To bring this Ph.D. thesis full circle with its original motivation for the need for advanced energy storage technologies, open questions in the field of SSBs are addressed. Inhomogeneous metal deposition is a major challenge in addition to contact loss on the anode side. This leads to filament or dendrite penetration into the SE, representing a mesoscopic failure mechanism of SSBs. In this context, it may be interesting to see to what extent this process influences the impedance and whether certain signatures of dendrite growth and filament deposition can be identified. Possible applications would be early detection systems to prevent complete cell failure. Another issue that has not yet been addressed is that many (battery) materials conduct multiple charge carrier species and not just one type as it is the case for ISEs. Establishing an appropriate transport description can be considered as a starting point for detailed studies of cathodes and composites. The IS analysis for these materials is usually based on macroscopic TLMs consisting of a few one-dimensional transport channels coupled in parallel to account for the interactions between them. This well-established concept is suitable for fitting the impedance response, but again neglects the structural geometry of the real system. It is expected that the projection of the multidimensional system onto a lower-dimensional TLM will lead to the derivation of inaccurate material-specific transport quantities and misinterpretation of structure-related features, similar to the studies performed on the brick layer model. Initial attempts to adapt the transport description in the electric network model may consist of simply using modified versions of TLMs as local equivalent circuit elements within the node network. However, one must take into account the length scales at which transport is modeled and the structural resolution of the system, i.e., $\lambda_{\mathrm{dB}} < d_i$. A diffusive description of ion transport is valid for voxel sizes down to nanometers, but for electron transport this is only possible for voxel sizes larger than several tens of nanometers. In other words, there is a nonzero probability that quantum effects influence the electron transport behavior. Therefore, it will be necessary in the future to develop new concepts to extend the (electron) transport description to the microscopic level (i.e., the nanometer scale).

These are all exciting research topics based on the implemented modeling workflow that can make a small contribution to the hopefully successful development of SSB concepts and thus to the realization of the energy transition. I would like to conclude my Ph.D. thesis with an appropriate quotation from Justus Freiherr von Liebig, which I believe should be paid more attention to in the turbulent times we are living in today.

"*The progress of mankind is due exclusively to the progress of natural sciences, not to morals, religion or philosophy*."

– Justus Freiherr von Liebig (1803 – 1873)

References

1. Macdonald, J. R.; Johnson, W. B., Fundamentals of Impedance Spectroscopy. In *Impedance Spectroscopy*, 2018; pp 1-20.
2. Dimensions https://app.dimensions.ai/discover/publication (accessed 09/22/2022).
3. Enerdata World Energy & Climate Statistics - Yearbook 2022. https://yearbook.enerdata.net/ (accessed 10/06/2022).
4. Enerdata Global Energy & Climate Outlook 2050. https://eneroutlook.enerdata.net/ (accessed 10/06/2022).
5. Bundesamt, S. Bruttostromerzeugung in Deutschland. https://www.destatis.de/DE/Themen/Branchen-Unternehmen/Energie/Erzeugung/Tabellen/bruttostromerzeugung.html (accessed 10/06/2022).
6. IEE, F. Das Barometer der Energiewende. https://www.herkulesprojekt.de/de/Barometer/barometer_2019.html (accessed 10/06/2022).
7. Tipler, P. A.; Mosca, G., *Physik: für Studierende der Naturwissenschaften und Technik*. Springer-Verlag: 2019.
8. Povh, B.; Rith, K.; Scholz, C.; Zetsche, F., *Teilchen und Kerne* Springer Berlin, Heidelberg: 2009; p XII, 419.
9. Cook, J.; Nuccitelli, D.; Green, S. A.; Richardson, M.; Winkler, B.; Painting, R.; Way, R.; Jacobs, P.; Skuce, A., Quantifying the consensus on anthropogenic global warming in the scientific literature. *Environmental Research Letters* **2013,** *8* (2), 024024.
10. Cook, J.; Oreskes, N.; Doran, P. T.; Anderegg, W. R. L.; Verheggen, B.; Maibach, E. W.; Carlton, J. S.; Lewandowsky, S.; Skuce, A. G.; Green, S. A.; Nuccitelli, D.; Jacobs, P.; Richardson, M.; Winkler, B.; Painting, R.; Rice, K., Consensus on consensus: a synthesis of consensus estimates on human-caused global warming. *Environmental Research Letters* **2016,** *11* (4), 048002.
11. Kahle, M.; Kempf, M.; Martin, B.; Glaser, R., Classifying the 2021 "Ahrtal" flood event using hermeneutic interpretation, natural language processing, and instrumental data analyses. *Environmental Research Communications* **2022**.
12. Huang, Y.; Weis, J.; Vereecken, H.; Hendricks Franssen, H.-J., Long-term trends in agricultural droughts over Netherlands and Germany: how extreme was the year 2018? *Hydrology and Earth System Sciences Discussions* **2021**, 1-27.
13. Masson-Delmotte, V.; Zhai, P.; Pirani, A.; Connors, S. L.; Péan, C.; Berger, S.; Caud, N.; Chen, Y.; Goldfarb, L.; Gomis, M., Climate change 2021: the physical science basis. *Contribution of working group I to the sixth assessment report of the intergovernmental panel on climate change* **2021**, 2.
14. Directorate-General for Financial Stability, F. S. a. C. M. U. EU taxonomy: Complementary Climate Delegated Act to accelerate decarbonisation. https://finance.ec.europa.eu/publications/eu-taxonomy-complementary-climate-delegated-act-accelerate-decarbonisation_enhttps://finance.ec.europa.eu/publications/eu-taxonomy-complementary-climate-delegated-act-accelerate-decarbonisation_en (accessed 10/06/2022).
15. Directorate-General for Financial Stability, F. S. a. C. M. U. EU taxonomy for sustainable activities. https://finance.ec.europa.eu/sustainable-finance/tools-and-standards/eu-taxonomy-sustainable-activities_en (accessed 10/06/2022).
16. Kim, Y.; Kim, M.; Kim, W., Effect of the Fukushima nuclear disaster on global public acceptance of nuclear energy. *Energy policy* **2013,** *61*, 822-828.
17. Saenko, V.; Ivanov, V.; Tsyb, A.; Bogdanova, T.; Tronko, M.; Demidchik, Y.; Yamashita, S., The Chernobyl accident and its consequences. *Clinical Oncology* **2011,** *23* (4), 234-243.

18. Deng, D.; Zhang, L.; Dong, M.; Samuel, R. E.; Ofori-Boadu, A.; Lamssali, M., Radioactive waste: a review. *Water Environ. Res* **2020,** *92* (10), 1818-1825.
19. Wirtschaft, S. Japan plant Bau neuer Atomkraftwerke. https://www.spiegel.de/wirtschaft/unternehmen/trotz-fukushima-japan-plant-den-bau-neuer-atomkraftwerke-a-78b83352-3ee8-4d32-a50f-08439027d8f2 (accessed 10/06/2022).
20. Welter, P. Japan entwickelt neuen Atomreaktor. https://www.faz.net/aktuell/wirtschaft/unternehmen/atomkraft-mitsubishi-heavy-entwickelt-neuen-reaktor-in-japan-18351843.html (accessed 10/06/2022).
21. Haas, T.; Herberg, J.; Löw-Beer, D., From carbon democracy to post-fossil capitalism? The German coal phase-out as a crossroads of sustainability politics. *Sustainability: Science, Practice and Policy* **2022,** *18* (1), 384-399.
22. McCauley, D.; Brown, A.; Rehner, R.; Heffron, R.; van de Graaff, S., Energy justice and policy change: An historical political analysis of the German nuclear phase-out. *Applied Energy* **2018,** *228*, 317-323.
23. Nolting, L.; Praktiknjo, A., Can we phase-out all of them? Probabilistic assessments of security of electricity supply for the German case. *Applied Energy* **2020,** *263*, 114704.
24. Graedel, T. E.; Barr, R.; Chandler, C.; Chase, T.; Choi, J.; Christoffersen, L.; Friedlander, E.; Henly, C.; Jun, C.; Nassar, N. T.; Schechner, D.; Warren, S.; Yang, M.-y.; Zhu, C., Methodology of Metal Criticality Determination. *Environmental Science & Technology* **2012,** *46* (2), 1063-1070.
25. Peck, D.; Kandachar, P.; Tempelman, E., Critical materials from a product design perspective. *Materials & Design (1980-2015)* **2015,** *65*, 147-159.
26. Mbah, R. E.; Wasum, D., Russian-Ukraine 2022 War: A Review of the Economic Impact of Russian-Ukraine Crisis on the USA, UK, Canada, and Europe. *Advances in Social Sciences Research Journal* **2022,** *9* (3), 144-153.
27. Granqvist, C. G.; Arvizu, M. A.; Bayrak Pehlivan, İ.; Qu, H. Y.; Wen, R. T.; Niklasson, G. A., Electrochromic materials and devices for energy efficiency and human comfort in buildings: A critical review. *Electrochim. Acta* **2018,** *259*, 1170-1182.
28. Syrrakou, E.; Papaefthimiou, S.; Yianoulis, P., Eco-efficiency evaluation of a smart window prototype. *Sci. Total Environ.* **2006,** *359* (1), 267-282.
29. Allouhi, A.; El Fouih, Y.; Kousksou, T.; Jamil, A.; Zeraouli, Y.; Mourad, Y., Energy consumption and efficiency in buildings: current status and future trends. *Journal of Cleaner Production* **2015,** *109*, 118-130.
30. Tällberg, R.; Jelle, B. P.; Loonen, R.; Gao, T.; Hamdy, M., Comparison of the energy saving potential of adaptive and controllable smart windows: A state-of-the-art review and simulation studies of thermochromic, photochromic and electrochromic technologies. *Sol. Energy Mater. Sol. Cells* **2019,** *200*, 109828.
31. Kamat, P. V., Lithium-Ion Batteries and Beyond: Celebrating the 2019 Nobel Prize in Chemistry – A Virtual Issue. *ACS Energy Letters* **2019,** *4* (11), 2757-2759.
32. NobelPrice.org, The Nobel Prize in Chemistry 2019 Nobel Media AB: 2019.
33. Brodd, R. J.; Bullock, K. R.; Leising, R. A.; Middaugh, R. L.; Miller, J. R.; Takeuchi, E., Batteries, 1977 to 2002. *J. Electrochem. Soc.* **2004,** *151* (3), K1.
34. Kurzweil, P.; Dietlmeier, O. K., *Elektrochemische Speicher*. Springer: 2015.
35. Eckhardt, J. K.; Risius, P. E.; Czerner, M.; Heiliger, C., Ab initio Description of Disorder Effects in Layered Cathode Active Materials by the Coherent Potential Approximation. *J. Phys.: Condens. Matter* **2022,** *34* (32).
36. Nazri, G.-A.; Pistoia, G., *Lithium batteries: science and technology*. Springer Science & Business Media: 2008.
37. Ellis, B. L.; Lee, K. T.; Nazar, L. F., Positive electrode materials for Li-ion and Li-batteries. *Chem. Mater.* **2010,** *22* (3), 691-714.
38. Li, W.; Song, B.; Manthiram, A., High-voltage positive electrode materials for lithium-ion batteries. *Chem. Soc. Rev.* **2017,** *46* (10), 3006-3059.
39. Ozawa, K., Lithium Ion Rechargeable Batteries. *Wiley-VCH Verlag GmbH &Co. KGaA: Weinheim* **2009**.
40. Yoshio, M.; Noguchi, H., A review of positive electrode materials for lithium-ion batteries. *Lithium-Ion Batteries* **2009**, 9-48.

41. Gür, T. M., Review of electrical energy storage technologies, materials and systems: challenges and prospects for large-scale grid storage. *Energy Environ. Sci.* **2018,** *11* (10), 2696-2767.
42. Li, H., Practical evaluation of Li-ion batteries. *Joule* **2019,** *3* (4), 911-914.
43. Korthauer, R., *Handbuch lithium-ionen-batterien*. Springer: 2013.
44. Janek, J.; Zeier, W. G., A Solid Future for Battery Development. *Nature Energy* **2016,** *1* (9), 1-4.
45. Kane, M. Tesla's 4680-Type Battery Cell Teardown: Specs Revealed. https://insideevs.com/news/598656/tesla-4680-battery-cell-specs/ (accessed 10/21/2022).
46. Liu, J.; Bao, Z.; Cui, Y.; Dufek, E. J.; Goodenough, J. B.; Khalifah, P.; Li, Q.; Liaw, B. Y.; Liu, P.; Manthiram, A., Pathways for practical high-energy long-cycling lithium metal batteries. *Nature Energy* **2019,** *4* (3), 180-186.
47. Ulvestad, A., A brief review of current lithium ion battery technology and potential solid state battery technologies. *arXiv preprint arXiv:1803.04317* **2018**.
48. Shen, Y.; Zhang, Y.; Han, S.; Wang, J.; Peng, Z.; Chen, L., Unlocking the energy capabilities of lithium metal electrode with solid-state electrolytes. *Joule* **2018,** *2* (9), 1674-1689.
49. Kato, Y.; Shiotani, S.; Morita, K.; Suzuki, K.; Hirayama, M.; Kanno, R., All-solid-state batteries with thick electrode configurations. *The journal of physical chemistry letters* **2018,** *9* (3), 607-613.
50. Gallagher, K. G.; Trask, S. E.; Bauer, C.; Woehrle, T.; Lux, S. F.; Tschech, M.; Lamp, P.; Polzin, B. J.; Ha, S.; Long, B.; Wu, Q.; Lu, W.; Dees, D. W.; Jansen, A. N., Optimizing Areal Capacities through Understanding the Limitations of Lithium-Ion Electrodes. *J. Electrochem. Soc.* **2015,** *163* (2), A138-A149.
51. Landesfeind, J.; Gasteiger, H. A., Temperature and Concentration Dependence of the Ionic Transport Properties of Lithium-Ion Battery Electrolytes. *J. Electrochem. Soc.* **2019,** *166* (14), A3079-A3097.
52. Lin, D.; Liu, Y.; Cui, Y., Reviving the lithium metal anode for high-energy batteries. *Nature nanotechnology* **2017,** *12* (3), 194-206.
53. Betz, J.; Bieker, G.; Meister, P.; Placke, T.; Winter, M.; Schmuch, R., Theoretical versus practical energy: a plea for more transparency in the energy calculation of different rechargeable battery systems. *Advanced energy materials* **2019,** *9* (6), 1803170.
54. Ortmann, T.; Burkhardt, S.; Eckhardt, J. K.; Fuchs, T.; Ding, Z.; Sann, J.; Rohnke, M.; Ma, Q.; Tietz, F.; Fattakhova-Rohlfing, D.; Kübel, C.; Guillon, O.; Heiliger, C.; Janek, J., Kinetics and Pore Formation of the Sodium Metal Anode on NASICON-Type $Na_{3.4}Zr_2Si_{2.4}P_{0.6}O_{12}$ for Sodium Solid-State Batteries. *Advanced Energy Materials* **2023,** *13* (5).
55. Perveen, T.; Siddiq, M.; Shahzad, N.; Ihsan, R.; Ahmad, A.; Shahzad, M. I., Prospects in anode materials for sodium ion batteries - A review. *Renewable and Sustainable Energy Reviews* **2020,** *119*, 109549.
56. Bay, M.-C.; Wang, M.; Grissa, R.; Heinz, M. V. F.; Sakamoto, J.; Battaglia, C., Sodium Plating from Na-β″-Alumina Ceramics at Room Temperature, Paving the Way for Fast-Charging All-Solid-State Batteries. *Advanced Energy Materials* **2020,** *10* (3), 1902899.
57. Wang, C.; Gao, J.; Gao, X.; Zhao, Y., Stabilizing the Na/$Na_3Zr_2Si_2PO_{12}$ interface through intrinsic feature regulation of $Na_3Zr_2Si_2PO_{12}$. *Cell Reports Physical Science* **2021,** *2* (7), 100478.
58. Zhang, Z.; Wenzel, S.; Zhu, Y.; Sann, J.; Shen, L.; Yang, J.; Yao, X.; Hu, Y.-S.; Wolverton, C.; Li, H.; Chen, L.; Janek, J., $Na_3Zr_2Si_2PO_{12}$: A Stable Na^+-Ion Solid Electrolyte for Solid-State Batteries. *ACS Applied Energy Materials* **2020,** *3* (8), 7427-7437.
59. Krauskopf, T.; Dippel, R.; Hartmann, H.; Peppler, K.; Mogwitz, B.; Richter, F. H.; Zeier, W. G.; Janek, J., Lithium-Metal Growth Kinetics on LLZO Garnet-Type Solid Electrolytes. *Joule* **2019,** *3* (8), 2030-2049.
60. Cheng, X.-B.; Zhang, R.; Zhao, C.-Z.; Zhang, Q., Toward safe lithium metal anode in rechargeable batteries: a review. *Chem. Rev.* **2017,** *117* (15), 10403-10473.
61. Takeda, Y.; Yamamoto, O.; Imanishi, N., Lithium Dendrite Formation on a Lithium Metal Anode from Liquid, Polymer and Solid Electrolytes. *Electrochemistry* **2016,** *84* (4), 210-218.
62. Tarascon, J.-M.; Armand, M., Issues and challenges facing rechargeable lithium batteries. In *Materials for sustainable energy: a collection of peer-reviewed research and review articles from Nature Publishing Group*, World Scientific: 2011; pp 171-179.
63. Bieker, G.; Winter, M.; Bieker, P., Electrochemical in situ investigations of SEI and dendrite formation on the lithium metal anode. *PCCP* **2015,** *17* (14), 8670-8679.

64. Cortes, F. J. Q.; Lewis, J. A.; Tippens, J.; Marchese, T. S.; McDowell, M. T., How Metallic Protection Layers Extend the Lifetime of NASICON-Based Solid-State Lithium Batteries. *J. Electrochem. Soc.* **2019,** *167* (5), 050502.
65. Xu, K., Nonaqueous Liquid Electrolytes for Lithium-Based Rechargeable Batteries. *Chem. Rev.* **2004,** *104* (10), 4303-4418.
66. Tarascon, J. M.; Armand, M., Issues and challenges facing rechargeable lithium batteries. In *Materials for Sustainable Energy*, Co-Published with Macmillan Publishers Ltd, UK: 2010; pp 171-179.
67. Asano, T.; Sakai, A.; Ouchi, S.; Sakaida, M.; Miyazaki, A.; Hasegawa, S., Solid halide electrolytes with high lithium-ion conductivity for application in 4 V class bulk-type all-solid-state batteries. *Adv. Mater.* **2018,** *30* (44), 1803075.
68. Kato, Y.; Hori, S.; Saito, T.; Suzuki, K.; Hirayama, M.; Mitsui, A.; Yonemura, M.; Iba, H.; Kanno, R., High-power all-solid-state batteries using sulfide superionic conductors. *Nature Energy* **2016,** *1* (4), 1-7.
69. Lee, Y.-G.; Fujiki, S.; Jung, C.; Suzuki, N.; Yashiro, N.; Omoda, R.; Ko, D.-S.; Shiratsuchi, T.; Sugimoto, T.; Ryu, S.; Ku, J. H.; Watanabe, T.; Park, Y.; Aihara, Y.; Im, D.; Han, I. T., High-energy long-cycling all-solid-state lithium metal batteries enabled by silver–carbon composite anodes. *Nature Energy* **2020,** *5* (4), 299-308.
70. Bielefeld, A.; Weber, D. A.; Janek, J., Modeling Effective Ionic Conductivity and Binder Influence in Composite Cathodes for All-Solid-State Batteries. *ACS Appl Mater Interfaces* **2020,** *12* (11), 12821-12833.
71. Vishnugopi, B. S.; Kazyak, E.; Lewis, J. A.; Nanda, J.; McDowell, M. T.; Dasgupta, N. P.; Mukherjee, P. P., Challenges and Opportunities for Fast Charging of Solid-State Lithium Metal Batteries. *ACS Energy Letters* **2021,** *6* (10), 3734-3749.
72. Goodenough, J. B.; Kim, Y., Challenges for rechargeable Li batteries. *Chem. Mater.* **2010,** *22* (3), 587-603.
73. Koerver, R., Factorial Energy: Transformational Semi-Solid-State Technology. In *Solid-State Batteries V (From Fundamentals to Application) - An International Bunsen Discussion Meeting (IBDM)*, 2022.
74. Xiao, Y.; Wang, Y.; Bo, S.-H.; Kim, J. C.; Miara, L. J.; Ceder, G., Understanding interface stability in solid-state batteries. *Nature Reviews Materials* **2020,** *5* (2), 105-126.
75. Koerver, R.; Aygün, I.; Leichtweiß, T.; Dietrich, C.; Zhang, W.; Binder, J. O.; Hartmann, P.; Zeier, W. G.; Janek, J. r., Capacity fade in solid-state batteries: interphase formation and chemomechanical processes in nickel-rich layered oxide cathodes and lithium thiophosphate solid electrolytes. *Chem. Mater.* **2017,** *29* (13), 5574-5582.
76. Koerver, R.; Zhang, W.; de Biasi, L.; Schweidler, S.; Kondrakov, A. O.; Kolling, S.; Brezesinski, T.; Hartmann, P.; Zeier, W. G.; Janek, J., Chemo-mechanical expansion of lithium electrode materials–on the route to mechanically optimized all-solid-state batteries. *Energy Environ. Sci.* **2018,** *11* (8), 2142-2158.
77. Dong, D.; Zhou, B.; Sun, Y.; Zhang, H.; Zhong, G.; Dong, Q.; Fu, F.; Qian, H.; Lin, Z.; Lu, D., Polymer electrolyte glue: A universal interfacial modification strategy for all-solid-state Li batteries. *Nano Lett.* **2019,** *19* (4), 2343-2349.
78. Fu, K.; Gong, Y.; Dai, J.; Gong, A.; Han, X.; Yao, Y.; Wang, C.; Wang, Y.; Chen, Y.; Yan, C., Flexible, solid-state, ion-conducting membrane with 3D garnet nanofiber networks for lithium batteries. *Proceedings of the National Academy of Sciences* **2016,** *113* (26), 7094-7099.
79. Keller, M.; Varzi, A.; Passerini, S., Hybrid electrolytes for lithium metal batteries. *J. Power Sources* **2018,** *392*, 206-225.
80. Wang, C.; Yang, Y.; Liu, X.; Zhong, H.; Xu, H.; Xu, Z.; Shao, H.; Ding, F., Suppression of lithium dendrite formation by using LAGP-PEO (LiTFSI) composite solid electrolyte and lithium metal anode modified by PEO (LiTFSI) in all-solid-state lithium batteries. *ACS Appl. Mater. Interfaces* **2017,** *9* (15), 13694-13702.
81. Stolz, L.; Pfeiffer, F.; Baghernejad, M.; Winter, M.; Kasnatscheew, J., Remark on Conductivity Measurements: The Special Case of Polymer-Based Single-Ion Conducting Electrolytes on Blocking Electrodes. *ACS Applied Energy Materials* **2022**.

82. Zhang, Q.; Liu, K.; Ding, F.; Liu, X., Recent advances in solid polymer electrolytes for lithium batteries. *Nano Research* **2017,** *10* (12), 4139-4174.
83. Ohno, S.; Banik, A.; Dewald, G. F.; Kraft, M. A.; Krauskopf, T.; Minafra, N.; Till, P.; Weiss, M.; Zeier, W. G., Materials design of ionic conductors for solid state batteries. *Progress in Energy* **2020,** *2* (2), 022001.
84. Zhang, Z.; Shao, Y.; Lotsch, B.; Hu, Y.-S.; Li, H.; Janek, J.; Nazar, L. F.; Nan, C.-W.; Maier, J.; Armand, M., New horizons for inorganic solid state ion conductors. *Energy Environ. Sci.* **2018,** *11* (8), 1945-1976.
85. McGrogan, F. P.; Swamy, T.; Bishop, S. R.; Eggleton, E.; Porz, L.; Chen, X.; Chiang, Y. M.; Van Vliet, K. J., Compliant Yet Brittle Mechanical Behavior of Li_2S–P_2S_5 Lithium-Ion-Conducting Solid Electrolyte. *Advanced Energy Materials* **2017,** *7* (12), 1602011.
86. Bielefeld, A.; Weber, D. A.; Janek, J., Microstructural Modeling of Composite Cathodes for All-Solid-State Batteries. *The Journal of Physical Chemistry C* **2019,** *123* (3), 1626-1634.
87. Minnmann, P.; Quillman, L.; Burkhardt, S.; Richter, F. H.; Janek, J., Editors' choice—quantifying the impact of charge transport bottlenecks in composite cathodes of all-solid-state batteries. *J. Electrochem. Soc.* **2021,** *168* (4), 040537.
88. Walther, F.; Koerver, R.; Fuchs, T.; Ohno, S.; Sann, J.; Rohnke, M.; Zeier, W. G.; Janek, J., Visualization of the Interfacial Decomposition of Composite Cathodes in Argyrodite-Based All-Solid-State Batteries Using Time-of-Flight Secondary-Ion Mass Spectrometry. *Chem. Mater.* **2019,** *31* (10), 3745-3755.
89. Walther, F.; Randau, S.; Schneider, Y.; Sann, J.; Rohnke, M.; Richter, F. H.; Zeier, W. G.; Janek, J., Influence of Carbon Additives on the Decomposition Pathways in Cathodes of Lithium Thiophosphate-Based All-Solid-State Batteries. *Chem. Mater.* **2020,** *32* (14), 6123-6136.
90. Lewis, J. A.; Tippens, J.; Cortes, F. J. Q.; McDowell, M. T., Chemo-mechanical challenges in solid-state batteries. *Trends in Chemistry* **2019,** *1* (9), 845-857.
91. McDowell, M. T.; Cortes, F. J. Q.; Thenuwara, A. C.; Lewis, J. A., Toward High-Capacity Battery Anode Materials: Chemistry and Mechanics Intertwined. *Chem. Mater.* **2020,** *32* (20), 8755-8771.
92. Ruess, R.; Schweidler, S.; Hemmelmann, H.; Conforto, G.; Bielefeld, A.; Weber, D. A.; Sann, J.; Elm, M. T.; Janek, J., Influence of NCM particle cracking on kinetics of lithium-ion batteries with liquid or solid electrolyte. *J. Electrochem. Soc.* **2020,** *167* (10), 100532.
93. Shi, T.; Tu, Q.; Tian, Y.; Xiao, Y.; Miara, L. J.; Kononova, O.; Ceder, G., High Active Material Loading in All-Solid-State Battery Electrode via Particle Size Optimization. *Advanced Energy Materials* **2020,** *10* (1), 1902881.
94. Burkhardt, S.; Friedrich, M. S.; Eckhardt, J. K.; Wagner, A. C.; Bohn, N.; Binder, J. R.; Chen, L.; Elm, M. T.; Janek, J.; Klar, P. J., Charge Transport in Single NCM Cathode Active Material Particles for Lithium-Ion Batteries Studied under Well-Defined Contact Conditions. *ACS Energy Letters* **2019,** *4* (9), 2117-2123.
95. Eckhardt, J. K. Examination of the Partial Electronic Conductivity of Mixed Ionic and Electronic Conducting Secondary Particles. Justus Liebig University, 2017.
96. Kim, D. H.; Oh, D. Y.; Park, K. H.; Choi, Y. E.; Nam, Y. J.; Lee, H. A.; Lee, S.-M.; Jung, Y. S., Infiltration of Solution-Processable Solid Electrolytes into Conventional Li-Ion-Battery Electrodes for All-Solid-State Li-Ion Batteries. *Nano Lett.* **2017,** *17* (5), 3013-3020.
97. Wang, P.; Qu, W.; Song, W. L.; Chen, H.; Chen, R.; Fang, D., Electro–chemo–mechanical issues at the interfaces in solid-state lithium metal batteries. *Adv. Funct. Mater.* **2019,** *29* (27), 1900950.
98. Krauskopf, T.; Hartmann, H.; Zeier, W. G.; Janek, J., Toward a Fundamental Understanding of the Lithium Metal Anode in Solid-State Batteries—An Electrochemo-Mechanical Study on the Garnet-Type Solid Electrolyte $Li_{6.25}Al_{0.25}La_3Zr_2O_{12}$. *ACS Appl. Mater. Interfaces* **2019,** *11* (15), 14463-14477.
99. Lee, C.; Han, S. Y.; Lewis, J. A.; Shetty, P. P.; Yeh, D.; Liu, Y.; Klein, E.; Lee, H.-W.; McDowell, M. T., Stack Pressure Measurements to Probe the Evolution of the Lithium–Solid-State Electrolyte Interface. *ACS Energy Letters* **2021,** *6* (9), 3261-3269.
100. Hatzell, K. B.; Chen, X. C.; Cobb, C. L.; Dasgupta, N. P.; Dixit, M. B.; Marbella, L. E.; McDowell, M. T.; Mukherjee, P. P.; Verma, A.; Viswanathan, V.; Westover, A. S.; Zeier, W. G., Challenges in Lithium Metal Anodes for Solid-State Batteries. *ACS Energy Letters* **2020,** *5* (3), 922-934.

101. Krauskopf, T.; Richter, F. H.; Zeier, W. G.; Janek, J., Physicochemical Concepts of the Lithium Metal Anode in Solid-State Batteries. *Chem. Rev.* **2020,** *120* (15), 7745-7794.
102. Luntz, A. C.; Voss, J.; Reuter, K., Interfacial challenges in solid-state Li ion batteries. ACS Publications: 2015; Vol. 6, pp 4599-4604.
103. Kerman, K.; Luntz, A.; Viswanathan, V.; Chiang, Y.-M.; Chen, Z., Practical challenges hindering the development of solid state Li ion batteries. *J. Electrochem. Soc.* **2017,** *164* (7), A1731.
104. Xu, R.; Xia, X.; Zhang, S.; Xie, D.; Wang, X.; Tu, J., Interfacial challenges and progress for inorganic all-solid-state lithium batteries. *Electrochim. Acta* **2018,** *284*, 177-187.
105. Krauskopf, T.; Mogwitz, B.; Hartmann, H.; Singh, D. K.; Zeier, W. G.; Janek, J., The Fast Charge Transfer Kinetics of the Lithium Metal Anode on the Garnet-Type Solid Electrolyte $Li_{6.25}Al_{0.25}La_3Zr_2O_{12}$. *Advanced Energy Materials* **2020,** *10* (27), 2000945.
106. Krauskopf, T.; Mogwitz, B.; Rosenbach, C.; Zeier, W. G.; Janek, J., Diffusion Limitation of Lithium Metal and Li–Mg Alloy Anodes on LLZO Type Solid Electrolytes as a Function of Temperature and Pressure. *Advanced Energy Materials* **2019,** *9* (44), 1902568.
107. Naik, K. G.; Chatterjee, D.; Mukherjee, P. P., Solid Electrolyte–Cathode Interface Dictates Reaction Heterogeneity and Anode Stability. *ACS Appl. Mater. Interfaces* **2022,** *14* (40), 45308-45319.
108. Fuchs, T.; Haslam, C. G.; Moy, A. C.; Lerch, C.; Krauskopf, T.; Sakamoto, J.; Richter, F. H.; Janek, J., Increasing the Pressure-Free Stripping Capacity of the Lithium Metal Anode in Solid-State-Batteries by Carbon Nanotubes. *Advanced Energy Materials* **2022,** *12* (26), 2201125.
109. Li, Y.-C.; Xiang, W.; Xiao, Y.; Wu, Z.-G.; Xu, C.-L.; Xu, W.; Xu, Y.-D.; Wu, C.; Yang, Z.-G.; Guo, X.-D., Synergy of doping and coating induced heterogeneous structure and concentration gradient in Ni-rich cathode for enhanced electrochemical performance. *J. Power Sources* **2019,** *423*, 144-151.
110. Shi, J.-L.; Xiao, D.-D.; Zhang, X.-D.; Yin, Y.-X.; Guo, Y.-G.; Gu, L.; Wan, L.-J., Improving the structural stability of Li-rich cathode materials via reservation of cations in the Li-slab for Li-ion batteries. *Nano research* **2017,** *10* (12), 4201-4209.
111. Lee, J.-T.; Wang, F.-M.; Cheng, C.-S.; Li, C.-C.; Lin, C.-H., Low-temperature atomic layer deposited Al_2O_3 thin film on layer structure cathode for enhanced cycleability in lithium-ion batteries. *Electrochim. Acta* **2010,** *55* (12), 4002-4006.
112. Zhang, X.; Belharouak, I.; Li, L.; Lei, Y.; Elam, J. W.; Nie, A.; Chen, X.; Yassar, R. S.; Axelbaum, R. L., Structural and electrochemical study of Al_2O_3 and TiO_2 coated $Li_{1.2}Ni_{0.13}Mn_{0.54}Co_{0.13}O_2$ cathode material using ALD. *Advanced Energy Materials* **2013,** *3* (10), 1299-1307.
113. Neudeck, S.; Strauss, F.; Garcia, G.; Wolf, H.; Janek, J.; Hartmann, P.; Brezesinski, T., Room temperature, liquid-phase Al_2O_3 surface coating approach for Ni-rich layered oxide cathode material. *Chem. Commun.* **2019,** *55* (15), 2174-2177.
114. Chen, Y.; Zhang, Y.; Chen, B.; Wang, Z.; Lu, C., An approach to application for $LiNi_{0.6}Co_{0.2}Mn_{0.2}O_2$ cathode material at high cutoff voltage by TiO_2 coating. *J. Power Sources* **2014,** *256*, 20-27.
115. Neudeck, S.; Walther, F.; Bergfeldt, T.; Suchomski, C.; Rohnke, M.; Hartmann, P.; Janek, J. r.; Brezesinski, T., Molecular surface modification of NCM622 cathode material using organophosphates for improved Li-ion battery full-cells. *ACS Appl. Mater. Interfaces* **2018,** *10* (24), 20487-20498.
116. Fuller, T. F.; Doyle, M.; Newman, J., Simulation and Optimization of the Dual Lithium Ion Insertion Cell. *J. Electrochem. Soc.* **1994,** *141* (1), 1-10.
117. Doyle, C. M., *Design and simulation of lithium rechargeable batteries*. University of California, Berkeley: 1995.
118. Ramadesigan, V.; Northrop, P. W. C.; De, S.; Santhanagopalan, S.; Braatz, R. D.; Subramanian, V. R., Modeling and Simulation of Lithium-Ion Batteries from a Systems Engineering Perspective. *J. Electrochem. Soc.* **2012,** *159* (3), R31-R45.
119. Torchio, M.; Magni, L.; Gopaluni, R. B.; Braatz, R. D.; Raimondo, D. M., LIONSIMBA: A Matlab Framework Based on a Finite Volume Model Suitable for Li-Ion Battery Design, Simulation, and Control. *J. Electrochem. Soc.* **2016,** *163* (7), A1192-A1205.
120. Sulzer, V.; Marquis, S. G.; Timms, R.; Robinson, M.; Chapman, S. J., Python Battery Mathematical Modelling (PyBaMM). *Journal of Open Research Software* **2021,** *9* (1).
121. Xavier Raynaud; Halvor Møll Nilsen; Simon Clark; Johansson, A., BattMoTeam/BattMo: v0.1.0-beta. *Zenodo* **2022**.

122. Braun, P.; Uhlmann, C.; Weiss, M.; Weber, A.; Ivers-Tiffée, E., Assessment of all-solid-state lithium-ion batteries. *J. Power Sources* **2018,** *393*, 119-127.
123. Park, J.; Kim, K. T.; Oh, D. Y.; Jin, D.; Kim, D.; Jung, Y. S.; Lee, Y. M., Digital Twin-Driven All-Solid-State Battery: Unraveling the Physical and Electrochemical Behaviors. *Advanced Energy Materials* **2020,** *10* (35), 2001563.
124. Bielefeld, A.; Weber, D. A.; Rueß, R.; Glavas, V.; Janek, J., Influence of Lithium Ion Kinetics, Particle Morphology and Voids on the Electrochemical Performance of Composite Cathodes for All-Solid-State Batteries. *J. Electrochem. Soc.* **2022,** *169* (2), 020539.
125. Horii, M.; Christianson, R. J.; Mutha, H.; Bachman, J. C., Modeling the effect of electrolyte microstructure on conductivity and solid-state Li-ion battery performance. *J. Power Sources* **2022,** *528*.
126. Becker-Steinberger, K.; Schardt, S.; Horstmann, B.; Latz, A., Statics and Dynamics of Space-Charge-Layers in Polarized Inorganic Solid Electrolytes. *arXiv preprint arXiv:2101.10294* **2021**.
127. Falconi, A. Electrochemical Li-Ion battery modeling for electric vehicles. Communaute Universite Grenoble Alpes, 2017.
128. Ohno, S.; Bernges, T.; Buchheim, J.; Duchardt, M.; Hatz, A.-K.; Kraft, M. A.; Kwak, H.; Santhosha, A. L.; Liu, Z.; Minafra, N.; Tsuji, F.; Sakuda, A.; Schlem, R.; Xiong, S.; Zhang, Z.; Adelhelm, P.; Chen, H.; Hayashi, A.; Jung, Y. S.; Lotsch, B. V.; Roling, B.; Vargas-Barbosa, N. M.; Zeier, W. G., How Certain Are the Reported Ionic Conductivities of Thiophosphate-Based Solid Electrolytes? An Interlaboratory Study. *ACS Energy Letters* **2020,** *5* (3), 910-915.
129. Burkhardt, S.; Elm, M. T.; Lani-Wayda, B.; Klar, P. J., In Situ Monitoring of Lateral Hydrogen Diffusion in Amorphous and Polycrystalline WO_3 Thin Films. *Advanced Materials Interfaces* **2018,** *5* (6), 1701587.
130. Geng, Z.; Chien, Y.-C.; Lacey, M. J.; Thiringer, T.; Brandell, D., Validity of solid-state Li^+ diffusion coefficient estimation by electrochemical approaches for lithium-ion batteries. *Electrochim. Acta* **2022,** *404*, 139727.
131. Kohlrausch, F.; Nippoldt, W., Ueber die Gültigkeit der Ohm'schen Gesetze für Elektrolyte und eine numerische Bestimmung des Leitungswiderstandes der verdünnten Schwefelsäure durch alternirende Ströme. *Annalen der Physik* **1869,** *214* (11), 370-390.
132. Kohlrausch, F., Ueber electrische Widerstandsbestimmung mit Wechselströmen. *Annalen der Physik* **1893,** *285* (6), 225-256.
133. Heaviside, O., *Electromagnetic Theory*. The Electrician: 1893.
134. Warburg, E., Ueber das Verhalten sogenannter unpolarisirbarer Elektroden gegen Wechselstrom. *Annalen der Physik* **1899,** *303* (3), 493-499.
135. Schanne, O. F.; Ruiz, P.; Ceretti, E., *Impedance measurements in biological cells*. Wiley: 1977.
136. Cole, K. S., *Membranes, ions and impulses: a chapter of classical biophysics*. Univ of California Press: 1972; Vol. 1.
137. Sluyters, J. H., On the impedance of galvanic cells: I. Theory. *Recl. Trav. Chim. Pays-Bas* **1960,** *79* (10), 1092-1100.
138. Sluyters, J. H.; Oomen, J. J. C., On the impedance of galvanic cells: II. Experimental verification. *Recl. Trav. Chim. Pays-Bas* **1960,** *79* (10), 1101-1110.
139. Armstrong, R. D.; Firman, R. E.; Thirsk, H. R., The a.c. impedance of complex electrochemical reactions. *Faraday Discussions of the Chemical Society* **1973,** *56* (0), 244-263.
140. Archer, W. I.; Armstrong, R. D., The application of A. C. impedance methods to solid electrolytes. In *Electrochemistry: Volume 7*, Thirsk, H. R., Ed. The Royal Society of Chemistry: 1980; Vol. 7, pp 157-202.
141. Grahame, D. C., Effects of dielectric saturation upon the diffuse double layer and the free energy of hydration of ions. *J. Chem. Phys.* **1950,** *18* (7), 903-909.
142. Randles, J. E. B.; Somerton, K. W., Kinetics of rapid electrode reactions. Part 3.—Electron exchange reactions. *Trans. Faraday Society* **1952,** *48* (0), 937-950.
143. Randles, J. E. B.; Somerton, K. W., Kinetics of rapid electrode reactions. Part 4.—Metal ion exchange reaction at amalgam electrodes. *Trans. Faraday Society* **1952,** *48* (0), 951-955.
144. Macdonald, J. R., Capacitance and Conductance Effects in Photoconducting Alkali Halide Crystals. *J. Chem. Phys.* **1955,** *23* (2), 275-295.

145. Hickling, A., Studies in electrode polarisation. Part IV.—The automatic control of the potential of a working electrode. *Trans. Faraday Society* **1942,** *38*, 27-33.
146. Wellstead, P., Frequency Response Analysis. *Solartron Instruments* **1983**.
147. Gabrielli, C., Identification of Electrochemical Process by Frequency Response Analysis. *Solartron Electronic Group* **1980**.
148. Macdonald, D. D., A brief history of electrochemical impedance spectroscopy. *Center for Electrochemical Science and Technology Pennsylvania State University* **2002**.
149. Boukamp, B. A., A Nonlinear Least Squares Fit procedure for analysis of immittance data of electrochemical systems. *Solid State Ionics* **1986,** *20* (1), 31-44.
150. Macdonald, J. R.; Garber, J., Analysis of impedance and admittance data for solids and liquids. *J. Electrochem. Soc.* **1977,** *124* (7), 1022.
151. Bauerle, J. E., Study of solid electrolyte polarization by a complex admittance method. *J. Phys. Chem. Solids* **1969,** *30* (12), 2657-2670.
152. Bard, A. J.; Faulkner, L. R.; White, H. S., *Electrochemical methods: fundamentals and applications*. John Wiley & Sons: 2022.
153. Orazem, M. E.; Tribollet, B., Electrochemical impedance spectroscopy. *New Jersey* **2008**, 383-389.
154. Wang, S.; Zhang, J.; Gharbi, O.; Vivier, V.; Gao, M.; Orazem, M. E., Electrochemical impedance spectroscopy. *Nature Reviews Methods Primers* **2021,** *1* (1), 41.
155. Irvine, J. T. S.; Sinclair, D. C.; West, A. R., Electroceramics: Characterization by Impedance Spectroscopy. *Adv. Mater.* **1990,** *2* (3), 132-138.
156. Kremer, F.; Schönhals, A., *Broadband dielectric spectroscopy*. Springer Science & Business Media: 2002.
157. Ohm, G. S., Vorläufige Anzeige des Gesetzes, nach welchem Metalle die Contaktelektricität leiten. *Annalen der Physik* **1825,** *80* (5), 79-88.
158. Macdonald, J. R.; Brachman, M. K., Linear-System Integral Transform Relations. *Rev. Mod. Phys.* **1956,** *28* (4), 393-422.
159. Agarwal, P.; Crisalle, O. D.; Orazem, M. E.; Garcia-Rubio, L. H., Application of measurement models to impedance spectroscopy: II. Determination of the stochastic contribution to the error structure. *J. Electrochem. Soc.* **1995,** *142* (12), 4149.
160. Agarwal, P.; Orazem, M. E.; Garcia-Rubio, L. H., Application of Measurement Models to Impedance Spectroscopy: III. Evaluation of Consistency with the Kramers-Kronig Relations. *J. Electrochem. Soc.* **1995,** *142* (12), 4159.
161. Boukamp, B., Electrochemical Impedance Spectroscopy in Solid State Ionics: Recent Advances. *Solid State Ionics* **2004,** *169* (1-4), 65-73.
162. Dokko, K.; Mohamedi, M.; Fujita, Y.; Itoh, T.; Nishizawa, M.; Umeda, M.; Uchida, I., Kinetic characterization of single particles of $LiCoO_2$ by AC impedance and potential step methods. *J. Electrochem. Soc.* **2001,** *148* (5), A422.
163. Huang, J.; Li, Z.; Zhang, J., Dynamic electrochemical impedance spectroscopy reconstructed from continuous impedance measurement of single frequency during charging/discharging. *J. Power Sources* **2015,** *273*, 1098-1102.
164. Itagaki, M.; Kobari, N.; Yotsuda, S.; Watanabe, K.; Kinoshita, S.; Ue, M., In situ electrochemical impedance spectroscopy to investigate negative electrode of lithium-ion rechargeable batteries. *J. Power Sources* **2004,** *135* (1-2), 255-261.
165. Stoynov, Z.; Savova-Stoynov, B., Impedance study of non-stationary systems: four-dimensional analysis. *Journal of electroanalytical chemistry and interfacial electrochemistry* **1985,** *183* (1-2), 133-144.
166. Abrantes, J. C. C.; Labrincha, J. A.; Frade, J. R., Applicability of the Brick Layer Model to Describe the Grain Boundary Properties of Strontium Titanate Ceramics. *J. Eur. Ceram. Soc.* **2000,** *20* (10), 1603-1609.
167. Beekmans, N. M.; Heyne, L., Correlation between Impedance, Microstructure and Composition of Calcia-Stabilized Zirconia. *Electrochim. Acta* **1976,** *21* (4), 303-310.
168. Kidner, N. J.; Perry, N. H.; Mason, T. O.; Garboczi, E. J., The Brick Layer Model Revisited: Introducing the Nano-Grain Composite Model. *J. Am. Ceram. Soc.* **2008,** *91* (6), 1733-1746.
169. van Dijk, T.; Burggraaf, A. J., Grain Boundary Effects on Ionic Conductivity in Ceramic $Gd_xZr_{1-x}O_{2-(x/2)}$ Solid Solutions. *physica status solidi (a)* **1981,** *63* (1), 229-240.

170. Verkerk, M. J.; Middelhuis, B. J.; Burggraaf, A. J., Effect of Grain Boundaries on the Conductivity of High-Purity ZrO_2–Y_2O_3 Ceramics. *Solid State Ionics* **1982,** *6* (2), 159-170.
171. Guo, X.; Waser, R., Electrical Properties of the Grain Boundaries of Oxygen Ion Conductors: Acceptor-Doped Zirconia and Ceria. *Prog. Mater Sci.* **2006,** *51* (2), 151-210.
172. Näfe, H., Ionic conductivity of ThO_2- and ZrO_2-based electrolytes between 300 and 2000 K. *Solid State Ionics* **1984,** *13* (3), 255-263.
173. Jamnik, J.; Maier, J., Treatment of the Impedance of Mixed Conductors Equivalent Circuit Model and Explicit Approximate Solutions. *J. Electrochem. Soc.* **1999,** *146* (11), 4183-4188.
174. Jamnik, J.; Maier, J., Generalised equivalent circuits for mass and charge transport: chemical capacitance and its implications. *PCCP* **2001,** *3* (9), 1668-1678.
175. Jamnik, J.; Maier, J.; Pejovnik, S., A powerful electrical network model for the impedance of mixed conductors. *Electrochim. Acta* **1999,** *44* (24), 4139-4145.
176. Draper, N. R.; Smith, H., *Applied regression analysis*. John Wiley & Sons: 1998; Vol. 326.
177. Macdonald, J. R., Impedance Spectroscopy: Old Problems and New Developments. *Elecrrochimica Acta* **1990,** *35* (10), 9.
178. Ciucci, F.; Chen, C., Analysis of Electrochemical Impedance Spectroscopy Data Using the Distribution of Relaxation Times: A Bayesian and Hierarchical Bayesian Approach. *Electrochim. Acta* **2015,** *167*, 439-454.
179. Macdonald, J. R., Impedance spectroscopy and its use in analyzing the steady-state AC response of solid and liquid electrolytes. *Journal of Electroanalytical Chemistry and Interfacial Electrochemistry* **1987,** *223* (1), 25-50.
180. Zahnow, J.; Bernges, T.; Wagner, A.; Bohn, N.; Binder, J. R.; Zeier, W. G.; Elm, M. T.; Janek, J., Impedance Analysis of NCM Cathode Materials: Electronic and Ionic Partial Conductivities and the Influence of Microstructure. *ACS Applied Energy Materials* **2021,** *4* (2), 1335-1345.
181. Sonn, V.; Leonide, A.; Ivers-Tiffée, E., Combined Deconvolution and CNLS Fitting Approach Applied on the Impedance Response of Technical Ni*v*8YSZ Cermet Electrodes. *J. Electrochem. Soc.* **2008,** *155* (7), B675.
182. Klotz, D.; Schmidt, J. P.; Kromp, A.; Weber, A.; Ivers-Tiffée, E., The Distribution of Relaxation Times as Beneficial Tool for Equivalent Circuit Modeling of Fuel Cells and Batteries. *ECS Transactions* **2019,** *41* (28), 25-33.
183. Dion, F.; Lasia, A., The use of regularization methods in the deconvolution of underlying distributions in electrochemical processes. *J. Electroanal. Chem.* **1999,** *475* (1), 28-37.
184. Boukamp, B. A., Distribution (function) of relaxation times, successor to complex nonlinear least squares analysis of electrochemical impedance spectroscopy? *Journal of Physics: Energy* **2020,** *2* (4), 042001.
185. Boukamp, B. A.; Rolle, A., Analysis and Application of Distribution of Relaxation Times in Solid State Ionics. *Solid State Ionics* **2017,** *302*, 12-18.
186. Ivers-Tiffée, E.; Weber, A., Evaluation of electrochemical impedance spectra by the distribution of relaxation times. *J. Ceram. Soc. Jpn.* **2017,** *125* (4), 193-201.
187. Danzer, M. A. Generalized Distribution of Relaxation Times Analysis for the Characterization of Impedance Spectra *Batteries* [Online], 2019.
188. Shi, F.; Kolb, J. F., Enhanced resolution impedimetric analysis of cell responses from the distribution of relaxation times. *Biosens. Bioelectron.* **2020,** *157*, 112149.
189. Effendy, S.; Song, J.; Bazant, M. Z., Analysis, Design, and Generalization of Electrochemical Impedance Spectroscopy (EIS) Inversion Algorithms. *J. Electrochem. Soc.* **2020,** *167* (10), 106508.
190. Quattrocchi, E.; Wan, T. H.; Curcio, A.; Pepe, S.; Effat, M. B.; Ciucci, F., A general model for the impedance of batteries and supercapacitors: The non-linear distribution of diffusion times. *Electrochim. Acta* **2019,** *324*.
191. Song, J.; Bazant, M. Z., Electrochemical Impedance Imaging via the Distribution of Diffusion Times. *Phys. Rev. Lett.* **2018,** *120* (11), 116001.
192. Wan, T. H.; Saccoccio, M.; Chen, C.; Ciucci, F., Influence of the Discretization Methods on the Distribution of Relaxation Times Deconvolution: Implementing Radial Basis Functions with DRTtools. *Electrochim. Acta* **2015,** *184*, 483-499.
193. Groetsch, C., *The theory of Tikhonov regularization for Fredholm equations*. Pitman Publishing: 1984.

194. Saccoccio, M.; Wan, T. H.; Chen, C.; Ciucci, F., Optimal Regularization in Distribution of Relaxation Times applied to Electrochemical Impedance Spectroscopy: Ridge and Lasso Regression Methods - A Theoretical and Experimental Study. *Electrochim. Acta* **2014,** *147*, 470-482.
195. Schlüter, N.; Ernst, S.; Schröder, U., Direct Access to the Optimal Regularization Parameter in Distribution of Relaxation Times Analysis. *ChemElectroChem* **2020,** *7* (16), 3445-3458.
196. Boukamp, B. A., Fourier transform distribution function of relaxation times; application and limitations. *Electrochim. Acta* **2015,** *154*, 35-46.
197. Schichlein, H., System Identification: A New Modelling Approach for SOFC Single Cells. *ECS Proceedings Volumes* **1999,** *1999-19* (1), 1069-1077.
198. Schichlein, H.; Müller, A. C.; Voigts, M.; Krügel, A.; Ivers-Tiffée, E., Deconvolution of electrochemical impedance spectra for the identification of electrode reaction mechanisms in solid oxide fuel cells. *J. Appl. Electrochem.* **2002,** *32* (8), 875-882.
199. Hershkovitz, S.; Baltianski, S.; Tsur, Y., Harnessing evolutionary programming for impedance spectroscopy analysis: A case study of mixed ionic-electronic conductors. *Solid State Ionics* **2011,** *188* (1), 104-109.
200. Tesler, A. B.; Lewin, D. R.; Baltianski, S.; Tsur, Y., Analyzing results of impedance spectroscopy using novel evolutionary programming techniques. *J. Electroceram.* **2010,** *24* (4), 245-260.
201. Hörlin, T., Maximum entropy in impedance spectroscopy of non-inductive systems. *Solid State Ionics* **1993,** *67* (1), 85-96.
202. Hörlin, T., Deconvolution and maximum entropy in impedance spectroscopy of noninductive systems. *Solid State Ionics* **1998,** *107* (3), 241-253.
203. Hahn, M.; Schindler, S.; Triebs, L.-C.; Danzer, M. A., Optimized Process Parameters for a Reproducible Distribution of Relaxation Times Analysis of Electrochemical Systems. *Batteries* **2019,** *5* (2).
204. Zhang, Y.; Chen, Y.; Li, M.; Yan, M.; Ni, M.; Xia, C., A high-precision approach to reconstruct distribution of relaxation times from electrochemical impedance spectroscopy. *J. Power Sources* **2016,** *308*, 1-6.
205. Žic, M.; Pereverzyev, S.; Subotić, V.; Pereverzyev, S., Adaptive multi-parameter regularization approach to construct the distribution function of relaxation times. *GEM - International Journal on Geomathematics* **2019,** *11* (1), 2.
206. Mertens, A.; Granwehr, J., Two-dimensional impedance data analysis by the distribution of relaxation times. *Journal of Energy Storage* **2017,** *13*, 401-408.
207. Gavrilyuk, A. L.; Osinkin, D. A.; Bronin, D. I., The use of Tikhonov regularization method for calculating the distribution function of relaxation times in impedance spectroscopy. *Russ. J. Electrochem.* **2017,** *53* (6), 575-588.
208. Effat, M. B.; Ciucci, F., Bayesian and Hierarchical Bayesian Based Regularization for Deconvolving the Distribution of Relaxation Times from Electrochemical Impedance Spectroscopy Data. *Electrochim. Acta* **2017,** *247*, 1117-1129.
209. Huang, J.; Papac, M.; O'Hayre, R., Towards robust autonomous impedance spectroscopy analysis: A calibrated hierarchical Bayesian approach for electrochemical impedance spectroscopy (EIS) inversion. *Electrochim. Acta* **2021,** *367*, 137493.
210. Li, X.; Ahmadi, M.; Collins, L.; Kalinin, S. V., Deconvolving distribution of relaxation times, resistances and inductance from electrochemical impedance spectroscopy via statistical model selection: Exploiting structural-sparsity regularization and data-driven parameter tuning. *Electrochim. Acta* **2019,** *313*, 570-583.
211. Liu, J.; Ciucci, F., The Gaussian process distribution of relaxation times: A machine learning tool for the analysis and prediction of electrochemical impedance spectroscopy data. *Electrochim. Acta* **2020,** *331*.
212. Liu, J.; Ciucci, F., The Deep-Prior Distribution of Relaxation Times. *J. Electrochem. Soc.* **2020,** *167* (2), 026506.
213. Krasnikova, I. V.; Pogosova, M. A.; Sanin, A. O.; Stevenson, K. J., Toward Standardization of Electrochemical Impedance Spectroscopy Studies of Li-Ion Conductive Ceramics. *Chem. Mater.* **2020,** *32* (6), 2232-2241.
214. Balaya, P.; Bhattacharyya, A. J.; Jamnik, J.; Zhukovskii, Y. F.; Kotomin, E. A.; Maier, J., Nano-ionics in the context of lithium batteries. *J. Power Sources* **2006,** *159* (1), 171-178.

215. Labelle, A. J.; Thon, S. M.; Masala, S.; Adachi, M. M.; Dong, H.; Farahani, M.; Ip, A. H.; Fratalocchi, A.; Sargent, E. H., Colloidal Quantum Dot Solar Cells Exploiting Hierarchical Structuring. *Nano Lett.* **2015,** *15* (2), 1101-1108.
216. Lee, W.; Muhammad, S.; Sergey, C.; Lee, H.; Yoon, J.; Kang, Y.-M.; Yoon, W.-S., Advances in the Cathode Materials for Lithium Rechargeable Batteries. *Angew. Chem. Int. Ed.* **2020,** *59* (7), 2578-2605.
217. Li, W.; Liu, J.; Zhao, D., Mesoporous materials for energy conversion and storage devices. *Nature Reviews Materials* **2016,** *1* (6), 16023.
218. Maier, J., Nanoionics: ionic charge carriers in small systems. *PCCP* **2009,** *11* (17), 3011-3022.
219. Maier, J., Pushing Nanoionics to the Limits: Charge Carrier Chemistry in Extremely Small Systems. *Chem. Mater.* **2014,** *26* (1), 348-360.
220. Pei, Y.; Tan, G.; Feng, D.; Zheng, L.; Tan, Q.; Xie, X.; Gong, S.; Chen, Y.; Li, J.-F.; He, J.; Kanatzidis, M. G.; Zhao, L.-D., Integrating Band Structure Engineering with All-Scale Hierarchical Structuring for High Thermoelectric Performance in PbTe System. *Advanced Energy Materials* **2017,** *7* (3), 1601450.
221. Tuller, H. L., Ionic conduction in nanocrystalline materials. *Solid State Ionics* **2000,** *131* (1), 143-157.
222. Wang, L.; Hong, M.; Sun, Q.; Wang, Y.; Yue, L.; Zheng, S.; Zou, J.; Chen, Z.-G., Hierarchical Structuring to Break the Amorphous Limit of Lattice Thermal Conductivity in High-Performance SnTe-Based Thermoelectrics. *ACS Appl. Mater. Interfaces* **2020,** *12* (32), 36370-36379.
223. Hink, S.; Wagner, N.; Bessler, W. G.; Roduner, E. Impedance Spectroscopic Investigation of Proton Conductivity in Nafion Using Transient Electrochemical Atomic Force Microscopy (AFM) *Membranes* [Online], 2012, p. 237-252.
224. Bessler, W. G., A new computational approach for SOFC impedance from detailed electrochemical reaction–diffusion models. *Solid State Ionics* **2005,** *176* (11), 997-1011.
225. Bessler, W. G., Rapid Impedance Modeling via Potential Step and Current Relaxation Simulations. *J. Electrochem. Soc.* **2007,** *154* (11), B1186.
226. Bessler, W. G.; Gewies, S.; Vogler, M., A new framework for physically based modeling of solid oxide fuel cells. *Electrochim. Acta* **2007,** *53* (4), 1782-1800.
227. Fronczek, D. N.; Bessler, W. G., Insight into lithium–sulfur batteries: Elementary kinetic modeling and impedance simulation. *J. Power Sources* **2013,** *244*, 183-188.
228. Gewies, S.; Bessler, W. G., Physically based impedance modeling of Ni/YSZ cermet anodes. *J. Electrochem. Soc.* **2008,** *155* (9), B937.
229. Fleig, J., The Influence of Inhomogeneous Potential Distributions on the Electrolyte Resistance in Solid Oxide Fuel Cells. *ECS Proceedings Volumes* **1997,** *1997-40* (1), 1374-1384.
230. Fleig, J., The Influence of Non-Ideal Microstructures on the Analysis of Grain Boundary Impedances. *Solid State Ionics* **2000,** *131* (1), 117-127.
231. Fleig, J., The grain boundary impedance of random microstructures: numerical simulations and implications for the analysis of experimental data. *Solid State Ionics* **2002,** *150* (1), 181-193.
232. Fleig, J., Impedance Spectroscopy on Solids: The Limits of Serial Equivalent Circuit Models. *J. Electroceram.* **2004,** *13* (1), 637-644.
233. Fleig, J.; Maier, J., Finite Element Calculations of Impedance Effects at Point Contacts. *Electrochim. Acta* **1996,** *41* (7), 1003-1009.
234. Fleig, J.; Maier, J., Point contacts in solid state ionics: finite element calculations and local conductivity measurements. *Solid State Ionics* **1996,** *86-88*, 1351-1356.
235. Fleig, J.; Maier, J., The Influence of Laterally Inhomogeneous Contacts on the Impedance of Solid Materials: A Three-Dimensional Finite-Element Study. *J. Electroceram.* **1997,** *1* (1), 73-89.
236. Fleig, J.; Maier, J., Rough electrodes in solid and liquid electrochemistry: impact of morphology on the impedance. *Solid State Ionics* **1997,** *94* (1), 199-207.
237. Fleig, J.; Maier, J., The Influence of Current Constriction on the Impedance of Polarizable Electrodes: Application to Fuel Cell Electrodes. *J. Electrochem. Soc.* **1997,** *144* (11), L302-L305.
238. Fleig, J.; Maier, J., A Finite Element Study on the Grain Boundary Impedance of Different Microstructures. *J. Electrochem. Soc.* **1998,** *145* (6), 2081-2089.
239. Fleig, J.; Maier, J., The impedance of ceramics with highly resistive grain boundaries: validity and limits of the brick layer model. *J. Eur. Ceram. Soc.* **1999,** *19* (6), 693-696.

240. Fleig, J.; Maier, J., Finite-Element Calculations on the Impedance of Electroceramics with Highly Resistive Grain Boundaries: I, Laterally Inhomogeneous Grain Boundaries. *J. Am. Ceram. Soc.* **1999,** *82* (12), 3485-3493.
241. Göbel, H., *Einführung in die Halbleiter-Schaltungstechnik*. Springer Berlin Heidelberg: 2014.
242. Birkholz, O.; Gan, Y.; Kamlah, M., Modeling the effective conductivity of the solid and the pore phase in granular materials using resistor networks. *Powder Technol.* **2019,** *351*, 54-65.
243. Gather, F.; Heiliger, C.; Klar, P. J., NeMo: A network model program for analyzing the thermoelectric properties of meso and nanostructured composite materials. *Prog. Solid State Chem.* **2011,** *39* (3), 97-107.
244. Gather, F.; Heiliger, C.; Klar, P. J., Modeling of interface roughness in thermoelectric composite materials. *J Phys Condens Matter* **2011,** *23* (33), 335301.
245. Eckhardt, J. K.; Burkhardt, S.; Zahnow, J.; Elm, M. T.; Janek, J.; Klar, P. J.; Heiliger, C., Understanding the Impact of Microstructure on Charge Transport in Polycrystalline Materials Through Impedance Modelling. *J. Electrochem. Soc.* **2021,** *168* (9), 090516-090528.
246. Kirchhoff, G., Ueber die Auflösung der Gleichungen, auf welche man bei der Untersuchung der linearen Vertheilung galvanischer Ströme geführt wird. *Annalen der Physik* **1847,** *148* (12), 497-508.
247. Kidner, N. J.; Homrighaus, Z. J.; Ingram, B. J.; Mason, T. O.; Garboczi, E. J., Impedance/Dielectric Spectroscopy of Electroceramics–Part 1: Evaluation of Composite Models for Polycrystalline Ceramics. *J. Electroceram.* **2005,** *14* (3), 283-291.
248. Kidner, N. J.; Homrighaus, Z. J.; Ingram, B. J.; Mason, T. O.; Garboczi, E. J., Impedance/Dielectric Spectroscopy of Electroceramics—Part 2: Grain Shape Effects and Local Properties of Polycrystalline Ceramics. *J. Electroceram.* **2005,** *14* (3), 293-301.
249. Becker, J.; Biebl, F.; Glatt, E.; Cheng, L.; Grießer, A.; Groß, M.; Linden, S.; Mosbach, D.; Wagner, C.; Weber, A.; Westerteiger, R. *GeoDict (Release 2022)*, Math2Market GmbH: 2022.
250. Hart, K. A.; Rimoli, J. J., Generation of Statistically Representative Microstructures with Direct Grain Geometry Control. *Computer Methods in Applied Mechanics and Engineering* **2020,** *370*, 113242.
251. Hart, K. A.; Rimoli, J. J., MicroStructPy: A Statistical Microstructure Mesh Generator in Python. *SoftwareX* **2020,** *12*, 100595.
252. Kremer, S. Impedance Spectroscopy on Ceramic Lithium-Ion Conductors and their Modeling. Justus Liebig University, 2022.
253. Eckhardt, J. K.; Kremer, S.; Fuchs, T.; Minnmann, P.; Schubert, J.; Burkhardt, S.; Elm, M. T.; Klar, P. J.; Heiliger, C.; Janek, J., Influence of Microstructure on the Material Properties of LLZO Ceramics Derived by Impedance Spectroscopy and Brick Layer Model Analysis. *ACS Appl Mater Interfaces* **2023,** *15* (40), 47260-47277.
254. Zahnow, J.; Bastianello, M.; Janek, J.; Elm, M. T., Defect Chemistry of Individual Grains with and without Grain Boundaries of Al-Doped Ceria Determined Using Well-Defined Microelectrodes. *The Journal of Physical Chemistry C* **2022,** *126* (5), 2737-2746.
255. Gerstl, M.; Navickas, E.; Friedbacher, G.; Kubel, F.; Ahrens, M.; Fleig, J., The separation of grain and grain boundary impedance in thin yttria stabilized zirconia (YSZ) layers. *Solid State Ion* **2011,** *185* (1), 32-41.
256. Hicken, J. E.; Zingg, D. W., A Simplified and Flexible Variant of GCROT for Solving Nonsymmetric Linear Systems. *SIAM Journal on Scientific Computing* **2010,** *32* (3), 1672-1694.
257. Eckhardt, J. K. Implementation of a Network for Modelling the Influence of the Microstructure on Measured and Simulated Impedance Spectra. Justus Liebig University, 2019.
258. Uredat, P.; Kodaira, R.; Horiguchi, R.; Hara, S.; Beyer, A.; Volz, K.; Klar, P. J.; Elm, M. T., Anomalous Angle-Dependent Magnetotransport Properties of Single InAs Nanowires. *Nano Lett.* **2020,** *20* (1), 618-624.
259. Uredat, P.; Elm, M. T.; Horiguchi, R.; Klar, P. J.; Hara, S., The transport properties of InAs nanowires: an introduction to MnAs/InAs heterojunction nanowires for spintronics. *J. Phys. D: Appl. Phys.* **2020,** *53* (33), 333002.
260. Uredat, P.; Hille, P.; Schörmann, J.; Eickhoff, M.; Klar, P. J.; Elm, M. T., Consistent description of mesoscopic transport: Case study of current-dependent magnetoconductance in single GaN:Ge nanowires. *Phys. Rev. B.* **2019,** *100* (8), 085409.

261. Herbert, J. Implementierung einer DRT-Analyse Software zur Untersuchung von Impedanzspektren. Justus Liebig University, 2021.
262. Brinker, C. J.; Lu, Y.; Sellinger, A.; Fan, H., Evaporation-Induced Self-Assembly: Nanostructures Made Easy. *Adv. Mater.* **1999,** *11* (7), 579-585.
263. Ren, Y.; Ma, Z.; Bruce, P. G., Ordered mesoporous metal oxides: synthesis and applications. *Chem. Soc. Rev.* **2012,** *41* (14), 4909-4927.
264. Grosso, D.; Boissière, C.; Smarsly, B.; Brezesinski, T.; Pinna, N.; Albouy, P. A.; Amenitsch, H.; Antonietti, M.; Sanchez, C., Periodically ordered nanoscale islands and mesoporous films composed of nanocrystalline multimetallic oxides. *Nature Mater.* **2004,** *3* (11), 787-792.
265. Reitz, C.; Haetge, J.; Suchomski, C.; Brezesinski, T., Facile and General Synthesis of Thermally Stable Ordered Mesoporous Rare-Earth Oxide Ceramic Thin Films with Uniform Mid-Size to Large-Size Pores and Strong Crystalline Texture. *Chem. Mater.* **2013,** *25* (22), 4633-4642.
266. Weidmann, C.; Brezesinski, K.; Suchomski, C.; Tropp, K.; Grosser, N.; Haetge, J.; Smarsly, B. M.; Brezesinski, T., Morphology-Controlled Synthesis of Nanocrystalline η-Al_2O_3 Thin Films, Powders, Microbeads, and Nanofibers with Tunable Pore Sizes from Preformed Oligomeric Oxo-Hydroxo Building Blocks. *Chem. Mater.* **2012,** *24* (3), 486-494.
267. Eckhardt, J. K.; Heiliger, C.; Elm, M. T., Understanding the Impedance of Mesoporous Oxides: Reliable Determination of the Material-Specific Conductivity. *ACS Appl. Mater. Interfaces* **2023,** *15* (29), 35332-35341.
268. Holm, R., *Electric Contacts: Theory and Application*. Springer Verlag: 1967; p 484.
269. Slade, P. G., *Electrical contacts: principles and applications*. CRC press: 2017; p 1311.
270. Greenwood, J. A., Constriction resistance and the real area of contact. *Br. J. Appl. Phys.* **1966,** *17* (12), 1621.
271. McDowell, M. T., In Situ Investigation of Lithium Interface Evolution in Solid-State Batteries. In *Lithium Metal Anodes and their Application in Batteries an International Online Symposium*, Center for Materials Research: 2022.
272. Eckhardt, J. K.; Klar, P. J.; Janek, J.; Heiliger, C., Interplay of Dynamic Constriction and Interface Morphology between Reversible Metal Anode and Solid Electrolyte in Solid State Batteries. *ACS Appl. Mater. Interfaces* **2022,** *14* (31), 35545-35554.
273. Eckhardt, J. K.; Fuchs, T.; Burkhardt, S.; Klar, P. J.; Janek, J.; Heiliger, C., 3D Impedance Modeling of Metal Anodes in Solid-State Batteries–Incompatibility of Pore Formation and Constriction Effect in Physical-Based 1D Circuit Models. *ACS Appl. Mater. Interfaces* **2022,** *14* (37), 42757-42769.
274. Eckhardt, J. K.; Fuchs, T.; Burkhardt, S.; Klar, P. J.; Janek, J.; Heiliger, C., Guidelines for Impedance Analysis of Parent Metal Anodes in Solid-State Batteries and the Role of Current Constriction at Interface Voids, Heterogeneities, and SEI. *Advanced Materials Interfaces* **2023,** *10* (8), 2202354-2202373.
275. Zhang, X.; Wang, Q. J.; Harrison, K. L.; Roberts, S. A.; Harris, S. J., Pressure-Driven Interface Evolution in Solid-State Lithium Metal Batteries. *Cell Reports Physical Science* **2020,** *1* (2), 100012.
276. Singh, D. K.; Fuchs, T.; Krempaszky, C.; Mogwitz, B.; Burkhardt, S.; Richter, F. H.; Janek, J., Overcoming Anode Instability in Solid-State Batteries through Control of the Lithium Metal Microstructure. *Adv. Funct. Mater.* **2022,** *33* (1).
277. Singh, D. K.; Fuchs, T.; Krempaszky, C.; Schweitzer, P.; Lerch, C.; Richter, F. H.; Janek, J., Origin of the lithium metal anode instability in solid-state batteries during discharge. *Matter* **2023,** *6* (5), 1463-1483.

2. Publications

2.1 Effect of Microstructure on Impedance Analysis

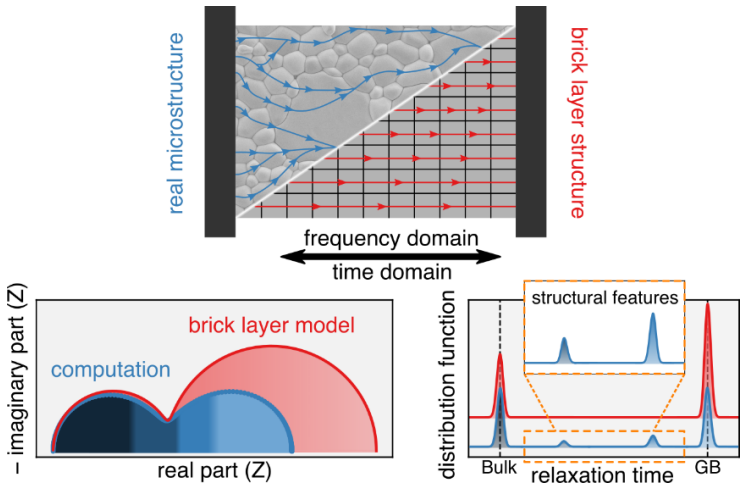

Abstract

Charge transport in polycrystalline electronic or ionic conductors is usually analyzed by serial macroscopic equivalent circuits, e.g., the brick layer model, which assume a homogeneous electric potential distribution across the sample. In such analyses, the microstructure is highly idealized and usually not representative of the actual microstructure. Here, we use a network model approach to investigate the impact of the sample's microstructure on the impedance. We find that this influence can be severe and should not be ignored. The interplay between microscopic transport paths affects the impedance response, which is reflected in both the frequency and the time domain. Especially in the distribution of relaxation times additional signals are identified and studied systematically. These additional contributions cannot be assigned to a microscopic transport process as usually done in a conventional analysis based on an equivalent circuit model fitted to the impedance data. The neglect of the peculiarities of the real microstructure in impedance analyses based on the brick layer model may yield deviations in the order of 100% in terms of the derived microscopic transport parameters. The microstructures used as input for the modelling are digitalized electron microscope images of polycrystalline samples.

Reference

Understanding the Impact of Microstructure on Charge Transport in Polycrystalline Materials Through Impedance Modelling. Janis K. Eckhardt, Simon Burkhardt, Julian Zahnow, Matthias T. Elm, Jürgen Janek, Peter J. Klar, and Christian Heiliger *J. Electrochem. Soc.* **2021**, 168, 9, 090516-090528. (DOI: 10.1149/1945-7111/ac1cfe)

Reproduced with permission

Journal of The Electrochemical Society, 2021 **168** 090516

Understanding the Impact of Microstructure on Charge Transport in Polycrystalline Materials Through Impedance Modelling

Janis K. Eckhardt,[1,2,z] Simon Burkhardt,[2,3] Julian Zahnow,[2,3] Matthias T. Elm,[2,3,4] Jürgen Janek,[2,3] Peter J. Klar,[2,4] and Christian Heiliger[1,2]

[1]*Institute for Theoretical Physics, Justus-Liebig-University Giessen, D-35392 Giessen, Germany*
[2]*Center for Materials Research (ZfM), Justus-Liebig-University Giessen, D-35392 Giessen, Germany*
[3]*Institute of Physical Chemistry, Justus-Liebig-University Giessen, D-35392 Giessen, Germany*
[4]*Institute of Experimental Physics I, Justus-Liebig-University Giessen, D-35392 Giessen, Germany*

Charge transport in polycrystalline electronic or ionic conductors is usually analyzed by serial macroscopic equivalent circuits, e.g., the brick layer model, which assume a homogeneous electric potential distribution across the sample. In such analyses, the microstructure is highly idealized and usually not representative of the actual microstructure. Here, we use a network model approach to investigate the impact of the sample's microstructure on the impedance. We find that this influence can be severe and should not be ignored. The interplay between microscopic transport paths affects the impedance response, which is reflected in both the frequency and the time domain. Especially in the distribution of relaxation times additional signals are identified and studied systematically. These additional contributions cannot be assigned to a microscopic transport process as usually done in a conventional analysis based on an equivalent circuit model fitted to the impedance data. The neglect of the peculiarities of the real microstructure in impedance analyses based on the brick layer model may yield deviations in the order of 100 % in terms of the derived microscopic transport parameters. The microstructures used as input for the modelling are digitalized electron microscope images of polycrystalline samples.

Manuscript submitted April 3, 2021; revised manuscript received July 29, 2021. Published September 20, 2021.

Supplementary material for this article is available online

The functioning of many electrical devices, such as, e.g., sensors, batteries, thermoelectric or optoelectronic devices, relies on efficient electronic and/or ionic charge transport. The selection of materials with an optimized microstructure often controls the function of the device.[1–10] Examples are many semiconductor devices, in which layer thicknesses are optimized based on band gap engineering.[11–13] The microstructure approach is widely used, e.g., in the suppression of phonon transport in thermoelectric materials[14–18] or the formation of percolation networks in composite cathodes for batteries.[19–23] Active materials for electrochemical energy storage often show a specific microstructure optimizing transport of electronic and ionic charge carriers.[24–32] In other cases, the microstructure of the material is inherent to the fabrication process, e.g., in the case of sintered ceramics or polycrystalline thin films with a specific grain size distribution.[6,33,34] An understanding of the resulting microscopic transport paths and their relation to the nano-, micro-, and mesostructure is essential for achieving maximum device performance as well as for identifying failure mechanisms, e.g., due to local Joule heating along the main microscopic transport path.

Therefore, the interpretation of charge transport properties in terms of a microstructure with distributed local properties is an essential task, as conventional transport measurements only yield macroscopic transport parameters such as the mean or effective conductivity.[35,36] In-depth knowledge about microscopic transport paths and processes either requires tedious local probe measurements, which do not allow a 3D approach, or the precise assessment and geometric modelling of the sample microstructure on different length scales. Impedance spectroscopy (IS) is used excessively to characterize the macroscopic charge transport by measuring the frequency-dependent complex impedance.[37] This allows distinguishing transport processes with different relaxation times, at least to a certain extent.[38–40] Thus, data acquisition requires comparably small efforts, making IS an exceedingly popular, powerful, and versatile tool.

Usually, so-called equivalent circuits of idealized circuit components, such as, e.g., parallel resistor-capacitor (*RC*) elements, are used for modeling impedance spectra. Each component represents a specific charge transport mechanism, such as, e.g., transport across grain boundaries, intragrain bulk transport, or charge transfer at electrodes. The impedance spectrum of an equivalent circuit with a relatively small number of parameters is then calculated and fitted to the experimental data, resulting in macroscopic capacitances and resistances (plus inductances in rare cases). Finally, these macroscopic transport parameters are interpreted in terms of microscopic transport processes, assuming a simplified geometric model. By this, conductivity or permittivity values are assigned to constituents of the sample, e.g., bulk, grain boundaries, surface regions, interfaces, etc. Recently, Krasnikova et al. demonstrated that there are multiple external (measurement procedure) and internal (sample characteristics) parameters that influence the derived conductivity values and their uncertainties.[41] We will show by a comparison of the results of the brick layer model and of our implemented network model that the influence of microstructure on the derived transport parameters is even more severe.

The "equivalent circuit approach" and the definition of macroscopic idealized circuit elements necessarily reduces the dimensionality of charge transport in a sample to one dimension. As shown below, it may yield correct results for the conductivity of the bulk material, but may also cause significant deviations for the grain boundary conductivity. A more advanced way to obtain grain boundary parameters is to use the boundary layer approach developed by Beekmans and Heyne, which was later called the brick layer model (BLM).[42–47] Within this model, the microstructure of a polycrystalline solid is approximated by a 3D-arrangement of face-sharing cubic grains with a constant edge length and grain boundary layers with a constant thickness in between.[33] The potential gradient driving the charge transport varies along the macroscopic transport direction only, an assumption that does not necessarily hold in polycrystalline samples. The dimensionality of the 3D charge transport is reduced to quasi-1D-charge transport through N equal and independent pathways. More realistic features of a polycrystalline solid, e.g., the distribution of grain size, variation of grain shape, or pores are neglected. As highlighted in previous studies, e.g., by Maier and Fleig, the equality of all charge transport pathways in the

[z]E-mail: janis.k.eckhardt@theo.physik.uni-giessen.de

Journal of The Electrochemical Society, 2021 168 090516

BLM leads to quantitative and qualitative deviations from a realistic picture.[39,48–50] The consequences are severe ranging from the misinterpretation of the transport mechanisms to the extraction of inaccurate material parameters, as shown below.

To investigate these effects systematically, the real microstructure of a sample needs to be implemented into a representative model structure. Different strategies are reported in the literature, e.g., the finite-difference[51,52] or the finite-element method.[39,48,53–56] The simulated impedance in these studies, however, was exclusively analyzed in the frequency domain, i.e., in Nyquist plots. In this representation of the complex impedance, qualitative results are easily obtained while quantitative conclusions are challenging. The transformation of the impedance from the frequency domain to the time domain yields the so-called distribution of relaxation times (DRT), which is a more useful data representation in this case.[57–59] The DRT generally facilitates the identification and separation of different charge transport processes as well as the assignment of characteristic time constants to them.[23,60] However, noise signals, bad contacts or inappropriate reconstruction algorithms can result in additional features (pseudo peaks) and other deviations from the ideal DRT.[57,61,62]

In the following, we introduce a novel network model to simulate the impedance response of polycrystalline samples with non-ordered arrangements of micro- and nanocrystalline grains in the frequency and time domain. The computational results are based on digitalized real microstructures imaged by electron microscopy. The analysis of the simulated impedance spectra reveal that the interplay between different microscopic transport paths causes additional contributions to the macroscopic frequency-dependent impedance, which give rise to additional signals in the DRT. This effect originates from the asymmetry of the microstructure as a whole and cannot be captured by one-dimensional models such as the BLM. The interpretation of these contributions solely in terms of local properties of the material is prone to error and will lead to misinterpretations of the experimental data. The numerical simulations by the network model are complemented by a comprehensive case study based on an application of the BLM to a simplified model system consisting of two different charge transport pathways. The impedance of the two-path-model can be solved analytically. The equations derived prove unambiguously that such additional DRT contributions arise solely due to the asymmetry of the microstructure and the resulting interplay between microscopic transport paths.

Computational Details

Generation of a three-dimensional microstructure and a nodal network.—A three-dimensional microstructure consisting of individual grains with an arbitrary shape is generated based on a scanning electron microscopy (SEM) image of the surface of a polycrystalline sample (see Fig. 1a). The two-dimensional surface information is discretized into an array of cubic voxels with an edge length of $d = 100$ nm. While this leads to artificially created depth information, the approach described in the following can be applied to any three-dimensional microstructure. A variation of the depth of the voxels in 2D transport simulations leads to quantitative changes but does not affect qualitative correlations. It can be considered as a scaling factor that modulates the exact values of the simulated impedances, which are therefore given in arbitrary units. Every voxel is assigned to a specific grain in the microstructure. This allows voxels of the same grain to be distinguished from those of different grains, as well as charge transport within a grain to be distinguished from charge transport across a grain boundary. The nodal network derived from this microstructure is based on nodes that are located in the center of every voxel. Since the surface of the SEM image is transferred into a single layer of voxels, the charge transport in two dimensions is simulated. A simplified illustration of the derivation of the nodal network from a given microstructure is shown in Fig. 1.

Description of charge transport through the nodal network.—The charge transport between two nodes in the nodal network is described using equivalent circuit elements that consist of a resistor R and a capacitor C in parallel (RC-elements). The values for R and C are directly correlated to the conductivity σ and the permittivity ε of the underlying microscopic transport processes in the bulk of the grain and across the grain boundary. While the impedance network can be built to account for mixed ionic and electronic conduction within the material, only one charge carrier, i.e., either electronic or ionic conduction was assumed here. The charge transport between two nodes of the same grain is described by two identical RC-elements in series with R_{Bulk} and C_{Bulk} resulting from the conductivity σ_{Bulk} and the permittivity $\varepsilon_{\mathrm{Bulk}}$ of the bulk material. The charge transport between two nodes of different grains is described by the same two RC-elements resulting from bulk properties but adding one additional RC-element in a serial circuit. The parameters of this additional RC-element are R_{GB} and C_{GB} and result from the conductivity σ_{GB} and the permittivity $\varepsilon_{\mathrm{GB}}$ of the grain boundaries. The conductivities and the permittivities were assumed to be independent from the excitation frequency. The values for the corresponding resistances R_i and capacitances C_i are calculated according to

$$R_i = \sigma_i^{-1} \cdot \frac{L}{A} \quad [1]$$

$$C_i = \varepsilon_i \cdot \frac{A}{L} \quad [2]$$

where A and L denote the interface area between two neighboring voxels and the distance in which the underlying microscopic transport process is taking place, respectively. Thus, in this work, the area A is given by the edge length of the voxels ($A = d^2$). For bulk transport, L equals $d/2$, while for the grain boundary transport L is equal to the thickness of the grain boundary δ_{GB}. The latter is considered to include the grain interface (core region) and the adjacent space charge region. The derivation of an impedance network from a given microstructure is illustrated in Fig. 1d.

The impedance network obtained from this procedure was used to simulate the impedance of six different microstructures (see Supporting Information, available online at stacks.iop.org/JES/168/090516/mmedia). For this purpose, a nodal analysis was conducted, which is based on the complex-valued potential distribution inside the impedance network (see Supporting Information for further computational details). The analysis is performed for a fixed angular frequency of the applied AC field. To simulate the impedance over an extended frequency range, the nodal analysis is repeated for different angular frequencies. Polarization effects at both electrodes have not been considered in the computations to avoid the occurrence of an additional (maybe overlapping) signal in the impedance spectra. Such effects can, however, easily be implemented into the computations.

The simulation of the spectra based on the equivalent circuit and the DRT analyses were performed using the commercial software RelaxIS 3 (version 3.0.17.10, rhd instruments GmbH & Co. KG).

Results and Discussion

Realistic microstructure model and experimental data.—*Challenges in interpreting impedance data gathered in experimental studies.*—The theoretical approach presented in this work is motivated by experimental results on the impedance of a microcrystalline ceria (CeO_2) thin film. The grain structure of the film at its surface can be assessed by using SEM. Information on the charge transport properties through this microstructure has been gathered by impedance measurements (see Supporting Information for experimental details).

According to the microstructure depicted in Fig. 1a, three different microscopic transport processes can in principle occur in the sample. These are the transport through the bulk of the grain, the transport across the grain boundary, and the transport along the grain

Journal of The Electrochemical Society, 2021 **168** 090516

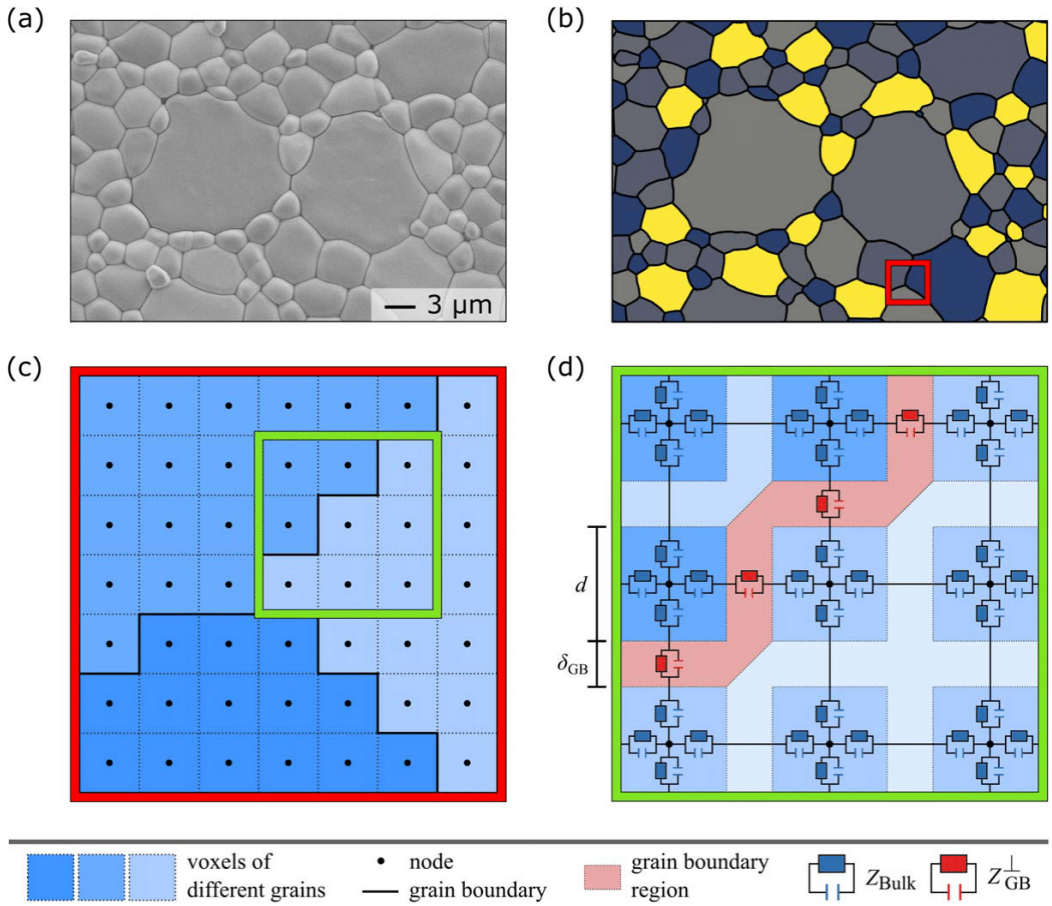

Figure 1. Schematic depiction of the generation of an impedance network based on a discretized two-dimensional microstructure. (a) SEM image of an experimentally investigated ceria thin film. (b) Computational model system of the microstructure. (c) Detail of a representative microstructure that is discretized into squares with an edge length *d* and nodes in the center of the squares. (d) Description of the local charge transport situations between the nodes. The situations considered within the polycrystalline material, namely bulk transport and transport across grain boundaries, are represented by the corresponding *RC*-elements.

boundary. A fourth macroscopic charge transport process arises from the transport across the sample-electrode interface. However, oxide ceramics, such as ceria and zirconia, with an average grain size in the micrometer range typically exhibit blocking grain boundaries, i.e., the transport of ions and electrons along grain boundaries is negligible.[63–66] Thus, three main contributions to the macroscopic impedance of the system that arise from microscopic transport processes are expected. The three transport processes should be reflected in the impedance spectrum by three semicircles since they should possess different characteristic time constants.

As an example and motivation, Fig. 2a shows a typical impedance spectrum of a microcrystalline CeO_2 thin film in a Nyquist plot. The impedance data are obtained by using an interdigitated electrode assembly. In a standard analysis, this measurement is analyzed as follows: While the semicircle at low frequencies can be easily identified as the contribution from the electrode, there is only one other distorted semicircle visible at higher frequencies. Thus, only two semicircles are observed, instead of the anticipated three semicircles. This suggests that the semicircles corresponding to the microscopic transport processes across grain boundaries and across the bulk of the grains have merged and cannot be easily distinguished in the Nyquist plot. Such behavior is typically observed in nanocrystalline or mesoporous oxides.[6,65,67,68] To deconvolve the single contributions to the total impedance without additional experimental information, the measured impedance data is transferred into the time domain (see Fig. 2b).

The calculated DRT and thus the number of distinguishable local maxima, which are referred to as "signals" in the following, strongly depends on the computational parameters, such as the discretization and interpolation parameters, as well as the quality of the experimental data.[61] Based on the variety of parameters, it becomes evident that the performance and interpretation of the DRT is not trivial. The preprocessing of the data and the tuning of the DRT parameters requires sufficient knowledge about the system to be examined. An insufficient execution leads to wrong results and thus to misinterpretations of spectral features. Here, by using a set of typical parameters, nine signals can be observed in the DRT. Since the number of signals should correspond to the number of time constants of charge transport processes in the structure, three signals should be correlated to the aforementioned three microscopic transport processes. The points marked in green in the Nyquist plot correspond to the semicircle assigned to the electrode. By omitting these points in the calculation of the DRT, signals 7, 8, and 9 in the DRT can be assigned to processes related to the electrode. Since the peak position of a signal corresponds to the characteristic time constant τ and the area below a peak corresponds to the resistance *R*, the capacitances related to the microscopic processes can be calculated based on $C = \tau \cdot R^{-1}$. The capacitance calculated

Journal of The Electrochemical Society, 2021 **168** 090516

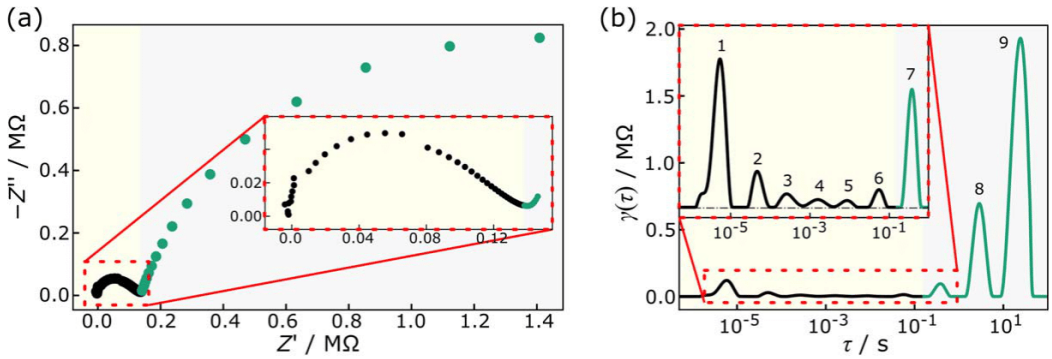

Figure 2. Typical experimental impedance spectrum of a ceria thin film deposited on an alumina substrate. The thin film was ∼1 μm thick and consisted of columnar grains extending down to the substrate. The impedance data are displayed in a Nyquist plot (a) and a DRT (b). Points and curves marked in green are caused by the electrode. The *y*-axis of the inset in (b) is magnified 13 times.

for signal 1 is 50 pF, which is typical for a microscopic bulk transport process.[40] There remain signals 2 to 6 in the DRT, which are weaker and for which an explanation is lacking. The standard procedure anticipates that only one of them may correspond to the third microscopic process, i.e., the transport across the grain boundaries. The other signals are usually explained based on additional effects such as experimental noise or the occurrence of a constriction effect within the system under investigation.[69,70]

This example clearly shows the dilemma of relating the macroscopic transport property, i.e. the frequency-dependent impedance, to the microscopic transport taking place inside the sample. There is no one-to-one correspondence between the number of semicircles required for fitting the Nyquist plot, the number of signals in the DRT, and the number of microscopic transport processes, which can be realistically assumed to occur within the sample. Additional effects, which may explain a large number of less intense signals in the DRT, need to be sought. It is beyond the scope of this work, to address the origins of all additional impedance signals observed in the experimental data of this particular ceria sample. The data solely serve as a motivation to seek a deeper understanding of possible origins of impedance contributions in general. In what follows, we demonstrate that additional DRT signals may originate also from the microstructure of the sample itself apart from flaws in the analysis. For this purpose, a thorough theoretical analysis of a model system based on a realistic microstructure is performed. The occurrence of microstructure related additional DRT signals is not restricted to this particular sample but is a general feature which may occur in polycrystalline materials. To prove this conclusion, a minimal model system consisting of two independent transport paths is devised and analytical expressions are derived, which show unambiguously that additional DRT signals may arise from the microstructure itself.

Modeling and analyzing the impedance of realistic microstructures.—For the theoretical study, an SEM image of the microcrystalline CeO_2 thin film (see Fig. 1a) is discretized to generate a suitable computational model system reflecting the microstructure of a real sample. It is important to note that only a small section of the CeO_2 thin film serves as input for the model system, i.e., the computational impedance will not describe the experimental results in detail. A network model is used to generate synthetic impedance data that is free of any experimental noise. This ensures that the impedance spectrum and the DRT contain information that originates solely from the impedance network itself. The computational result is then analyzed in the frequency and the time domain. By this, the impact of individual contributions of different microscopic features on the impedance spectrum as well as on the DRT is studied systematically. The results of the analysis prove that the microstructure yields different microscopic transport paths with each path contributing to the total impedance of the system. It is demonstrated that structural contributions to the total impedance exist. This leads to additional signals, especially in the DRT, that cannot be assigned to a specific microscopic transport process, e.g., through grains or grain boundaries. While the results shown in the following are obtained from the impedance network derived from the SEM image in Fig. 1a, similar results were obtained in computations with five more microstructures depicted in Fig. S1 in the Supporting Information.

The impedance of the discretized microstructure in Fig. 1b was simulated and is depicted in Fig. 3a (black curve). The microscopic transport parameters considered are the conductivities σ_i and the permittivities ε_i characteristic for grain boundaries (i = GB) and the grains (i = Bulk). The numerical values for the microscopic transport parameters are $\sigma_{\text{Bulk}} = \sigma_0$, $\varepsilon_{\text{Bulk}} = 100 \cdot \varepsilon_0$, $\sigma_{\text{GB}} = 2.5 \cdot 10^{-3} \cdot \sigma_0$, and $\varepsilon_{\text{GB}} = 22.5 \cdot \varepsilon_0$. The conductivity σ_0 was chosen to be equal to 1 mS cm^{-1}, but its exact value does not affect the qualitative behavior of the simulated impedance. A fixed value for δ_{GB} (grain boundary core and adjacent space charge region) of 10 nm is used in accordance with values reported in the literature.[34] The simulated impedance appears to show the characteristic features of two semicircles in a Nyquist plot.

Comparison between the impedance of the network model and the impedance of the BLM.—To assess the impact of the microstructure on the impedance, a comparison of the simulated impedance with a model that is based on a heavily simplified microstructure, i.e. the BLM, is drawn. For this purpose, the microscopic parameters σ_{Bulk}, $\varepsilon_{\text{Bulk}}$, σ_{GB}, and ε_{GB} of the network model were used as input parameters for the BLM. Within the BLM, the structure is assumed to be built of cubic grains of the same size. The average grain size (3.36 μm) was determined based on the actual microstructure as depicted in Fig. 1a. These grains were assumed to be separated by grain boundary layers of a constant thickness (δ_{GB} = 10 nm). By accounting for the ratio of grain boundary volume to grain volume, the microscopic parameter pairs of conductivity and permittivity can be translated into pairs of macroscopic transport parameters (R_i, C_i).[43,45,63] These calculated macroscopic parameters can be used to simulate the impedance response of the simplified microstructure within the BLM (green curve).

The differences between the BLM-derived green curve and the network model-derived black curve demonstrate the consequences of neglecting the microstructure in simulating charge transport. The impedance calculated based on the structural assumptions of the BLM (green curve) differs significantly from the impedance resulting from the nodal analysis that accounts for the realistic microstructure. Here, the BLM overestimates the macroscopic grain boundary resistance R_{GB} by 83 % compared to the macroscopic grain boundary resistance derived from the network model (excluding the contributions of the additional signals, which will be introduced and discussed below). This deviation varies between

Journal of The Electrochemical Society, 2021 **168** 090516

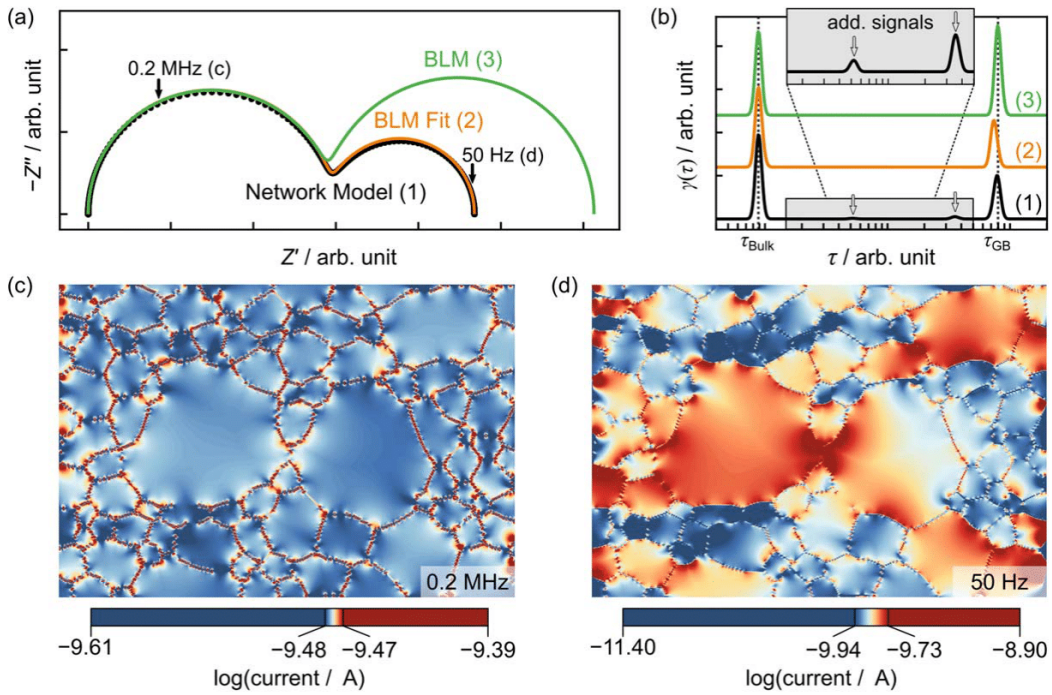

Figure 3. Computational results of impedance data of a thin film (cf. Fig. 1b) in Nyquist (a) and DRT (b) representation. While the orange curve corresponds to a fit using the BLM as an equivalent circuit, the green curve stems from a calculation using the BLM structure and the actual microscopic transport parameters. At high frequencies (c), the current density is homogeneously distributed throughout the structure, while at low frequencies (d) different transport paths through the structure are visible. The following microscopic transport parameters $\sigma_{Bulk} = \sigma_0$, $\varepsilon_{Bulk} = 100 \cdot \varepsilon_0$, $\sigma_{GB} = 2.5 \cdot 10^{-3} \cdot \sigma_0$, $\varepsilon_{GB} = 22.5 \cdot \varepsilon_0$, and $\delta_{GB} = 10$ nm were used in the simulation.

41 % and 83 % for the different microstructures investigated. The derived parameters are listed in Table I. Contrary, the BLM underestimates the macroscopic grain boundary capacity C_{GB} by 42 % compared to the simulation depicted in Fig. 3a. This underestimation varies between 23 % and 42 % for the different microstructures investigated. The deviations of the bulk parameters, however, are less than 0.1 %.

An alternative approach to investigate the influence of the microstructure on the impedance is to fit the impedance of an equivalent circuit consisting of two *RC*-elements in series (orange curve) to the impedance of the network model (black curve). The fitting parameters of both *RC*-elements, which represent the transport across grain boundaries and in the bulk of the grains in BLM-related models, yield two pairs of capacitance and resistance, i.e., (R_{GB}, C_{GB}) and (R_{Bulk}, C_{Bulk}). The microscopic parameter pairs of permittivity (ε_{Bulk}^{BLM}, ε_{GB}^{BLM}) and conductivity (σ_{Bulk}^{BLM}, σ_{GB}^{BLM}) can be derived from the assumptions regarding the microstructure within the BLM.[43,45,63]

The values σ_{Bulk}^{BLM}, ε_{Bulk}^{BLM}, σ_{GB}^{BLM}, and ε_{GB}^{BLM} derived by the fitting procedure and the structural assumptions used in the BLM (orange curve) deviate considerably from the microscopic parameters σ_{Bulk}, ε_{Bulk}, σ_{GB}, and ε_{GB} used as input parameters to simulate the impedance of the real microstructure (black curve). For this specific choice of parameters, the microscopic parameters describing the grain boundary process, σ_{GB}^{BLM} and ε_{GB}^{BLM}, are 83 % and 72 % larger, respectively, than the corresponding input values used to simulate the impedance of the microstructure, σ_{GB} and ε_{GB}. The deviations between σ_{GB}^{BLM} and σ_{GB}, as well as between ε_{GB}^{BLM} and ε_{GB} vary between 41 % and 83 % and between 31 % and 72 %, respectively, for the different microstructures investigated (see Table I). In contrast, σ_{Bulk}^{BLM} and ε_{Bulk}^{BLM} are almost equal to σ_{Bulk} and ε_{Bulk}. According to this comparison, the application of the BLM to analyze experimental impedance data would lead to an overestimation of the microscopic charge transport parameters σ_{GB} and ε_{GB}.

Understanding the influence of the microstructure on charge transport.—The cause of the significant errors made when using the BLM for analyzing the simulated impedance provided by the network model is the representation of the sample's microstructure by an ordered arrangement of mono-sized cubic grains. This oversimplification of the real microstructure leads to a quasi-1D transport in the BLM. This condition, however, is not satisfied, since the real sample exhibits a broad distribution of grain sizes (see Fig. 1a) and their spatial distribution will lead to local potential gradients, which deviate from the macroscopic current direction. Consequently, a distribution of the local current density results, which is depicted exemplarily in Figs. 3c and 3d for two different frequencies of the exciting AC electric field. The color plots of the current density distribution in the plane of the sample structure result from the nodal analysis (see also Fig. S4 for color plots with a directly comparable color scale).

It can be seen in Fig. 3c and Fig. S3 that the current density distribution at high frequencies is almost homogeneously distributed within the grains. Slight deviations of the local currents from the macroscopic current directions are only observed at the grain boundaries. Thus, the microscopic transport paths can be considered parallel to the macroscopic current direction from left to right. The reason is that the grain boundaries are dielectrically short-circuited in this frequency range and play a minor role. Therefore, the microscopic transport parameters determining the high-frequency impedance response are the two bulk parameters only. These two considerations, namely that the microscopic transport paths are parallel to the macroscopic current direction and that the impedance response is dominated by the microscopic transport parameters of bulk, are in accordance with the assumptions of the BLM and, thus, explain why $\sigma_{Bulk} \cong \sigma_{Bulk}^{BLM}$ and $\varepsilon_{Bulk} \cong \varepsilon_{Bulk}^{BLM}$. Furthermore, it

Journal of The Electrochemical Society, 2021 **168** 090516

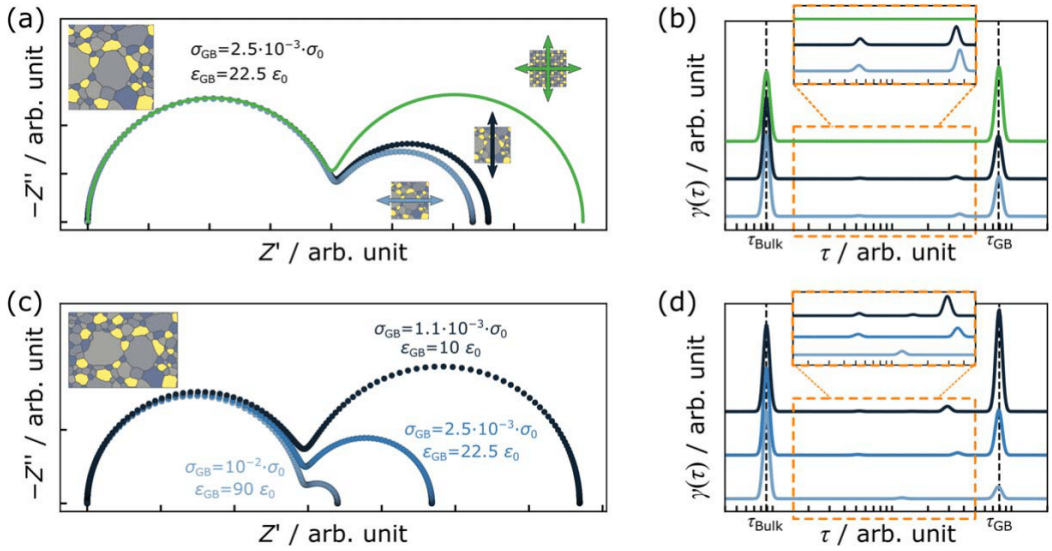

Figure 4. Simulated impedance resulting from horizontal (light blue) and vertical (dark blue) charge transport through a squared microstructure in a Nyquist (a) and DRT (b) representation. The impedance resulting from the BLM using the same input parameters and an average grain size of 3.44 μm (green) is shown for comparison. The influence of the input parameters on the impedance is studied by simulating the impedance of the rectangular microstructure (Fig. 1b) as depicted in a Nyquist (c) and DRT (d) representation. The number of resolvable additional signals in the DRT, their amplitudes and the time constants strongly depend on the microstructure, the macroscopic transport direction (top) and the microscopic grain boundary transport parameters (bottom). The computational results are based on the following parameters: $\sigma_{Bulk} = \sigma_0$, $\varepsilon_{Bulk} = 100 \cdot \varepsilon_0$, $\delta_{GB} = 10$ nm.

explains why the impedance of the BLM agrees with the impedance derived by the network model with the same microscopic transport parameters in the high-frequency region (left semicircle in Fig. 3a).

In contrast, the current density at low frequencies is higher in larger grains than in smaller ones as depicted in Fig. 3d. This results in several distinguishable microscopic transport paths of the charge carriers through the sample. The microscopic paths are not parallel to the macroscopic current direction from left to right. The dominant microscopic transport paths are those with few grain boundaries only. Such a distinction between different microscopic transport paths as well as the influence of the microscopic charge transport parameters σ_i and ε_i on them cannot be captured by the BLM. The number of grain boundaries that are crossed by the dominating transport pathways strongly depends on the average grain size assumed for the BLM. A larger average grain size leads to a lower number of grain boundaries crossed by the charge carriers and a smaller average grain size, hence, leads to a larger number of grain boundaries crossed by the charge carriers. Therefore, the assumption regarding the average grain size has a major impact on the results derived from the BLM. For the average grain size derived from the SEM image in Fig. 1a, the number of grain boundaries crossed by charge carriers is higher for the BLM than for the network model. Since these transport pathways dominate the impedance response at lower frequencies, their contribution to the impedance is overestimated by the BLM. Therefore, the semicircle of the impedance response in the low-frequency range, representing the grain boundary contribution in Fig. 3a, is much larger in the green curve than in the black curve. As has already been pointed out, also an underestimation of the grain boundary contribution to the overall impedance at low frequencies is possible, depending on the average grain size assumed. Furthermore, by averaging over a distribution of grains and reducing the microstructure to an average grain size, the information on the actual shape of individual grains is neglected. As demonstrated by Maier and Fleig, the shape of the grains also affects whether the BLM-derived grain boundary parameters are over- or underestimated.[39,55]

Deconvolution of individual impedance contributions in the time-domain.—The standard procedure to deconvolve overlapping or merged semicircles and to determine the time constants of microscopic transport processes is to transfer the impedance data into the time domain (see Fig. 3b). The DRT of the impedance modeled by the network model (black) reveals four signals. Two stronger ones occur at a high and low time constant, respectively, and two weaker ones occur in the intermediate time range. It should be noted that the model only takes two microscopic transport processes into account, i.e., the transport through the grain and across the grain boundary. The signals with the highest and lowest time constant can be clearly identified as being characteristics of these two transport processes. Consequently, the two time constants in the intermediate time range cannot be related to microscopic transport processes but must have other origins. One of these signals directly affects the low-frequency semicircle in the Nyquist plot, whereas the high-frequency semicircle is almost ideal. Fleig and Maier found a similar distortion of the low-frequency semicircle in FEM simulations of polycrystalline ceramics.[39,48,55] They argued that the frequency-dependent switching between current paths is the origin of the non-ideality of the low-frequency semicircle. Here, the DRT even reveals a second additional signal. Due to its small intensity and consequently its small resistance value, its direct observation in the Nyquist plot is challenging.

In addition to the DRT of the impedance considering the real microstructure (black), the DRT of the BLM fitting result (orange) and the impedance calculated based on the structural assumptions of the BLM (green) are also depicted. Both exhibit two signals in the DRT only, and no additional signals occur. The reason is that the DRT in both cases is derived from a simple equivalent circuit of two *RC*-elements in series, each represented by one of the two signals.

The signal with the smallest time constant in all three DRT can be assigned to the microscopic transport within a grain. This signal shows very similar time constant and amplitude in each DRT. The situation is different in the case of the signal with the largest time constant on the right of the three DRT. It is indicative of the microscopic transport across the grain boundaries. As somewhat anticipated, the systematic errors in the determination of the microscopic transport parameters using the BLM-based fitting approach (red) are also translated into the time-domain. This

Journal of The Electrochemical Society, 2021 **168** 090516

Table I. Deviations in the derived transport parameters using the BLM. The parameters of the network model computation were used as reference while calculating the errors, e.g., $\Delta\sigma_{GB} = (\sigma_{GB}^{BLM} - \sigma_{GB})/\sigma_{GB}$. A positive sign means that the BLM is overestimating the respective parameter, whereas the quantities with a negative sign are underestimated. The following microscopic transport parameters $\sigma_{Bulk} = \sigma_0$, $\varepsilon_{Bulk} = 100 \cdot \varepsilon_0$, and $\delta_{GB} = 10$ nm were used in the computations.

Figure	$10^3 \cdot \sigma_{GB}/\sigma_0$	$\varepsilon_{GB}/\varepsilon_0$	ΔR_{GB} / %	ΔC_{GB} / %	$\Delta\sigma_{GB}$ / %	$\Delta\varepsilon_{GB}$ / %
S1 (a)	2.50	22.5	41.52	−23.89	41.52	31.38
S1 (b)	2.50	22.5	46.03	−29.16	46.03	41.16
S1 (c)	2.50	22.5	65.55	−35.82	65.55	55.82
3 (a)	2.50	22.5	83.24	−41.75	83.24	71.67
S1 (e)	2.50	22.5	57.80	−34.01	57.80	51.53
S1 (f)	2.50	22.5	64.77	−36.92	64.77	58.53
4 (a) ↔	2.50	22.5	81.00	−40.55	81.00	68.21
4 (a) ↕	2.50	22.5	62.55	−33.79	62.55	51.03
4 (b)	10.0	90.0	66.38	−34.27	66.38	52.13
4 (b)	2.50	22.5	83.24	−41.75	83.24	71.67
4 (b)	1.11	10.0	93.14	−44.95	93.14	81.64

leads to a variation of the time constant from the actual value characteristic for the transport across the grain boundary. The deviation is related to the occurrence of the additional signals in the DRT that is derived from the impedance calculated using the network model. Moreover, a comparison of the amplitudes of the signals that are characteristic for the grain boundary charge transport also reveals deviations among the three approaches. While the amplitude derived within the network model (blue) and the one resulting from fitting the network model impedance with the BLM (red) are similar, the signal amplitude resulting from the BLM with the exact same input parameters (green) is significantly larger. The already mentioned overestimation of the number of grain boundaries results in a larger grain boundary resistance, which is also transferred into the time domain and explains this behavior. This observation highlights the notable error in the BLM-derived transport parameters of the grain boundary process. The comparison underlines again that BLM-based models fail in describing subtleties of the impedance behavior of polycrystalline samples. The number of signals in the DRT of BLM-based models always equals the number of expected transport processes within the material, other than in many experiments.

Influence of the macroscopic transport direction on the impedance of the system.—Another weakness of the BLM is revealed when a square-shaped detail of the thin film with a random grain structure is considered as shown in the inset of Fig. 4a. In terms of the BLM, the impedance of a polycrystalline sample is independent of the transport direction from left to right (horizontal transport, light blue arrow) or from top to bottom (vertical transport, dark blue arrow). This independence originates from the fact that the results within the BLM depend only on the fraction of grain boundary volume with respect to the total sample volume (green curve). In contrast, the impedances of the square-shaped sample simulated by the network model for the two different transport directions differ significantly. For this particular set of input parameters regarding charge transport (σ_{Bulk}, ε_{Bulk}, σ_{GB}, and ε_{GB}) and microstructure in the BLM (average grain size in the excerpt 3.44 μm), the output parameters of the BLM overestimate the macroscopic charge transport parameters (R_{Bulk}, C_{Bulk}, R_{GB}, and C_{GB}) compared to the output parameters resulting from the network model.

Figure 4b depicts the DRT corresponding to the impedance simulated in two different directions based on the network model. The DRT resulting from the impedance calculated within the BLM (green) is also shown for comparison. The DRT signals on the left and on the far right, which correspond to the microscopic transport mechanisms in the bulk of the grain and across the grain boundary, respectively, are basically the same. The simulated impedance for horizontal transport (light blue curve) and vertical transport (dark blue curve) reveals two additional DRT signals, which occur in the intermediate time region. The time constants of these additional signals, as well as the areas below them, differ for the two considered transport directions. The behavior of the additional DRT signals strongly underlines again, that these signals depend on the peculiarities of the microscopic structure of the sample with respect to the macroscopic current direction. These peculiarities of the microscopic structure cannot be captured by the BLM, in which the impedance does not even depend on the charge transport direction. Predicting the exact number of additional DRT signals, their magnitudes, and their time constants is challenging even for almost similar samples in terms of average grain size and shape.

Impact of the microscopic transport parameters on the simulated impedance.—In addition to the actual microstructure, the values for the microscopic transport parameters describing the transport across grain boundaries and through the bulk of the grains affect the current density distribution. Thus, the spatially resolved local current density and the total impedance of the sample should reflect such variations as they result in a different network of dominant transport paths.

To investigate this in more detail, a parameter study is performed, focusing on the macroscopic transport from left to right through the microstructure depicted in Fig. 1a. Three different parameter sets for the microscopic grain boundary transport parameters (σ_{GB}, ε_{GB}) were considered. Each parameter set has the same relaxation time, in the sense that $\tau_{GB} = R_{GB} \cdot C_{GB} = \varepsilon_{GB}/\sigma_{GB}$ is the same for a facet of a cubic voxel corresponding to a grain boundary. The bulk transport parameters ($\sigma_{Bulk} = \sigma_0$, $\varepsilon_{Bulk} = 100 \cdot \varepsilon_0$) and, thus, the corresponding relaxation time, as well as the constant thickness of a grain boundary $\delta_{GB} = 10$ nm are unchanged in all simulations.

Figure 4c depicts the three computations in a Nyquist plot. The blue curve is identical to the previous consideration (see Fig. 3a), using $\sigma_{GB} = 2.5 \cdot 10^{-3} \cdot \sigma_0$, and $\varepsilon_{GB} = 22.5 \cdot \varepsilon_0$ for the microscopic grain boundary transport parameters. Additionally, the impedance of the same microstructure was simulated with a conductivity across grain boundaries being 4 times larger (light blue) or 2.25 times smaller (dark blue), while adjusting ε_{GB} accordingly to keep τ_{GB} constant. As expected, the main impact on the impedance response arises in the low-frequency semicircles of the Nyquist plots as it is determined by the grain boundary properties. In contrast, the high-frequency semicircles corresponding to bulk charge transport are very similar as the parameter pair for bulk transport is not varied.

To quantify the impact of the input parameters on the deviations resulting from employing the BLM to analyze the impedance, the impedance of two *RC*-elements in series was fitted to the simulated impedance of the network model. The obtained macroscopic parameters R_i and C_i were interpreted within the framework of the BLM to derive microscopic transport parameters (σ_{Bulk}^{BLM}, ε_{Bulk}^{BLM}, σ_{GB}^{BLM}, ε_{GB}^{BLM}) as was described in the context of Fig. 3. The deviation of the bulk transport parameters (σ_{Bulk}^{BLM}, ε_{Bulk}^{BLM}) from the input parameters of the network model is <2 %. In contrast, the derived

Journal of The Electrochemical Society, 2021 **168** 090516

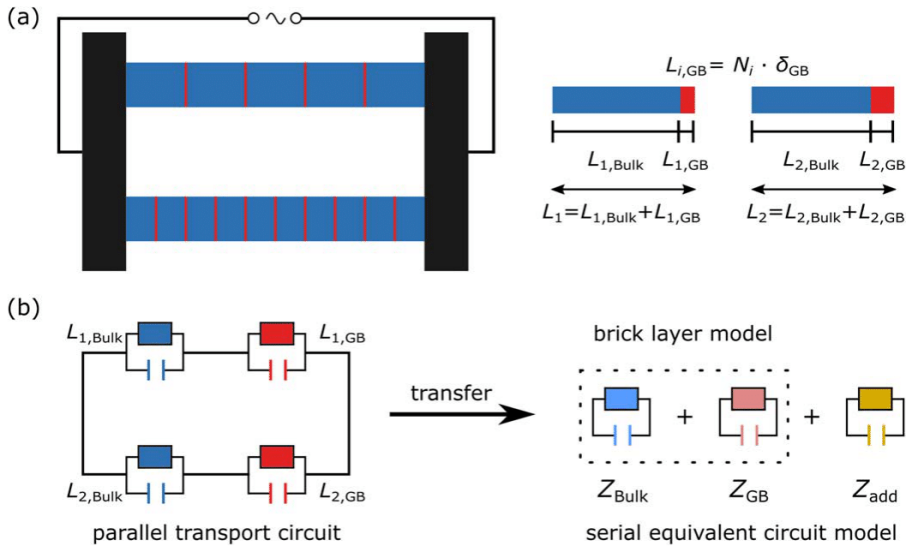

Figure 5. (a) Model structure for studying the composition of the total impedance of two non-interacting transport paths (TPM). While L_i ($i = 1, 2$) denotes the length of a transport path, δ_{GB} describes the width of a single grain boundary. N_i represents the number of grain boundaries in each path. (b) Transfer of the model structure into the corresponding parallel equivalent circuit. Transformation of the parallel equivalent circuit into a serial equivalent circuit model with three *RC*-elements. The first two elements correspond to the BLM-based equivalent circuit, while the third *RC*-element is representative for additional impedance signals observed and discussed before.

microscopic grain boundary conductivities σ_{GB}^{BLM} overestimate the input parameter for the simulation considering the real microstructure σ_{GB} in a range between 66 % and 94 %, depending on the parameter set. Similarly, the derived permittivities ε_{GB}^{BLM} overestimate the input value ε_{GB} in a range between 52 % and 82 %. The error of the BLM-derived transport parameters increases for smaller grain boundary conductivities σ_{GB}. This observation clearly demonstrates that not only the microstructure of the sample affects the relative deviation occurring when using the BLM approach to extract the actual set of microscopic transport parameters. The magnitude of the parameters themselves also plays a role.

Figure 4d shows the three computational results obtained from varying the conductivity across grain boundaries in the time domain. Each DRT reveals more than the two signals characteristic for the two transport mechanisms assumed in the simulation, i.e., transport across grain boundaries and through grains. While the amplitude of the signal on the left of each DRT is almost constant, the amplitude of the signal on the right of each DRT decreases with increasing grain boundary conductivity. This is expected due to their assignment to the microscopic bulk transport process (whose input parameters were not varied) and to the microscopic transport across grain boundaries (whose input parameters were deliberately varied), respectively. The number of additional signals in the intermediate time range in the DRT, however, varies throughout the series. Furthermore, it should be noted that not only their characteristic relaxation time varies, but also their amplitude. Nevertheless, some trends can be observed. The number of resolvable additional signals increases with decreasing grain boundary conductivity. In case of the highest grain boundary conductivity (light blue) there is only one additional signal visible, in case of the intermediate grain boundary conductivity (blue) two and in case of the lowest grain boundary conductivity (dark blue) even three signals are observed. The amplitude of the most prominent additional signal decreases with increasing grain boundary conductivity.

Summary and consequences for the analysis of experimental results.—It is demonstrated that the application of BLM-based models for analyzing the impedance response of polycrystalline solids may lead to significant quantitative deviations between the extracted microscopic transport parameters (ε_{Bulk}^{BLM}, ε_{GB}^{BLM}, σ_{Bulk}^{BLM}, σ_{GB}^{BLM}) and the actual values (ε_{Bulk}, ε_{GB}, σ_{Bulk}, σ_{GB}). Qualitative deviations arise in the spectral features in the frequency domain as well as in the time domain. The DRT of impedance data, accounting for a realistic microstructure of the sample, may exhibit more signals than there are microscopic transport processes present in the sample. This is in accordance with many experimental findings. Additional signals may appear anywhere in the DRT and the impedance spectrum, i.e., in the whole frequency or relaxation-time range between the two main signals depending on the interplay between the actual microstructure and the microscopic transport parameters of the material's constituents. Thereby, the number of additional signals, their relaxation time, and their amplitude in the DRT are affected. Thus, the microstructure significantly influences the total impedance and may cause additional signals in the impedance. The following section explores this hypothesis and provides further proof for its correctness.

Comprehensive analysis of the impedance of non-interacting transport paths.—To obtain a deeper understanding of contributions to the total impedance of complex microstructures that are not described by simple (macroscopic) equivalent circuits, we use an even further simplified model system (see Fig. 5a). The simplified model considers only transport through two independent transport paths of variable length L_i ($i = 1, 2$) and variable number of grain boundaries N_i in both pathways. This system is referred to as "two-path-model" (TPM) in the following. It represents the simplest extension of a 1D model and is used to elucidate qualitatively the origin of the individual contributions other than grain and grain boundary processes to the total impedance.

Derivation of an analytical expression for the microstructural contribution to the impedance.—Since the two transport paths do not interact, the grain fraction (blue) of each path can be separated from its grain boundary fraction (red). The transport length across grain boundaries $L_{i,GB}$ can be calculated by multiplying the number of grain boundaries in the transport path N_i with the constant thickness δ_{GB} of a single grain boundary. Similarly, the transport length through the grain

Journal of The Electrochemical Society, 2021 **168** 090516

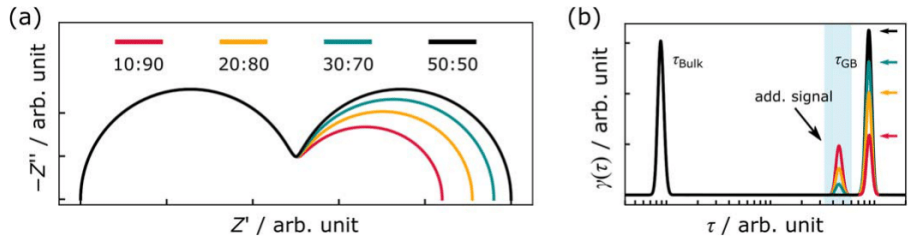

Figure 6. Computational results in the frequency domain (a) and time domain (b) depending on the distribution of grain boundaries between the two independent non-interacting transport paths of equal bulk transport lengths. The total number of grain boundaries is constant in all simulations. Contrary to the limiting case of two equal transport paths (black; BLM), an additional signal appears in the spectrum in case of an asymmetric distribution of grain boundaries between the paths. The computational results are based on the following parameters: $\sigma_{Bulk}/\sigma_{GB} = 100$, $\varepsilon_{Bulk}/\varepsilon_{Bulk} = 1$, $L_{Bulk,tot} = 100$ μm, and $L_{GB,tot} = 1$ μm.

$L_{i,Bulk}$ is calculated. Due to these simplifications, a parallel equivalent circuit can be derived from the structure. Here, each pathway consists of two *RC*-elements representing the transport through the grain and the transport across grain boundaries, respectively (see Fig. 5b). In the limiting case of equal bulk transport lengths $L_{i,Bulk}$ and equal grain boundary transport lengths $L_{i,GB}$ in both paths, this system corresponds to two paths within the BLM. The parallel equivalent circuit can be transferred into an equivalent circuit consisting of two *RC*-elements in series. The parameters of these *RC*-elements, R_{Bulk}, R_{GB}, C_{Bulk}, and C_{GB}, result from both transport paths and represent the bulk and grain boundary properties of the material.

The one-to-one translation of two microscopic transport processes in two transport paths (parallel circuit) into two macroscopic transport parameters (serial equivalent circuit) is in general not valid. This transformation is only possible if both transport paths are identical. Otherwise, an additional impedance contribution Z_{add} to the total impedance occurs, which does not correspond to a microscopic transport process. Due to the simple structural design of the TPM and the assumption that the transport paths do not interact with each other, the system can be mathematically described without much effort. As shown in the Supporting Information, analytical expressions for the resistance and capacitance of the three *RC*-elements in the serial circuit of Fig. 5b can be derived. In particular, the dependence of the resistance R_{add} and the capacitance C_{add} of the additional impedance Z_{add} on the structural composition and the transport parameters of the bulk and grain boundary process is of special interest:

$$R_{add} = \frac{(L_{2,Bulk} \cdot L_{1,GB} - L_{1,Bulk} \cdot L_{2,GB})^2}{A \cdot L_{Bulk,tot} \cdot L_{GB,tot} \cdot \sigma_{Bulk} \cdot \sigma_{GB} \cdot (L_{Bulk,tot}/\sigma_{Bulk} + L_{GB,tot}/\sigma_{GB})} \quad [3]$$

$$C_{add} = \frac{A \cdot L_{Bulk,tot} \cdot L_{GB,tot} \cdot (L_{Bulk,tot} \cdot \varepsilon_{GB} + L_{GB,tot} \cdot \varepsilon_{Bulk})}{(L_{2,Bulk} \cdot L_{1,GB} - L_{1,Bulk} \cdot L_{2,GB})^2} \quad [4]$$

$$\tau_{add} = \frac{(L_{Bulk,tot} \cdot \varepsilon_{GB} + L_{GB,tot} \cdot \varepsilon_{Bulk})}{\sigma_{Bulk} \cdot \sigma_{GB} \cdot (L_{Bulk,tot}/\sigma_{Bulk} + L_{GB,tot}/\sigma_{GB})} \quad [5]$$

Here, $L_{Bulk,tot}$ and $L_{GB,tot}$ represent the sum of the bulk and grain boundary transport length, respectively. The parameter A is the interface area of the transport path in Eqs. 3 and 4 and, thus, only a scaling factor in this quasi-1D-model. The variation of this parameter provides only quantitative changes in the total impedance and its individual contributions. No qualitative changes result from variations of this factor. The set of equations already underlines that the BLM cannot account for this additional signal. When considering two identical transport paths, the expression in parenthesis in Eq. 3 is zero yielding a resistance value $R_{add} = 0$. Although the relaxation time τ_{add} is non-zero, a corresponding DRT signal cannot be observed because the area below the signal corresponds to R_{add} and is also zero.

Impact of the asymmetry of two transport paths on additional impedance signals.—To study the influence of the (micro-)structural design on the additional signal in more detail, two pathways with equal bulk transport lengths $L_{1,Bulk} = L_{2,Bulk} = L_{Bulk} = 50$ μm were considered. The total number of grain boundaries and, thus, $L_{GB,tot} = 1$ μm was kept constant in these simulations, while the number of grain boundaries were systematically redistributed between the two transport channels corresponding to different $L_{1,GB}$: $L_{2,GB}$ ratios. The numerical values for the ratio of the microscopic transport parameters were fixed to $\sigma_{Bulk}/\sigma_{GB} = 100$ and $\varepsilon_{Bulk}/\varepsilon_{GB} = 1$.

Figure 6a shows the computational results in a Nyquist representation. The black curve corresponds to the balanced situation of the two transport paths where the grain boundary distribution ratio is 50:50 between both channels. This corresponds to the structural situation of the BLM. Varying the distribution of grain boundaries between the two pathways leads to more asymmetric structural situations. The high-frequency semicircle does not change with increasing asymmetry between both paths. In contrast, the low-frequency semicircle decreases in size, as expected, with increasing asymmetry of the two paths. Furthermore, the red curve with the highest asymmetry (10:90) clearly shows that the low-frequency semicircle is also distorted.

For a qualitative analysis of the additional signal in the four simulations and the evolution of their parameters, each impedance spectrum is transferred into the time domain (see Fig. 6b). In case of balanced transport channels (black), the corresponding DRT shows two signals only, in accordance with the standard interpretation. An additional third peak cannot be detected as expected from Eqs. 3, 4, and 5. In the case of transport paths with different numbers of grain boundaries ($N_1 \neq N_2$), there are always three signals distinguishable in each DRT. The amplitude of two of these signals is significantly larger compared to the amplitude of the third signal, which is located in the intermediate time range.

The two outer signals can be clearly identified as being characteristic for the two considered microscopic transport processes in the system. The amplitude and the relaxation time of the signal on the left of each DRT is always the same for all computations in accordance with our assumptions regarding the bulk process. The relaxation time of the signal on the right of the four DRT, which is related to the grain boundary transport, is not affected by asymmetric structural situations. Its amplitude, however, decreases with increasing asymmetry as indicated by the horizontal arrows in the figure.

As outlined above, the additional signal in the intermediate time range of the three DRT reflects the structural design of the pathways. The comparison of this signal in each DRT reveals the trend that the more asymmetric the two transport paths become, the larger the amplitude of the signal becomes. The evolution of the amplitude perfectly reflects the behavior of the resistance R_{add} according to Eq. 3. Its value increases with increasing asymmetry. It is worth noting that in the particular case, in which the ratio of the number of grain boundaries is 10:90, the amplitude of the additional signal has become comparable to the amplitude of the grain boundary signal.

Journal of The Electrochemical Society, 2021 **168** 090516

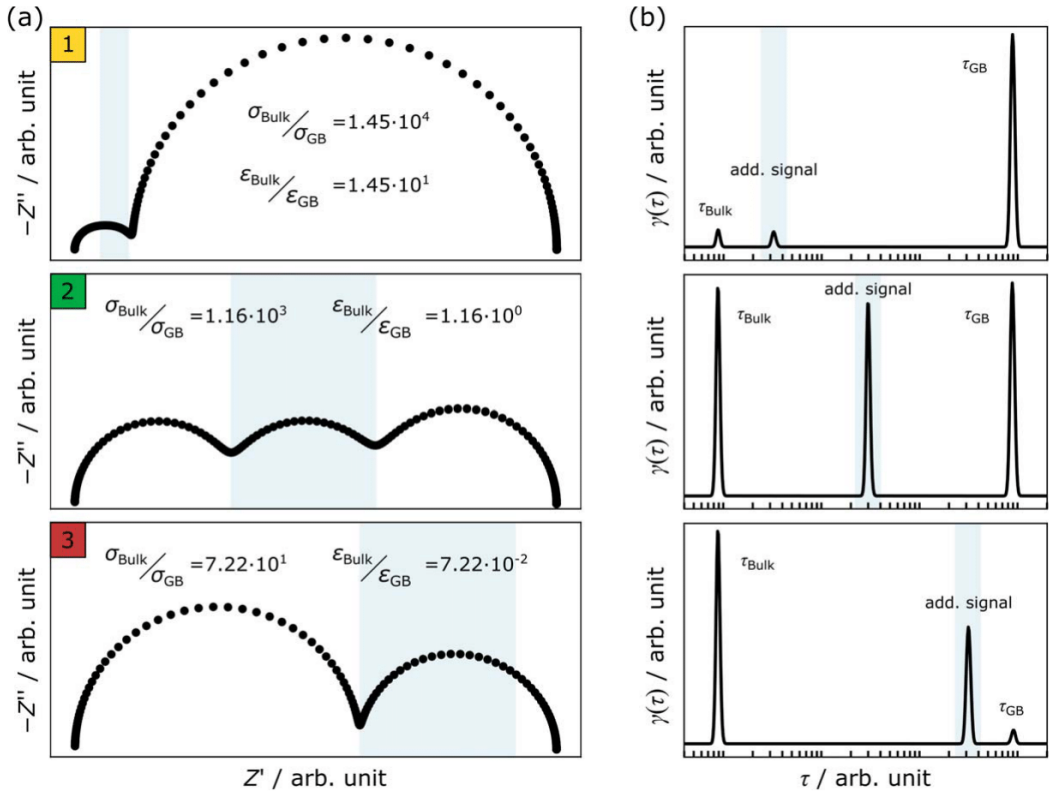

Figure 7. Dependence of additional impedance signals on the transport parameters σ_i and ε_i of the bulk and grain boundary transport process. In the frequency domain (a) additional contributions to the Nyquist plots (shaded area) may affect the high-frequency, the low-frequency or even both semicircles depending on the choice of transport parameters. In the time domain (b), additional signals occur in the corresponding DRT, which vary in relaxation time as well as in peak area. All computational results were obtained using the same bulk parameters $L_{Bulk,tot}$ = 200 μm and assuming an inhomogeneous distribution (1:100) of the number of grain boundaries $L_{GB,tot}$ = 5.05 μm between the two paths.

Moreover, it is demonstrated that the relaxation time of the signal is independent of the distribution of grain boundaries between the two transport paths. This observation agrees with the derived expression for the relaxation time, since no quantity in Eq. 5 is affected by the asymmetry. A detailed discussion for more complex systems regarding the relaxation time of this signal, compared with those of the bulk and grain boundary processes, is given in the Supporting Information.

Impact of the transport parameters on the additional impedance contribution for fixed pathways.—As already anticipated from the analytical expressions for R_{add}, C_{add}, and τ_{add}, the signal of the additional contribution to the impedance will vary in relaxation time as well as in intensity depending on the choice of the microscopic transport parameters (σ_{Bulk}, ε_{Bulk}, σ_{GB}, ε_{GB}). To demonstrate that the evolution of the additional signal is even independent of the structural design, the model system remained unchanged in this series of simulations. Two pathways of equal bulk transport lengths ($L_{1,Bulk} = L_{2,Bulk} = L_{Bulk}$ = 100 μm) were considered. The total length of the transport through grain boundaries was set to $L_{GB,tot}$ = 5.05 μm and a ratio of the grain boundary number of 1:100 between the two transport paths was assumed. The conductivity $\sigma_{Bulk} = \sigma_0$ and permittivity $\varepsilon_{Bulk} = 10^4\ \varepsilon_0$ of the bulk transport process were kept constant. The conductivity σ_{GB} and permittivity ε_{GB} of the grain boundary transport process were systematically varied such that $\tau_{GB} = \varepsilon_{GB}/\sigma_{GB}$ remained constant. Nevertheless, parameter sets (σ_{GB}, ε_{GB}) fulfilling these severe restrictions can be found, which allow to shift the relaxation time of the additional impedance signal τ_{add} across the entire intermediate time range between the relaxation times of the two microscopic transport mechanisms. Here, three parameter sets (σ_{Bulk}, ε_{Bulk}, σ_{GB}, ε_{GB}) observing the opposed restrictions will be exemplarily discussed. More details on the dependence of the impedance response on the choice of parameters for a fixed asymmetry can be found in the Supporting Information.

Figure 7a shows the impedance simulated for three selected parameter sets in the Nyquist plot. The additional impedance signal contributing to the total impedance occurs in the high-frequency range, in the intermediate frequency range, and in the low-frequency range, respectively. The computational results point out that this $R_{add}C_{add}$-element can exclusively distort either the bulk semicircle (case 1, high frequency) or the grain boundary semicircle (case 3, low frequency). Moreover, the additional contribution may even appear as another third separate semicircle (case 2, intermediate frequency) in the impedance spectrum. In particular the last example, case 2, drastically highlights that it is questionable to always correlate a semicircle in the Nyquist plot with an actual transport mechanism or reaction process in a sample.

The same holds for the time domain (Fig. 7b). In the three calculated DRT, the additional signal occurs in the vicinity of the bulk signal (case 1), in the vicinity of the grain boundary signal (case 3), and in the middle between the two microscopic charge transport signals (case 2). The amplitude of the additional signal in case 1 and 2 is almost equal to the amplitude of the bulk signal. In case 1, the grain boundary signal is much larger than the two other ones and in case 2 all three signals are of equal amplitude. In case 3, the amplitudes decrease from left to right in the DRT, i.e., the bulk signal has the highest intensity, the additional signal has an intermediate intensity, and the grain boundary signal has the lowest intensity. Thus, it cannot be concluded that the additional

Journal of The Electrochemical Society, 2021 **168** 090516

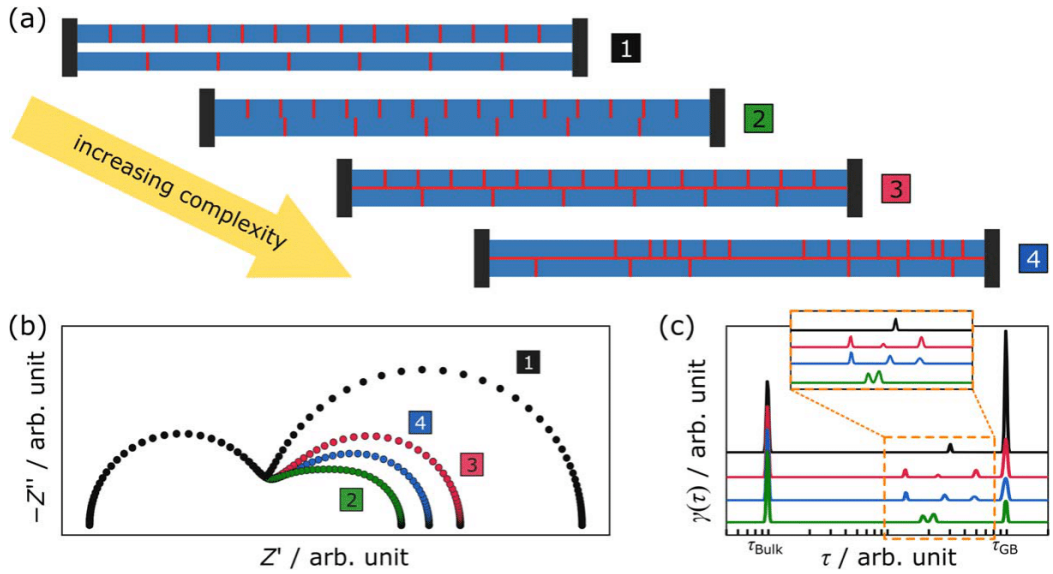

Figure 8. Systematic study of the impact of frequency-dependent switching of current paths on the impedance response. The complexity of the schematically depicted model systems (a) was increased successively while keeping the ratio of the number of grain boundaries in the two macroscopic pathways of equal bulk transport lengths constant (70:30). The increase in complexity was realized by starting from non-interacting transport paths with an equally spaced grain boundary arrangement in both paths (1). By joining two sample halves together, a structure with interacting pathways is realized while keeping the spatial arrangement of the vertical grain boundaries (2). An additional horizontal grain boundary is added affecting the probability of switching between both interacting pathways (3). In contrast to equally spaced vertical grain boundaries, a random arrangement of such grain boundaries in both halves of the sample is simulated while keeping the horizontal grain boundary (4). The computational results in the frequency domain (b) and time domain (c) reveal that the multidimensional transport leads to additional contributions in the impedance compared to the quasi-1D non-interacting case (black). The computational results are based on the following parameters: $\sigma_{Bulk}/\sigma_{GB}$ = 100, $\varepsilon_{Bulk}/\varepsilon_{Bulk}$ = 1, $L_{Bulk,tot}$ = 100 μm, and $L_{GB,tot}$ = 1 μm.

signal is always lower in intensity than the other two signals originating from the two microscopic transport processes. This finding highlights the danger of misinterpreting an additional signal in the DRT to originate from a microscopic transport process with an intermediate relaxation time.

Appearance of multiple additional contributions in the impedance spectrum.—The computational results obtained for the realistic microstructure can be almost fully explained in terms of the TPM. It was demonstrated that additional signals in the impedance response may occur within the entire frequency range depending on the interplay of the microscopic structure and the transport parameters. However, it should be noted that the TPM cannot yield more than one additional signal in the DRT other than in experiments or more realistic, and therefore also more complex model systems. It is reasonable to assume that more transport paths or the interaction between two of them result in more additional signals as demonstrated in the Supporting Information. A qualitative study reveals that the behavior of multiple additional signals in case of more than two non-interacting transport paths is similar to the one of the single additional signal regarding the TPM.

Transition from non-interacting to interacting transport paths.—The impedance analysis using the network model and the consideration of the non-interacting TPM represent two extreme cases. The two separated channels of the non-interacting TPM represent two macroscopic pathways. In this particular arrangement, where the local potential gradient in each channel is always parallel to the path direction, these macroscopic transport paths are equal to the corresponding microscopic transport paths. Charge carrier switching between the two pathways cannot occur because of their spatial separation. In contrast, the network model is applied to representative parts of real structures. The sample acts as one macroscopic lead, i.e., one macroscopic transport path. Due to the spatial inhomogeneity of the sample, the direction of the local potential gradient varies throughout the sample and many interacting microscopic transport paths arise.

In order to validate the qualitative statements of the TPM with respect to the interpretation of the results of the network model on real structures, we have included the interaction between the two transport paths of the TPM by merging the two halves of the sample and allowing carrier transfer between them. Thereby, we considered two pathways of equal bulk transport lengths $L_{1,Bulk} = L_{2,Bulk} = 50$ μm as starting point. The total number of grain boundaries corresponding to $L_{GB,tot} = 1$ μm was kept constant. The grain boundaries were split in a ratio of 70:30 between the two transport channels. The numerical values for the ratio of the microscopic transport parameters were fixed to $\sigma_{Bulk}/\sigma_{GB} = 100$ and $\varepsilon_{Bulk}/\varepsilon_{GB} = 1$.

Figure 8a shows exemplarily the model systems that we considered. Structure (1) represents the non-interacting TPM already discussed in the previous section defined by a spatial separation between lower and upper half of the sample. The grain boundaries within each pathway are spaced equally leading to a larger spacing in the lower path shown in the figure. The design of model structure (2) is identical to that of (1), but the two halves of the sample are now merged together in a way that charge carriers may move freely between its lower and upper half, i.e., the transport channels interact. This is the basis of frequency-dependent switching of current paths. Structure (3) represents an extension of structure (2) by adding a horizontal grain boundary between the two macroscopic pathways. In case of the model parameters chosen, this grain boundary makes the switching of current paths energetically less favorable compared to structure (2). The arrangement of grain boundaries in realistic systems, however, is not symmetric or equidistant (see Fig. 1). Therefore, structure (4) considers a random arrangement of grain boundaries in both halves of the sample while keeping the 70:30 distribution between the two halves as well as the horizontal grain boundary.

Figure 8b shows the simulated impedance responses in a Nyquist representation. While the high-frequency semicircle is identical for

Journal of The Electrochemical Society, 2021 **168** 090516

all structures considered, significant variations in the low-frequency range of the impedance curves are visible. The non-interacting TPM (1, black) shows the largest impedance. This result is not surprising, since the charge carriers in the energetically less favorable transport path (top) cannot switch to the pathway with fewer grain boundaries (bottom).

The comparison of the computational results considering interacting pathways reveals that the model system without horizontal grain boundary (2, green) shows the smallest impedance. The absence of the horizontal grain boundary facilitates the spatial switching of current paths, since there is no additional impedance contribution apart from the increased bulk transport length. However, the multidimensional transport does not only lead to a quantitative change of the impedance spectrum, but also to qualitative deviations. The switching of pathways causes a much stronger distortion of the low-frequency semicircle. The interaction of the two halves of the sample increases the number of possible microscopic transport paths through the structure. As already demonstrated in the non-interacting case, the parallel connection of several different transport paths can lead to more than one additional impedance contribution (see Fig. S8).

The red curve is calculated for model structure (3) with a horizontal grain boundary between the upper and lower half of the sample. Since an additional grain boundary has to be crossed at each switching of carriers between the two halves, the impedance values increase compared to the green curve of structure (2). Consequently, the distortion of the low-frequency semicircle becomes less visible than for structure (2). The quantitative result, however, strongly depends on the local distribution of the grain boundaries within the two halves of the sample. The computed impedance curve of structure (4, blue) with a random distribution of the vertical grain boundaries shows a smaller impedance compared to the results for sample (3, red), which also possesses a horizontal grain boundary but exhibits equally spaced grain boundaries. A random arrangement of the positions of vertical grain boundaries in both sample halves can lead to regions where the spacing is larger or smaller between individual grain boundaries, which favors a switching of transport paths and decreases the impedance. Figures S9 and S10 show simulations for ten structures of type (4) differing in the random arrangement of the vertical grain boundaries with and without an additional horizontal grain boundary, respectively. The results highlight the massive impact of the spatial grain boundary distribution on the low-frequency impedance.

As expected, the effects described are also reflected in the time domain (see Fig. 8c). The amplitude of the leftmost signal of the corresponding DRT of all four model structures, which can be assigned to the bulk process, is virtually the same in all cases. In contrast, the amplitude of the DRT signal at high relaxation times, which originates from the grain boundary transport, significantly changes depending on the model structure considered. The magnitude of these amplitudes reflects well the expectation regarding the average number of grain boundaries crossed in the transport process ((1) > (3) > (4) > (2)) in the case of the four model structures (1) to (4). In the intermediate time range, significant differences appear in the individual DRTs. While in case of the non-interacting transport paths (1, black) one additional signal is visible, the DRTs for interacting pathways show two (2, green) or three (3, red and 4, blue) additional signals, respectively. The appearance of multiple signals is not surprising, since the interaction of the two 1D transport paths leads to more non-equivalent microscopic 2D pathways. The time constants and corresponding amplitudes in the DRT of structures (3) and (4) are comparable because of the same structural composition regarding the bulk and grain boundary volume fractions. A similar behavior is also observed in the DRTs of the random structures shown in the Supporting Information (see Figs. S9 and S10). Moreover, the comparison of the amplitudes of all additional signals in the DRT of structure (2, green) with the corresponding grain boundary peak at high relaxation times shows that the contribution of the former to the impedance is comparable to the contribution of the latter one. This makes the analysis of impedance spectra of small inhomogeneous samples very difficult as it shows that global geometry effects of the carrier transport paths have a major impact on the sample response.

Our discussion as a whole underlines the importance of including detailed structural information in the analysis of experimental impedance data. This is essential to avoid an incorrect assignment of impedance features in the frequency as well as in the time domain, which may lead to false conclusions about the microscopic processes taking place inside the sample.

Conclusions

In summary, a novel impedance network model is presented, which accounts for the sample (micro-)structure on microscopic and macroscopic length scales in a realistic way. The computational results of realistic model structures demonstrate that additional impedance signals may occur in the frequency-dependent impedance response as well as in the corresponding DRT. The additional signals cannot be assigned to microscopic transport mechanisms but may be of similar magnitude than those corresponding to the microscopic transport mechanisms. The occurrence of these additional signals in the impedance spectrum and in the corresponding DRT are determined by the interplay of the sample's microstructure as a whole and the microscopic transport parameters. It is demonstrated that such signals are also observed in experiments. These facts highlight that a correct analysis of the impedance response with the aim of understanding the transport processes and extracting reliable microscopic transport parameters requires a proper accounting for the structural features of the samples in the model. This necessity holds, in particular, for samples with disorder on a microscopic scale such as polycrystalline samples with a grain structure or mesoporous samples.

The BLM and comparable quasi one-dimensional models imply inherently that the local potential gradient is parallel to the main current direction. Thus, these models cannot account for additional features in the impedance response due to the missing interplay between microstructure and microscopic transport parameters. These models usually assume a one-to-one correspondence between impedance features and microscopic transport processes. Thus, care must be taken when using such models for the analysis of experimental impedance data as impedance features may be easily misinterpreted as additional transport processes or the extracted microscopic transport parameters are erroneous.

It is worth noting that such additional features may already be observed in the impedance response of polycrystalline samples with rather macroscopic dimensions despite an averaging over a multitude of microscopic transport paths. This suggests that the impact of the microstructure will be the more important the smaller the samples are. On the one hand, this makes the analysis of the impedance data of such structures even more challenging. On the other hand, it offers the opportunity to better understand the relationship between transport and structure on the microscale. A full structural characterization of individual thin-film samples with dimensions of a few $(10 \cdot 10)\ \mu m^2$ is feasible with non-invasive scanning probe techniques or even destructive probes such as FIB after performing the transport measurements. In this context, it is worth noting that the network model presented here may be easily expanded to account for additional structural effects such as pores or electrodes as well as additional microscopic transport mechanisms such as transport along grain boundaries. Thus, it provides a powerful tool for the analysis of the impedance response of samples with pronounced microstructural features.

Acknowledgments

We acknowledge computational resources provided by the HPC Core Facility and the HRZ of the Justus-Liebig-University Giessen. We would like to thank MSc. Philipp Risius and Dr. Marcel Giar of HPC-Hessen, funded by the State Ministry of Higher Education, Research, and the Arts, for programming advice. Financial support is

provided by the DFG via the GRK (Research Training Group) 2204 "Substitute Materials for sustainable Energy Technologies". M.T.E. gratefully acknowledges financial support by the DFG via the project No. EL 863/3-1 and by the German Federal Ministry of Education and Research (BMBF) via the NanoMatFutur project NiKo (03XP0093). J.J. and S.B. acknowledge financial support by the German Federal Ministry of Education and Research within the cluster of competence FESTBATT (projects 03XP0177A and 03XP0180).

ORCID

Janis K. Eckhardt https://orcid.org/0000-0002-2799-0599
Matthias T. Elm https://orcid.org/0000-0001-7014-5772
Jürgen Janek https://orcid.org/0000-0002-9221-4756

References

1. A. J. Labelle, S. M. Thon, S. Masala, M. M. Adachi, H. Dong, M. Farahani, A. H. Ip, A. Fratalocchi, and E. H. Sargent, *Nano Lett.*, **15**, 1101 (2015).
2. Y. Lee, S.-H. Lo, J. Androulakis, C.-I. Wu, L.-D. Zhao, D.-Y. Chung, T. P. Hogan, V. P. Dravid, and M. G. Kanatzidis, *J. Am. Chem. Soc.*, **135**, 5152 (2013).
3. L. Wang, M. Hong, Q. Sun, Y. Wang, L. Yue, S. Zheng, J. Zou, and Z.-G. Chen, *ACS Appl. Mater. Interfaces*, **12**, 36370 (2020).
4. Y. Pei et al., *Adv. Energy Mater.*, **7**, 1601450 (2017).
5. F. Gather, C. Heiliger, and P. J. Klar, *J. Phys.: Condens. Matter*, **23**, 335301 (2011).
6. H. L. Tuller, *Solid State Ionics*, **131**, 143 (2000).
7. P. Balaya, A. J. Bhattacharyya, J. Jamnik, Y. F. Zhukovskii, E. A. Kotomin, and J. Maier, *J. Power Sources*, **159**, 171 (2006).
8. W. Li, J. Liu, and D. Zhao, *Nat. Rev. Mater.*, **1**, 16023 (2016).
9. J. Maier, *Phys. Chem. Chem. Phys.*, **11**, 3011 (2009).
10. J. Maier, *Chem. Mater.*, **26**, 348 (2014).
11. F. Capasso, *Science*, **235**, 172 (1987).
12. A. M. Smith and S. Nie, *Acc. Chem. Res.*, **43**, 190 (2010).
13. A. Chaves et al., *npj 2D Mater. Appl.*, **4**, 29 (2020).
14. Y. Xiao and L.-D. Zhao, *npj Quantum Mater.*, **3**, 55 (2018).
15. F. Gather, C. Heiliger, and P. J. Klar, *Prog. Solid State Chem.*, **39**, 97 (2011).
16. S. Yamasaka, Y. Nakamura, T. Ueda, S. Takeuchi, and A. Sakai, *Sci. Rep.*, **5**, 14490 (2015).
17. E. Güneş, F. Gundlach, M. T. Elm, P. J. Klar, S. Schlecht, M. S. Wickleder, and E. Müller, *ACS Appl. Mater. Interfaces*, **9**, 44756 (2017).
18. C. H. Will, M. T. Elm, P. J. Klar, B. Landschreiber, E. Güneş, and S. Schlecht, *J. Appl. Phys.*, **114**, 193707 (2013).
19. S. Burkhardt, M. S. Friedrich, J. K. Eckhardt, A. C. Wagner, N. Bohn, J. R. Binder, L. Chen, M. T. Elm, J. Janek, and P. J. Klar, *ACS Energy Lett.*, **4**, 2117 (2019).
20. A. Bielefeld, D. A. Weber, and J. Janek, *J. Phys. Chem. C*, **123**, 1626 (2019).
21. X. Wang et al., *J. Power Sources*, **359**, 270 (2017).
22. W. Lee, S. Muhammad, C. Sergey, H. Lee, J. Yoon, Y.-M. Kang, and W.-S. Yoon, *Angew. Chem. Int. Ed.*, **59**, 2578 (2020).
23. J. Zahnow, T. Bernges, A. Wagner, N. Bohn, J. R. Binder, W. G. Zeier, M. T. Elm, and J. Janek, *ACS Appl. Energy Mater.*, **4**, 1335 (2021).
24. Z. Sang, K. Ke, and I. Manas-Zloczower, *Small*, **15**, 1903487 (2019).
25. M. Tiemann, *Chem. - Eur. J.*, **13**, 8376 (2007).
26. F. A. Harraz, *Sens. Actuators, B*, **202**, 897 (2014).
27. A. S. Aricò, P. Bruce, B. Scrosati, J.-M. Tarascon, and W. van Schalkwijk, *Nat. Mater.*, **4**, 366 (2005).
28. P. G. Bruce, B. Scrosati, and J.-M. Tarascon, *Angew. Chem. Int. Ed.*, **47**, 2930 (2008).
29. L. A. Dubraja, D. Boll, C. Reitz, D. Wang, D. Belić, A. Mazilkin, B. Breitung, H. Hahn, M. T. Elm, and T. Brezesinski, *ACS Appl. Nano Mater.*, **2**, 7126 (2019).
30. Y. Ren, Z. Ma, and P. G. Bruce, *Chem. Soc. Rev.*, **41**, 4909 (2012).
31. J. Yue, C. Suchomski, P. Voepel, R. Ellinghaus, M. Rohnke, T. Leichtweiss, M. T. Elm, and B. M. Smarsly, *J. Mater. Chem. A*, **5**, 1978 (2017).
32. E. Celik, Y. Ma, T. Brezesinski, and M. T. Elm, *Phys. Chem. Chem. Phys.*, **23**, 10706 (2021).
33. G. Gregori, R. Merkle, and J. Maier, *Prog. Mater. Sci.*, **89**, 252 (2017).
34. X. Guo, W. Sigle, and J. Maier, *J. Am. Ceram. Soc.*, **86**, 77 (2003).
35. A. Bielefeld, D. A. Weber, and J. Janek, *ACS Appl. Mater. Interfaces*, **12**, 12821 (2020).
36. B. Tjaden, D. J. L. Brett, and P. R. Shearing, *Int. Mater. Rev.*, **63**, 47 (2018).
37. J. R. Macdonald and W. B. Johnson, "Fundamentals of Impedance Spectroscopy." *Impedance Spectroscopy: Theory, Experiment, and Applications*, ed. E. Barsoukov and J. R. Macdonald (John Wiley & Sons, Inc., Hoboken, NJ) 3rd ed., 1 (2018).
38. J. E. Bauerle, *J. Phys. Chem. Solids*, **30**, 2657 (1969).
39. J. Fleig and J. Maier, *J. Electrochem. Soc.*, **145**, 2081 (1998).
40. J. T. S. Irvine, D. C. Sinclair, and A. R. West, *Adv. Mater.*, **2**, 132 (1990).
41. I. V. Krasnikova, M. A. Pogosova, A. O. Sanin, and K. J. Stevenson, *Chem. Mater.*, **32**, 2232 (2020).
42. N. M. Beekmans and L. Heyne, *Electrochim. Acta*, **21**, 303 (1976).
43. T. van Dijk and A. J. Burggraaf, *Phys. Status Solidi A*, **63**, 229 (1981).
44. M. J. Verkerk, B. J. Middelhuis, and A. J. Burggraaf, *Solid State Ionics*, **6**, 159 (1982).
45. J. C. C. Abrantes, J. A. Labrincha, and J. R. Frade, *J. Eur. Ceram. Soc.*, **20**, 1603 (2000).
46. C. Kjølseth, H. Fjeld, Ø. Prytz, P. I. Dahl, C. Estournès, R. Haugsrud, and T. Norby, *Solid State Ionics*, **181**, 268 (2010).
47. T. Krauskopf, H. Hartmann, W. G. Zeier, and J. Janek, *ACS Appl. Mater. Interfaces*, **11**, 14463 (2019).
48. J. Fleig, *J. Electroceram.*, **13**, 637 (2004).
49. N. J. Kidner, N. H. Perry, T. O. Mason, and E. J. Garboczi, *J. Am. Ceram. Soc.*, **91**, 1733 (2008).
50. J. S. Dean, J. H. Harding, and D. C. Sinclair, *J. Am. Ceram. Soc.*, **97**, 885 (2014).
51. N. J. Kidner, Z. J. Homrighaus, B. J. Ingram, T. O. Mason, and E. J. Garboczi, *J. Electroceram.*, **14**, 283 (2005).
52. N. J. Kidner, Z. J. Homrighaus, B. J. Ingram, T. O. Mason, and E. J. Garboczi, *J. Electroceram.*, **14**, 293 (2005).
53. J. Fleig and J. Maier, *Electrochim. Acta*, **41**, 1003 (1996).
54. J. Fleig and J. Maier, *J. Eur. Ceram. Soc.*, **19**, 693 (1999).
55. J. Fleig, *Solid State Ionics*, **131**, 117 (2000).
56. J. Fleig, *Solid State Ionics*, **150**, 181 (2002).
57. T. H. Wan, M. Saccoccio, C. Chen, and F. Ciucci, *Electrochim. Acta*, **184**, 483 (2015).
58. E. Ivers-Tiffée and A. Weber, *J. Ceram. Soc. Jpn.*, **125**, 193 (2017).
59. Y. Zhang, Y. Chen, and F. Chen, *J. Power Sources*, **277**, 277 (2015).
60. A. Leonide, V. Sonn, A. Weber, and E. Ivers-Tiffée, *J. Electrochem. Soc.*, **155**, B36 (2008).
61. A. L. Gavrilyuk, D. A. Osinkin, and D. I. Bronin, *Russ. J. Electrochem.*, **53**, 575 (2017).
62. Y. Zhang, Y. Chen, M. Li, M. Yan, M. Ni, and C. Xia, *J. Power Sources*, **308**, 1 (2016).
63. X. Guo and R. Waser, *Prog. Mater. Sci.*, **51**, 151 (2006).
64. A. Jasper, J. A. Kilner, and D. W. McComb, *Solid State Ionics*, **179**, 904 (2008).
65. E. B. Lavik, I. Kosacki, H. L. Tuller, Y. M. Chiang, and J. Y. Ying, *J. Electroceram.*, **1**, 7 (1997).
66. J. P. Parras, C. Cao, Z. Ma, R. Mücke, L. Jin, R. Dunin-Borkowski, O. Guillon, and R. A. De Souza, *J. Am. Ceram. Soc.*, **103**, 1755 (2020).
67. M. T. Elm, J. D. Hofmann, C. Suchomski, J. Janek, and T. Brezesinski, *ACS Appl. Mater. Interfaces*, **7**, 11792 (2015).
68. I. Kosacki and H. U. Anderson, *Ionics*, **6**, 294 (2000).
69. J. Fleig and J. Maier, *J. Electrochem. Soc.*, **144**, L302 (1997).
70. J. L. Hertz and H. L. Tuller, *Solid State Ionics*, **178**, 915 (2007).

2.2 Microstructural Influence in the Material Characterization of Garnet-Type Ceramics

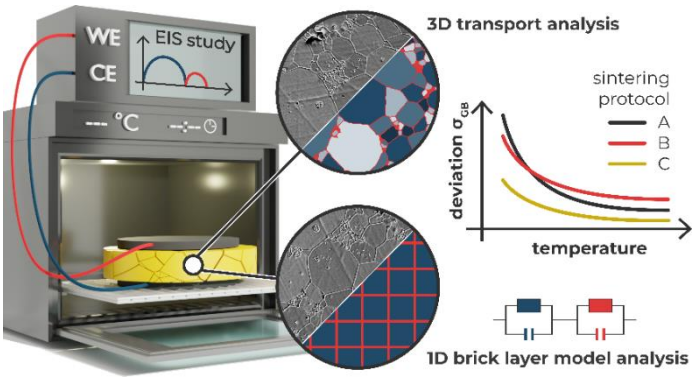

Abstract

Variants of garnet-type $Li_7La_3Zr_2O_{12}$ are being intensively studied as separator materials in solid-state battery research. The material-specific transport properties, such as bulk and grain boundary conductivity, are of prime interest and are mostly investigated by impedance spectroscopy. Data evaluation is usually based on the 1D brick layer model, which assumes a homogeneous microstructure of identical grains. Real samples show microstructural inhomogeneities in grain size and porosity due to the complex behavior of grain growth in garnets that is very sensitive to the sintering protocol. However, the true microstructure is often omitted in impedance data analysis, hindering interlaboratory reproducibility and comparability of results reported in the literature. Here, we use a combinatorial approach of structural analysis and 3D transport modeling to explore the effects of microstructure on the derived material-specific properties of garnet-type ceramics. For this purpose, Al-doped $Li_7La_3Zr_2O_{12}$ pellets with different microstructures are fabricated and electrochemically characterized. A machine learning assisted image segmentation approach is used for statistical analysis and quantification of the microstructural changes during sintering. A detailed analysis of transport through statistically modelled twin microstructures demonstrate that the transport parameters derived from a 1D brick layer model approach show uncertainties up to 150%, only due to variations in grain size. These uncertainties can be even larger in the presence of porosity. This study helps to better understand the role of the microstructure of a polycrystalline electroceramics and its influence on experimental results.

Reference

Influence of Microstructure on the Material Properties of LLZO Ceramics Derived by Impedance Spectroscopy and Brick Layer Model Analysis. Janis K. Eckhardt[Δ], Sascha Kremer[Δ], Till Fuchs, Philip Minnmann, Johannes Schubert, Simon Burkhardt, Matthias T. Elm, Peter J. Klar, Christian Heiliger, and Jürgen Janek *ACS Appl. Mater. Interfaces* **2023**, 15, 40, 47260-47277. (DOI: 10.1021/acsami.3c10060)

[Δ] indicates shared first authorship.

Reproduced with permission

ACS APPLIED MATERIALS & INTERFACES

www.acsami.org Research Article

Influence of Microstructure on the Material Properties of LLZO Ceramics Derived by Impedance Spectroscopy and Brick Layer Model Analysis

Janis K. Eckhardt,*,⊥ Sascha Kremer,*,⊥ Till Fuchs, Philip Minnmann, Johannes Schubert, Simon Burkhardt, Matthias T. Elm, Peter J. Klar, Christian Heiliger,* and Jürgen Janek*

Cite This: ACS Appl. Mater. Interfaces 2023, 15, 47260–47277 Read Online

ACCESS | Metrics & More | Article Recommendations | Supporting Information

ABSTRACT: Variants of garnet-type $Li_7La_3Zr_2O_{12}$ are being intensively studied as separator materials in solid-state battery research. The material-specific transport properties, such as bulk and grain boundary conductivity, are of prime interest and are mostly investigated by impedance spectroscopy. Data evaluation is usually based on the one-dimensional (1D) brick layer model, which assumes a homogeneous microstructure of identical grains. Real samples show microstructural inhomogeneities in grain size and porosity due to the complex behavior of grain growth in garnets that is very sensitive to the sintering protocol. However, the true microstructure is often omitted in impedance data analysis, hindering the interlaboratory reproducibility and comparability of results reported in the literature. Here, we use a combinatorial approach of structural analysis and three-dimensional (3D) transport modeling to explore the effects of microstructure on the derived material-specific properties of garnet-type ceramics. For this purpose, Al-doped $Li_7La_3Zr_2O_{12}$ pellets with different microstructures are fabricated and electrochemically characterized. A machine learning-assisted image segmentation approach is used for statistical analysis and quantification of the microstructural changes during sintering. A detailed analysis of transport through statistically modeled twin microstructures demonstrates that the transport parameters derived from a 1D brick layer model approach show uncertainties up to 150%, only due to variations in grain size. These uncertainties can be even larger in the presence of porosity. This study helps to better understand the role of the microstructure of polycrystalline electroceramics and its influence on experimental results.

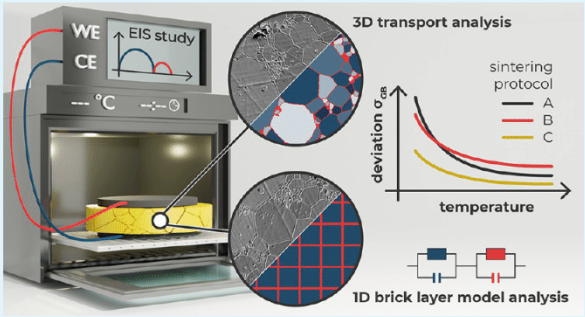

KEYWORDS: *solid-state battery, lithium metal anode, microstructure, brick layer model, impedance spectroscopy, LLZO, machine learning*

1. INTRODUCTION

The role of electric energy storage technologies, i.e., batteries, is ever-increasing. Recently, the concept of the solid-state battery (SSB) has been attracting strong interest as it has the potential to further advance lithium-ion battery technology.[1−3] The ultimate target for the anode material is lithium metal due to its low redox potential of $E_H = -3.04$ V and high theoretical capacity of $q_{th} = 3861$ mAh/g.[4,5] The successful implementation of the reversible lithium metal anode concept, however, is hampered especially by morphological instabilities at the metal anode interface and dendrite formation due to inhomogeneous metal dissolution and deposition.[6−8] This places high demands on potential solid electrolyte (SE) separator materials. These demands include, e.g., ensuring homogeneous current flow, compensating for volume changes at the interface, and providing high mechanical resistance to dendrite growth.

Garnet-type solid electrolytes such as $Li_{6.25}Al_{0.25}La_3Zr_2O_{12}$ (LLZO) have received considerable attention for use as separators in SSBs since they combine high ionic conductivities of a few mS·cm^{-1} and chemical compatibility with lithium metal.[3,9−11] This, together with the mechanical properties of garnets, i.e., high Young's modulus, hardness, and fracture toughness, makes LLZO a highly suitable and attractive candidate for fundamental investigations, e.g., of the interface kinetics of the lithium metal anode.[12] This includes the investigation of "anode-free" SSB concepts, the impact of solid

Received: July 11, 2023
Accepted: September 12, 2023
Published: September 26, 2023

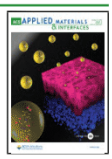

https://doi.org/10.1021/acsami.3c10060
ACS Appl. Mater. Interfaces 2023, 15, 47260−47277

ACS Applied Materials & Interfaces www.acsami.org Research Article

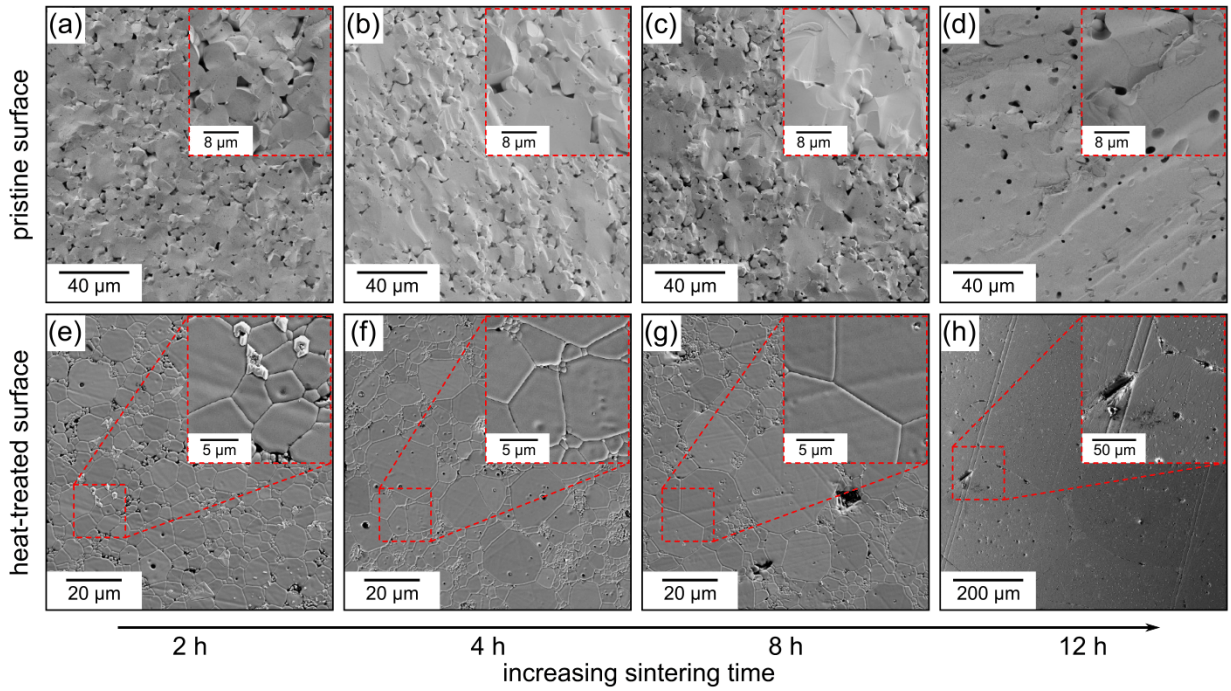

Figure 1. Representative SEM images of the pristine and heat-treated surfaces of the LLZO pellets sintered for 2 h in (a) and (e), 4 h in (b) and (f), 8 h in (c) and (g), and 12 h in (d) and (h) at 1230 °C. The homogeneity of the grain structure changes with increasing sintering time due to abnormal grain growth. This is also true for the pore structure with the collapse of the initial small intergranular contacts (i.e., sinter necks) and the fusion of pores into the bulk of the grains.

or ionic liquid interlayers, the effect of microstructured three-dimensional solid electrolyte architectures, the understanding of dendrite formation, or the effect of the modification of the lithium metal electrode (e.g., using composite or alloying approaches) on the electrode performance parameters, to name just a few.[13−21]

Although the nominal composition of garnet solid electrolytes is often the same in many studies, interlaboratory reproducibility is not necessarily guaranteed. Reasons are very likely differences in the actual fabrication processes (e.g., sintering protocol or particle homogenization), which result in considerable variations of the polycrystalline microstructure of the ceramics obtained.[22] It is well-known that LLZO exhibits abnormal grain growth when the sintering temperatures are too high, i.e., discontinuities in the grain growth rate lead to individual coarse grains.[23,24] Thus, the sintering protocol (e.g., processing temperatures and sintering time or pressing and annealing steps)[22] strongly affects the grain size distribution and porosity in the microstructure.[25−28] In consequence, the comparison of electrochemical results of different research groups reported in the literature is challenging, in particular, as the effect of the actual microstructure is usually not properly considered in the data interpretation. This concerns the derived material properties and also the derived conclusions about material alterations (e.g., lithium loss) or the formation of different phases, e.g., at grain boundaries (GB).[29,30] At this point, we would like to note that we stick to the commonly used term "microstructure" in describing the polycrystalline grain pattern with typical dimensions in the order of a few micrometers. One might infer whether it is more reasonable to use the term "mesostructure" instead, but this is not yet an established term in the field of ceramics.[31]

The electrical transport properties of electroceramics such as LLZO are typically investigated by using electrochemical impedance spectroscopy (EIS). Various microscopic processes in the system, such as bulk and grain boundary transport, can be separated in the frequency domain if they have different time constants.[32] The macroscopic transport parameters (i.e., resistances R_i and capacitances C_i) are usually determined by using simple one-dimensional equivalent circuit models (ECM), such as two *RC*-elements in series. The parameter pairs (R_i, C_i) are then interpreted using the so-called brick layer model (BLM).[33−35] The BLM assumes a polycrystalline sample with a highly ordered arrangement of identical grains in a matrix separated by a thin intergranular phase. The symmetric BLM microstructure and the resulting 1D transport paths allow the derivation of analytical formulas to easily calculate conductivities σ_i and permittivities ε_i. However, it is usually ignored that the BLM cannot provide error-free microscopic transport quantities, including activation energies.[36] Deviations from the idealized BLM microstructure in a real system, e.g., due to a non-uniform grain size distribution and pores, affect the dimensionality and homogeneity of the transport through the real system.[37,38] As a result, the uncertainty in the BLM-derived transport quantities is a function of the spatial arrangement of the grains and the conductivity ratio of bulk and grain boundary transport.[39] In the past, Abrantes et al. have investigated such effects for strontium titanate ceramics.[40] However, transferring their results to other material systems is not straightforward.

The lack of dedicated studies regarding microstructure-related uncertainties in the transport properties of LLZO obtained by BLM analysis hinders interlaboratory comparability. In this study, we therefore perform a comprehensive

https://doi.org/10.1021/acsami.3c10060
ACS Appl. Mater. Interfaces 2023, 15, 47260−47277

analysis of experiments and simulations to estimate the uncertainty in the BLM-derived transport quantities. To this end, different sintering protocols are used to deliberately manipulate the microstructure of LLZO pellets, covering a wide range of LLZO microstructures typically found in experimental studies in the literature. In addition to visual characterization, a machine learning (ML) assisted image segmentation approach is used for statistical analysis and quantification of sintering-induced microstructural changes. The experimental EIS characterization of the individual LLZO samples using the standard 1D BLM approach suggests continuous changes in material-specific properties with sintering time. However, by performing 3D transport computations through statistically modeled twin microstructures, we show that the material-specific properties have not necessarily changed during sintering. In the case of a dense microstructure, the grain bulk conductivity evaluation is not affected much by the use of the BLM, but the uncertainty in the BLM-derived grain boundary conductivity can be up to 150% due to variations in grain size in the real microstructure alone. The impact of porosity on bulk and grain boundary transport parameters is even more severe and depends strongly on the spatial pore distribution in the ceramic. Both kinds of microstructural defects also affect the derived values of the activation energies of the transport processes.

2. RESULTS

2.1. Microstructural Changes during Sintering of LLZO Ceramics. Different aluminum-doped LLZO pellets ($Li_{6.25}Al_{0.25}La_3Zr_2O_{12}$) were prepared using a conventional solid-state synthesis route similar to that reported by Krauskopf et al.[41] A detailed description can be found in the Supporting Information. Four different groups of LLZO samples are examined. The groups differ in the duration of the final sintering step of the synthesis. They are labeled below according to the sintering times of 2 h, 4 h, 8 h, and 12 h. X-ray diffraction (XRD) measurements confirm the phase purity of the individual LLZO pellets. The diffraction maxima in the XRD patterns of each ground pellet can be indexed to the cubic garnet structure with space group $Ia\bar{3}d$ (no. 230) and lattice parameter a = 12.968 Å, as shown in Figure S2. No signatures of secondary phases, such as $La_2Zr_2O_7$ or other crystalline impurities, are visible in the XRD data. This demonstrates that the crystal structure and phase purity of the bulk material of the LLZO pellets are independent of the sintering time.

2.1.1. Visual Analysis of the Effect of Sintering on the Microstructure. The changes in the sintering protocol affect particularly the microstructure of the individual LLZO pellets. This includes the size distribution, the shape distribution, the spatial distribution, and the orientation of grains and pores. Hereafter, the terms *"grain structure"* and *"pore structure"* are used to refer specifically to these effects in the individual phases of the overall microstructure. Figure 1a–d shows scanning electron microscopy (SEM) images of fractured pellet edges at sintering times between 2 and 12 h at 1230 °C. The images obtained are suitable for distinguishing between the actual material and pores but not between individual grains of the material. Therefore, we use a variant of the thermal grooving technique reported by Sato et al. to visualize the grain boundaries (see Experimental Details for more details).[42] The resulting grain structures are shown in Figure 1e–h. A direct comparison of the pristine and heat-treated LLZO surfaces reveals that dense areas in the former are sometimes due to multiple well-sintered grains rather than a single grain. Overall, the observed variation in the microstructure is in line with the typical sintering behavior known for LLZO ceramics. It also fits recent results by Moy et al. on the effect of aluminum concentration on microstructure evolution:[23−27]

- 2 h sintering time: The microstructure in Figure 1a,e shows the closest resemblance to the initial state of compressed spherical particles. It is characterized by a uniform grain size distribution. The pores appear to be regularly distributed throughout the sample and are predominantly located between the individual grains, leading to small intergranular contacts (i.e., sinter necks).
- 4 h sintering time: The first signs of the onset of abnormal grain growth can be identified in the microstructure shown in Figure 1b,f.[23,25−27] Rearrangement of the pore structure leads to the collapse of the sinter necks. The overall microstructure appears to be denser. There are local regions where only a few pores are present. This indicates a densification process commonly observed during the sintering of ceramics.[43]
- 8 h sintering time: Progressive abnormal grain growth results in strong inhomogeneities in the grain structure. The microstructure in Figure 1c,g features single coarse grains with extensions up to 100 μm with small grains <5 μm clustered close to them. The pore distribution has not changed significantly. The volumetric porosity is unchanged, indicating that the initial densification process has already been completed after 4 h of sintering.
- 12 h sintering time: The microstructure is homogenized again. Figure 1d,h reveals the formation of an interconnected grain network with almost macroscopic dimensions (i.e., several 0.1 mm). Only a few regions of small grains <25 μm can be observed. The pore structure has not changed significantly. The pores are found mainly at the interfaces between the grains. This qualitative behavior persists at even longer sintering times, resulting in percolation paths between opposing sample edges that cross only about 4 grains, as shown in Figure S3.

2.1.2. Machine Learning-Assisted Statistical Analysis of the Microstructure. We perform a statistical analysis based on ML-assisted image segmentation of the sintered pellets to quantify the microstructural changes in grain and pore size with the sintering time. A detailed description of the image segmentation pipeline can be found in the Supporting Information. A proper analysis, however, was possible only for the groups of pellets that were sintered for less than 12 h. In the case of the 12 h group, widely varying grain sizes prevent the sample surface from being probed with uniform resolution, which in turn leads to a bias in the data. The input dataset for determining the grain size distribution of the LLZO pellets relies on two-dimensional (2D) SEM images of the heat-treated sample surface (up to 0.15 mm^2 at a structural resolution of 70 nm), as shown in Figure S5. The number of segmented grains ranges from 5500 to 7000. In addition, we performed an analysis of the porosity and pore size distribution. It is based on selected 2D cross-sections from focused ion beam scanning electron microscopy (FIB SEM) tomography data (see Figure S6) since the pores were clogged

https://doi.org/10.1021/acsami.3c10060
ACS Appl. Mater. Interfaces 2023, 15, 47260−47277

ACS Applied Materials & Interfaces www.acsami.org Research Article

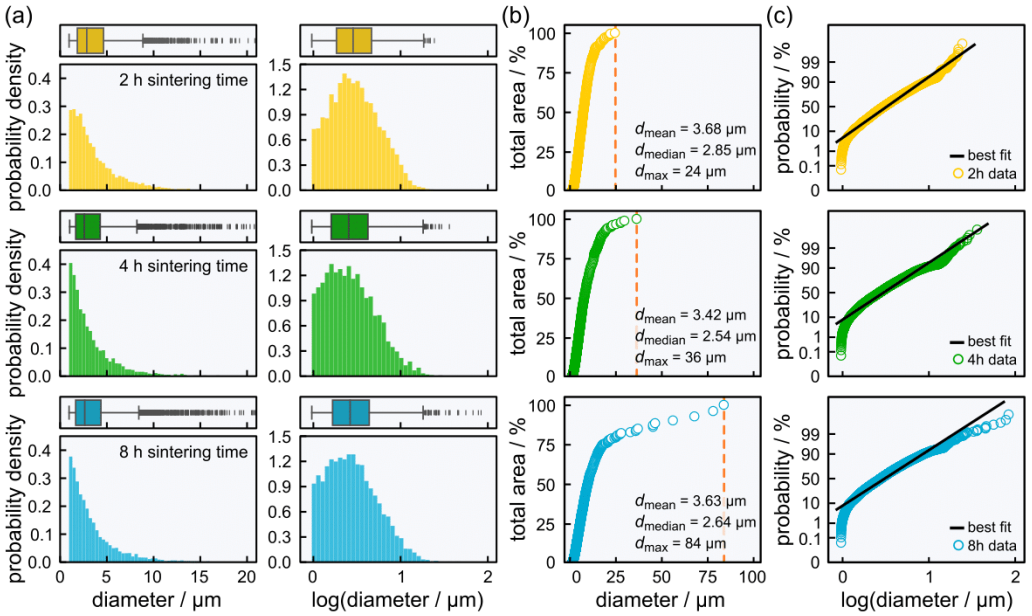

Figure 2. Statistical analysis of the grain size distribution of the LLZO pellets sintered for 2 h (top row), 4 h (middle row), and 8 h (bottom row) based on machine learning-assisted image segmentation. (a) The shapes of the histograms with linear and logarithmic grain diameter axes differ only slightly, while the number of outliers in the box-and-whisker diagrams increases with sintering time. (b) Abnormal grain growth in LLZO results in a disproportionately large volume fraction being distributed among a few grains in the cumulative probability distribution. (c) The good description of the distribution functions by a linear fit function (black) in the log-normal probability diagram indicates that the majority of grains follow a log-normal distribution.

by particle abrasion after thermal treatment. The sample volume probed was approximately 10^6 μm^3, and the spatial resolution of the tomographic 3D image was about 100 nm. The number of segmented pores ranges from 4000 to 6000. In the following analysis, we distinguish between different types of densities: (1) the probability density $n_k(d)$ with k = (grain, pore) of segmented elements with a certain size d, (2) the volumetric density $\Lambda(t)$ of the pellets after different sintering times t = (2 h, 4 h, 8 h), and (3) the theoretical mass density of LLZO ρ_{LLZO} = 5.12 g/cm^3.

2.1.2.1. Quantitative Changes of the Grain Structure During Sintering. Figure 2 depicts the results of the statistical analysis of the sample microstructure for sintering times between 2 and 8 h. At first glance, the grain size data in histogram representation (i.e., probability density n_{grain} vs grain size d) shown in Figure 2a do not exhibit any significant differences. Plotting the data with a linear x-axis shows that the probability density n_{grain} decreases drastically with increasing grain size d. Considering the logarithmic grain size $\log(d)$ as input data results in a different bin size, which allows us to resolve a gradual increase of the probability density n_{grain} to a maximum value, followed by a steady decrease, leading to an asymmetric shape of the grain size distribution. The size range between 1 and 10 μm accounts for about 96% of the segmented grains. Median grain size (i.e., the central value in the sorted list of sampled grains) and the mean grain size $\bar{d}_i = (\sum_i d_i)/N$, where d_i is the sampled grain size of grain i and N is the number of segmented grains, are often used as statistical descriptors for different microstructures. In our case, both yield fairly similar results with 2.5−2.9 and 3.4−3.7 μm for the former and the latter, respectively. Thus, averaging alone cannot capture appropriately the structural inhomogeneities, which occur with increasing sintering time and that are visually observed in the SEM images (see Figure 1).

Larger differences are evident in the maximum grain size, which increases by a factor of 3.5 from 24 to 84 μm with increasing sintering time. The top graphs in Figure 2a show the box-and-whisker diagrams of the individual distribution functions to unravel the distinct differences in the microstructure. The colored box represents the first and third quartiles of the distribution, and the vertical line inside represents its median. Whisker boundaries are based on 1.5 of the interquartile range, and outliers from this interval are indicated by small vertical lines. The comparison of the individual diagrams reveals that, as the sintering time increases, the first quartile shifts toward smaller grain sizes, the number of outliers increases, and these shift toward larger grain sizes. This demonstrates that with increasing sintering duration, several grains are growing significantly at the expense of smaller grains that are shrinking.

A similar behavior can also be observed in the cumulative area distribution, i.e., the sum of the relative area fraction of segmented grains vs grain size. The individual distribution functions in Figure 2b show the same trends, with a sharp increase followed by a smooth convergence. Quantitative variations are particularly prominent when comparing the samples sintered for 4 h (green) and 8 h (cyan). In the latter case, the increase in area fraction is much flatter, meaning that larger grains become more important, and the overall microstructure becomes increasingly inhomogeneous. For instance, less than 0.3% of the segmented grains have diameters larger than 25 μm but account for more than 20% of the total area in the data of the 8 h sample. Consequently, longer sintering times result in a disproportionately large volume fraction being distributed among a few grains, which

https://doi.org/10.1021/acsami.3c10060
ACS Appl. Mater. Interfaces 2023, 15, 47260−47277

ACS Applied Materials & Interfaces www.acsami.org Research Article

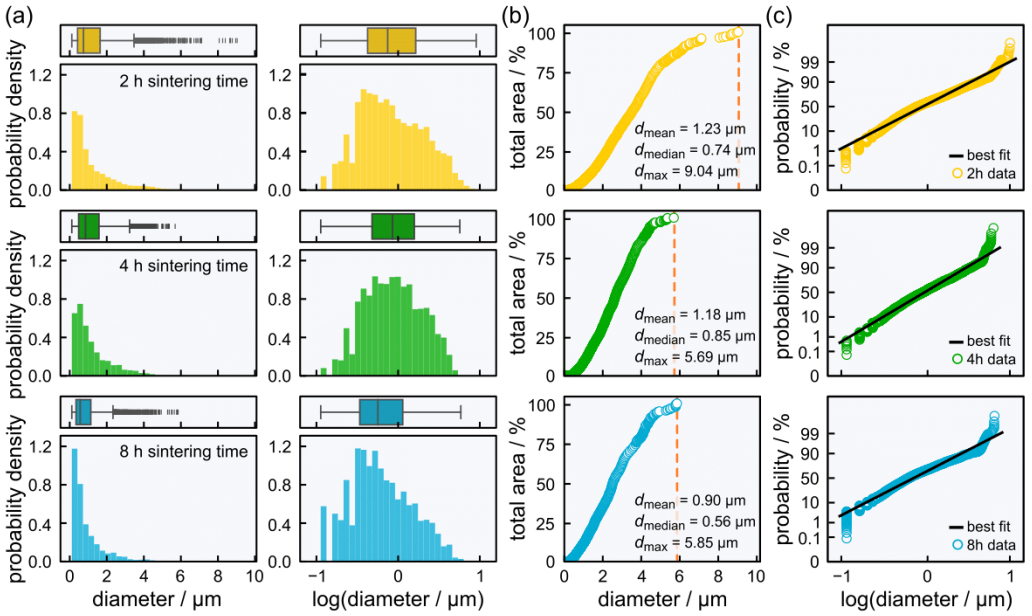

Figure 3. Statistical analysis of the pore size distribution in the LLZO pellets sintered for 2 h (top row), 4 h (middle row), and 8 h (bottom row) based on machine learning-assisted image segmentation. (a) The shapes of the histograms and of the box-and-whisker diagrams with linear and logarithmic grain diameter axes differ only slightly with respect to sintering time. (b) The cumulative probability distribution reveals no major differences in pore size. (c) The majority of the sampled pores meet the criteria of a log-normal distribution, as indicated by the linear fit (black) in the log-normal probability plot.

then determine the characteristics of the system (e.g., mechanical or electrochemical properties).[44,45]

The grain size distribution in regular polycrystals usually follows a log-normal distribution. This is indicated by a linear relation in the normal probability plot, i.e., standard normal probabilities vs logarithm of the grain size. In the case of the sintered LLZO pellets, however, a sharp increase in probability is followed by an almost linear response as shown in Figure 2c. In particular, the behavior for grain sizes below 1 μm is not captured by a log-normal distribution. One of the reasons for this is the use of a threshold to identify grains in the image segmentation process. In contrast, the behavior of larger grain sizes is well captured. A linear function (black) properly describes the grain size distribution of the samples sintered for 2 h (yellow) and 4 h (green). In the case of the sample sintered for 8 h (cyan), significant deviations are also observed for grain sizes above 25 μm. This is related to abnormal grain growth, which leads to a bimodal grain size distribution with increasing sintering time.[23,25−27]

2.1.2.2. Quantitative Changes of the Pore Structure During Sintering. Figure 3 shows the results of the statistical analysis of the pore structure corresponding to different sintering times. The individual size distributions are rather similar in the histogram representation (i.e., probability density n_{pore} vs pore size d) and independent of sintering time, as depicted in Figure 3a. The probability density n_{pore} drops sharply with an increasing pore size in the case of the representation with a linear pore size axis. Interestingly, the distribution function of the sample sintered for 4 h is somewhat broader, i.e., the probability density of smaller pores decreases in favor of larger pores in the intermediate size range. However, the functional behavior of the distributions shows no significant differences on the logarithmic scale when $\log(d)$ is considered as input data for the histogram representation. The segmented pore sizes vary between 0.2 and 9.0 μm, and averaging yields a median size of 0.6−0.9 μm and a mean size of 0.9−1.2 μm. This indicates that the pore size distribution in the considered volume of the individual LLZO pellets (i.e., 10^6 μm^3) is not much different from a statistical point of view. The result is consistent with the box-and-whisker diagrams, which reveal no disproportionately large pores in the distribution. The maximum size decreases slightly with sintering time from 9.0 to 5.7 μm. The cumulative area distributions in Figure 3b do not show distinct differences, and the normal probability plot in Figure 3c reveals an almost linear relationship for most of the segmented pores, indicating a log-normal distribution of the pore sizes.

The statistical analysis of the pore structure based on image segmentation shows an increase in volumetric pellet density Λ from 92% after 2 h to 94% after 4 and 8 h sintering time. This trend is consistent with the calculated volumetric pellet density Λ based on the mass density of LLZO ρ_{LLZO}, i.e., $\Lambda = (m/V)/\rho_{LLZO}$, where V is the volume of the pellet and m is its mass. The calculation shows that the volumetric pellet density Λ increases slightly from 94% for the sample sintered for 2 h to 95% for the 4 and 8 h sintered samples. The observation agrees with the behavior visually observed in the SEM images (see Figure 1), which show an initial densification process followed by a spatial reorganization of the pore structure at constant porosity. The constant porosity is due to the slow kinetics of closing the pores that are buried within the bulk of grains during the sintering process, unlike the pores located at grain boundaries.[46] This is consistent with the statistical analysis in Figure 3a, which shows a disproportionate increase in the number of medium-sized pores for longer sintering times at the expense of larger pores in the histogram.

2.1.3. Comparison with LLZO Microstructures Reported in the Literature. A data mining study on the reported synthesis

https://doi.org/10.1021/acsami.3c10060
ACS Appl. Mater. Interfaces 2023, 15, 47260−47277

ACS Applied Materials & Interfaces www.acsami.org Research Article

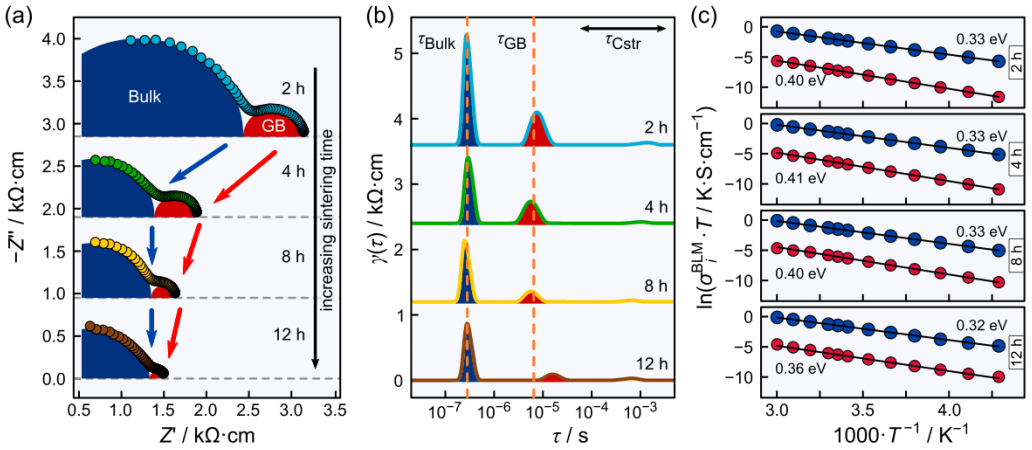

Figure 4. Experimental impedance characterization of LLZO pellets under equilibrium using an ideally reversible (Li) electrode arrangement. The impedance data of the individual LLZO pellets were recorded at 25 °C. For clarity, impedance values for frequencies below 100 Hz are not shown. The impedance spectra over the full frequency range can be found in Figure S8. (a) The bulk contribution (blue) initially shrinks and then remains almost constant, while the grain boundary contribution (red) decreases continuously with sintering time. (b) The time constants in the DRT for sintering times of up to 8 h each agree well. A further increase of the sintering time to 12 h results in a shift of the grain boundary time constant τ_{GB} to longer relaxation times. (c) The temperature dependence of the impedance contributions in the Arrhenius diagram is almost the same for sintering times up to 8 h, while the grain boundary activation energy decreases by more than 40 meV for the sample sintered for 12 h.

conditions of LLZO ceramics by Mahbub et al. revealed a large variance in the sintering protocols, especially with respect to the process temperature and pressure in the individual steps.[22] Such differences in the synthesis protocol result in a variety of microstructures with different degrees of grain size homogeneity and wide ranges of pellet volumetric densities Λ. Reported LLZO grain sizes in such sintered samples vary from 1 to 600 μm, while volumetric pellet densities Λ between 60% and almost 100% are observed.[28,47−49] Ideal SE separators should be completely dense with zero porosity and should show a uniform grain size distribution in order to yield improved performance parameters, such as high fracture toughness, high effective conductivity, homogeneous current distribution, and strong mechanical resistance to dendrite or filament growth. However, this is difficult to achieve in practice. Most studies investigating the application of the lithium metal anode in SSB consider LLZO separators with volumetric pellet densities Λ greater than 92%. Lower volumetric pellet densities Λ are usually observed when studying and tuning the sintering behavior of LLZO ceramics.

The LLZO ceramics fabricated in this study cover almost the entire range of grain sizes typically observed in the literature while maintaining an almost constant volumetric pellet density Λ of about 94%. The pellet sintered for 2 h is representative of a uniform grain size distribution, while the sample sintered for 8 h captures the effect of a bimodal grain size distribution. The microstructures of the other two pellets sintered for 4 and 12 h represent intermediate cases, with the onset of abnormal grain growth after 4 h of sintering and rehomogenization of the microstructure after 12 h of sintering. Furthermore, the sample sintered for 2 h is representative of an intergranular pore arrangement, while especially the samples sintered for 4 and 8 h show the effect of an intragranular pore arrangement.

2.2. Understanding the Impact of Sintering Time on the Material Properties of LLZO. Differences in sintering duration may alter not only the microstructure of LLZO ceramics but also their conductivity. An extensive literature search reveals a large variation in reported conductivity data for nominally the same material, in some cases more than an order of magnitude variation.[3,47−49] This can be due to changes in the material-specific properties, such as lithium loss within the structure or the formation of different phases at grain boundaries, but it may also originate solely from its microstructure.[24,29,30] To elucidate the effect of the sintering protocol on the electrochemical properties of LLZO, we perform a combinatorial analysis of experiments and simulations. First, we experimentally study the impedance behavior of the different LLZO pellets described in the previous sections and derive their microscopic transport quantities using the standard 1D brick layer model analysis approach.[33−35] The results are then compared with 3D transport computations using statistically modeled twin microstructures based on the ML-assisted analysis of the microstructural changes of the LLZO ceramics during sintering. This allows us to correlate microstructural changes in grain and pore size distributions with the experimentally observed differences in the electrochemical properties of individual pellets.

2.2.1. Influence of Sintering Time on the Experimentally Derived Transport Parameters. Temperature-dependent potentiostatic EIS measurements are performed between −40 and 60 °C with an ideally reversible Li|LLZO|Li and a blocking Au|LLZO|Au electrode setup. Here, the ideal reversible electrode configuration refers to the cell preparation approach reported by Krauskopf et al. (see Experimental Details) and the absence of any interface contributions.[41] The impedance results for both electrode arrangements are consistent. In what follows, we focus on the measurement results obtained with the ideally reversible electrode configuration only, while an overview of the results with the blocking electrode configuration is given in the Supporting Information. Note that all impedance spectra are normalized to the sample dimensions to account for the slightly different diameters and thicknesses of the individual pellets studied.

Figure 4a depicts the impedance response of the individual LLZO pellets at room temperature in a Nyquist representation.

https://doi.org/10.1021/acsami.3c10060
ACS Appl. Mater. Interfaces 2023, 15, 47260−47277

Each impedance spectrum consists of a semicircle at high frequencies, which is only partially captured in the measured frequency range, and a fully mapped semicircle at medium frequencies. They can be assigned to transport within the bulk of grains (blue) and transport across grain boundaries (red) based on their capacitance and their apex frequencies of about 5 MHz and 50 kHz, respectively.[32] Extending the sintering time from 2 to 4 h leads to a decrease in the bulk contribution from 2.47 to 1.39 kΩ·cm, while it remains almost constant for longer sintering times. In contrast, the grain boundary contribution decreases continuously from initially 0.70 kΩ·cm after 2 h of sintering to 0.21 kΩ·cm after 12 h of sintering. The qualitative evolution of the total resistance (i.e., R_{Bulk} + R_{GB}) is comparable to the computational study by Kim et al.[43] However, a quantitative analysis of the functional behavior requires additional measurements at different sintering times.

We transfer the impedance into the time domain by performing a distribution of relaxation times (DRT) analysis in order to study the effect of the sintering time on the time characteristics of the two transport processes. The resulting DRTs look qualitatively the same and differ only in small details, as shown in Figure 4b. Each distribution function $\gamma(\tau)$ consists of two larger signals for relaxation times between 10^{-7} and 10^{-4} s and a small signal in the range of 10^{-3} s. The former two originate from bulk (blue) and grain boundary (red) transport within the sample. The amplitude of the bulk signal first drops and then remains almost constant with sintering time, while that of the grain boundary signal decreases continuously. This is consistent with the results in the frequency domain since the area under a signal is proportional to its resistance. Interestingly, the time constant of the bulk transport is independent of the sintering time, in contrast to that of the grain boundary transport, which increases by about a factor of 2 when going from 8 h sintering time to 12 h sintering time. The third signal occurring at longer relaxation times originates from remaining pores at the LilLLZO interfaces during cell assembly. They lead to geometric current constriction (Cstr) effects, as recently discussed in the literature.[50−53]

To quantify the changes in impedance with sintering time, we perform an ECM analysis considering two *RQ*-elements in series. These represent bulk and grain boundary transport within the sample. The capacitance C_i of both processes is given by Brug's formula $C_i = (Q_i/R_i^{\alpha-1})^{1/\alpha}$, where α is the ideality factor of the constant phase element Q_i.[54] The macroscopic parameter pairs (R_i, C_i) with i = (Bulk, GB) are then transformed into microscopic transport quantities (σ_i^{BLM}, ε_i^{BLM}) using the brick layer model approach.[33−35] The bulk parameters (σ_{Bulk}^{BLM}, ε_{Bulk}^{BLM}) can be calculated based on the cell constant of the system using the standard formulas for resistors and plate capacitors. The grain boundary quantities (σ_{GB}^{BLM}, ε_{GB}^{BLM}) can be determined using

$$\sigma_{GB}^{BLM} = \sigma_{GB,geo}^{BLM} = \frac{1}{R_{GB}} \cdot \frac{L}{A} \cdot \frac{\delta_{GB}}{d + \delta_{GB}} \quad (1)$$

$$\varepsilon_{GB}^{BLM} = \varepsilon_{GB,geo}^{BLM} = C_{GB} \cdot \frac{L}{A} \cdot \frac{\delta_{GB}}{d + \delta_{GB}} \quad (2)$$

where L is the thickness of the sample, A denotes the electrode area, and d is the grain size. In experiments, the geometric prefactor $\delta_{GB}/(d + \delta_{GB})$ in eqs 1 and 2, reflecting the microstructure of the sample, is often unknown. Thus, the equations are usually rearranged to depend instead on the ratio between the macroscopic bulk and grain boundary capacitances C_{Bulk}/C_{GB}.

$$\sigma_{GB}^{BLM} = \frac{1}{R_{GB}} \cdot \frac{L}{A} \cdot \frac{C_{Bulk}}{C_{GB}} \cdot \frac{\varepsilon_{GB}}{\varepsilon_{Bulk}} \quad (3)$$

$$\varepsilon_{GB}^{BLM} = C_{GB} \cdot \frac{L}{A} \cdot \frac{C_{Bulk}}{C_{GB}} \cdot \frac{\varepsilon_{GB}}{\varepsilon_{Bulk}} \quad (4)$$

The comparison of the former eqs 1 and 2 with the new eqs 3 and 4 allows the derivation of an expression for the calculation of the grain boundary thickness δ_{GB}^{BLM} in the microstructure.

$$\delta_{GB}^{BLM} = d \cdot \frac{\varepsilon_{GB} \cdot C_{Bulk}}{\varepsilon_{Bulk} \cdot C_{GB} - \varepsilon_{GB} \cdot C_{Bulk}} \quad (5)$$

A detailed discussion regarding the origin of the analytical formulas, i.e., eqs 1−5, is given in the Supporting Information. Apparently, eqs 3−5 depend not only on bulk and grain boundary capacitances but also on their permittivities, which are challenging to determine experimentally. However, for oxide materials such as ZrO_2, CeO_2, or $SrTiO_3$, it is well-known that they are quite similar, i.e., $\varepsilon_{Bulk}^{mic} \approx \varepsilon_{GB}^{mic}$.[55−57] This allows for simplifying the equations so that they depend only on known quantities:

$$\sigma_{GB}^{BLM} = \sigma_{GB,cap}^{BLM} = \frac{1}{R_{GB}} \cdot \frac{L}{A} \cdot \frac{C_{Bulk}}{C_{GB}} \quad (6)$$

$$\varepsilon_{GB}^{BLM} = \varepsilon_{GB,cap}^{BLM} = C_{GB} \cdot \frac{L}{A} \cdot \frac{C_{Bulk}}{C_{GB}} \quad (7)$$

$$\delta_{GB}^{BLM} = d \cdot \frac{C_{Bulk}}{C_{GB} - C_{Bulk}} \quad (8)$$

This assumption (i.e., $\varepsilon_{Bulk} = \varepsilon_{GB}$) may be questionable in the case of LLZO due to various mechanisms leading to grain boundary resistance, such as microcracks and segregation of impurities or amorphous phases.[58] Nevertheless, it is widely used in the literature to analyze EIS data of LLZO ceramics, although it may lead to some degree of inaccuracy in σ_{GB}^{BLM} and δ_{GB}^{BLM}.[59−61] In the following, we also stick to eqs 6−8 and assume that bulk and grain boundary permittivities are the same. In addition, we adapt the notation (σ_{GB}^{BLM}, ε_{GB}^{BLM}) according to ($\sigma_{GB,j}^{BLM}$, $\varepsilon_{GB,j}^{BLM}$) with j = (geo, cap) to distinguish between the two calculation methods. Here, the index "geo" refers to the calculation with the geometric prefactor, i.e., eqs 1 and 2, and "cap" to the calculation using the capacitance ratio, i.e., eqs 6 and 7. They only give identical results for the BLM structural assumptions but not necessarily for a realistic microstructure.

Table 1 summarizes the results of the BLM analysis of our experimental data at room temperature. For all temperatures, we use the capacitance ratio measured at −40 °C to calculate $\sigma_{GB,cap}^{BLM}$ since the ratio varies only slightly in the experiments, and each semicircle is fully captured in the measured frequency range. Moreover, the ratio is supposed to be temperature-independent in the BLM picture due to its correlation with the geometric prefactor (see eq S42). The magnitude of all derived transport quantities agrees well with the values reported in the literature.[48,49,59,60] The microscopic bulk parameters (σ_{Bulk}^{BLM}, ε_{Bulk}^{BLM}) nearly double when the sintering time is increased from 2 to 4 h and then remain almost unchanged for longer

https://doi.org/10.1021/acsami.3c10060
ACS Appl. Mater. Interfaces 2023, 15, 47260−47277

Table 1. Overview of the Experimental Transport Parameters at Different Sintering Times Determined at Room Temperature with BLM Analysis[a]

t/h	2	4	8	12
$\varepsilon_{Bulk}^{BLM}/\varepsilon_0$	118	185	183	209
σ_{Bulk}^{BLM}/mS·cm^{-1}	0.41	0.72	0.76	0.78
$E_{a,Bulk}$/meV	331	329	327	322
$\sigma_{GB,geo}^{BLM}/\mu$S·cm^{-1}	3.93	5.85	8.94	6.75
$\sigma_{GB,cap}^{BLM}/\mu$S·cm^{-1}	2.41	5.12	7.86	6.19
$E_{a,GB}$/meV	402	408	398	364
δ_{GB}^{BLM}/nm	7	10	11	11

[a]The capacitance ratio used to calculate $\sigma_{GB,cap}^{BLM}$ is determined at −40 °C.

sintering times. The time constant $\tau_{Bulk}^{BLM} = \varepsilon_{Bulk}^{BLM}/\sigma_{Bulk}^{BLM}$ is maintained in each case. Interestingly, the grain boundary conductivity $\sigma_{GB,j}^{BLM}$ increases steadily by roughly a factor of 3 up to a sintering time of 8 h, followed by a slight decrease when the sintering time is further increased to 12 h. Note that the calculation via the geometric prefactor and via the capacitance ratio yield comparable results, except for the sample sintered for 2 h, where both differ by about 60%. The resulting time constants $\tau_{GB,j}^{BLM} = \varepsilon_{GB,j}^{BLM}/\sigma_{GB,j}^{BLM}$ with j = (geo, cap) differ by no more than a factor of 2 for different sintering times. The grain boundary thickness δ_{GB}^{BLM} in the pellets appears to increase from 7 to 10 nm when the sintering time is increased to 4 h and then remains almost constant. This is within the range of values reported in the literature.[41,58,59,62]

The qualitative trends in the changes of material parameters with the sintering time are similar for the different temperatures considered. To analyze the temperature dependence in the individual LLZO ceramics in more detail, we consider the corresponding Arrhenius diagrams $\ln[\sigma_i^{BLM} \cdot T]$ vs T^{-1} with i = (Bulk, GB,cap) shown in Figure 4c. The activation energies $E_{a,i}$ listed in Table 1 can be determined from the slopes of the corresponding linear fit functions (black lines). The uncertainty of the derived results is <4 meV. Apparently, sintering times between 2 and 8 h have no major effect on the activation energy. The bulk value of about 330 meV and the grain boundary value of roughly 405 meV vary only slightly by less than 10 meV for different sintering times. This seems reasonable in view of possible inaccuracies and also in the ECM fitting of the impedance spectra. In addition, the magnitude is in good agreement with the values reported in the literature.[41,59,62−64] Larger differences are observed in the case of the LLZO pellets sintered for 12 h. In particular, $E_{a,GB}$ drops by more than 40 meV, which cannot be explained by uncertainties in the data analysis alone.

Altogether, the findings of the BLM analysis shown in Table 1 indicate that the material-specific parameters of LLZO (σ_i^{BLM}, ε_i^{BLM}) change continuously with sintering time. The observed trends could be explained by, e.g., lithium loss from the ceramics at elevated temperatures or changes in the chemical composition of the grain boundaries. For instance, there are several reports in the literature where different Li−Al−O phases have been identified at the grain boundaries.[24,29,30] It is not clear, however, whether this is the sole or the true reason for the underlying effect. The changes in the macroscopic bulk and grain boundary parameters (R_i, C_i) in the impedance spectrum shown in Figure 4a can also be explained (solely) by the microstructural changes during sintering, i.e., the collapse of the sintering necks and the reduction of the grain boundary to bulk volume ratio in the dominant transport path as observed in Figure 1. This means the differences between the actual microstructure and the idealized (highly symmetric) sample microstructure assumed in the BLM introduce uncertainties in the 1D BLM analysis result.[36−38,62] Other geometric effects, such as a static constriction effect at the electrode interface due to cell preparation (i.e., the size of the

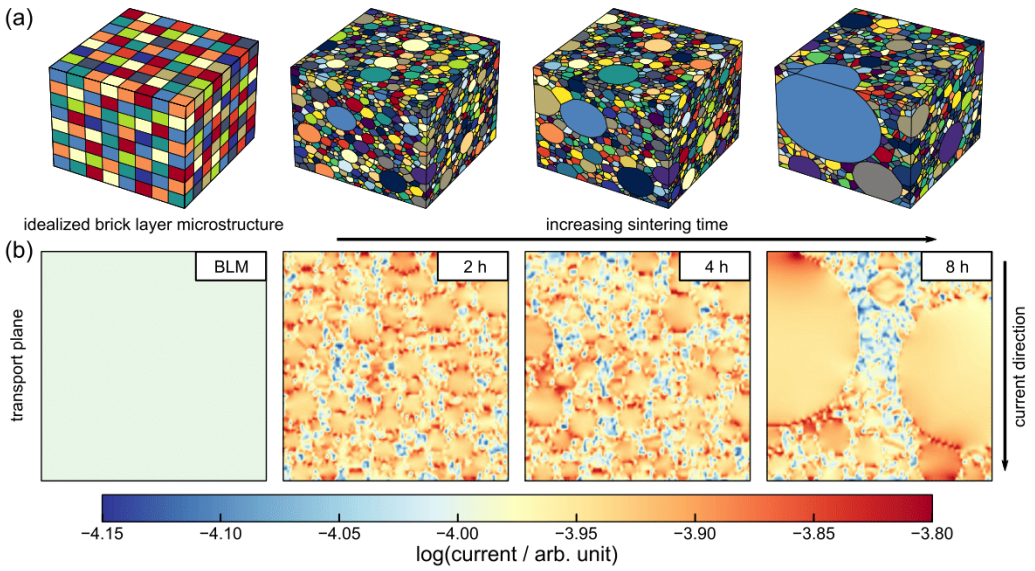

Figure 5. Effect of sintering-induced microstructural changes on the DC ion transport in the system. The microscopic transport parameters considered are the same in all cases. (a) Spatial images of BLM and dense statistically modeled twin microstructures based on the grain size distributions of the synthesized LLZO pellets shown in Figure 2. The color indicates different grains of the same bulk material. (b) The homogeneity of the current distribution in the microstructure decreases with increasing sintering time. As a result, deviations from the 1D transport behavior observed in the BLM become more pronounced due to the formation of 3D percolation paths.

https://doi.org/10.1021/acsami.3c10060
ACS Appl. Mater. Interfaces 2023, 15, 47260−47277

ACS Applied Materials & Interfaces www.acsami.org Research Article

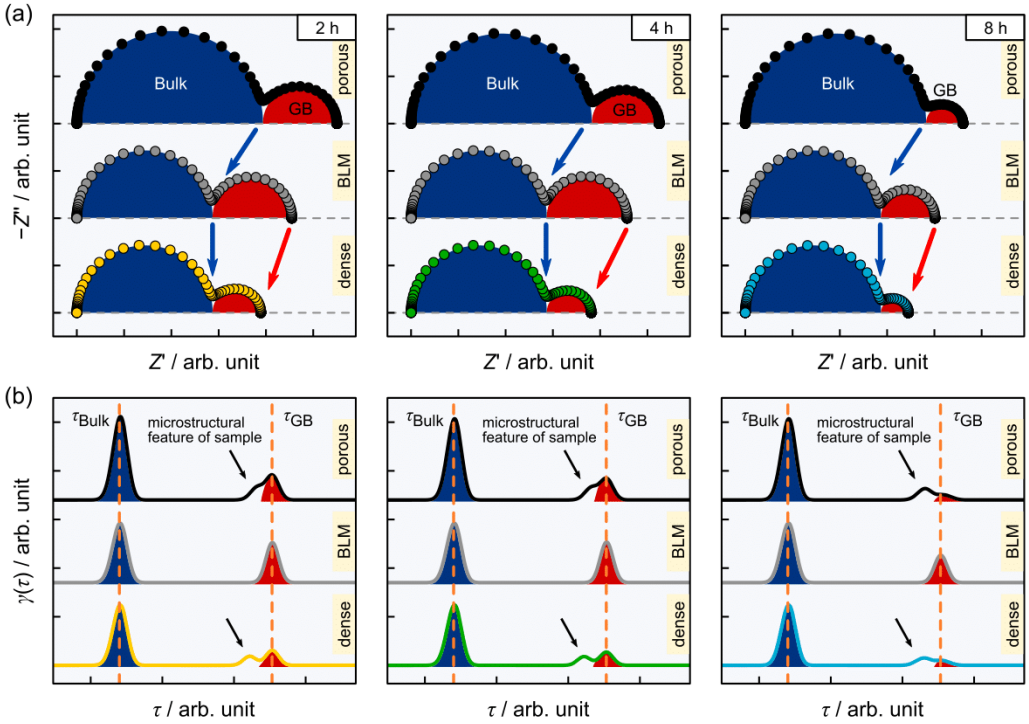

Figure 6. Effect of the microstructure on the electrochemical impedance. The computations consider a BLM microstructure (gray) as well as dense (colored) and porous (black) statistically modeled twin microstructures based on the grain and pore size distributions of the synthesized LLZO pellets. The microscopic transport parameters used for the computations are the same in all cases. (a) The bulk impedance of the BLM and the dense statistically modeled twin microstructure agree well, while the grain boundary contribution is overestimated for the BLM microstructure. Pores in the statistically modeled microstructure scale the impedance, which also leads to changes of the bulk contribution compared to the BLM microstructure. (b) The microscopic time constants for bulk and grain boundary transport in the DRT are maintained in each computation. Signals in the intermediate relaxation time range are related to the disorder in the microstructure, i.e., to geometric deviations from the highly symmetric BLM microstructure.[36]

electrode is smaller than that of the sample surface) and uncertainties in the ECM analysis or in the determination of electrode area and sample thickness, may also play a role.[50,65]

The significant influence of the real microstructure of the sample on electrochemical material analysis has recently been demonstrated in an experimental study by Ohno et al.[66] The authors investigated the interlaboratory reproducibility of EIS experiments to determine the ionic conductivity and activation energy of thiophosphate-based solid electrolytes. Different sample preparation methods of supplied powder material (e.g., pelletizing pressure, etc.) led to large variances in both quantities, even though identical raw materials were employed. Similar microstructural effects can be expected with respect to the accuracy of the 1D BLM analysis of the LLZO pellets sintered under different conditions. Therefore, a detailed theoretical analysis is performed to estimate the extent to which sintering-induced microstructural changes affect the BLM-derived transport parameters shown in Table 1.

2.2.2. Revealing the Effect of the Microstructure on the BLM Analysis through Transport Modeling. We used a combinatorial approach of microstructural analysis and transport modeling for our theoretical investigation. The transport computations rely on a 3D electric network model,[36] and the statistically modeled twin microstructures considered are based on Voronoi tessellation[67,68] with the results of the statistical microstructure analyses as input data (see Computational Details for more information). To account for intersection probability effects in the 2D SEM image datasets for the ML-assisted segmentation approach, the grain and pore size distributions (see Figures 2 and 3) were first transformed using the Saltykov method to estimate the true 3D size distributions.[69,70] Although Voronoi tessellation cannot perfectly capture the effect of the spatial arrangement of the pores or grains in a specific microstructure, it is well suited to estimate the uncertainties in the BLM-derived transport properties.[37,38,47] This refers to the fact that the simulated model systems cover all of the statistical changes in grain and pore size during sintering. In total, a series of ten dense and ten porous statistically modeled twin microstructures are considered for each sintering time to account for the quantitative effects of the spatial pore or grain distribution in the microstructure on the transport properties. In each computation, we use the same microscopic transport parameters, i.e., those derived at room temperature from the experimental EIS analysis of the LLZO pellet sintered for 4 h. Moreover, we consider the ideal case that bulk and grain boundary permittivity are identical, i.e., $\varepsilon_{Bulk} = \varepsilon_{GB}$. Therefore, the simulations will solely elucidate the influence of the microstructure on the impedance and the subsequent 1D BLM analysis result. It should be noted that the following qualitative results are independent of the set of transport parameters selected from Table 1 and that the effect of different temperatures will be considered later in the discussion.

https://doi.org/10.1021/acsami.3c10060
ACS Appl. Mater. Interfaces 2023, 15, 47260−47277

Figure 5a shows the idealized BLM microstructure compared to dense statistically modeled twin microstructures for sintering times ranging from 2 to 8 h. Apparently, the deviation of the actual microstructure from that assumed in the BLM increases with sintering time, as the size and shape of individual grains vary more with longer sintering times. This behavior has a major effect on ion transport through the material and, thus, on the performance of a device where the material is incorporated.[71] Figure 5b depicts a cross-section of the direct current (DC) distribution in the transport plane for the different microstructures. The highly symmetric grain arrangement in the BLM features 1D transport, which is indicated by a homogeneous current distribution in the system. For the actual, more realistic microstructures, the interplay of grains of different shapes and sizes and their spatial distribution in the microstructure result in the formation of 3D percolation paths along larger grains. This leads to inhomogeneous current distributions. The homogeneity of the current distribution decreases with sintering time due to abnormal grain growth, which is particularly pronounced for the sample sintered for 8 h. The differences in charge transport behavior affect the macroscopic transport properties (R_i, C_i) with i = (Bulk, GB), which are then used to derive the microscopic material parameters (σ_i, ε_i) using the 1D BLM approach. Therefore, inaccuracies in the calculation results are to be expected. This is also true for the porous microstructures since the analytical formulas of the BLM rely on a dense microstructure, i.e., the BLM does not account for the effect of pores.

Figure 6a shows exemplarily the Nyquist representation of the computed impedance for three sets of microstructures with a sintering time of 2, 4, and 8 h. Each of the sets depicts the impedance spectrum of a dense statistically modeled twin microstructure (colored), a corresponding highly ordered BLM microstructure (gray), and a porous statistically modeled twin microstructure (black). The same qualitative trends are observed independent of sintering time, i.e., they are independent of the grain size distribution. All spectra visually consist of two contributions, i.e., a bulk semicircle (blue) at high frequencies and a grain boundary semicircle (red) at low frequencies. The comparison of the impedances at fixed sintering times reveals that the bulk contribution of the BLM microstructure and that of the dense statistically modeled twin microstructure are similar, while the BLM microstructure exhibits a slightly increased grain boundary contribution. The presence of additional pores within the statistically modeled twin microstructure increases both bulk and grain boundary contributions compared to the other two microstructures.

The differences in the impedance are a consequence of the frequency-dependent evolution of the transport paths through the microstructures (see Figure S10).[36] At high frequencies around $1/\tau_{Bulk}$, the grain boundaries in the system are dielectrically conductive (i.e., $Z_{GB}(\omega = 1/\tau_{Bulk}) \approx 0$) with a negligible effect on charge transport. Therefore, the bulk contribution is not affected when varying the grain structure in the case of dense samples. With decreasing frequency, the grain boundaries become electrically conductive (i.e., $Z_{GB} \neq 0$), i.e., higher resistive. As a result, energetically preferred percolation paths along larger grains are formed, where fewer grain boundaries are crossed (cf. Figure 5b). This effect is particularly pronounced when a wide grain size distribution is present in the microstructure. These frequency-dependent percolation effects are not captured by the 1D BLM, where all transport paths are identical and exhibit the same number of grain boundaries. Therefore, the BLM microstructure leads to an overestimation of the grain boundary impedance compared to the actual inhomogeneous microstructure.[36]

Pores in the microstructure always lead to an increase in the DC resistance. This is related to both the reduction of the volume fraction of bulk material and the resulting increase in the tortuosity of the forming transport paths. The quantitative effect on individual impedance contributions and the total resistance depends strongly on their spatial distribution in the microstructure. This has recently been highlighted in the case of porous electrode interfaces[37,50] and mesoporous thin films.[72] It is also illustrated in Figure S11 for a statistically modeled twin microstructure of the sample sintered for 8 h. As for grain boundaries, the impact of pores on the shape of the impedance spectrum depends on the time scale.[73] The impedance response of pores changes from dielectrically conducting to electrically insulating as the frequency decreases. In the former case, no major effects on the evolving transport paths are expected (i.e., quasi-1D transport), while in the latter case, they act as blocking barriers enforcing detours of the charge carriers. The increased bulk and grain boundary resistance in Figure 6a indicates that the pores exhibit blocking behavior even at frequencies in the range of $1/\tau_{Bulk}$. The associated tortuosity factors of the bulk and grain boundary signals are not necessarily the same due to changes in the transport paths when the grain boundaries become electrically conductive with decreasing frequency.

We calculate the individual distribution functions $\gamma(\tau)$ in order to analyze the time characteristics of the computed impedance spectra. The DRT results in Figure 6b show two major signals at small and large relaxation times, representing bulk and grain boundary transport, respectively. Except for the ordered BLM microstructure, the non-ordered microstructures reveal an additional geometric signal near the grain boundary time constant, which arises from competing transport paths through the system. The origin of these geometric signals has recently been derived analytically by us.[36] Interestingly, the time constants of both microscopic transport processes are not affected by the different microstructures considered.[51] This holds true for all statistical model systems studied here. Thus, (sintering-related) changes in the microstructure alone do not change the time characteristics of electric transport processes in the case of LLZO.

The computed impedance spectra shown in Figure 6a can now be used to identify the differences between the true material-specific transport parameters and those obtained when performing a 1D BLM analysis based on an idealized microstructure. To this end, the spectra of the dense and porous statistically modeled twin microstructures are fitted with a 1D ECM consisting of two RC-elements. The macroscopic parameter pairs (R_i, C_i) with i = (Bulk, GB) are then translated into microscopic ones (σ_i^{BLM}, ε_i^{BLM}) using the cell constant in the case of bulk transport. For grain boundary transport, both the geometric prefactor and the capacitance ratio are considered in the calculation according to eqs 1 and 6, giving rise to grain boundary conductivities $\sigma_{GB,geo}^{BLM}$ and $\sigma_{GB,cap}^{BLM}$, respectively. Table S2 summarizes the results of the 1D BLM analysis of the computed impedance for dense and porous microstructures and various sintering times. It also includes the relative deviation between the derived BLM parameters (σ_i^{BLM}, ε_i^{BLM}) and the actual microscopic transport parameters (σ_i, ε_i) used in the 3D transport computations, e.g., $(\sigma_i^{BLM} - \sigma_i)/\sigma_i$. A

https://doi.org/10.1021/acsami.3c10060
ACS Appl. Mater. Interfaces 2023, 15, 47260−47277

ACS Applied Materials & Interfaces www.acsami.org Research Article

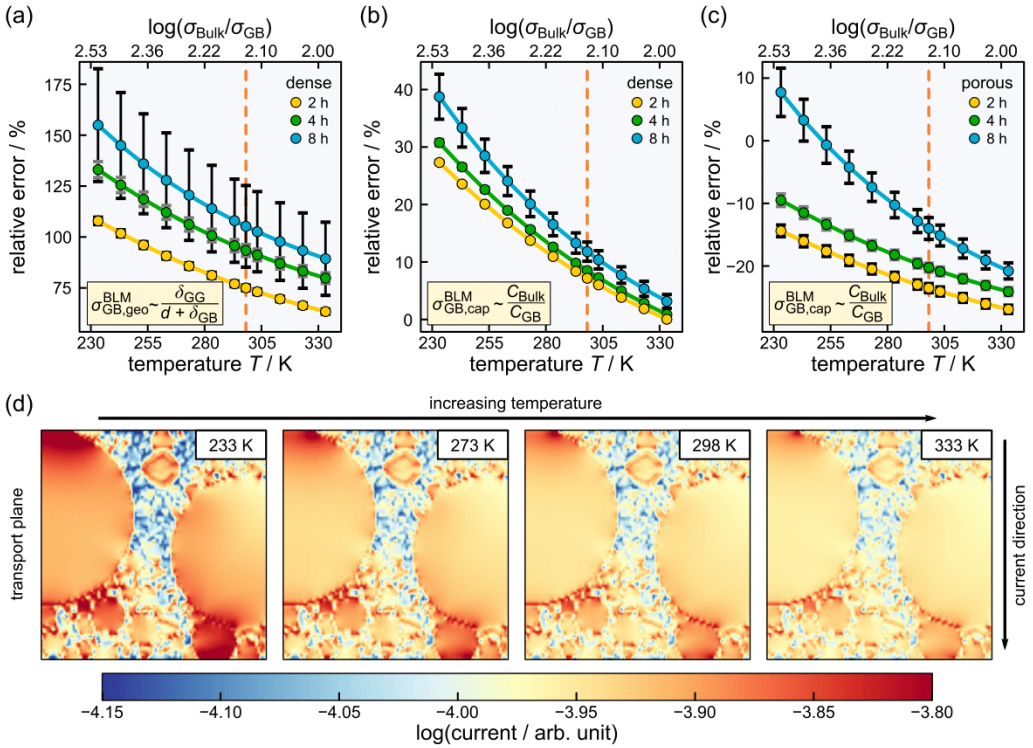

Figure 7. Temperature dependence of the inaccuracy of the grain boundary conductivity $(\sigma_{GB,j}^{BLM} - \sigma_{GB})/\sigma_{GB}$ determined with the 1D BLM approach. The bold markers and error bars represent the mean error and standard deviation, respectively, based on ten statistically modeled twin microstructures. The dashed orange line indicates room temperature. (a, b) For dense microstructures, the deviation from the true conductivity decreases with the homogeneity of the grain size distribution and with temperature. Calculating the grain boundary conductivity using (a) the geometry factor $\sigma_{GB,geo}^{BLM}$ gives a worse result than using (b) the capacity ratio $\sigma_{GB,cap}^{BLM}$. Note that the simulations do not account for possible inaccuracies in the assumed permittivity ratio and in the (experimental) measurement of capacitances that would affect the calculation result in (b). (c) Pores within the microstructure lead to different quantitative deviations. The derived conductivities $\sigma_{GB,cap}^{BLM}$ tend to be too small, depending on the number and arrangement of pores in the microstructure. (d) The homogeneity of the current distribution in the microstructure increases with temperature as the ratio of bulk-to-grain boundary conductivity decreases.

visualization of the deviation is shown in Figure 7a–c (see the dashed orange line at room temperature).

For the dense statistically modeled twin microstructures, the differences between the bulk parameters (σ_{Bulk}^{BLM}, ε_{Bulk}^{BLM}) obtained from the 1D BLM analysis and the actual material parameters (σ_{Bulk}, ε_{Bulk}) are negligible. In contrast, the grain boundary conductivity $\sigma_{GB,cap}^{BLM}$ is overestimated by about 15% when using the capacitance ratio in the calculation, while $\sigma_{GB,geo}^{BLM}$ exceeds the actual grain boundary conductivity σ_{GB} by roughly 100% considering the geometric prefactor. This means that both derived BLM values $\sigma_{GB,j}^{BLM}$ are too large. Nevertheless, the actual time constants of the microscopic transport processes are almost preserved when performing the BLM analysis, i.e., $\tau_i^{BLM} = \varepsilon_i^{BLM}/\sigma_i^{BLM} \approx \tau_i$. As expected, the microstructures with a broader grain size distribution exhibit a larger deviation in grain boundary conductivity $\sigma_{GB,j}^{BLM}$ since their microstructure deviates to a greater extent from the highly symmetric microstructure assumed in the BLM. Apparently, the grain boundary conductivity $\sigma_{GB,cap}^{BLM}$ gives a much smaller deviation than $\sigma_{GB,geo}^{BLM}$. In reality, however, the deviations of $\sigma_{GB,cap}^{BLM}$ are likely to be somewhat larger since the assumption $\varepsilon_{Bulk} = \varepsilon_{GB}$ underlying eq 6 may not be perfectly satisfied in the case of LLZO due to various mechanisms leading to grain boundary resistance. In addition, measured capacitances are often susceptible to interference from external sources. The deviations of $\sigma_{GB,geo}^{BLM}$ are independent of this but depend on the estimate of average grain size and grain boundary thickness in the sample. Thus, both calculation methods are shown to provide a realistic range of uncertainty for the BLM-derived grain boundary conductivity.

To assess the range of possible deviations in the material parameters due to the 1D BLM analysis, we also examine the effect of varying temperature, which changes the conductivity ratio between bulk and grain boundary, as both processes exhibit different activation energies (cf. Table 1). To this end, the computed impedance of $N = 10$ different statistically modeled twin microstructures of each model system (i.e., sintering time) is analyzed by using the BLM approach. Figure 7a–c shows the mean deviations of the derived grain boundary conductivity $(\sum_i(\sigma_{GB,j}^{BLM,i} - \sigma_{GB})/\sigma_{GB})/N$ with j = (geo, cap) for the different sintering times as a function of temperature T. The error bars represent the standard deviation. The increase in sensitivity with sintering time (i.e., the bandwidth of possible deviations) indicates that the role of local grain arrangement is significant for inhomogeneous microstructures with bimodal grain size distributions. Interestingly, the sensitivity in the deviation of the grain boundary conductivity using the geometry factor $\sigma_{GB,geo}^{BLM}$ in the calculation is significantly larger than that using the capacitance ratio $\sigma_{GB,cap}^{BLM}$.

https://doi.org/10.1021/acsami.3c10060
ACS Appl. Mater. Interfaces 2023, 15, 47260–47277

ACS Applied Materials & Interfaces www.acsami.org Research Article

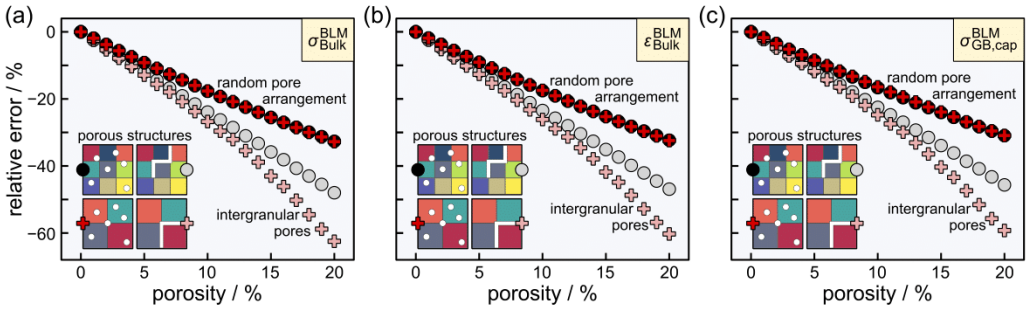

Figure 8. Quantitative estimate of the porosity-related inaccuracy in the 1D BLM analysis for (a) the bulk conductivity σ_{Bulk}^{BLM}, (b) the bulk permittivity ε_{Bulk}^{BLM}, and (c) the grain boundary conductivity $\sigma_{GB,cap}^{BLM}$. To this end, a highly symmetric BLM microstructure with grain sizes of 4 μm (black, gray) and 8 μm (red, coral) was considered, where the pores are randomly distributed (black, red) or specifically arranged between the grains (gray, coral). The pores in the microstructure are shown in white, while the grains of the same bulk material are shown in different colors.

The results in Figure 7a,b are based on dense statistically modeled twin microstructures. The deviations from the actual grain boundary conductivity σ_{GB} cover a wide range: from about 175% to about 60% for $\sigma_{GB,geo}^{BLM}$ and from 40% to almost 0% for $\sigma_{GB,cap}^{BLM}$. Here, the inaccuracy decreases with temperature. Abrantes et al. reported similar experimental observations on the grain boundary characteristics of strontium titanate ceramics.[40] This trend is due to the fact that the bulk and grain boundary conductivities become more and more similar with increasing temperature, resulting in a homogenization of the DC distribution in the microstructure, as shown in Figure 7d. As a result, differences between the actual transport behavior in the real system and that assumed in the BLM are reduced.

The presence of pores in the microstructures results in different quantitative deviations, as highlighted in Figure 7c. Nevertheless, the qualitative behavior is consistent with the analysis for dense microstructures. This shows that the effect of the pore geometry and distribution superimposes the effect of grain geometry and distribution, i.e., the deviation of the grain boundary quantities is an average of both effects. Note that the magnitude of the deviation depends on temperature, i.e., the conductivity ratio between bulk and grain boundary transport. This means that the curves in the dense case depicted in Figure 7a,b are not only shifted by a constant along the y-axis. Interestingly, the grain boundary conductivities $\sigma_{GB,cap}^{BLM}$ tend in some cases to be underestimated due to the pores (see also Figure S12 for the evolution of $\sigma_{GB,geo}^{BLM}$). Therefore, the identification of general trends regarding the inaccuracy of a 1D BLM analysis is challenging.

However, to provide a quantitative estimate of the influence of porosity on the 1D BLM analysis with only little impact on the grain structure, we consider two BLM microstructures (i.e., a highly ordered array of identical cubic grains separated by a grain boundary phase) with grain sizes of 4 and 8 μm. On this basis, two model systems are generated for each microstructure, in which 1 μm large pores are arranged in a random manner or are specifically placed between the grains (see inset in Figure 8). In a series of impedance computations, the porosity is varied between 0 and 20%. Figure 8 shows the relative deviation for (a) the bulk conductivity σ_{Bulk}^{BLM}, (b) the bulk permittivity ε_{Bulk}^{BLM}, and (c) the grain boundary conductivity $\sigma_{GB,cap}^{BLM}$ (see Figure S13 for $\sigma_{GB,geo}^{BLM}$). In all cases, the qualitative trends and almost all of the quantitative inaccuracies are the same. Pores always lead to an underestimation of the microscopic transport parameters as the BLM is only defined for a dense microstructure, i.e., charge transport takes place in a larger volume fraction of bulk material. In this highly simplified model system, deviations of up to −70% can be observed for the bulk and grain boundary transport parameters with increasing porosity. The range of the uncertainty seems reasonable in light of theoretical studies on the inaccuracies observed for mesoporous thin films.[72] The exact value of the inaccuracy, however, depends strongly on the arrangement of the pores and also on the grain sizes in the microstructure. While the relative error increases linearly for a random pore arrangement (black and red curves), there is a larger and nonlinear increase for the intergranular pore models (gray and coral curves). The latter is due to severe geometric current constriction effects in the microstructure, resulting in a high sensitivity of macroscopic resistances R_i to porosity changes. This effect is more pronounced for larger grain sizes in the microstructure (coral curve), i.e., the relative deviation is larger in this case. In contrast, the grain size does not seem to have an effect on the porosity range considered when a random pore arrangement is assumed, i.e., the curves overlap (black, red) in this case.

In addition to the BLM-derived transport quantities, the grain boundary thickness δ_{GB}^{BLM} estimated from the capacity ratio C_{Bulk}/C_{GB} and mean grain size $\overline{d}$ via eq 8 is also subject to deviations. For the computed impedance spectra considering the dense and porous statistically modeled twin microstructures (see Figure 6a), the derived values δ_{GB}^{BLM} underestimate the true grain boundary thickness δ_{GB} by about 30%, as shown in Table S2. In reality, the deviation may be even higher if the assumption about bulk and grain boundary permittivity is not met, i.e., if $\varepsilon_{Bulk} \neq \varepsilon_{GB}$. Interestingly, the inaccuracy is also a function of temperature (see Figure S14). The reason is that the redistribution of current density in nonordered microstructures with temperature results in changes of the capacitance ratio C_{Bulk}/C_{GB}, although the microstructure is not affected (i.e., the geometric prefactor $\delta_{GB}/(d + \delta_{GB})$ is constant). This effect is not captured by the simple 1D BLM due to its highly symmetric structural arrangement and the resulting homogeneous current distribution in the system (see Figure 5a).

The temperature-related changes in the current distribution through the microstructure can also affect the analysis of the temperature dependence of the individual transport processes. To derive the activation energies $E_{a,i}$ of the bulk and grain boundary transport, the BLM-derived conductivities σ_i^{BLM} are considered in the Arrhenius representation. The results listed

https://doi.org/10.1021/acsami.3c10060
ACS Appl. Mater. Interfaces 2023, 15, 47260−47277

in Table S2 show that the activation energies differ slightly from the actual quantities of $E_{a,Bulk}$ = 329 meV and $E_{a,GB}$ = 0.408 meV chosen for the computations. The deviation of the bulk value is only marginal (i.e., ≈0%), while that of the grain boundary value is up to 21 meV. This corresponds to a maximum mismatch of about 5%, which decreases with increasing homogeneity of the microstructure. Interestingly, Ohno et al. reported variations of similar magnitude for identical thiophosphate-based SE powder materials processed into samples by different methods.[66] This finding again emphasizes the importance of the microstructure of the sample for the interpretation of macroscopic measurements to derive microscopic material parameters, such as conductivities or activation energies. However, the influence of microstructural effects, such as constriction phenomena or temperature-related changes of the net of current paths, on derived activation energies is usually overlooked in the literature.

2.2.3. Estimating the Impact of Microstructure on Experimentally Determined Transport Parameters. Based on the theoretical studies, it is now possible to estimate the impact of the sintering-induced microstructural changes on the transport parameters of LLZO ceramics determined via 1D BLM analysis of experimental data (Table 1). The comparison of the conductivities obtained from samples prepared with different sintering protocols shows that σ_{Bulk}^{BLM} varies by a maximum factor of almost 2, $\sigma_{GB,geo}^{BLM}$ by a factor of about 2, and $\sigma_{GB,cap}^{BLM}$ by a factor of roughly 3 (see Table S3). The consideration of the dense statistically modeled twin microstructures in the simulations revealed systematic trends, such as an increase of the accuracy in extracting $\sigma_{GB,j}^{BLM}$ with homogenization of the microstructure. The deviation between $\sigma_{GB,j}^{BLM}$ and the true grain boundary conductivity σ_{GB} can reach up to 150% due to the grain size distribution alone (see Figure 7), while that of σ_{Bulk}^{BLM} is independent of it. It is noteworthy, however, that the accuracies observed differ by less than 20% among the individual microstructure types considered. Therefore, the increase in grain size during sintering alone does not explain the experimental differences in the bulk and grain boundary conductivities.

The computations demonstrate that the presence of pores inside the microstructure has a major influence on the derived transport quantities. The bulk permittivity and conductivity (ε_{Bulk}^{BLM}, σ_{Bulk}^{BLM}) are both underestimated, while the pore structure superimposes the effect of the grain structure in the case of grain boundary conductivity, i.e., the deviation of $\sigma_{GB,j}^{BLM}$ is an average of both effects. The quantitative influence of the porosity on the transport parameters is not easy to predict since it depends on the distribution of the pores in the microstructure (see Figure 8). This is also evident from the comparison of the experimentally determined bulk permittivities ε_{Bulk}^{BLM} observed for samples prepared with different sintering times, as shown in Table 1. Although the porosity in the ceramics is almost identical, ε_{Bulk}^{BLM} increases by about 60% when going from 2 h sintering time to 4 h. This in turn is consistent with the microstructural analysis, which revealed a major change in the pore structure at this time period with the collapse of sinter necks and the accumulation of pores within the bulk of grains (see Figure 1).

Thus, to achieve a certain degree of comparability between the experimentally derived transport parameters, the influence of the different pore structures must be eliminated. One way to account for the sinter necks in the microstructure of the sample sintered for 2 h is to normalize its transport quantities according to the bulk permittivity of the other pellets, which is approximately constant. This means multiplying the parameters by the constant factor $\varepsilon_{Bulk,4h}^{BLM}/\varepsilon_{Bulk,2h}^{BLM}$. The comparison of the modified conductivities at different sintering times shows that the maximum deviation is about 20% for σ_{Bulk}^{BLM}, about 50% for $\sigma_{GB,geo}^{BLM}$, and about 100% for $\sigma_{GB,cap}^{BLM}$ (see Table S4). As a result, the estimated differences are quite small. If we now add up all possible errors in the 1D BLM analysis results, such as inaccuracies due to the microstructure, systematic errors in the EIS experiments (e.g., manual cell assembly), errors in the ECM fitting procedure, or the determination of geometric quantities to calculate the cell constants, we end up in a similar range for the uncertainty. This means that the observed changes in experimental transport parameters are all within the error range of the 1D BLM analysis. Therefore, it is reasonable to assume that the real material-specific parameters of the LLZO ceramics do not change during sintering.

This conclusion is supported by the observed time characteristics and temperature dependence of the bulk and grain boundary processes. The analysis of the computed data shows that microstructural changes have no major effect on the intrinsic parameters describing the microscopic transport processes, i.e., no major changes in time constants and activation energies are found. This is consistent with the experimental results for the LLZO pellets with sintering times of up to 8 h. In contrast, the large changes in the time constant and activation energy of the grain boundary process for the sample sintered for 12 h cannot be explained by microstructural variations alone. In this case, some kind of material alteration, such as lithium loss from the sample or changes in the chemical composition of the grain boundaries, e.g., by segregation, cannot be ruled out.[24,29,30] A full clarification requires further detailed chemical analysis, which is beyond the scope of this work.

3. SUMMARY AND CONCLUSIONS

The study presents a comprehensive analysis of experiments and simulations to explore the effects of the microstructure on the electrochemical transport properties of garnet-type solid electrolytes. Based on machine learning-assisted microstructural analysis of LLZO ceramics synthesized with different sintering protocols, 3D transport computations through statistically modeled twin microstructures are performed to impugn the validity of the commonly used 1D brick layer model for interpreting experimental impedance data. The following recommendation for the BLM analysis of impedance data can be derived:

- The actual microstructure of the LLZO ceramic has a major impact on the accuracy of the transport parameters derived by the 1D BLM approach. This includes not only the conductivity and permittivity of bulk or grain boundary transport but also their activation energies and the estimate of the grain boundary thickness in the microstructure.
- The interplay between the grain structure and the pore structure determines the quantitative deviation between the true material-specific transport parameters of LLZO and those derived by the BLM approach. The grain structure alone can result in inaccuracies of up to 150% in the grain boundary conductivity. The effect of porosity on both bulk and grain boundary quantities can be even more severe and strongly depends on the

https://doi.org/10.1021/acsami.3c10060
ACS Appl. Mater. Interfaces 2023, 15, 47260−47277

spatial distribution of pores in the microstructure. Deviations of up to −70% have been observed for a highly simplified BLM model microstructure, but they can also be even higher for more realistic grain microstructures.

- Sintering-related changes in the microstructure alone do not change the time characteristics of electric transport processes such as bulk or grain boundary transport. This means that their apex frequency in the impedance spectrum and time constant in the DRT remain the same.

The consideration of these recommendations in the analysis of the experimental impedance data of the different LLZO ceramics indicates that the variation of the BLM-derived transport parameters is mainly due to sintering-induced microstructural changes rather than to compositional material alteration. In consequence, the study as a whole emphasizes the importance of microstructural analysis for a proper interpretation of macroscopic (impedance) measurements to derive microscopic material parameters. It provides a guide to estimate the true value range of transport quantities, helping experimentalists distinguish between microstructural effects and true changes in the material-specific properties. This will improve the understanding, modeling, and optimization of the characteristics of solid electrolytes, and it will also increase the interlaboratory compatibility of reported results.

4. EXPERIMENTAL DETAILS

4.1. Crystal Structure Characterization. The phase purity of the individual LLZO pellets was investigated using a PANalytical Empyrean powder diffractometer in Bragg−Brentano θ−θ geometry. A Cu Kα radiation X-ray source (λ_1 = 1.5405980 Å; λ_2 = 1.5444260 Å) was used and operated at 40 kV and 40 mA. Measurements were carried out in the 2θ range between 10 and 80° with a step size of 0.026° using a PIXcel3D 1 × 1 detector. For this purpose, the individual pellets were manually ground to a powder and placed on a (911)-oriented silicon zero background holder. Pawley refinement was performed by using the TOPAS-Academic V7 software package (Bruker). A specimen displacement factor has been included to account for the height error in the Bragg−Brentano geometry. The background was described by a ninth-order polynomial function, and the profile by Thompson-Cox-Hastings pseudo-Voigt functions.

4.2. Microstructural Characterization. Each LLZO pellet was split into two pieces for qualitative analysis of the microstructure. The fracture edges were investigated by using a Carl Zeiss Ultra field emission scanning electron microscopy instrument (Merlin). The air-sensitive samples were transferred from the glovebox to the vacuum chamber of the SEM instrument with a Leica transfer module system (EM VCT500). The SEM images were acquired with a 3 kV accelerating voltage and an electron current of 100 pA.

A variant of the thermal grooving technique reported by Sato et al. was used to visualize grain boundaries for the quantitative analysis of grain sizes.[42] First, rough impurities were removed from the sample surface by using coarse-grained sandpaper (320 grit SiC, Buehler, CarbiMet). The surface was then polished in a two-step process with fine-grained sandpaper (600 and 1000 grit). Next, samples were heated to 950 °C (100 °C·h^{-1}) under 500 sccm oxygen flow and kept at this temperature for 1.5 h. The surface was subsequently cleaned from the pyrochlore phase using scientific cleaning cloths, once soaked with water and once soaked with isopropanol. Afterward, some of the pores were clogged with particle abrasion from the polishing steps.

Focused ion beam scanning electron microscopy analyses were performed to study the volumetric porosity and pore size distributions at cross-sections of the pellets. To this end, an XEIA3 system (TESCAN GmbH) was used. First, the pellet surfaces were polished using fine-grained sandpaper (600 grit to 1000 grit). The samples were then attached to a Leica stub with adhesive copper tape and transferred by using the Leica EM VCT500 system (Leica Microsystems GmbH). The pellet surfaces were masked by an approximately 10 nm platinum layer and a second layer consisting of a 20 μm copper foil to reduce surface charging effects. U-trenches were cut into the pellet surfaces with a 30 keV energy Xe^+ ion beam. Subsequently, tomography data were acquired using the 3D acquisition wizard feature by alternating milling and imaging sequences. The slice thickness was set to approximately 100 nm, and the pixel size was set to 100 nm. Beam currents for coarse milling and slicing steps were set to 2 μA and 32 nA, respectively.

4.3. Cell Assembly and Electrochemical Characterization. All preparation steps were performed in a glovebox under an argon atmosphere (MBraun LabMaster, $p(H_2O)/p < 0.1$ ppm, $p(O_2)/p < 1$ ppm). To manufacture symmetrical Au|LLZO|Au cells, the surface of each LLZO sample was first polished with sandpaper (500 grit to 1000 grit). Gold electrodes with a thickness of 200 nm and a diameter of 6 mm were then prepared by thermal evaporation. The cells were contacted with nickel current collectors and sealed in pouch bags to ensure an inert atmosphere during the impedance measurements.

Symmetrical Li|LLZO|Li cells were prepared following the procedure described by Krauskopf et al.[41] The surfaces of the LLZO pellets were first polished with sandpaper (1000 grit) and manually brought into contact with the lithium electrodes. The lithium foils used, with a thickness of about ∼100 μm, were freshly prepared by flattening a small chunk of lithium in a press. The lithium electrodes with a diameter of 6 mm were punched out and attached to a copper foil (8 mm in size). Symmetric cells with two ideally reversible lithium electrodes were fabricated by isostatically pressing the clean lithium foils on the individual LLZO pellets at 380 MPa for 45 min. The cells were then sandwiched between two nickel current collectors and sealed in pouch bags.

A VMP300 potentiostat (BioLogic Sciences Instruments) in combination with EC-Lab (version 11) software was used for the electrochemical characterization. Temperature-controlled tests were carried out in a climate chamber (WKL 64, WEISS) between −40 and 60 °C. Potentiostatic electrochemical impedance spectroscopy measurements were performed in a frequency range between 7 MHz and 100 mHz, with a voltage amplitude of 10 mV.

5. COMPUTATIONAL DETAILS

5.1. Generation of Model Microstructures. The 3D model systems considered consist of a polycrystalline ceramic sandwiched between two metal electrodes. The size of the electrode area matches that of the sample surface, and an ideal physically stable contact is assumed, i.e., $A_{electrode} = A_{SE} = A_{contact}$. We consider a cubic shape of the sample ($L_x = L_y = L_z$) with a volume of (100 μm)^3 and a thickness of the grain boundaries, including the adjacent space-charge regions, of 10 nm. Three different types of statistical twin microstructures for the LLZO ceramics are modeled based on the experimentally observed grain and pore size distributions at sintering times between 2 and 8 h. Simple BLM microstructures are generated based on the mean grain size determined in the single statistical analysis of the LLZO pellets. The statistical twin microstructures are simulated using the open-source software *MicroStructPy* (version 1.5.6, Georgia Tech Research Corporation).[67,68] The application used allows, e.g., the generation of polycrystalline multiphase microstructures with certain grain geometries, grain size distributions, and phase fractions based on Voronoi tessellation. A detailed description is given in the literature by Hart et al.[67,68] We simulate ten dense and ten porous statistical twin microstructures for each sintering time. The quality of the resulting microstructures was evaluated by comparing the cumulative size distribution(s) of the input data with those of the model systems.

https://doi.org/10.1021/acsami.3c10060
ACS Appl. Mater. Interfaces 2023, 15, 47260−47277

5.2. Transport Description and Choice of Materials Parameters. The transport computations rely on a 3D electric network model. Pores within the solid electrolyte are mimicked by capacitors. Ionic transport within the solid electrolyte (i.e., transport through the bulk of grains and transport across grain boundaries) is described by different *RC*-elements. This also holds true for the charge transfer reaction at both metal electrode interfaces. Low-frequency diffusion processes at the interfaces are not considered. The local transport parameters ($R_{\mathrm{loc},i}$, $C_{\mathrm{loc},i}$) of the circuit elements are calculated by using the standard formulas for resistors and plate capacitors. A detailed description of setting up the 3D electric network model and computing an impedance spectrum is given in our previous studies.[36,50,51]

In each computation, we consider the same material parameters derived from the temperature-dependent impedance measurement of the Li|LLZO$_{4h}$|Li arrangement. Both metal electrode|SE interfaces are assumed to be ideally reversible, and transport within the metal electrode is considered to be resistance-free, i.e., $Z_{\mathrm{elec}} = Z_{\mathrm{CT}} = 0$. Bulk and grain boundary conductivity σ_i at different temperatures are calculated assuming an Arrhenius behavior, i.e., $\sigma_i(T) = \sigma_{0,i}/T \cdot \exp[-E_{\mathrm{a},i}/(k_{\mathrm{B}}\cdot T)]$, where the prefactor $\sigma_{0,i}$ reflects the conductivity at infinite temperature and $E_{\mathrm{a},i}$ is the activation energy. The electric bulk values were set to ($\sigma_{0,\mathrm{Bulk}}$ = 76 410 K·S/cm, $E_{\mathrm{a,Bulk}}$ = 329 meV), and the grain boundary quantities are described by ($\sigma_{0,\mathrm{GB}}$ = 12 258 K·S/cm, $E_{\mathrm{a,GB}}$ = 408 meV). The relative permittivities are assumed to be temperature-independent and set to $\varepsilon_{\mathrm{Bulk}} = \varepsilon_{\mathrm{GB}} = 200$. The permittivity of the pores is set to vacuum permittivity, i.e., $\varepsilon_{\mathrm{Pore}} = \varepsilon_0$.

5.3. Analysis of the Experimental Impedance Data and the Computed Impedance Series. The computed impedance spectra by the 3D electric network model and the experimental spectra are analyzed in the frequency domain by fitting them with a 1D equivalent circuit model. They are also evaluated in the time domain by performing a distribution of relaxation times analysis. Both types of analyses were performed using the commercial software RelaxIS 3 (version 3.0.20.19, rhd instruments GmbH & Co. KG).

The computed impedance spectra are almost free of any noise signals. The Kramers–Kronig test yields negligible residuals in the order of 10^{-8}.[74] Therefore, all of the data points were included in the impedance analysis. The ECM consists of two *RC*-elements connected in series, which represent bulk transport and transport across grain boundaries. In the DRT analysis, we only use a small regularization term due to the high quality of the data.[75]

The error structure in the experimental impedance spectra is somewhat more pronounced. Thus, records in the high- and low-frequency range with residuals greater than 3% in the Kramers–Kronig test were not included in the data evaluation.[74] In the ECM analysis, the LLZO ceramic is described by two *RQ*-elements connected in series, representing bulk and grain boundary transport. In the case of the reversible and blocking electrode arrangements, the interface is represented by an *RQ*-element and a *Q*-element, respectively. The DRT was calculated using exclusively the real part of the impedance as the residuals are in the range of a few 0.1% only. No additional data points were generated by interpolation, and the second derivative of the distribution function $\gamma(\tau)$ was used in the Tikhonov regularization problem.[75]

■ ASSOCIATED CONTENT

Supporting Information

The Supporting Information is available free of charge at https://pubs.acs.org/doi/10.1021/acsami.3c10060.

Description of LLZO synthesis; XRD analysis; details about microstructure analysis and image segmentation; derivation of the analytical brick layer model formulas; experimental EIS data and analysis for blocking and reversible electrode arrangement; simulated current distribution within statistically modeled digital twin structure and corresponding EIS data; overview of brick layer model analysis of simulated data; temperature dependence of the uncertainty in grain boundary conductivity and thickness; contingency tables of experimentally determined brick layer model parameters (PDF)

■ AUTHOR INFORMATION

Corresponding Authors

Janis K. Eckhardt – *Institute for Theoretical Physics, Justus Liebig University, Giessen D-35392, Germany; Institute of Physical Chemistry, Justus Liebig University, Giessen D-35392, Germany; Center for Materials Research (ZfM), Justus Liebig University, Giessen D-35392, Germany;* orcid.org/0000-0002-2799-0599; Email: janis.k.eckhardt@theo.physik.uni-giessen.de

Sascha Kremer – *Institute of Physical Chemistry, Justus Liebig University, Giessen D-35392, Germany; Center for Materials Research (ZfM), Justus Liebig University, Giessen D-35392, Germany;* orcid.org/0009-0009-3739-8749; Email: sascha.kremer@phys.chemie.uni-giessen.de

Christian Heiliger – *Institute for Theoretical Physics, Justus Liebig University, Giessen D-35392, Germany; Center for Materials Research (ZfM), Justus Liebig University, Giessen D-35392, Germany*; Email: christian.heiliger@physik.uni-giessen.de

Jürgen Janek – *Institute of Physical Chemistry, Justus Liebig University, Giessen D-35392, Germany; Center for Materials Research (ZfM), Justus Liebig University, Giessen D-35392, Germany;* orcid.org/0000-0002-9221-4756; Email: juergen.janek@phys.chemie.uni-giessen.de

Authors

Till Fuchs – *Institute of Physical Chemistry, Justus Liebig University, Giessen D-35392, Germany; Center for Materials Research (ZfM), Justus Liebig University, Giessen D-35392, Germany*

Philip Minnmann – *Institute of Physical Chemistry, Justus Liebig University, Giessen D-35392, Germany; Center for Materials Research (ZfM), Justus Liebig University, Giessen D-35392, Germany;* orcid.org/0000-0002-9646-0487

Johannes Schubert – *Institute of Physical Chemistry, Justus Liebig University, Giessen D-35392, Germany; Center for Materials Research (ZfM), Justus Liebig University, Giessen D-35392, Germany;* orcid.org/0009-0003-3148-6672

Simon Burkhardt – *Institute of Physical Chemistry, Justus Liebig University, Giessen D-35392, Germany; Center for Materials Research (ZfM), Justus Liebig University, Giessen D-35392, Germany*

Matthias T. Elm – *Institute of Physical Chemistry, Justus Liebig University, Giessen D-35392, Germany; Center for Materials Research (ZfM) and Institute of Experimental*

https://doi.org/10.1021/acsami.3c10060
ACS Appl. Mater. Interfaces 2023, 15, 47260–47277

Physics I, Justus Liebig University, Giessen D-35392, Germany; orcid.org/0000-0001-7014-5772

Peter J. Klar − *Center for Materials Research (ZfM) and Institute of Experimental Physics I, Justus Liebig University, Giessen D-35392, Germany;* orcid.org/0000-0002-4513-0330

Complete contact information is available at: https://pubs.acs.org/10.1021/acsami.3c10060

Author Contributions

[⊥]J.K.E. and S.K. contributed equally to this work.

Notes

The authors declare no competing financial interest.

■ ACKNOWLEDGMENTS

The authors thank Dr. Felix Hartmann for helpful discussions on the evaluation of the XRD data and Elisa Monte for the preparation of the graphical abstract. The authors acknowledge computational resources provided by the HPC Core Facility and the HRZ of the Justus-Liebig-University Giessen. The authors would like to thank MSc. Philipp Risius and Dr. Marcel Giar of HPC-Hessen, funded by the State Ministry of Higher Education, Research, and the Arts (HMWK), for programming advice. J.K.E. acknowledges financial support from the DFG via the GRK (Research Training Group) 2204 "Substitute Materials for Sustainable Energy Technologies". J.J., S.K., P.M., and S.B. acknowledge financial support from the German Federal Ministry of Education and Research within the cluster of competence FESTBATT (projects 03XP0177A, 03XP0180, and 03XP0428E). J.J. and T.F. acknowledge funding from the German Federal Ministry of Education and Research (BMBF) of the LiSI and LiSI2 project, grant identifiers 03XP0224E and 03XP0509B. M.T.E. acknowledges financial support from the Heisenberg Program (Grant EL 863/6-1, project number 498993886) from the German Research Foundation (DFG).

■ REFERENCES

(1) Janek, J.; Zeier, W. G. A Solid Future for Battery Development. *Nat. Energy* **2016**, *1* (9), No. 16141.

(2) Randau, S.; Weber, D. A.; Kötz, O.; Koerver, R.; Braun, P.; Weber, A.; Ivers-Tiffée, E.; Adermann, T.; Kulisch, J.; Zeier, W. G.; Richter, F. H.; Janek, J. Benchmarking the Performance of All-Solid-State Lithium Batteries. *Nat. Energy* **2020**, *5* (3), 259−270.

(3) Janek, J.; Zeier, W. G. Challenges in Speeding up Solid-State Battery Development. *Nat. Energy* **2023**, *8* (3), 230−240.

(4) Niu, C.; Lee, H.; Chen, S.; Li, Q.; Du, J.; Xu, W.; Zhang, J.-G.; Whittingham, M. S.; Xiao, J.; Liu, J. High-Energy Lithium Metal Pouch Cells with Limited Anode Swelling and Long Stable Cycles. *Nat. Energy* **2019**, *4* (7), 551−559.

(5) Chen, Y.; Wang, Z.; Li, X.; Yao, X.; Wang, C.; Li, Y.; Xue, W.; Yu, D.; Kim, S. Y.; Yang, F.; Kushima, A.; Zhang, G.; Huang, H.; Wu, N.; Mai, Y.-W.; Goodenough, J. B.; Li, J. Li Metal Deposition and Stripping in a Solid-State Battery via Coble Creep. *Nature* **2020**, *578* (7794), 251−255.

(6) Krauskopf, T.; Mogwitz, B.; Hartmann, H.; Singh, D. K.; Zeier, W. G.; Janek, J. The Fast Charge Transfer Kinetics of the Lithium Metal Anode on the Garnet-Type Solid Electrolyte $Li_{6.25}Al_{0.25}La_3Zr_2O_{12}$. *Adv. Energy Mater.* **2020**, *10* (27), No. 2000945.

(7) Krauskopf, T.; Richter, F. H.; Zeier, W. G.; Janek, J. Physicochemical Concepts of the Lithium Metal Anode in Solid-State Batteries. *Chem. Rev.* **2020**, *120* (15), 7745−7794.

(8) Naik, K. G.; Chatterjee, D.; Mukherjee, P. P. Solid Electrolyte−Cathode Interface Dictates Reaction Heterogeneity and Anode Stability. *ACS Appl. Mater. Interfaces* **2022**, *14* (40), 45308−45319.

(9) Zhu, Y.; Connell, J. G.; Tepavcevic, S.; Zapol, P.; Garcia-Mendez, R.; Taylor, N. J.; Sakamoto, J.; Ingram, B. J.; Curtiss, L. A.; Freeland, J. W.; Fong, D. D.; Markovic, N. M. Dopant-Dependent Stability of Garnet Solid Electrolyte Interfaces with Lithium Metal. *Adv. Energy Mater.* **2019**, *9* (12), No. 1803440.

(10) Ma, C.; Cheng, Y.; Yin, K.; Luo, J.; Sharafi, A.; Sakamoto, J.; Li, J.; More, K. L.; Dudney, N. J.; Chi, M. Interfacial Stability of Li Metal−Solid Electrolyte Elucidated via in Situ Electron Microscopy. *Nano Lett.* **2016**, *16* (11), 7030−7036.

(11) Nakayama, M.; Kotobuki, M.; Munakata, H.; Nogami, M.; Kanamura, K. First-Principles Density Functional Calculation of Electrochemical Stability of Fast Li Ion Conducting Garnet-Type Oxides. *Phys. Chem. Chem. Phys.* **2012**, *14* (28), 10008−10014.

(12) Wolfenstine, J.; Allen, J. L.; Sakamoto, J.; Siegel, D. J.; Choe, H. Mechanical Behavior of Li-Ion-Conducting Crystalline Oxide-Based Solid Electrolytes: A Brief Review. *Ionics* **2018**, *24* (5), 1271−1276.

(13) Fuchs, T.; Haslam, C. G.; Moy, A. C.; Lerch, C.; Krauskopf, T.; Sakamoto, J.; Richter, F. H.; Janek, J. Increasing the Pressure-Free Stripping Capacity of the Lithium Metal Anode in Solid-State-Batteries by Carbon Nanotubes. *Adv. Energy Mater.* **2022**, *12* (26), No. 2201125.

(14) Fuchs, T.; Becker, J.; Haslam, C. G.; Lerch, C.; Sakamoto, J.; Richter, F. H.; Janek, J. Current-Dependent Lithium Metal Growth Modes in "Anode-Free" Solid-State Batteries at the CulLLZO Interface. *Adv. Energy Mater.* **2022**, *13* (1), No. 2203174.

(15) Fuchs, T.; Mogwitz, B.; Otto, S.-K.; Passerini, S.; Richter, F. H.; Janek, J. Working Principle of an Ionic Liquid Interlayer During Pressureless Lithium Stripping on $Li_{6.25}Al_{0.25}La_3Zr_2O_{12}$ (LLZO) Garnet-Type Solid Electrolyte. *Batteries Supercaps* **2021**, *4* (7), 1145−1155.

(16) Krauskopf, T.; Mogwitz, B.; Rosenbach, C.; Zeier, W. G.; Janek, J. Diffusion Limitation of Lithium Metal and Li−Mg Alloy Anodes on LLZO Type Solid Electrolytes as a Function of Temperature and Pressure. *Adv. Energy Mater.* **2019**, *9* (44), No. 1902568.

(17) Hitz, G. T.; McOwen, D. W.; Zhang, L.; Ma, Z.; Fu, Z.; Wen, Y.; Gong, Y.; Dai, J.; Hamann, T. R.; Hu, L.; Wachsman, E. D. High-Rate Lithium Cycling in a Scalable Trilayer Li-Garnet-Electrolyte Architecture. *Mater. Today* **2019**, *22*, 50−57.

(18) Wang, M. J.; Carmona, E.; Gupta, A.; Albertus, P.; Sakamoto, J. Enabling "Lithium-Free" Manufacturing of Pure Lithium Metal Solid-State Batteries through in Situ Plating. *Nat. Commun.* **2020**, *11* (1), No. 5201.

(19) Haslam, C.; Sakamoto, J. Stable Lithium Plating in "Lithium Metal-Free" Solid-State Batteries Enabled by Seeded Lithium Nucleation. *J. Electrochem. Soc.* **2023**, *170* (4), No. 040524.

(20) Reisecker, V.; Flatscher, F.; Porz, L.; Fincher, C.; Todt, J.; Hanghofer, I.; Hennige, V.; Linares-Moreau, M.; Falcaro, P.; Ganschow, S.; Wenner, S.; Chiang, Y. M.; Keckes, J.; Fleig, J.; Rettenwander, D. Effect of Pulse-Current-Based Protocols on the Lithium Dendrite Formation and Evolution in All-Solid-State Batteries. *Nat. Commun.* **2023**, *14* (1), No. 2432.

(21) Tsai, C.-L.; Roddatis, V.; Chandran, C. V.; Ma, Q.; Uhlenbruck, S.; Bram, M.; Heitjans, P.; Guillon, O. $Li_7La_3Zr_2O_{12}$ Interface Modification for Li Dendrite Prevention. *ACS Appl. Mater. Interfaces* **2016**, *8* (16), 10617−10626.

(22) Mahbub, R.; Huang, K.; Jensen, Z.; Hood, Z. D.; Rupp, J. L. M.; Olivetti, E. A. Text Mining for Processing Conditions of Solid-State Battery Electrolytes. *Electrochem. Commun.* **2020**, *121*, No. 106860.

(23) Zeng, X.; Martinolich, A. J.; See, K. A.; Faber, K. T. Dense Garnet-Type Electrolyte with Coarse Grains for Improved Air Stability and Ionic Conductivity. *J. Energy Storage* **2020**, *27*, No. 101128.

(24) Moy, A. C.; Häuschen, G.; Fattakhova-Rohlfing, D.; Wolfenstine, J. B.; Finsterbusch, M.; Sakamoto, J. The Effects of Aluminum Concentration on the Microstructural and Electrochemical

Properties of Lithium Lanthanum Zirconium Oxide. *J. Mater. Chem. A* **2022**, *10* (41), 21955−21972.
(25) Yang, L.; Dai, Q.; Liu, L.; Shao, D.; Luo, K.; Jamil, S.; Liu, H.; Luo, Z.; Chang, B.; Wang, X. Rapid Sintering Method for Highly Conductive $Li_7La_3Zr_2O_{12}$ Ceramic Electrolyte. *Ceram. Int.* **2020**, *46* (8, Part A), 10917−10924.
(26) Huang, X.; Xiu, T.; Badding, M. E.; Wen, Z. Two-Step Sintering Strategy to Prepare Dense Li-Garnet Electrolyte Ceramics with High Li^+ Conductivity. *Ceram. Int.* **2018**, *44* (5), 5660−5667.
(27) Ji, Y.; Zhou, C.; Lin, F.; Li, B.; Yang, F.; Zhu, H.; Duan, J.; Chen, Z. Submicron-Sized Nb-Doped Lithium Garnet for High Ionic Conductivity Solid Electrolyte and Performance of Quasi-Solid-State Lithium Battery. *Materials* **2020**, *13* (3), 560.
(28) Sharafi, A.; Haslam, C. G.; Kerns, R. D.; Wolfenstine, J.; Sakamoto, J. Controlling and Correlating the Effect of Grain Size with the Mechanical and Electrochemical Properties of $Li_7La_3Zr_2O_{12}$ Solid-State Electrolyte. *J. Mater. Chem. A* **2017**, *5* (40), 21491−21504.
(29) Paolella, A.; Zhu, W.; Bertoni, G.; Savoie, S.; Feng, Z.; Demers, H.; Gariepy, V.; Girard, G.; Rivard, E.; Delaporte, N.; Guerfi, A.; Lorrmann, H.; George, C.; Zaghib, K. Discovering the Influence of Lithium Loss on Garnet $Li_7La_3Zr_2O_{12}$ Electrolyte Phase Stability. *ACS Appl. Energy Mater.* **2020**, *3* (4), 3415−3424.
(30) Hu, X.; Chen, S.; Wang, Z.; Chen, Y.; Yuan, B.; Zhang, Y.; Liu, W.; Yu, Y. Microstructure of the Li−Al−O Second Phases in Garnet Solid Electrolytes. *Nano Lett.* **2023**, *23* (3), 887−894.
(31) Letz, S. A.; Zhao, D.; März, M. Mesostructural Impact on the Macroscopic Stress State and Yield Locus of Porous Polycrystalline Silver. *Mater. Des.* **2022**, *219*, No. 110785.
(32) Irvine, J. T. S.; Sinclair, D. C.; West, A. R. Electroceramics: Characterization by Impedance Spectroscopy. *Adv. Mater.* **1990**, *2* (3), 132−138.
(33) Beekmans, N. M.; Heyne, L. Correlation between Impedance, Microstructure and Composition of Calcia-Stabilized Zirconia. *Electrochim. Acta* **1976**, *21* (4), 303−310.
(34) van Dijk, T.; Burggraaf, A. J. Grain Boundary Effects on Ionic Conductivity in Ceramic $Gd_xZr_{1-x}O_{2-(x/2)}$ Solid Solutions. *Phys. Status Solidi A* **1981**, *63* (1), 229−240.
(35) Verkerk, M. J.; Middelhuis, B. J.; Burggraaf, A. J. Effect of Grain Boundaries on the Conductivity of High-Purity ZrO_2−Y_2O_3 Ceramics. *Solid State Ionics* **1982**, *6* (2), 159−170.
(36) Eckhardt, J. K.; Burkhardt, S.; Zahnow, J.; Elm, M. T.; Janek, J.; Klar, P. J.; Heiliger, C. Understanding the Impact of Microstructure on Charge Transport in Polycrystalline Materials Through Impedance Modelling. *J. Electrochem. Soc.* **2021**, *168* (9), 090516−090528.
(37) Fleig, J. The Influence of Non-Ideal Microstructures on the Analysis of Grain Boundary Impedances. *Solid State Ionics* **2000**, *131* (1), 117−127.
(38) Fleig, J. Impedance Spectroscopy on Solids: The Limits of Serial Equivalent Circuit Models. *J. Electroceram.* **2004**, *13* (1), 637−644.
(39) Mariappan, C. R.; Yada, C.; Rosciano, F.; Roling, B. Correlation between Micro-Structural Properties and Ionic Conductivity of $Li_{1.5}Al_{0.5}Ge_{1.5}(PO_4)_3$ Ceramics. *J. Power Sources* **2011**, *196* (15), 6456−6464.
(40) Abrantes, J. C. C.; Labrincha, J. A.; Frade, J. R. Applicability of the Brick Layer Model to Describe the Grain Boundary Properties of Strontium Titanate Ceramics. *J. Eur. Ceram. Soc.* **2000**, *20* (10), 1603−1609.
(41) Krauskopf, T.; Hartmann, H.; Zeier, W. G.; Janek, J. Toward a Fundamental Understanding of the Lithium Metal Anode in Solid-State Batteries—An Electrochemo-Mechanical Study on the Garnet-Type Solid Electrolyte $Li_{6.25}Al_{0.25}La_3Zr_2O_{12}$. *ACS Appl. Mater. Interfaces* **2019**, *11* (15), 14463−14477.
(42) Sato, M.; Garcia-Mendez, R.; Sakamoto, J. Mapping Hot-Pressed $Li_{6.25}Al_{0.25}La_3Zr_2O_{12}$ (LLZO) Grains and Grain Boundaries through a Simple Thermal Grooving Technique. *J. Asian Ceram. Soc.* **2020**, *8* (3), 793−803.
(43) Kim, H.-S.; Park, J.-W. Computational Study on the Microstructural Evolution and the Change of Electrical Resistivity of Sintered Materials. *J. Electron. Mater.* **2009**, *38* (3), 475−481.
(44) Raeisinia, B.; Sinclair, C. W.; Poole, W. J.; Tomé, C. N. On the Impact of Grain Size Distribution on the Plastic Behaviour of Polycrystalline Metals. *Modell. Simul. Mater. Sci. Eng.* **2008**, *16* (2), No. 025001.
(45) Takaki, S. Review on the Hall-Petch Relation in Ferritic Steel. *Mater. Sci. Forum* **2010**, *654*−*656*, 11−16.
(46) Kang, S.-J. L. *Sintering: Densification, Grain Growth and Microstructure*; Elsevier, 2004; pp 1−280.
(47) Dixit, M. B.; Regala, M.; Shen, F.; Xiao, X.; Hatzell, K. B. Tortuosity Effects in Garnet-Type $Li_7La_3Zr_2O_{12}$ Solid Electrolytes. *ACS Appl. Mater. Interfaces* **2019**, *11* (2), 2022−2030.
(48) Dussart, T.; Rividi, N.; Fialin, M.; Toussaint, G.; Stevens, P.; Laberty-Robert, C. Critical Current Density Limitation of LLZO Solid Electrolyte: Microstructure vs Interface. *J. Electrochem. Soc.* **2021**, *168* (12), No. 120550.
(49) Huang, X.; Lu, Y.; Song, Z.; Xiu, T.; Badding, M. E.; Wen, Z. Preparation of Dense Ta-LLZO/MgO Composite Li-Ion Solid Electrolyte: Sintering, Microstructure, Performance and the Role of MgO. *J. Energy Chem.* **2019**, *39*, 8−16.
(50) Eckhardt, J. K.; Klar, P. J.; Janek, J.; Heiliger, C. Interplay of Dynamic Constriction and Interface Morphology between Reversible Metal Anode and Solid Electrolyte in Solid State Batteries. *ACS Appl. Mater. Interfaces* **2022**, *14* (31), 35545−35554.
(51) Eckhardt, J. K.; Fuchs, T.; Burkhardt, S.; Klar, P. J.; Janek, J.; Heiliger, C. 3D Impedance Modeling of Metal Anodes in Solid-State Batteries−Incompatibility of Pore Formation and Constriction Effect in Physical-Based 1D Circuit Models. *ACS Appl. Mater. Interfaces* **2022**, *14* (37), 42757−42769.
(52) Fleig, J.; Maier, J. Finite Element Calculations of Impedance Effects at Point Contacts. *Electrochim. Acta* **1996**, *41* (7), 1003−1009.
(53) Fleig, J.; Maier, J. The Influence of Laterally Inhomogeneous Contacts on the Impedance of Solid Materials: A Three-Dimensional Finite-Element Study. *J. Electroceram.* **1997**, *1* (1), 73−89.
(54) Brug, G. J.; van den Eeden, A. L. G.; Sluyters-Rehbach, M.; Sluyters, J. H. The Analysis of Electrode Impedances Complicated by the Presence of a Constant Phase Element. *J. Electroanal. Chem. Interfacial Electrochem.* **1984**, *176* (1), 275−295.
(55) Guo, X.; Maier, J. Grain Boundary Blocking Effect in Zirconia: A Schottky Barrier Analysis. *J. Electrochem. Soc.* **2001**, *148* (3), No. E121.
(56) Rodewald, S.; Fleig, J.; Maier, J. Microcontact Impedance Spectroscopy at Single Grain Boundaries in Fe-Doped $SrTiO_3$ Polycrystals. *J. Am. Ceram. Soc.* **2001**, *84* (3), 521−530.
(57) Guo, X.; Waser, R. Electrical Properties of the Grain Boundaries of Oxygen Ion Conductors: Acceptor-Doped Zirconia and Ceria. *Prog. Mater. Sci.* **2006**, *51* (2), 151−210.
(58) Cojocaru-Mirédin, O.; Schmieg, J.; Müller, M.; Weber, A.; Ivers-Tiffée, E.; Gerthsen, D. Quantifying Lithium Enrichment at Grain Boundaries in $Li_7La_3Zr_2O_{12}$ Solid Electrolyte by Correlative Microscopy. *J. Power Sources* **2022**, *539*, No. 231417.
(59) Tenhaeff, W. E.; Rangasamy, E.; Wang, Y.; Sokolov, A. P.; Wolfenstine, J.; Sakamoto, J.; Dudney, N. J. Resolving the Grain Boundary and Lattice Impedance of Hot-Pressed $Li_7La_3Zr_2O_{12}$ Garnet Electrolytes. *ChemElectroChem* **2014**, *1* (2), 375−378.
(60) Rettenwander, D.; Welzl, A.; Cheng, L.; Fleig, J.; Musso, M.; Suard, E.; Doeff, M. M.; Redhammer, G. J.; Amthauer, G. Synthesis, Crystal Chemistry, and Electrochemical Properties of $Li_{7-2x}La_3Zr_{2-x}Mo_xO_{12}$ (x = 0.1−0.4): Stabilization of the Cubic Garnet Polymorph via Substitution of Zr^{4+} by Mo^{6+}. *Inorg. Chem.* **2015**, *54* (21), 10440−10449.
(61) Wu, J.-F.; Guo, X. Origin of the Low Grain Boundary Conductivity in Lithium Ion Conducting Perovskites: $Li_{3x}La_{0.67-x}TiO_3$. *Phys. Chem. Chem. Phys.* **2017**, *19* (8), 5880−5887.
(62) Heo, T. W.; Grieder, A.; Wang, B.; Wood, M.; Hsu, T.; Akhade, S. A.; Wan, L. F.; Chen, L.-Q.; Adelstein, N.; Wood, B. C. Microstructural Impacts on Ionic Conductivity of Oxide Solid

https://doi.org/10.1021/acsami.3c10060
ACS Appl. Mater. Interfaces 2023, 15, 47260−47277

Electrolytes from a Combined Atomistic-Mesoscale Approach. *npj Comput. Mater.* **2021**, *7* (1), No. 214.
(63) Murugan, R.; Thangadurai, V.; Weppner, W. Fast Lithium Ion Conduction in Garnet-Type $Li_7La_3Zr_2O_{12}$. *Angew. Chem., Int. Ed.* **2007**, *46* (41), 7778−7781.
(64) Buschmann, H.; Dölle, J.; Berendts, S.; Kuhn, A.; Bottke, P.; Wilkening, M.; Heitjans, P.; Senyshyn, A.; Ehrenberg, H.; Lotnyk, A.; Duppel, V.; Kienle, L.; Janek, J. Structure and Dynamics of the Fast Lithium Ion Conductor "$Li_7La_3Zr_2O_{12}$". *Phys. Chem. Chem. Phys.* **2011**, *13* (43), 19378−19392.
(65) Krasnikova, I. V.; Pogosova, M. A.; Sanin, A. O.; Stevenson, K. J. Toward Standardization of Electrochemical Impedance Spectroscopy Studies of Li-Ion Conductive Ceramics. *Chem. Mater.* **2020**, *32* (6), 2232−2241.
(66) Ohno, S.; Bernges, T.; Buchheim, J.; Duchardt, M.; Hatz, A.-K.; Kraft, M. A.; Kwak, H.; Santhosha, A. L.; Liu, Z.; Minafra, N.; Tsuji, F.; Sakuda, A.; Schlem, R.; Xiong, S.; Zhang, Z.; Adelhelm, P.; Chen, H.; Hayashi, A.; Jung, Y. S.; Lotsch, B. V.; Roling, B.; Vargas-Barbosa, N. M.; Zeier, W. G. How Certain Are the Reported Ionic Conductivities of Thiophosphate-Based Solid Electrolytes? An Interlaboratory Study. *ACS Energy Lett.* **2020**, *5* (3), 910−915.
(67) Hart, K. A.; Rimoli, J. J. Generation of Statistically Representative Microstructures with Direct Grain Geometry Control. *Comput. Methods Appl. Mech. Eng.* **2020**, *370*, No. 113242.
(68) Hart, K. A.; Rimoli, J. J. MicroStructPy: A Statistical Microstructure Mesh Generator in Python. *SoftwareX* **2020**, *12*, No. 100595.
(69) Saltikov, S. A. The Determination of the Size Distribution of Particles in an Opaque Material from a Measurement of the Size Distribution of Their Sections. In *Stereology*; Springer, 1967; pp 163−173.
(70) Lopez-Sanchez, M. A.; Llana-Fúnez, S. An Evaluation of Different Measures of Dynamically Recrystallized Grain Size for Paleopiezometry or Paleowattometry Studies. *Solid Earth* **2015**, *6* (2), 475−495.
(71) Barai, P.; Fuchs, T.; Trevisanello, E.; Kim, H. K.; Richter, F. H.; Janek, J.; Srinivasan, V. Reaction Current Heterogeneity at the Interface between a Lithium Electrode and Polymer/Ceramic Composite Electrolytes. *ACS Appl. Energy Mater.* **2023**, *6* (4), 2160−2177.
(72) Eckhardt, J. K.; Heiliger, C.; Elm, M. T. Understanding the Impedance of Mesoporous Oxides: Reliable Determination of the Material-Specific Conductivity. *ACS Appl. Mater. Interfaces* **2023**, *15* (29), 35332−35341.
(73) Eckhardt, J. K.; Fuchs, T.; Burkhardt, S.; Klar, P. J.; Janek, J.; Heiliger, C. Guidelines for Impedance Analysis of Parent Metal Anodes in Solid-State Batteries and the Role of Current Constriction at Interface Voids, Heterogeneities, and SEI. *Adv. Mater. Interfaces* **2023**, *10* (8), 2202354−2202373.
(74) Boukamp, B. Electrochemical Impedance Spectroscopy in Solid State Ionics: Recent Advances. *Solid State Ionics* **2004**, *169* (1−4), 65−73.
(75) Wan, T. H.; Saccoccio, M.; Chen, C.; Ciucci, F. Influence of the Discretization Methods on the Distribution of Relaxation Times Deconvolution: Implementing Radial Basis Functions with DRTtools. *Electrochim. Acta* **2015**, *184*, 483−499.

https://doi.org/10.1021/acsami.3c10060
ACS Appl. Mater. Interfaces 2023, 15, 47260−47277

2.3 Reliable Determination of the Material-Specific Conductivity of Mesoporous Oxides

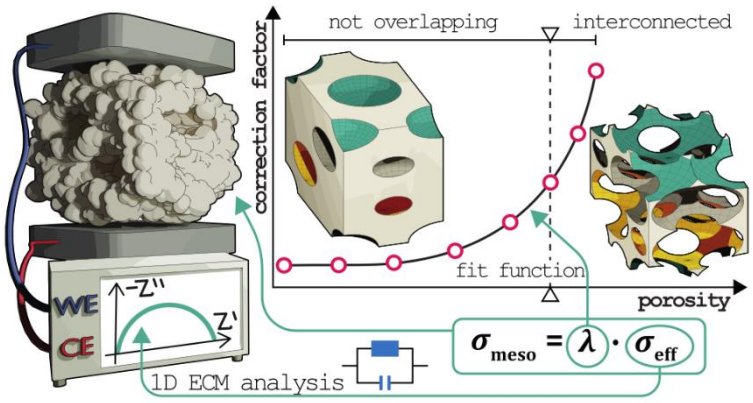

Abstract

The unique architecture of ordered mesoporous oxides makes them a promising class of materials for various electrochemical applications such as gas sensing or energy storage and conversion. The high accessibility of the internal surface allows tailoring their electrochemical properties, e.g., by adjusting the pore size or surface functionalization, resulting in superior device performance compared to nanoparticles or disordered mesoporous counterparts. However, optimization of the mesoporous architecture requires a reliable electrochemical characterization of the system. Unfortunately, the interplay between nanocrystalline grains, grain boundaries, and the open pore framework hinders a simple estimation of material-specific transport quantities using impedance spectroscopy. Here, we use a 3D electric network model to elucidate the impact of the pore structure on the electrical transport properties of mesoporous thin films. It is demonstrated that the impedance response is only dominated by the geometric current constriction effect arising from the regular pore network. Estimating the effective conductivity from the total resistance and the electrode geometry, thus, differs by more than one order of magnitude from the material-specific conductivity of the solid mesoporous framework. A detailed analysis of computed impedances for varying pore size allows the correlation of the effective conductivity with the material-specific conductivity. We derive an empirical expression, which accounts for the porous structure of the thin films and allows a reliable determination of the material-specific conductivity with an error of less than 8%.

Reference

Understanding the Impedance of Mesoporous Oxides – Reliable Determination of the Material-Specific Conductivity. Janis K. Eckhardt, Christian Heiliger, and Matthias T. Elm *ACS Appl. Mater. Interfaces* **2023**, 15, 29, 35332-35341. (DOI: 10.1021/acsami.3c05561)

Reproduced with permission

ACS APPLIED MATERIALS & INTERFACES

www.acsami.org Research Article

Understanding the Impedance of Mesoporous Oxides: Reliable Determination of the Material-Specific Conductivity

Janis K. Eckhardt,* Christian Heiliger, and Matthias T. Elm*

Cite This: ACS Appl. Mater. Interfaces 2023, 15, 35332−35341 Read Online

ACCESS | Metrics & More | Article Recommendations | Supporting Information

ABSTRACT: The unique architecture of ordered mesoporous oxides makes them a promising class of materials for various electrochemical applications, such as gas sensing or energy storage and conversion. The high accessibility of the internal surface allows tailoring of their electrochemical properties, e.g., by adjusting the pore size or surface functionalization, resulting in superior device performance compared to nanoparticles or disordered mesoporous counterparts. However, optimization of the mesoporous architecture requires reliable electrochemical characterization of the system. Unfortunately, the interplay between nanocrystalline grains, grain boundaries, and the open pore framework hinders a simple estimation of material-specific transport quantities by using impedance spectroscopy. Here, we use a 3D electric network model to elucidate the impact of the pore structure on the electrical transport properties of mesoporous thin films. It is demonstrated that the impedance response is dominated only by the geometric current constriction effect arising from the regular pore network. Estimating the effective conductivity from the total resistance and the electrode geometry, thus, differs by more than 1 order of magnitude from the material-specific conductivity of the solid mesoporous framework. A detailed analysis of computed impedances for varying pore size allows for the correlation of the effective conductivity with the material-specific conductivity. We derive an empirical expression that accounts for the porous structure of the thin films and allows a reliable determination of the material-specific conductivity with an error of less than 8%.

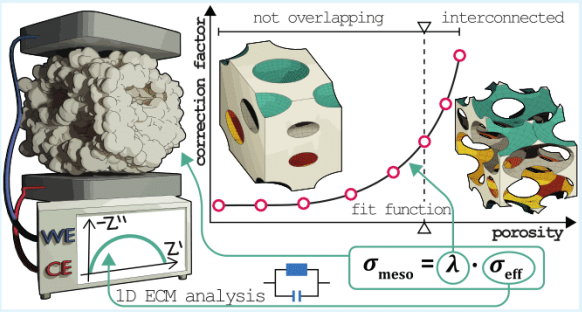

KEYWORDS: *mesoporous oxides, impedance modeling, current constriction, network model, electrical conductivity, electrochemical applications*

INTRODUCTION

Ordered mesoporous oxides are a highly interesting class of nanostructured materials due to their regular pore structures with pore sizes ranging between 2 and 50 nm.[1] Tremendous progress has been made in the development of different synthesis methods since the discovery of mesoporous silicas in the 1990s,[2−4] which nowadays allows the preparation of a large variety of different kinds of ordered mesoporous materials, including carbon,[5,6] metal oxides,[7−9] and non-oxide materials.[10,11] The preparation of mesoporous ceramic oxide thin films typically relies on a solution-phase co-assembly of inorganic precursors with an amphiphilic diblock copolymer using an evaporation-induced self-assembly (EISA) process followed by some post-annealing.[9,12−16] The diblock copolymer acts as a structure-directing agent and allows, at least to some extent, the variation of the pore symmetry and the pore size of the thin films.

The nanopores are surrounded by solid walls, which consist of single crystallites, forming a highly interconnected network. The regular pore arrangement together with the solid framework offers some distinct advantages compared to other oxide nanostructures, such as nanoparticles or mesoporous oxides with random or disordered pore structure. The open pore network guarantees the accessibility of the surrounding medium, i.e., gases or liquids can penetrate into the pores. This offers a large number of active surfaces sites. In addition, the interconnected crystallites provide continuous pathways for the transport of electrons and/or ions in the solid. This unique architecture makes ordered mesoporous oxides a valuable material class for a variety of applications,[14,17,18] such as gas sensing,[19,20] energy storage,[21−25] catalysis,[26,27] or photovoltaics,[28] with superior device performance.[29−31] In addition, the high accessibility of the surface allows the modification of the inner surface using atomic layer deposition.[32,33] This enables tailoring the properties at least

Received: April 18, 2023
Accepted: July 4, 2023
Published: July 13, 2023

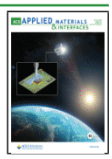

https://doi.org/10.1021/acsami.3c05561
ACS Appl. Mater. Interfaces 2023, 15, 35332−35341

ACS Applied Materials & Interfaces www.acsami.org Research Article

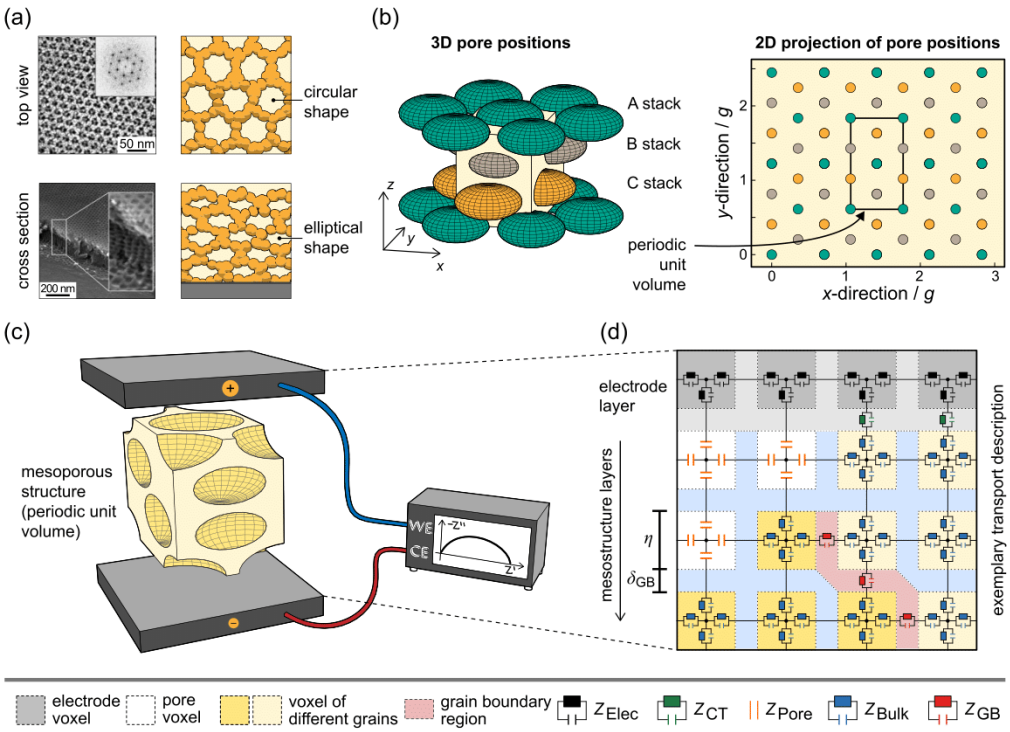

Figure 1. Overview of the mesoporous structures considered and the definition of the 3D electric network model used for the transport computations. (a) Surfactant-templating methods and evaporation-induced self-assembly processes enable the preparation of highly ordered open pore-solid architectures. The FESEM images are adapted with permission from ref 52. (b) The highly ordered mesoporous structures exhibit a fcc pore symmetry with ABC stacking order of the different layers. The 2D projection of the pore positions enables the identification of a periodic unit volume (black rectangle), sufficient for transport modeling. (c) The voltage is applied between the two homogeneous electrodes enclosing a periodic unit volume of the mesoporous structure. (d) Electric migration processes are described by different *RC*-elements, while pores are considered as capacitors. Credit: Elisa Monte/JLU Giessen.

to some extent, including the adjustment of the pore size,[34,35] functionalization of the surface,[36] or the improvement of the thermal stability of the mesoporous material.[37,38] The deposition of a thin coating has also a significant effect on the electrochemical properties.[39−41]

Most electrochemical applications rely on efficient transport of the charge carriers inside the solid framework. Thus, the characterization of the impact of the regular pore structure on the electrical properties is of great importance. In particular, the high number of interfaces, i.e., the grain boundaries between the single nanocrystallites as well as the surface area, can have a pronounced effect and may even dominate the overall behavior.[39,42,43] Electrochemical impedance spectroscopy is one of the most common methods to characterize charge transport in oxide ceramics.[44,45] It allows distinguishing between electric migration processes with different relaxation times, such as transport through single grains and across grain boundaries. Both processes appear as two separate semicircles in the Nyquist representation of the impedance, at least for microcrystalline samples.[44] In contrast, the impedance of the mesoporous thin films shows only one semicircle in the Nyquist diagram. This is typically justified with the size of the nanocrystallites, as a merging of the two semicircles has been reported when decreasing the grain size to the nanometer range.[46,47] Therefore, the interplay between grains, grain boundaries, and pore structure hinders a straightforward calculation of material-specific transport parameters, such as the bulk or grain boundary conductivity from the measured impedance. Mostly, only an effective conductivity of the mesoporous thin films is estimated simply by neglecting the porosity, i.e., a dense thin film is assumed.[48−50] The exclusive consideration of the electrode geometry, however, significantly underestimates the material-specific conductivity of the solid framework.

Apparently, only a detailed understanding of the impact of porosity, pore size, and grain boundary density on the electrochemical transport properties of ordered mesoporous oxides will enable the optimization of their structural properties for device applications. Therefore, a reliable determination of the material-specific conductivity of mesoporous oxides is desirable. In this work, we compute the impedance of ordered mesoporous thin films using a 3D electric network model.[51] Our simulated impedance spectra show only one semicircle in the Nyquist diagram, in agreement with experimental results. Evaluation of the impedance in the time domain by performing a distribution of relaxation times (DRT) analysis reveals that the geometric current constriction effect due to the porous structure dominates the impedance of mesoporous thin films. The individual DRT shows no signals corresponding to the transport through the grains and across the grain boundaries, i.e., our results demonstrate that it is not possible to separate these two transport processes using experimental impedance data. In addition, we compute the impedance of a series of mesoporous thin films whose pore size is systematically varied. From our results, a material-independent geometric correction factor can be derived,

https://doi.org/10.1021/acsami.3c05561
ACS Appl. Mater. Interfaces 2023, 15, 35332−35341

which allows the estimation of the material-specific conductivity of the mesoporous solid framework from the measured thin film impedance with an error of less than 8%.

COMPUTATIONAL DETAILS

Description of the Model Structures. Figure 1a shows typical field emission scanning electron microscopy (FESEM) images of mesoporous oxide thin films,[52] whose impedance is simulated in this work. The structures exhibit an ordered network of mesopores, which are surrounded by nanocrystalline walls with grain sizes of less than 20 nm. The top view FESEM image of the mesoporous thin films in Figure 1a confirms that the mesopores are uniform in size and shape. It indicates that the nanoscale structure persists throughout the bulk. Thereby, the grains and pores each form an interconnected network. Unidirectional lattice contraction during thermal treatment, however, leads to an anisotropic pore shape, i.e., the pores have an oblate instead of spherical shape.[53,54]

Various experimental methods such as scanning electron microscopy (SEM), grazing incidence small-angle X-ray scattering (GISAXS), and X-ray diffraction (XRD) confirm long-range periodicity of the pores with large recurrence intervals. More specifically, the mesopores form a face-centered cubic (fcc) structure with (111) orientation relative to the plane of the substrate.[55,56] Figure 1b shows the ABC stacking of the pores in a 3D representation and a 2D projection diagram. The different colors correspond to the individual stacks. For transport considerations, it is sufficient to focus on a single periodic unit volume, which builds the complete thin film through translational symmetry. A suitable candidate of this unit volume is represented by the black rectangle in the 2D projection diagram in Figure 1b. The pore positions within the periodic unit volume are given in the Supporting Information. A lattice contraction χ of 70% in the z-direction is considered to account for the oblate shape of the pores. Typically, the transport properties of mesoporous thin films are measured in in-plane geometry, i.e., perpendicular to the z-direction.[48−50] For the simulations, however, we consider all possible transport directions, i.e., the x-, y-, and z-direction. This means the voltage is applied between two homogeneous electrodes enclosing a single periodic unit volume, as shown exemplarily in Figure 1c for the z-direction. Here, the selected periodic unit volume exhibits the dimension $(1/\sqrt{2},\ \sqrt{3/2},\ 3(1-\chi)/\sqrt{3})\cdot g$, where $g = d\sqrt{2}$ is the lattice constant and d being the shortest distance between the centers of two pores.

In this study, we investigate two model systems of different size. These refer to pore distances of d_1 = 15 nm and d_2 = 20 nm. The structural resolution is identical in each model system. The grain structure of the mesoporous thin films is approximated by a Voronoi algorithm. The positions of the seeds for nanocrystallite growth are given in Figure S1. The regions, where two neighboring seeds start to overlap, define the position of the grain boundaries (GB) as shown in Figure S2. The uniform thickness of a grain boundary δ_{GB} including the adjacent space-charge region is assumed to be δ_{GB} = 2 nm, which is a typical value for the grain boundary thickness in ceramic oxides.[57,58] Throughout a computational series, we increase the radius r of the pores in the periodic unit volume starting from 0 nm until the grain network collapses. Simultaneously, we compute the resulting impedance response of each model system using a 3D electric network model.

Description of the 3D Impedance Network and Choice of Material Parameters. The impedance computations base on a 3D electric network, which we recently developed in order describe the impact of the microstructure on the impedance of ceramic oxides.[51] For the transport modeling of the mesoporous thin films, the structure is first divided into individual voxels with an edge length η. These are subsequently assigned to either a grain (yellow), a pore (white), or one of the two electrodes (gray). The transport between various voxels is then described by local equivalent circuit models, as shown in Figure 1d. Electric migration processes are considered by different RC-elements, i.e., a resistor R connected in parallel to a capacitor C. The different RC-elements include bulk transport through grains, transport across grain boundaries, and charge transfer at the electrode interfaces. Pores, in contrast, are solely represented by a capacitor C_{Pore}.

The individual transport processes in the electric network are distinguished by comparing the structural properties of adjacent voxels. Bulk transport within the mesoporous structure (blue, $2\cdot Z_{Bulk}$) or within the electrode (black, $2\cdot Z_{Elec}$) is described by two RC-elements connected in series. If the adjacent voxels are separated by a grain boundary, then the transport is modeled by adding an additional RC-element (red, $2\cdot Z_{Bulk} + Z_{GB}$) to the bulk description. Similarly, electric charge transfer across the electrode interface is considered by adding a third RC-element in series representing the charge transfer resistance and double-layer capacitance (green, $Z_{Elec} + Z_{CT} + Z_{Bulk}$). In contrast, pore transport is described by two capacitors in series (orange, $2\cdot Z_{Pore}$), or if the voxel adjacent to a pore represents the electrode or bulk material, transport is described by a serial connection of the capacitor representing the pore and the corresponding RC-element ($Z_{Elec} + Z_{Pore}$, or $Z_{Bulk} + Z_{Pore}$). Further details about setting up the 3D electric network and computing an impedance spectrum are given in our previous work.[51]

The local parameters $(\tilde{R}_i,\ \tilde{C}_i)$ of the individual circuit elements within the 3D electric network are based on conductivities σ_i, permittivities ε_i, and the structural resolution of the system. They are calculated according to the well-known rules for conductors and plate capacitors:

$$\tilde{R}_i = \frac{1}{\sigma_i}\cdot\frac{L_i}{A} \tag{1}$$

$$\tilde{C}_i = \varepsilon_i\cdot\frac{A}{L_i} \tag{2}$$

Here, $A = \eta^2$ denotes the interface area between two voxels, while L_i corresponds to the distance of the underlying transport process, i.e., $L_{Bulk} = \eta/2$ and $L_{GB} = \delta_{GB}$. The parameter ratios assumed in the computations for conductivity $\sigma_{Bulk} = 500\cdot\sigma_{GB}$ and for permittivity $\varepsilon_{Bulk} = \varepsilon_{GB}$ are in a typical range for oxides such as yttria-stabilized zirconia (YSZ), titania, or ceria.[57,59] The permittivity of the pore is set to the vacuum permittivity $\varepsilon_{Pore} = \varepsilon_0$, unless something else is stated explicitly. The transport within the electrodes and the electric charge transfer reaction at the electrode interfaces are assumed to be resistance-free ($Z_{Elec} = Z_{CT} = 0$). Therefore, dielectric pore transport and bulk and grain boundary transport are the only transport processes considered in this study.

Analysis of the Experimental Impedance Data and the Computed Impedance Series. The computed impedance spectra are analyzed in the frequency domain by

https://doi.org/10.1021/acsami.3c05561
ACS Appl. Mater. Interfaces 2023, 15, 35332−35341

ACS Applied Materials & Interfaces www.acsami.org Research Article

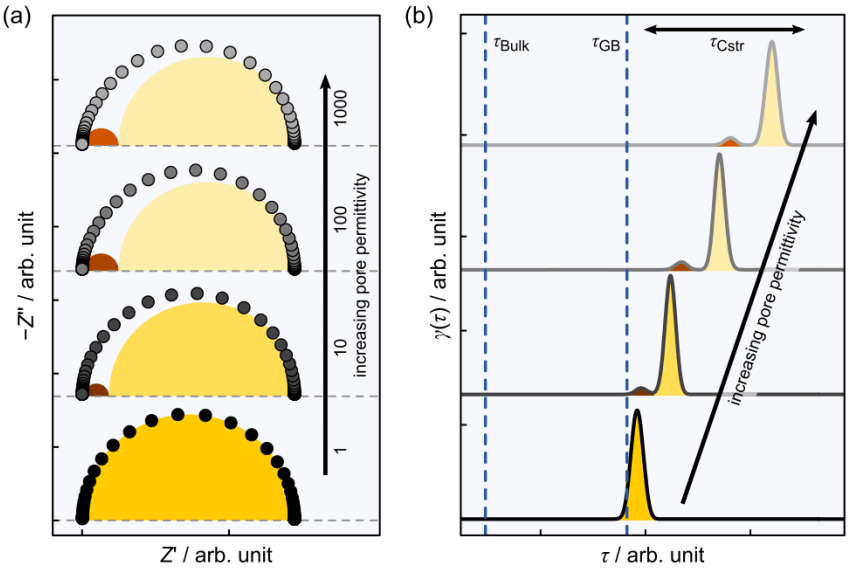

Figure 2. Computed impedance response of nanocrystalline mesoporous oxide thin films. The considered model structure exhibits an interconnected grain and pore network. The external potential gradient is applied in the *z*-direction. (a) A typical impedance spectrum features one semicircle in the Nyquist representation. Increasing the relative pore permittivity causes a slight distortion in the high frequency region. (b) DRT reveals the geometric nature of the observed impedance signals. Both shift toward longer relaxation times with increasing ε_{Pore}. Interestingly, no pristine contributions from bulk or grain boundary transport (dashed blue lines) can be resolved.

fitting them with a 1D equivalent circuit model (ECM). It consists of one *RC*-element representing the effective transport properties of the charge transport through the mesoporous thin films. It comprises bulk transport through the grains, transport across grain boundaries, and geometric current constriction due to the pore structure. The computed impedances are also evaluated in the time domain by performing a distribution of relaxation times analysis. Both types of analyses were performed using the commercial software RelaxIS 3 (version 3.0.20.19, rhd instruments GmbH & Co. KG). Because the Kramers−Kronig test yields negligible residuals in the order of 10^{-8}, all data points were included in the impedance analysis, and only a small regularization term was applied for the calculation of each DRT.[60,61]

RESULTS

Evaluation of the Impedance Response of Mesoporous Oxides. In Nyquist representation, the impedance spectra of dense microcrystalline oxides, such as YSZ, typically exhibit two semicircles, which are attributed to the electric transport through the grains and across the grain boundaries.[44,62] If the grain size reduces to the nanoscale, typically the two semicircles start to merge.[42] This is not necessarily related to a change in the time constants with decreasing grain size, which may lead to similar time characteristics of bulk and grain boundary transport. Rather, the drastic change of the ratio V_{GB}/V_{Bulk} between grain boundary volume and grain volume is of major significance. The quantitative alteration can be roughly estimated by considering two spherical grains with radii of 1 μm and 10 nm, including an outer grain boundary shell of 2 nm. In this hypothetical situation, the volume ratio changes by more than two orders of magnitude with decreasing grain size, from 82.66 to 0.28. A large grain boundary volume fraction together with a several orders of magnitude lower grain boundary conductivity σ_{GB} results in a dominant grain boundary impedance contribution that may superimpose the bulk signal (see Figure S3).

The presence of pores makes the evaluation of impedance data even more complex. As shown in early studies by Fleig and Maier[63−65] and also in recent works by Eckhardt et al.,[66−68] pores at the electrode interface lead to geometric contributions in the impedance spectrum. The so-called dynamic current constriction (Cstr) signals result from the change in the conduction behavior of pores with frequency. While pores are dielectrically conductive at elevated frequencies via a displacement current, they become insulating in the direct current (DC) frequency range. This is accompanied by a change in the transport paths of the charge carriers across the structure. The current distribution in the system, including material and pores, is almost homogeneous at high frequencies. In the DC range, in contrast, electrically insulating pores lead to an inhomogeneous current distribution in the system, i.e., the current only flows within the solid framework. The resulting increase in the tortuosity with decreasing frequency is reflected by an increase in impedance. Depending on the time range of the switching behavior of the pores (i.e., dielectrically conducting vs electrically insulating), either each impedance contribution in the spectrum is quantitatively affected (i.e., scaling of each signal) or the pores result in a separate semicircle in the Nyquist diagram.[66] Although the fingerprint in the latter case resembles a microscopic transport process, the constriction signal is solely geometric in nature. Its capacitance is strongly affected by the pore capacitance $C_{Cstr} \propto \varepsilon_{Pore}$ and the resistance averages over all electric migration processes in the structure,[66] i.e.

$$R_{Cstr} \propto \sum_i \alpha_i \cdot \sigma_i \tag{3}$$

https://doi.org/10.1021/acsami.3c05561
ACS Appl. Mater. Interfaces 2023, 15, 35332−35341

ACS Applied Materials & Interfaces www.acsami.org Research Article

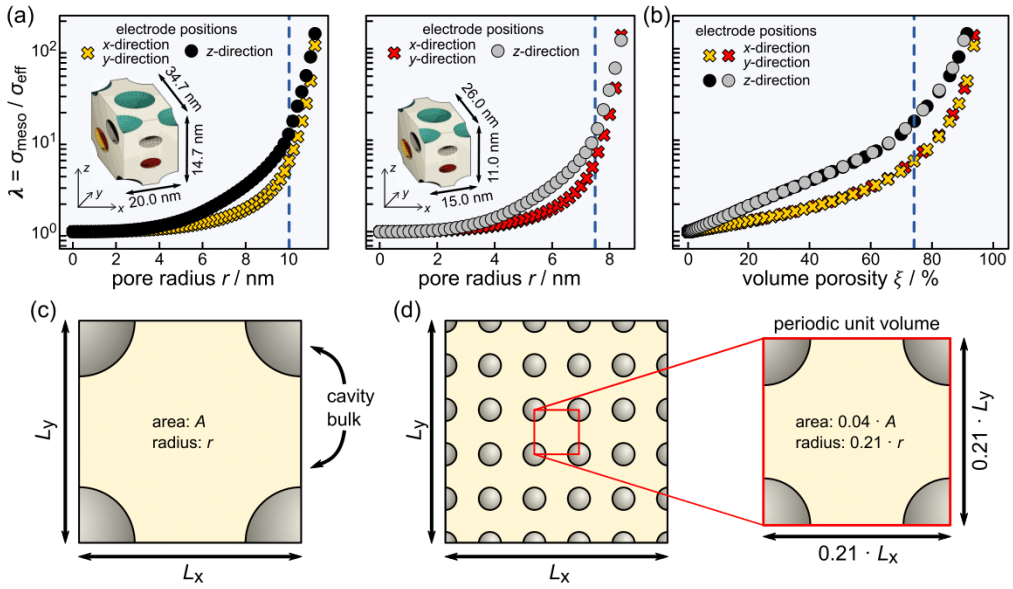

Figure 3. Influence of the mesoporous structure on the derived effective conductivity according to eq 4. (a) The size of the periodic unit volume does not alter the qualitative relationship between the conductivity ratio λ and pore radius r. The dashed blue line indicates the starting of the formation of an open pore network. (b) The conductivity ratio λ solely depends on volume porosity ξ rather than pore distance d or pore radii r. (c, d) This is due to the conservation of structural symmetry. The decrease of pore distance at fixed porosity leads to an identical periodic unit volume, but on a different length scale.

where the weighting factors α_i depend on the microstructural setup of the system including the ratio of grain boundary volume to grain volume V_{GB}/V_{Bulk}.[68] It is reasonable to assume that similar geometric effects also arise when pores are present within a ceramic sample. In consequence, the impedance of mesoporous thin films may in principle exhibit up to three contributions, representing bulk transport, transport across the grain boundaries, and the geometric current constriction effect. However, experimental impedance data of mesoporous ceramic oxide thin films typically exhibit only one semicircle in Nyquist representation.[25,48−50,69]

To clarify the origin of the single semicircle, we computed a series of impedance spectra for a fixed model structure. Thereby, the shortest distance between the centers of two pores d is set to 15 nm, and a pore radius r = 7.5 nm is considered. With these parameters, both the pores and the grains built an interconnected network. Throughout the study, the relative permittivity of the pores ε_{Pore} is varied systematically between 1 and 1000 to manipulate geometric impedance contributions only. Figure 2a shows the computed impedance spectra for four discrete ε_{Pore} values in the Nyquist representation with the potential applied in the z-direction. At first glance, each spectrum consists of one semicircle (yellow) in agreement with experimental results. However, a closer look at the spectra for relative permittivities larger than 1 indicates a slight distortion in the high-frequency region, which results from a second contribution (brown). This is consistent with computations that consider the external potential gradient in the x- or y-direction (see Figure S4). The impedance results for these two directions are identical due to the cubic symmetry of the system. However, they are quantitatively different from the result in the z-direction because the uniaxial lattice contraction leads to symmetry breaking.

Usually, the two contributions in experimental data would be interpreted to arise from bulk transport and transport across grain boundaries. To reassess this assignment, we transferred the impedances to the time domain by performing a DRT analysis. The distribution function $\gamma(\tau)$ for a relative permittivity of ε_{Pore} = 1 consists of one signal close to the time constant representing the microscopic grain boundary transport τ_{GB}. Figure 2b shows that this signal splits into two signals with increasing values of ε_{Pore}. Both signals shift toward longer relaxation times with increasing pore permittivity. This is characteristic for contributions that are geometric in nature. The time constants of electric migration processes are independent of the structural properties, as recently demonstrated in the literature[68] and also highlighted in Figure S5. Interestingly, the individual DRT shows no signals representing the bulk and grain boundary transport processes, whose time constants are indicated in Figure 2b as dashed lines. Consequently, the single semicircle in the experimental impedance spectrum of mesoporous thin films in Nyquist representation solely arises from the geometric constriction effect, i.e., a change of the crystallite size will not significantly affect the impedance response of the thin films. It is worth noting that even a finer sampling of the frequency range during the impedance measurement (i.e., increase of the number of data points) will not shift the relation between the signal intensities in favor of those representing the intrinsic electric migration processes. The reason is that the constriction effect due to the mesoporous structure always provides a contribution that is several orders of magnitude larger compared to the signals of the electric migration processes and therefore dominates the overall impedance. Thus, neither the pristine bulk nor the pristine grain boundary transport process can be resolved when measuring the impedance of nanocrystalline mesoporous thin films, even not by a DRT analysis.

Derivation of a Geometric Correction Factor for 1D Conductivity Analysis. The discussion of the computed

https://doi.org/10.1021/acsami.3c05561
ACS Appl. Mater. Interfaces 2023, 15, 35332−35341

ACS Applied Materials & Interfaces www.acsami.org Research Article

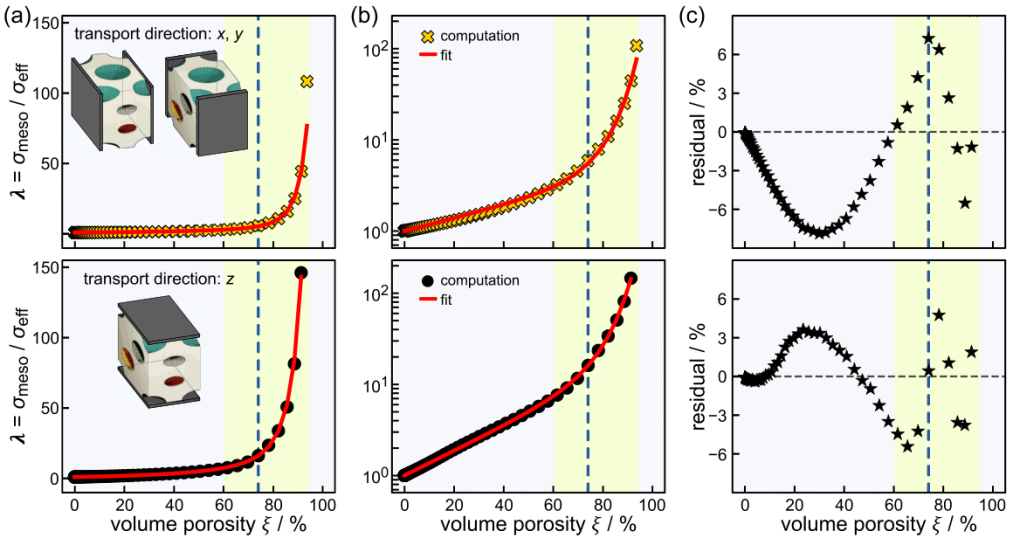

Figure 4. (a) Computed relation between the conductivity ratio and volume porosity. Typical experimentally determined porosity ranges are shown by the green region, while the dashed blue line indicates the starting of the open pore network formation. The red line corresponds to the parametrization curve fitted to the computed data. (b) The logarithm of the conductivity ratio λ (yellow, black) can well be parametrized (red) by a linear increase up to a volume porosity of about 50%, followed by an exponential increase until the solid grain network collapses. (c) The absolute residual values between computation and parametrization curve are less than 8%.

impedances in Figure 2 demonstrates that the measured impedance of mesoporous thin films mainly reflects the geometry of the mesoporous structure. Nonetheless, it is reasonable to estimate at least an effective conductivity σ_{eff} of the thin films from the measured impedance. Assuming a dense sample (i.e., porosity ξ = 0%), i.e., neglecting the porosity of the thin films, the effective conductivity can be estimated from the DC resistance R_{tot}:

$$\sigma_{eff} = \frac{1}{R_{tot}} \cdot \frac{L_{Elec}}{A_{Elec}} \quad (4)$$

where L_{Elec} describes the distance between the electrodes and A_{Elec} represents the electrode area.

The total resistance $R_{tot} \approx R_{Cstr}$ is mainly determined by the geometric constriction effect, which in turn is dominated by transport across grain boundaries. This is related to the large ratio of grain boundary volume to grain volume V_{GB}/V_{Bulk} in the nanocrystalline regime and due to their higher resistance compared to bulk transport. Therefore, the grain boundary conductivity σ_{GB} provides the largest contribution in the averaging when considering the constriction resistance R_{Cstr} in eq 3. However, estimating the effective conductivity σ_{eff} using eq 4 underestimates the material-specific conductivity, as the mesoporous structure is neglected. Thus, σ_{eff} only gives a bottom limit of the actual material parameters of the thin films, such as σ_{GB}. Fortunately, the regular arrangement of the pores allows a systematic study of the impact of geometric effects on σ_{eff} using our 3D electric network model. For this purpose, we homogenize the microstructure in the model system and consider only a single phase with an average conductivity σ_{meso} of the mesoporous structure. Throughout the computational study, two periodic unit volumes of different size with a pore distance d = 15 and 20 nm are considered. For each system, we successively increase the pore radii and compute the resulting impedance response. The obtained DC resistance enables the calculation of the effective conductivity σ_{eff} for each pore size by using eq 4, which in turn can then be compared with the material-specific conductivity σ_{meso} of the solid framework.

Figure 3a shows the change of the conductivity ratio $\lambda = \sigma_{meso}/\sigma_{eff}$ with increasing pore radius for the two periodic unit volumes with different shortest distances d between the centers of two pores. The circular symbols represent the results for a potential gradient applied along the z-direction, while the cross-shaped symbols correspond to a potential gradient applied along the x- or y-directions. As expected, the deviation between both conductivities increases non-linearly with pore radius and tends to infinity as the solid network collapses. The qualitative behavior is related, on the one hand, to the decrease in the bulk material and, on the other hand, to an increase of the transport path length, i.e., an change in tortuosity with increasing pore radius. The sensitivity of the conductivity ratio λ is particularly pronounced in the region, where the pores start to overlap forming an interconnected pore network. The radius, where the open pore network starts to form, is indicated in Figure 3a as a dashed blue line. Here, the material-specific conductivity σ_{meso} is about ten times larger than the effective conductivity σ_{eff}, which is obtained when neglecting the porosity of the thin films.

Interestingly, the shape of both functional trajectories of the conductivity ratio λ (for the same transport direction) with varying pore radius r is independent of the size of the periodic unit volume, i.e., the shortest distance d between the centers of two pores. As shown in Figure 3b, λ is determined solely by the volume porosity and not by the radius of the pores. Note that the non-overlapping data points (black, gray, yellow, red) at high porosity values are related to the large sensitivity of λ and the different sampled discrete porosity values. A negligible impact of the pore size on the effective conductivity has also been observed experimentally for mesoporous YSZ thin films with pore radii varying between 7 and 20 nm.[39] The reason for the pore-size-independent effective conductivity σ_{eff} for a fixed porosity is the conservation of symmetry. For illustration,

https://doi.org/10.1021/acsami.3c05561
ACS Appl. Mater. Interfaces 2023, 15, 35332−35341

Figure 3c depicts the periodic unit volume of a simple cubic surface with area A and pores (gray) of radius r at each of the four corners. If we now consider a different pore distance d while maintaining the same mesoporous arrangement and porosity ξ, the number of pores in area A increases, and the pore radii decrease, as shown in Figure 3d. In the resulting structure, we can then define a new smaller periodic unit volume, which builds up the full system through translation symmetry. Except for their lateral dimensions, the two periodic unit volumes are identical from a geometrical point of view. Therefore, also the transport paths through the structures are the same, but on a different length scale. Thus, the shortest distance d between the centers of two pores (i.e., the size of the periodic unit volume) and the pore radii have no effect on the conductivity ratio λ, if they feature the same porosity value ξ. Because this is a geometric effect related to the symmetry in the system, it is independent of pore size and pore wall characteristics. However, any kind of symmetry breaking, such as different pore geometries or inhomogeneities in crystallite size, will lead to (minor) deviations from this behavior.

Interestingly, Figure 3b reveals that the conductivity ratio λ follows a simple and well-defined functional relationship with volume porosity ξ. This allows the derivation of a material-independent empirical formula, which links the estimated effective conductivity σ_{eff} to the material-specific conductivity of the oxide material σ_{meso}. On a logarithmic scale, there is a linear increase in the conductivity ratio λ up to a porosity ξ of about 50%, followed by an exponential increase until the nanocrystalline grain network collapses. This corresponds to the functional relation $\log(\lambda) = a\cdot\xi + \exp(b + c\cdot\xi)$ that parametrizes λ with the three coefficients a, b, and c. Fitting this relation to the computed series of conductivity ratios for the different transport directions yields

$$\log[\lambda(\xi)] = \begin{cases} 0.705\cdot\xi + \exp(-8.04 + 8.79\cdot\xi), & x\text{-},\ y\text{-direction} \\ 1.35\cdot\xi + \exp(-8.04 + 8.71\cdot\xi), & z\text{-direction} \end{cases} \tag{5}$$

The simulated data (black, yellow) are well-described by these material-independent empirical formulas (red), as depicted in Figure 4. The absolute values of resulting residuals are below 8%, which is acceptable. The formula for the conductivity ratio in eq 5 depends only on the volume porosity ξ of the mesoporous structure. This in turn can be calculated from the shortest distance d between the centers of two pores and the pore radii r using the equation

$$\xi(r, d) = \begin{cases} \dfrac{4\sqrt{2}\cdot\pi}{3}\cdot\left(\dfrac{r}{d}\right)^3, & r \le \dfrac{d}{2\sqrt{2}} \\ \dfrac{\pi\cdot(-3d^3 + 36d\cdot r^2 - 40r^3)}{3\sqrt{2}\cdot d^3}, & r > \dfrac{d}{2\sqrt{2}} \end{cases} \tag{6}$$

A detailed derivation of this expression is given in the Supporting Information.

Note that the conductivity ratio λ for a certain porosity value ξ serves as a material-independent geometrical correction factor to the effective conductivity σ_{eff} in order to account for the mesoporous morphology of the thin films. This allows the determination of the material-specific conductivity σ_{meso} of the solid framework from the measured impedance, which in turn is dominated by the grain boundary conductivity in the nanocrystalline regime:

$$\sigma_{\text{meso}} = \lambda(\xi)\cdot\sigma_{\text{eff}} = \lambda(\xi)\cdot\frac{1}{R_{\text{tot}}}\cdot\frac{L_{\text{Elec}}}{A_{\text{Elec}}} \approx \sigma_{\text{GB}} \tag{7}$$

The region of volume porosity, which is typically found in mesoporous thin films prepared by the EISA method, is indicated in Figure 3b as a green area. Interestingly, the experimental porosity values estimated from the surface area and pore volume obtained by Brunauer–Emmett–Teller (BET) analysis are sometimes below the theoretical porosity value where the open pore network begins to form (dashed blue line).[55,70] This is probably due to non-idealities in the real mesoporous structure, such as variations in pore size and pore shape, which result in non-accessible pore space and certain isolated structural regions. It should be noted that such inhomogeneities in the real system have a minor quantitative effect on the measured impedance spectra. However, they do not affect the validity of the conclusions derived or the computed geometric correction factor. In the ideal case, our analysis shows that the material-specific conductivity σ_{meso} is about one to two orders of magnitude larger than the effective conductivity σ_{eff}, which is estimated from the impedance assuming a dense thin film. This demonstrates the necessity to account for the mesoporous structure using the derived material-independent correction factor for a reliable determination of the material-specific conductivity of the thin films. In particular, this will help to elucidate if and how variations of the pore size and the surface area may affect charge transport in the solid framework of the mesoporous thin films, e.g., due to the presence of a surface space charge region.

CONCLUSIONS

In this study, we use a 3D electric network model to compute the impedance response of ordered mesoporous oxide thin films. The simulated impedance spectra are characterized by one single semicircle in the Nyquist diagram, which is in agreement with experimental results. The evaluation of the computed spectra in the time domain by performing a DRT analysis reveals that the impedance is solely determined by the geometric current constriction effect, which arises due to the regular pore arrangement within the nanocrystalline thin films. The geometric contribution completely dominates the impedance of ordered mesoporous oxide thin films. Even for highly frequency-resolved sampling of the impedance, the large geometric constriction contribution impedes the separation of the bulk and grain boundary resistance contributions. However, a detailed analysis of computed impedance spectra of thin films with varying pore size allows us to correlate the impedance response with the material-specific conductivity of the mesoporous solid framework. We find that changes in the impedance with increasing pore size can directly be related to the increase in volume porosity of the thin films. This enables us to derive a material-independent geometric correction factor that accounts for the porous structure of the thin films. In addition, it allows for a reliable determination of the material-specific electrical conductivity of mesoporous thin films with an error of less than 8%. This offers the possibility to get a deeper understanding on the impact of the high surface area on the charge transport mechanism in ordered mesoporous oxides in order to optimize their properties for device applications.

https://doi.org/10.1021/acsami.3c05561
ACS Appl. Mater. Interfaces 2023, 15, 35332–35341

■ ASSOCIATED CONTENT

Supporting Information

The Supporting Information is available free of charge at https://pubs.acs.org/doi/10.1021/acsami.3c05561.

Details on the simulation of structural model systems, effect of pore permittivity and crystallite size on impedance response, and analytical consideration on porosity in mesoporous oxides (PDF)

■ AUTHOR INFORMATION

Corresponding Authors

Janis K. Eckhardt − *Institute for Theoretical Physics, Justus Liebig University, Giessen D-35392, Germany; Center for Materials Research (ZfM), Justus Liebig University, Giessen D-35392, Germany; Institute of Physical Chemistry, Justus Liebig University, Giessen D-35392, Germany;* orcid.org/0000-0002-2799-0599; Email: janis.k.eckhardt@theo.physik.uni-giessen.de

Matthias T. Elm − *Center for Materials Research (ZfM) and Institute of Experimental Physics I, Justus Liebig University, Giessen D-35392, Germany; Institute of Physical Chemistry, Justus Liebig University, Giessen D-35392, Germany;* orcid.org/0000-0001-7014-5772; Email: matthias.elm@phys.chemie.uni-giessen.de

Author

Christian Heiliger − *Institute for Theoretical Physics, Justus Liebig University, Giessen D-35392, Germany; Center for Materials Research (ZfM), Justus Liebig University, Giessen D-35392, Germany*

Complete contact information is available at: https://pubs.acs.org/10.1021/acsami.3c05561

Notes

The authors declare no competing financial interest.

■ ACKNOWLEDGMENTS

We greatly appreciate helpful discussions with Sascha Kremer. The authors thank Elisa Monte for assistance in the preparation of the graphical material. We acknowledge computational resources provided by the HPC Core Facility and the HRZ of the Justus-Liebig-University Giessen. We thank MSc. Philipp Risius and Dr. Marcel Giar of HPC-Hessen, funded by the State Ministry of Higher Education, Research, and the Arts (HMWK), for programming advice. Financial support is provided by the German Research Foundation (DFG) via the GRK (Research Training Group) 2204 "Substitute Materials for sustainable Energy Technologies". M.T.E. gratefully acknowledges financial support by the DFG via Grant EL 863/3-1 and the Heisenberg Program (Project 498993886, Grant EL 863/6-1).

■ REFERENCES

(1) Antonietti, M.; Ozin, G. A. Promises and Problems of Mesoscale Materials Chemistry or Why Meso? *Chem.—Eur. J.* **2004**, *10* (1), 28−41.

(2) Inagaki, S.; Fukushima, Y.; Kuroda, K. Synthesis of Highly Ordered Mesoporous Materials from a Layered Polysilicate. *J. Chem. Soc. Chem. Commun.* **1993**, No. 8, 680−682.

(3) Kresge, C. T.; Leonowicz, M. E.; Roth, W. J.; Vartuli, J. C.; Beck, J. S. Ordered Mesoporous Molecular Sieves Synthesized by a Liquid-Crystal Template Mechanism. *Nature* **1992**, *359* (6397), 710−712.

(4) Inagaki, S.; Fukushima, Y.; Kuroda, K. Synthesis and characterization of highly ordered mesoporous material; FSM-16, from a layered polysilicate. In *Stud. Surf. Sci. Catal.*, Weitkamp, J., Karge, H. G., Pfeifer, H., Hölderich, W., Eds.; Elsevier: 1994; Vol. *84*, pp 125−132.

(5) Liang, C.; Li, Z.; Dai, S. Mesoporous Carbon Materials: Synthesis and Modification. *Angew. Chem., Int. Ed.* **2008**, *47* (20), 3696−3717.

(6) Ryoo, R.; Joo, S. H.; Kruk, M.; Jaroniec, M. Ordered Mesoporous Carbons. *Adv. Mater.* **2001**, *13* (9), 677−681.

(7) Kondo, J. N.; Domen, K. Crystallization of Mesoporous Metal Oxides. *Chem. Mater.* **2008**, *20* (3), 835−847.

(8) Lee, J.; Christopher Orilall, M.; Warren, S. C.; Kamperman, M.; DiSalvo, F. J.; Wiesner, U. Direct Access to Thermally Stable and Highly Crystalline Mesoporous Transition-Metal Oxides with Uniform Pores. *Nat. Mater.* **2008**, *7* (3), 222−228.

(9) Zou, Y.; Zhou, X.; Ma, J.; Yang, X.; Deng, Y. Recent Advances in Amphiphilic Block Copolymer Templated Mesoporous Metal-Based Materials: Assembly Engineering and Applications. *Chem. Soc. Rev.* **2020**, *49* (4), 1173−1208.

(10) Trikalitis, P. N.; Rangan, K. K.; Bakas, T.; Kanatzidis, M. G. Varied Pore Organization in Mesostructured Semiconductors Based on the $[SnSe4]^{4-}$ Anion. *Nature* **2001**, *410* (6829), 671−675.

(11) Armatas, G. S.; Kanatzidis, M. G. Mesoporous Germanium-Rich Chalcogenido Frameworks with Highly Polarizable Surfaces and Relevance to Gas Separation. *Nat. Mater.* **2009**, *8* (3), 217−222.

(12) Brinker, C. J.; Lu, Y.; Sellinger, A.; Fan, H. Evaporation-Induced Self-Assembly: Nanostructures Made Easy. *Adv. Mater.* **1999**, *11* (7), 579−585.

(13) Wan, Y.; Zhao, D. On the Controllable Soft-Templating Approach to Mesoporous Silicates. *Chem. Rev.* **2007**, *107*, 2821−2860.

(14) Ren, Y.; Ma, Z.; Bruce, P. G. Ordered Mesoporous Metal Oxides: Synthesis and Applications. *Chem. Soc. Rev.* **2012**, *41* (14), 4909−4927.

(15) Li, D.; Zhou, H.; Honma, I. Design and Synthesis of Self-Ordered Mesoporous Nanocomposite through Controlled in-Situ Crystallization. *Nat. Mater.* **2004**, *3* (1), 65−72.

(16) Grosso, D.; Boissiere, C.; Smarsly, B.; Brezesinski, T.; Pinna, N.; Albouy, P. A.; Amenitsch, H.; Antonietti, M.; Sanchez, C. Periodically Ordered Nanoscale Islands and Mesoporous Films Composed of Nanocrystalline Multimetallic Oxides. *Nat. Mater.* **2004**, *3* (11), 787−792.

(17) Celik, E.; Ma, Y.; Brezesinski, T.; Elm, M. T. Ordered Mesoporous Metal Oxides for Electrochemical Applications: Correlation between Structure, Electrical Properties and Device Performance. *Phys. Chem. Chem. Phys.* **2021**, *23* (18), 10706−10735.

(18) Walcarius, A. Mesoporous Materials and Electrochemistry. *Chem. Soc. Rev.* **2013**, *42* (9), 4098.

(19) Wagner, T.; Haffer, S.; Weinberger, C.; Klaus, D.; Tiemann, M. Mesoporous Materials as Gas Sensors. *Chem. Soc. Rev.* **2013**, *42* (9), 4036−4053.

(20) Waitz, T.; Wagner, T.; Sauerwald, T.; Kohl, C.-D.; Tiemann, M. Ordered Mesoporous In_2O_3: Synthesis by Structure Replication and Application as a Methane Gas Sensor. *Adv. Funct. Mater.* **2009**, *19* (4), 653−661.

(21) Fröschl, T.; Hörmann, U.; Kubiak, P.; Kučerová, G.; Pfanzelt, M.; Weiss, C. K.; Behm, R. J.; Hüsing, N.; Kaiser, U.; Landfester, K.; Wohlfahrt-Mehrens, M. High Surface Area Crystalline Titanium Dioxide: Potential and Limits in Electrochemical Energy Storage and Catalysis. *Chem. Soc. Rev.* **2012**, *41* (15), 5313−5360.

(22) Ren, Y.; Ma, Z.; Qian, L.; Dai, S.; He, H.; Bruce, P. G. Ordered Crystalline Mesoporous Oxides as Catalysts for CO Oxidation. *Catal. Lett.* **2009**, *131* (1−2), 146−154.

(23) Rolison, D. R. Catalytic Nanoarchitectures - The Importance of Nothing and the Unimportance of Periodicity. *Science (1979)* **2003**, *299* (5613), 1698−1701.

(24) Li, W.; Liu, J.; Zhao, D. Mesoporous Materials for Energy Conversion and Storage Devices. *Nat. Rev. Mater.* **2016**, *1* (6), 16023.

(25) Yue, J.; Suchomski, C.; Voepel, P.; Ellinghaus, R.; Rohnke, M.; Leichtweiss, T.; Elm, M. T.; Smarsly, B. M. Mesoporous Niobium-Doped Titanium Dioxide Films from the Assembly of Crystalline Nanoparticles: Study on the Relationship between the Band Structure, Conductivity and Charge Storage Mechanism. *J. Mater. Chem. A Mater.* **2017**, *5* (5), 1978−1988.
(26) Weller, T.; Deilmann, L.; Timm, J.; Dörr, T. S.; Beaucage, P. A.; Cherevan, A. S.; Wiesner, U. B.; Eder, D.; Marschall, R. A Crystalline and 3D Periodically Ordered Mesoporous Quaternary Semiconductor for Photocatalytic Hydrogen Generation. *Nanoscale* **2018**, *10* (7), 3225−3234.
(27) Weller, T.; Sann, J.; Marschall, R. Pore Structure Controlling the Activity of Mesoporous Crystalline $CsTaWO_6$ for Photocatalytic Hydrogen Generation. *Adv. Energy Mater.* **2016**, *6* (16), 1600208.
(28) Grätzel, M. Mesoscopic Solar Cells for Electricity and Hydrogen Production from Sunlight. *Chem. Lett.* **2005**, *34* (1), 8−13.
(29) Brezesinski, T.; Wang, J.; Senter, R.; Brezesinski, K.; Dunn, B.; Tolbert, S. H. On the Correlation between Mechanical Flexibility, Nanoscale Structure, and Charge Storage in Periodic Mesoporous CeO_2 Thin Films. *ACS Nano* **2010**, *4* (2), 967−977.
(30) Wang, G.; Liu, H.; Liu, J.; Qiao, S.; Lu, G. M.; Munroe, P.; Ahn, H. Mesoporous $LiFePO_4$/C Nanocomposite Cathode Materials for High Power Lithium Ion Batteries with Superior Performance. *Adv. Mater.* **2010**, *22* (44), 4944−4948.
(31) Rauda, I. E.; Augustyn, V.; Dunn, B.; Tolbert, S. H. Enhancing Pseudocapacitive Charge Storage in Polymer Templated Mesoporous Materials. *Acc. Chem. Res.* **2013**, *46* (5), 1113−1124.
(32) Zscherp, M. F.; Glaser, J.; Becker, C.; Beyer, A.; Cop, P.; Schörmann, J.; Volz, K.; Elm, M. T. Epitaxial Growth and Structural Characterization of Ceria Deposited by Atomic Layer Deposition on High-Surface Porous Yttria-Stabilized Zirconia Thin Films. *Cryst. Growth Des* **2020**, *20* (4), 2194−2201.
(33) Elam, J. W.; Xiong, G.; Han, C. Y.; Wang, H. H.; Birrell, J. P.; Hryn, J. N.; Pellin, M. J.; Poco, J. F.; Satcher, J. H. Atomic Layer Deposition for the Conformal Coating of Nanoporous Materials. *MRS Proceedings* **2005**, *876*, R12.6.
(34) Dendooven, J.; Devloo-Casier, K.; Ide, M.; Grandfield, K.; Kurttepeli, M.; Ludwig, K. F.; Bals, S.; Van Der Voort, P.; Detavernier, C. Atomic Layer Deposition-Based Tuning of the Pore Size in Mesoporous Thin Films Studied by in Situ Grazing Incidence Small Angle X-Ray Scattering. *Nanoscale* **2014**, *6* (24), 14991−14998.
(35) Dendooven, J.; Goris, B.; Devloo-Casier, K.; Levrau, E.; Biermans, E.; Baklanov, M. R.; Ludwig, K. F.; Van Der Voort, P.; Bals, S.; Detavernier, C. Tuning the Pore Size of Ink-Bottle Mesopores by Atomic Layer Deposition. *Chem. Mater.* **2012**, *24* (11), 1992−1994.
(36) Dendooven, J.; Ramachandran, R. K.; Solano, E.; Kurttepeli, M.; Geerts, L.; Heremans, G.; Rongé, J.; Minjauw, M. M.; Dobbelaere, T.; Devloo-Casier, K.; Martens, J. A.; Vantomme, A.; Bals, S.; Portale, G.; Coati, A.; Detavernier, C. Independent Tuning of Size and Coverage of Supported Pt Nanoparticles Using Atomic Layer Deposition. *Nat. Commun.* **2017**, *8* (1), 1074.
(37) Dubraja, L. A.; Boll, D.; Reitz, C.; Wang, D.; Belić, D.; Mazilkin, A.; Breitung, B.; Hahn, H.; Elm, M. T.; Brezesinski, T. Thin Films of Thermally Stable Ordered Mesoporous Rh_2O_3(I) for Visible-Light Photocatalysis and Humidity Sensing. *ACS Appl. Nano Mater.* **2019**, *2* (11), 7126−7133.
(38) Kraffert, K.; Karg, M.; Schmack, R.; Clavel, G.; Boissiere, C.; Wirth, T.; Pinna, N.; Kraehnert, R. Stabilization of Mesoporous Iron Oxide Films against Sintering and Phase Transformations via Atomic Layer Deposition of Alumina and Silica. *Adv. Mater. Interfaces* **2018**, *5* (14), 1800360.
(39) Celik, E.; Cop, P.; Negi, R. S.; Mazilkin, A.; Ma, Y.; Klement, P.; Schörmann, J.; Chatterjee, S.; Brezesinski, T.; Elm, M. T. Design of Ordered Mesoporous CeO_2-YSZ Nanocomposite Thin Films with Mixed Ionic/Electronic Conductivity via Surface Engineering. *ACS Nano* **2022**, *16* (2), 3182−3193.
(40) Cop, P.; Celik, E.; Hess, K.; Moryson, Y.; Klement, P.; Elm, M. T.; Smarsly, B. M. Atomic Layer Deposition of Nanometer-Sized CeO_2 Layers in Ordered Mesoporous ZrO_2 Films and Their Impact on the Ionic/Electronic Conductivity. *ACS Appl. Nano Mater.* **2020**, *3* (11), 10757−10766.
(41) Celik, E.; Negi, R. S.; Bastianello, M.; Boll, D.; Mazilkin, A.; Brezesinski, T.; Elm, M. T. Tailoring the Protonic Conductivity of Porous Yttria-Stabilized Zirconia Thin Films by Surface Modification. *Phys. Chem. Chem. Phys.* **2020**, *22* (20), 11519−11528.
(42) Tuller, H. L. Ionic Conduction in Nanocrystalline Materials. *Solid State Ion* **2000**, *131* (1), 143−157.
(43) Maier, J. Defect Chemistry and Conductivity Effects in Heterogeneous Solid Electrolytes. *J. Electrochem. Soc.* **1987**, *134* (6), 1524−1535.
(44) Irvine, J. T. S.; Sinclair, D. C.; West, A. R. Electroceramics: Characterization by Impedance Spectroscopy. *Adv. Mater.* **1990**, *2* (3), 132−138.
(45) Bredar, A. R. C.; Chown, A. L.; Burton, A. R.; Farnum, B. H. Electrochemical Impedance Spectroscopy of Metal Oxide Electrodes for Energy Applications. *ACS Appl. Energy Mater.* **2020**, *3* (1), 66−98.
(46) Kosacki, I.; Anderson, H. U. Microstructure — Property Relationships in Nanocrystalline Oxide Thin Films. *Ionics (Kiel)* **2000**, *6* (3), 294−311.
(47) Knauth, P.; Tuller, H. L. Electrical and Defect Thermodynamic Properties of Nanocrystalline Titanium Dioxide. *J. Appl. Phys.* **1999**, *85* (2), 897−902.
(48) Baiutti, F.; Blanco-Portals, J.; Anelli, S.; Torruella, P.; López-Haro, M.; Calvino, J.; Estradé, S.; Torrell, M.; Peiró, F.; Tarancón, A. Tailoring the Transport Properties of Mesoporous Doped Cerium Oxide for Energy Applications. *J. Phys. Chem. C* **2021**, *125* (30), 16451−16463.
(49) Hartmann, P.; Brezesinski, T.; Sann, J.; Lotnyk, A.; Eufinger, J.-P.; Kienle, L.; Janek, J. Defect Chemistry of Oxide Nanomaterials with High Surface Area: Ordered Mesoporous Thin Films of the Oxygen Storage Catalyst CeO_2-ZrO_2. *ACS Nano* **2013**, *7* (4), 2999−3013.
(50) Elm, M. T.; Hofmann, J. D.; Suchomski, C.; Janek, J.; Brezesinski, T. Ionic Conductivity of Mesostructured Yttria-Stabilized Zirconia Thin Films with Cubic Pore Symmetry—On the Influence of Water on the Surface Oxygen Ion Transport. *ACS Appl. Mater. Interfaces* **2015**, *7* (22), 11792−11801.
(51) Eckhardt, J. K.; Burkhardt, S.; Zahnow, J.; Elm, M. T.; Janek, J.; Klar, P. J.; Heiliger, C. Understanding the Impact of Microstructure on Charge Transport in Polycrystalline Materials Through Impedance Modelling. *J. Electrochem. Soc.* **2021**, *168* (9), 090516.
(52) Brezesinski, K.; Wang, J.; Haetge, J.; Reitz, C.; Steinmueller, S. O.; Tolbert, S. H.; Smarsly, B. M.; Dunn, B.; Brezesinski, T. Pseudocapacitive Contributions to Charge Storage in Highly Ordered Mesoporous Group v Transition Metal Oxides with Iso-Oriented Layered Nanocrystalline Domains. *J. Am. Chem. Soc.* **2010**, *132* (20), 6982−6990.
(53) Wang, Y.; Brezesinski, T.; Antonietti, M.; Smarsly, B. Ordered Mesoporous Sb-, Nb-, and Ta-Doped SnO_2 Thin Films with Adjustable Doping Levels and High Electrical Conductivity. *ACS Nano* **2009**, *3* (6), 1373−1378.
(54) Brezesinski, T.; Wang, J.; Polleux, J.; Dunn, B.; Tolbert, S. H. Templated Nanocrystal-Based Porous TiO_2 Films for Next-Generation Electrochemical Capacitors. *J. Am. Chem. Soc.* **2009**, *131* (5), 1802−1809.
(55) Reitz, C.; Haetge, J.; Suchomski, C.; Brezesinski, T. Facile and General Synthesis of Thermally Stable Ordered Mesoporous Rare-Earth Oxide Ceramic Thin Films with Uniform Mid-Size to Large-Size Pores and Strong Crystalline Texture. *Chem. Mater.* **2013**, *25* (22), 4633−4642.
(56) Weidmann, C.; Brezesinski, K.; Suchomski, C.; Tropp, K.; Grosser, N.; Haetge, J.; Smarsly, B. M.; Brezesinski, T. Morphology-Controlled Synthesis of Nanocrystalline η-Al_2O_3 Thin Films, Powders, Microbeads, and Nanofibers with Tunable Pore Sizes from Preformed Oligomeric Oxo-Hydroxo Building Blocks. *Chem. Mater.* **2012**, *24* (3), 486−494.
(57) Guo, X.; Sigle, W.; Maier, J. Blocking Grain Boundaries in Yttria-Doped and Undoped Ceria Ceramics of High Purity. *J. Am. Ceram. Soc.* **2003**, *86* (1), 77−87.

https://doi.org/10.1021/acsami.3c05561
ACS Appl. Mater. Interfaces 2023, 15, 35332−35341

(58) Kim, S.; Maier, J. On the Conductivity Mechanism of Nanocrystalline Ceria. *J. Electrochem. Soc.* **2002**, *149* (10), J73.
(59) Guo, X.; Maier, J. Grain Boundary Blocking Effect in Zirconia: A Schottky Barrier Analysis. *J. Electrochem. Soc.* **2001**, *148* (3), No. E121.
(60) Boukamp, B. A. Electrochemical Impedance Spectroscopy in Solid State Ionics: Recent Advances. *Solid State Ion* **2004**, *169* (1), 65−73.
(61) Wan, T. H.; Saccoccio, M.; Chen, C.; Ciucci, F. Influence of the Discretization Methods on the Distribution of Relaxation Times Deconvolution: Implementing Radial Basis Functions with DRTtools. *Electrochim. Acta* **2015**, *184*, 483−499.
(62) Fleig, J.; Maier, J. A Finite Element Study on the Grain Boundary Impedance of Different Microstructures. *J. Electrochem. Soc.* **1998**, *145* (6), 2081−2089.
(63) Fleig, J.; Maier, J. The Influence of Current Constriction on the Impedance of Polarizable Electrodes: Application to Fuel Cell Electrodes. *J. Electrochem. Soc.* **1997**, *144* (11), L302.
(64) Fleig, J.; Maier, J. The Influence of Laterally Inhomogeneous Contacts on the Impedance of Solid Materials: A Three-Dimensional Finite-Element Study. *J. Electroceram* **1997**, *1* (1), 73−89.
(65) Fleig, J.; Maier, J. Point Contacts in Solid State Ionics: Finite Element Calculations and Local Conductivity Measurements. *Solid State Ion* **1996**, *86*−*88*, 1351−1356.
(66) Eckhardt, J. K.; Klar, P. J.; Janek, J.; Heiliger, C. Interplay of Dynamic Constriction and Interface Morphology between Reversible Metal Anode and Solid Electrolyte in Solid State Batteries. *ACS Appl. Mater. Interfaces* **2022**, *14* (31), 35545−35554.
(67) Eckhardt, J. K.; Fuchs, T.; Burkhardt, S.; Klar, P. J.; Janek, J.; Heiliger, C. Guidelines for Impedance Analysis of Parent Metal Anodes in Solid-State Batteries and the Role of Current Constriction at Interface Voids, Heterogeneities, and SEI. *Adv. Mater. Interfaces* **2023**, *10* (8), 2202354.
(68) Eckhardt, J. K.; Fuchs, T.; Burkhardt, S.; Klar, P. J.; Janek, J.; Heiliger, C. 3D Impedance Modeling of Metal Anodes in Solid-State Batteries-Incompatibility of Pore Formation and Constriction Effect in Physical-Based 1D Circuit Models. *ACS Appl. Mater. Interfaces* **2022**, *14* (37), 42757−42769.
(69) Einert, M.; Mellin, M.; Bahadorani, N.; Dietz, C.; Lauterbach, S.; Hofmann, J. P. Mesoporous High-Entropy Oxide Thin Films: Electrocatalytic Water Oxidation on High-Surface-Area Spinel $(Cr_{0.2}Mn_{0.2}Fe_{0.2}Co_{0.2}Ni_{0.2})_3O_4$ Electrodes. *ACS Appl. Energy Mater.* **2022**, *5* (1), 717−730.
(70) Reitz, C.; Reinacher, J.; Hartmann, P.; Brezesinski, T. Polymer-Templated Ordered Large-Pore Mesoporous Anatase-Rutile TiO_2:Ta Nanocomposite Films: Microstructure, Electrical Conductivity, and Photocatalytic and Photoelectrochemical Properties. *Catal. Today* **2014**, *225*, 55−63.

https://doi.org/10.1021/acsami.3c05561
ACS Appl. Mater. Interfaces 2023, 15, 35332−35341

2.4 Interplay of Dynamic Constriction and Interface Morphology

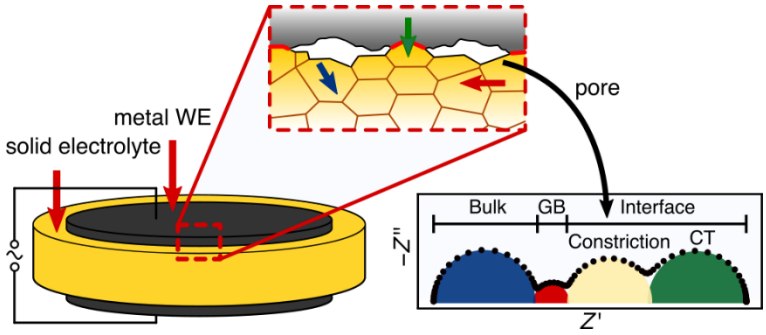

Abstract

In an all-solid-state battery, the electrical contact between its individual components is of key relevance in addition to the electrochemical stability of its interfaces. Impedance spectroscopy is particularly suited for the non-destructive investigation of interfaces and of their stability under load. Establishing a valid correlation between microscopic processes and the macroscopic impedance signal, however, is challenging and prone to errors. Here, we use a 3D electric network model to systematically investigate the effect of various electrode/sample interface morphologies on the impedance spectrum. It is demonstrated that the interface impedance generally results from a charge transfer step and a geometric constriction contribution. The weights of both signals depend strongly on the material parameters as well as on the interface morphology. Dynamic constriction results from a non-ideal local contact, e.g., from pores or voids, which reduce the electrochemical active surface area only in a certain frequency range. Constriction effects dominate the interface behavior for systems with small charge transfer resistance like garnet-type solid electrolytes in contact with a lithium metal electrode. An in-depth analysis of the origin and the characteristics of the constriction phenomenon and their dependence on the interface morphology is conducted. The discussion of the constriction effect provides further insight into the processes at the microscopic level, which are, e.g., relevant in the case of reversible metal anodes.

Reference

Interplay of Dynamic Constriction and Interface Morphology between Reversible Metal Anode and Solid Electrolyte in Solid State Batteries. Janis K. Eckhardt, Peter J. Klar, Jürgen Janek, and Christian Heiliger *ACS Appl. Mater. Interfaces* **2022**, 14, 31, 35545-35554. (DOI: 10.1021/acsami.2c07077)

Reproduced with permission

Artwork: This artwork was designed for the cover of ACS Applied Materials & Interfaces. Copyright © 2022, Elisa Monte/JLU Giessen.

ACS APPLIED MATERIALS & INTERFACES

www.acsami.org

Research Article

Interplay of Dynamic Constriction and Interface Morphology between Reversible Metal Anode and Solid Electrolyte in Solid State Batteries

Janis K. Eckhardt,* Peter J. Klar, Jürgen Janek, and Christian Heiliger

Cite This: *ACS Appl. Mater. Interfaces* 2022, 14, 35545−35554

Read Online

ACCESS | Metrics & More | Article Recommendations

ABSTRACT: In an all-solid-state battery, the electrical contact between its individual components is of key relevance in addition to the electrochemical stability of its interfaces. Impedance spectroscopy is particularly suited for the non-destructive investigation of interfaces and of their stability under load. Establishing a valid correlation between microscopic processes and the macroscopic impedance signal, however, is challenging and prone to errors. Here, we use a 3D electric network model to systematically investigate the effect of various electrode/sample interface morphologies on the impedance spectrum. It is demonstrated that the interface impedance generally results from a charge transfer step and a geometric constriction contribution. The weights of both signals depend strongly on the material parameters as well as on the interface morphology. Dynamic constriction results from a non-ideal local contact, e.g., from pores or voids, which reduce the electrochemical active surface area only in a certain frequency range. Constriction effects dominate the interface behavior for systems with small charge transfer resistance like garnet-type solid electrolytes in contact with a lithium metal electrode. An in-depth analysis of the origin and the characteristics of the constriction phenomenon and their dependence on the interface morphology is conducted. The discussion of the constriction effect provides further insight into the processes at the microscopic level, which are, e.g., relevant in the case of reversible metal anodes.

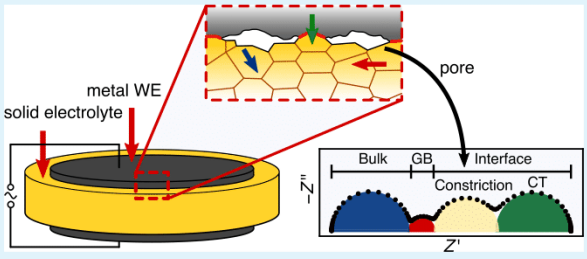

KEYWORDS: *reversible metal anode, interface morphology, pore formation, constriction effect, impedance modeling, garnet-type solid electrolyte, solid-state battery, electric network model*

1. INTRODUCTION

Examining the interfaces of all-solid-state batteries is challenging since they are hardly accessible non-destructively. Impedance spectroscopy (IS) is particularly suitable to systematically investigate changes of the interfaces during operation. Individual impedance contributions, e.g., grain boundary or bulk transport within a ceramic, can be separated from each other, if they differ in their frequency-dependent behavior. However, the correlation between microscopic changes of the interface morphology and the macroscopic impedance signal is nontrivial, making the interpretation of macroscopic impedance data in terms of microscopic processes prone to error.

In all-solid systems, an additional degree of sophistication arises in IS analysis since geometric effects contribute to the measured impedance signal in addition to chemical side reactions.[1−3] Thus, the impedance depends not only on the material properties of the solids involved but also on the preparation method of the system. While sputter deposition of the metal electrode typically yields a conformal coating of a sample surface, mechanical interface formation is likely to cause a porous interface accompanied by elastic and plastic deformation. Depending on the preparation conditions, pores of different shapes, sizes, and depths may arise and essentially determine the interface morphology. This also applies when a dynamic change of the system during operation leads to pore formation.[4,5]

Such a situation is often encountered in the case of reversible metal anodes, when a usually polycrystalline and cation-conducting solid electrolyte (SE) is in contact with an alkali metal electrode. In systems with thermodynamically stable interfaces, such as lithium metal in contact with $Li_{6.25}Al_{0.25}La_3Zr_2O_{12}$ (LLZO),[6−9] three different transport processes occur at the microscopic level, i.e., the charge

Received: April 21, 2022
Accepted: July 11, 2022
Published: July 25, 2022

https://doi.org/10.1021/acsami.2c07077
ACS Appl. Mater. Interfaces 2022, 14, 35545−35554

ACS Applied Materials & Interfaces www.acsami.org Research Article

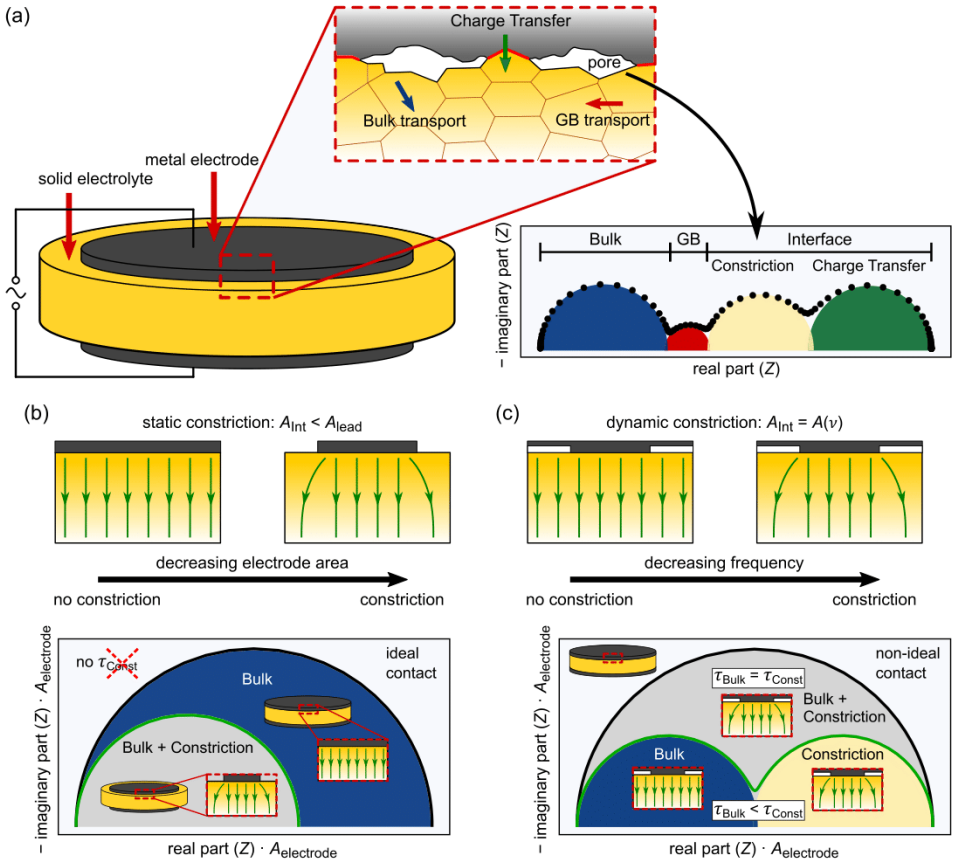

Figure 1. Overview of different types of current constriction at the electrode/sample interface. (a) Pores at the interface can lead to a separate or overlapping impedance contribution in the spectrum. This is related to the so-called constriction effect, which can be categorized in a "static" (classical) case of an ideal contact (b) and a "dynamic" (frequency-dependent) case of a non-ideal contact (c). In the classical case, the constriction only quantitatively affects the impedance of all transport signals (i.e., scaling), while in the frequency-dependent case, the impedance can be affected quantitatively (black) as well as qualitatively (green) by forming a separate signal that does not correspond to an electric migration process in the system at the microscopic level.

transfer (CT) step at the metal/SE interface and the bulk and grain boundary (GB) transport within the SE (see Figure 1a). It is therefore often mistakenly assumed that the impedance contains only contributions from the transport processes in the SE and the CT. Other origins of impedance signals and effects like the 3D microstructure of the SE (i.e., the geometrical arrangement of the grain boundary network)[10] or the pores at the interface are usually not considered in the interpretation of experimental data,[11−13] which can easily lead to misinterpretations as will be demonstrated by us.

The pores at the interface reduce the electrochemical active surface area. Thus, the ionic current lines in the SE become spatially focused at the contact spots (i.e., form "bottlenecks"). This effect is referred to as current constriction in what follows. This has been well documented in mostly qualitative form in metals[14,15] and in semiconductors.[16−19] The effect, however, is often considered to be "static", i.e., the constriction is assumed to be independent of external influences. It occurs, for example, when the electrode area A_{lead} is smaller than that of the sample A_{Int}. This means that the sample volume under the non-contacted surface area will also contribute to the transport due to the bended electric equipotential lines within the sample. The effect quantitatively affects all derived transport quantities (R_i, C_i) and depends on the ratio of sample surface area to contact area (see Figure 1b).

Current constriction, however, can also form "dynamically" in a system. This is important, especially when considering pores. At low frequencies, pores are truly locally current-blocking, and at high frequencies, the pores can transfer charge dielectrically (displacement current). Thus, their contribution to the impedance depends on excitation frequency ν and the constriction effect will disappear, if a certain frequency ν_{lim} is exceeded (see Figure 1c). Therefore, both qualitative and quantitative changes of the impedance are to be expected, i.e., the pores at the interface can also cause separate signals in the impedance spectrum (see Figure 1a), which are of purely geometric origin, i.e., due to interface morphology only. This has a major impact on the interpretation of IS results, especially regarding the assignment of the individual signals from the interface, i.e., CT step or constriction effect. Conversely, this means that IS data contain valuable information on the porous 3D microstructure of an electrode interface.

Current constriction is an established concept in the physics of electronic contacts but has not gained great attention in solid-state battery research so far, although it is of great

https://doi.org/10.1021/acsami.2c07077
ACS Appl. Mater. Interfaces 2022, 14, 35545−35554

ACS Applied Materials & Interfaces www.acsami.org Research Article

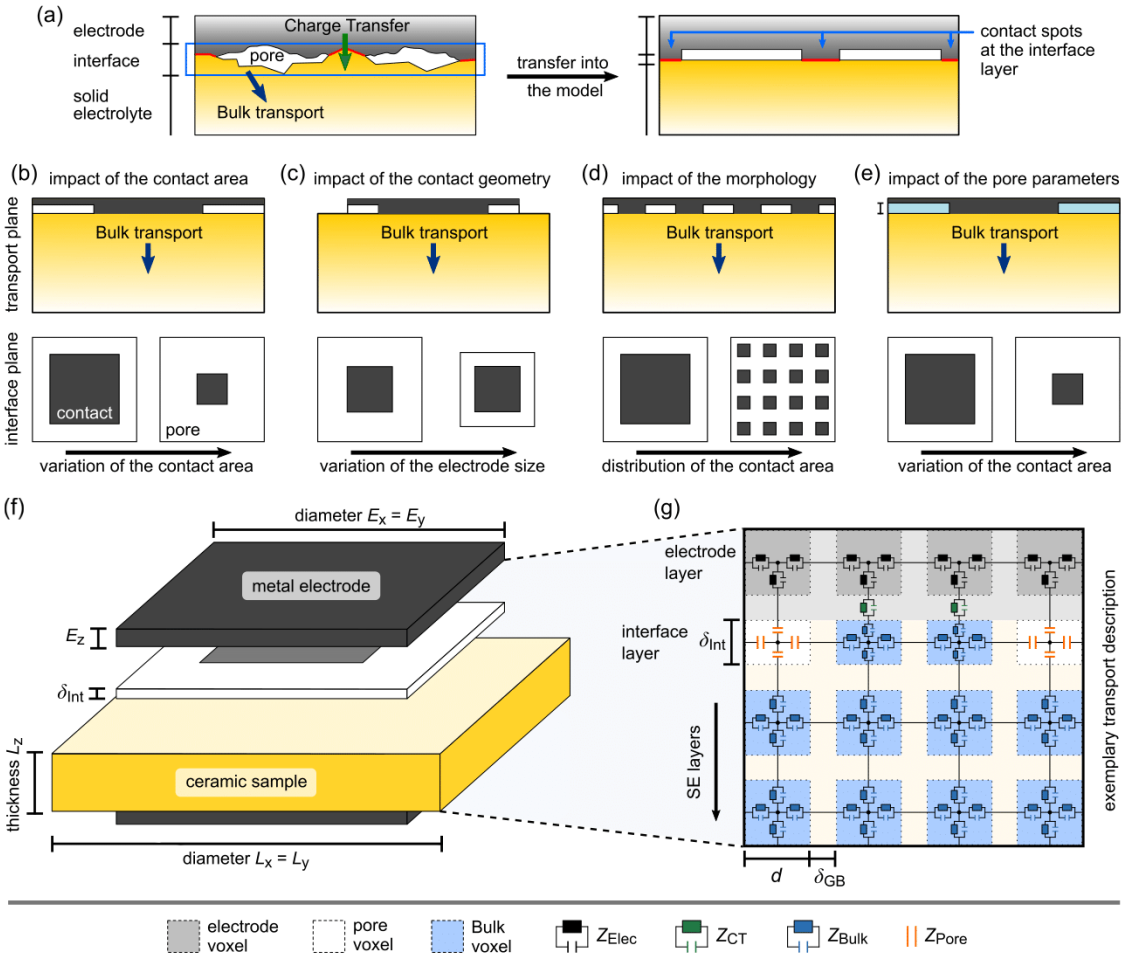

Figure 2. Overview of the definition of the 3D electric network model. (a) Transfer of the 2D projection of the real interface (blue box) into the model system. (b–e) Sketch of 2D projections of the simplified model systems for the systematic study of the dynamic constriction effect. (f) The voltage is applied between the homogeneous metal electrodes enclosing the homogeneous SE. The interface layer between the WE and SE causes the inhomogeneity of the system responsible for the dynamic constriction effect. (g) Bulk transport in the WE and the SE as well as the CT step at the electrode/SE interface is described by *RC*-elements, while the pores at the interface are considered as capacitors. For simplicity, the CT step at the metal/sample interface and transport within the electrode is assumed to be resistance-free ($Z_{Elec} = Z_{CT} = 0$).

importance, for example, for the potential commercial use of the lithium metal anode. Despite the extensive study of the constriction effect at solid/solid interfaces by Fleig and Maier,[20−25] it is not fully understood yet. Further research is needed to clarify how the constriction effect can be manipulated or even mitigated.

Using a 3D electric network model, we demonstrate that the interface contribution to the electrode impedance is generally composed of a CT signal and a geometric constriction signal. Both result from the interface but differ in their origins. While the former represents a microscopic electric migration process across the interface, the latter arises from the frequency-dependent change of the electrode area that actively contributes to the transport. The interdependence between the two effects is rather intriguing and needs careful case studies for different realistic situations encountered in experiments. Here, we focus on the specific situation typically observed for a garnet-type SE in all-solid state battery structures that can be well approximated by a homogeneous SE with negligible polarization resistances at the interfaces, i.e., a situation where the CT effect is negligible. This relevant and experimentally accessible situation reveals the pure constriction effect on the impedance data and defines an important starting point for a fundamental study of the interplay between the CT effect and constriction effect.

The systematic analysis presented in this study illustrates the impact of essential parameters such as the electrode geometry and the interface morphology on the dynamic constriction effect. For this purpose, simplified interface morphologies are assumed to highlight major trends and to elucidate fundamental dependencies. Both also qualitatively apply in the case of more realistic interface morphologies but will lose clarity due to disorder effects. The analysis as a whole demonstrates that a careful analysis of impedance data may yield valuable information, for example, on pore formation and dynamics at the metal anode interface.

2. COMPUTATIONAL DETAILS

2.1. Generation of a Three-Dimensional Microstructure. The dynamic constriction effect is studied using a three-

https://doi.org/10.1021/acsami.2c07077
ACS Appl. Mater. Interfaces 2022, 14, 35545−35554

ACS Applied Materials & Interfaces www.acsami.org Research Article

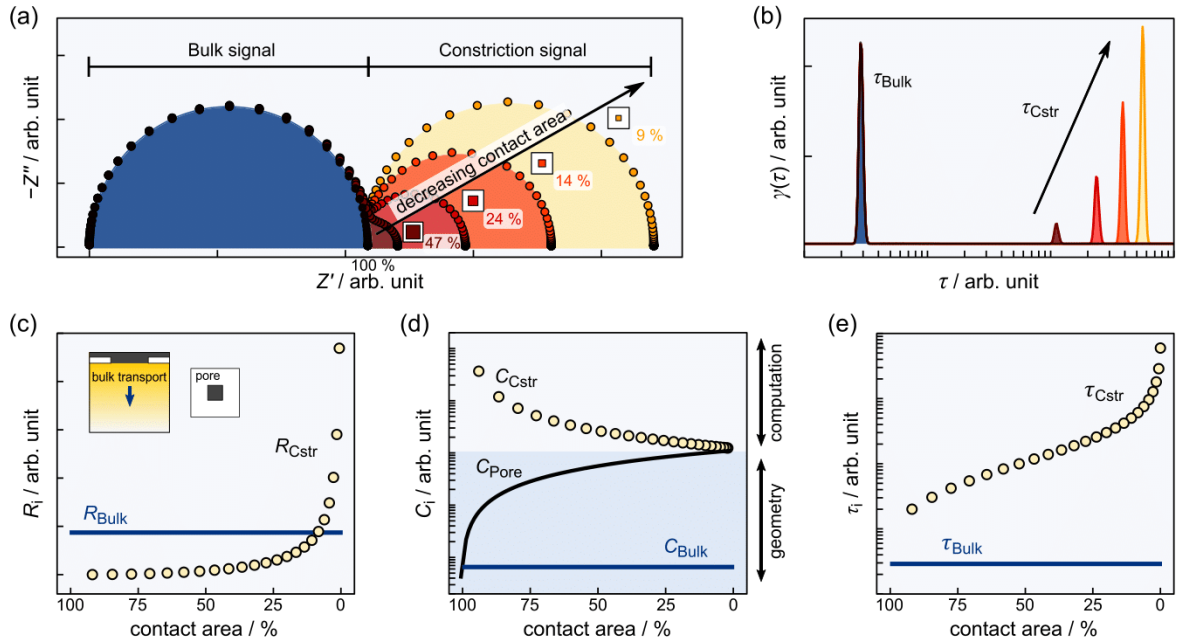

Figure 3. Impact of the contact area at the WE/SE interface on the impedance. (a) The constriction semicircle at low frequencies increases with decreasing contact area. (b) The DRT reveals a shift of the constriction signal toward larger relaxation times. (c–e) These observations are also evident considering the macroscopic transport quantities (R_i and C_i). With decreasing contact area, the limiting case of complete contact loss is approached, i.e., $R_{Cstr} \rightarrow \infty$ and $C_{Cstr} \rightarrow C_{Pore}$.

dimensional model system suitable for describing reversible metal anodes. The system under consideration consists of a parent metal electrode (e.g., Li, Na, and Ag), which is in contact with an SE. The complexity of the real system prevents a clear assignment of individual effects on the impedance. Therefore, some simplifications are necessary. We assume a homogeneous SE to better highlight the impact of the interface structure and morphology on the constriction effect. The network model used, however, can be easily extended to account for typical ceramic SE materials consisting of grains separated by grain boundaries.[10] Additionally, the number of geometric model parameters describing the interface is reduced by flattening the real interface and considering only pores of the same depth δ_{Int} in the system (see Figure 2a). The morphology is approximated by one or more square-shaped contact spots in the interface layer whose lateral extension is varied. Such a porous layer describes the averaged geometric properties of the interface.

Four variants of the simplified model system are studied where system parameters are systematically varied. This allows a qualitative investigation of the dynamic constriction effect with respect to its origin, the geometric impact of the electrode size, the effect of the interface morphology, and the impact of the pore characteristics, see Figure 2b–e from left to right, respectively. Despite these simplifications, the conclusions drawn from the computations with respect to the constriction effect are of a general nature and valid for all solid/solid interfaces. In particular, the qualitative results derived also apply to more complex morphologies and microstructures of the SE as observed in the real system.

In this study, we assume that the SE possesses a cubic shape ($L_x = L_y = L_z$) and that one of its surfaces is contacted by the working electrode (WE) forming the porous interface. The depth δ_{Int} of the pores between the WE and the SE is set to 1/5000 of the geometric extension L_z of the sample perpendicular to the surface, i.e., the nominal transport direction.

2.2. Description of Charge Transport through the System. A 3D impedance network is used to describe the transport processes between the electrode and SE across the porous interface of the model system. For this purpose, the entire sample volume (including the pores) is divided into individual voxels of edge length d. In this process, each voxel is assigned to either a grain within the sample (blue), a pore at the interface (white), or the metal electrode (gray). A single planar layer with voxels of constant thickness δ_{Int} is inserted between the electrode and the sample to describe the interface morphology and thus the contact between the WE and SE (see Figure 2f).

A nodal network must be set up to determine the impedance on the basis of the discretized model by assigning a node to the center of each voxel. The different transport processes can be distinguished from each other by comparing the structural properties of adjacent voxels. While the dielectric properties of the pores are modeled by a capacitor only, each electric charge transport process is described by an *RC*-element (see Figure 2g). The microscopic bulk transport within the ceramic is described by two *RC*-elements ($2 \cdot Z_{Bulk}$) connected in series to each other in the branch between two nodes. The charge transport within the electrode ($2 \cdot Z_{Elec}$) and the CT step at the metal/SE interface ($Z_{Elec} + Z_{CT} + Z_{Bulk}$) is described accordingly. In addition, transport between pore voxels and solid voxels, i.e., WE or SE, is described by the series connection of an *RC*-element with a capacitor ($Z_{Elec} + Z_{Pore}$ or $Z_{Bulk} + Z_{Pore}$) and the transport between two pore voxels is modeled by two serially connected capacitors ($2 \cdot Z_{Pore}$).

The resistances and capacitances of the local equivalent circuit elements are calculated according to the rules for

https://doi.org/10.1021/acsami.2c07077
ACS Appl. Mater. Interfaces 2022, 14, 35545−35554

ACS Applied Materials & Interfaces www.acsami.org Research Article

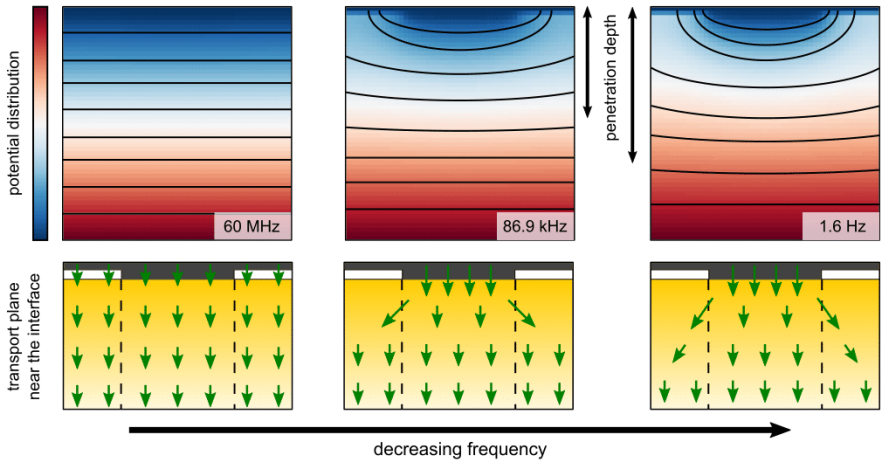

Figure 4. Frequency-dependent change of the potential distribution in the system. Cross section of a model system, consisting of a metal WE (gray), pore volume (white), and the homogenous SE. Green arrows indicate the current distribution at various frequencies. At high frequencies (left), the pores at the interface are dielectrically shorted and the entire electrode area contributes to the transport. At low frequencies (right), the pores are insulating and the electrode area as well as the SE volume actively contributing to the transport is reduced. The penetration depth increases for lower frequencies leading to the frequency-dependent constriction resistance.

conductors and plate capacitors. The bulk parameters (σ_{Bulk} = 0.46 mS/cm and ε_{Bulk} = 150·ε_0) are based on the solid electrolyte LLZO, and the permittivity of the pore ε_{Int} is in the range of vacuum permittivity ε_0.[11,26,27] The transport within the electrode and the CT step at the interface is assumed to be resistance-free as proven for garnet-type SEs (Z_{Elec} = Z_{CT} = 0).[11−13] Thus, bulk transport is the only electric migration process considered within the homogeneous SE system. The interplay of the constriction effect with other transport processes like a resistive CT step at the interface or the transport across grain boundaries (see Figure 2a) is beyond the scope of this paper and will be discussed in a subsequent work. Further details about setting up and solving the 3D network model and its solution are given in our previous work.[10]

2.3. Technical Details in the Analysis of the Computed Impedance Spectra. The simulation of the impedance spectra based on the simplified 1D fit equivalent circuit and the distribution of relaxation times (DRT) analyses were performed using the commercial software RelaxIS 3 (version 3.0.18.15, rhd instruments GmbH & Co. KG). The impedance spectra computed by the 3D electric network model are (almost) free of noise signals. The Kramers−Kronig test for these spectra yields residuals in the order of 10^{-6}%.[28] Thus, the results for all frequencies were considered in the analysis of the impedance spectra, and only a small regularization term was required in the calculation of each DRT.[29]

3. RESULTS

3.1. Origin of the Constriction Contribution in the Impedance. To understand the origin of the dynamic constriction effect and its impact on the impedance, we compute a series of impedance spectra of the model system, as depicted in Figure 2b. The electrode and SE surface are of the same size ($A_{electrode}$ = A_{SE}). The single square-shaped contact spot sandwiched between the square-shaped WE and the square-shaped sample surface is systematically varied in size ($A_{contact}$). The empty space between the WE and SE surface corresponds to the pore and constitutes a capacitor-like arrangement, i.e., WE−air−SE.

3.1.1. Impedance as Function of the Contact Area between the Electrode and SE. Figure 3a shows the impedance results for five different contact area sizes $A_{contact}$ between the WE and SE. Without pores at the interface (A_{SE} = $A_{electrode}$ = $A_{contact}$), the impedance consists of one semicircle only. The reduction of the contact area (A_{SE} = $A_{electrode}$ > $A_{contact}$), however, leads to the formation of a second semicircle at lower frequency without affecting the high-frequency contribution to the impedance. Thus, the latter is independent of the contact area $A_{contact}$ between the electrode and the SE and can be assigned to the bulk transport. The semicircle at low frequencies does not correspond to an additional electric microscopic transport process in the system. It solely arises due to the formation of pores at the interface and can be attributed to the resulting dynamic constriction effect.

The described behavior is also reflected in the corresponding DRTs[29,30] of the five impedance spectra (see Figure 3b). The DRT consists of a single signal at τ_{Bulk} when there is a full contact between the SE and WE. A second signal at a larger relaxation time τ_{Cstr} emerges when the contact area is reduced. The amplitude and the time constant of the second signal increase upon reducing the contact area $A_{contact}$.

The computed impedance spectra are fitted with a 1D equivalent circuit model consisting of two *RC*-elements connected in series to highlight the qualitative changes in the impedance (see Figure 3c). The bulk transport parameters (blue) are independent of the change in contact area $A_{contact}$. In contrast, the constriction resistance R_{Cstr} (yellow) shows a diverging behavior with decreasing contact area ($R_{Cstr} \rightarrow \infty$ for $A_{contact} \rightarrow 0$). The qualitative behavior is roughly consistent with that of a conductor ($R \sim 1/A_{contact}$). However, a simple functional relationship between constriction resistance R_{Cstr} and contact area $A_{contact}$ cannot be observed (c.f. Figure 6).

The computed constriction capacitance C_{Cstr} (yellow) decreases with decreasing contact area $A_{contact}$ (see Figure 3d). Since a decreasing contact area corresponds to an increase in pore volume at the interface, the corresponding geometric

https://doi.org/10.1021/acsami.2c07077
ACS Appl. Mater. Interfaces 2022, 14, 35545−35554

ACS Applied Materials & Interfaces www.acsami.org Research Article

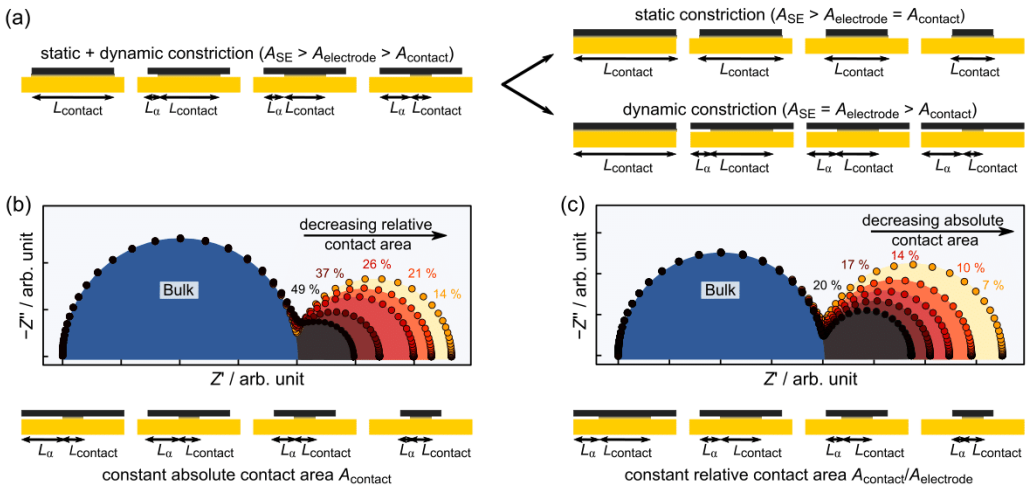

Figure 5. Impact of the electrode size on the constriction effect. (a) The relation of the electrode area $A_{electrode}$, the surface area of the sample A_{SE}, and the contact area $A_{contact}$ determines the kind of constriction that occurs within the system. Despite the constant absolute contact area $A_{contact}$ (b) or constant relative contact area $A_{contact}/A_{SE}$ (c), the dynamic constriction contribution in the impedance changes. Both descriptors alone are not sufficient to fully describe the dynamic constriction effect. The depicted impedance spectra were normalized to their individual bulk contribution to minimize the impact of the static constriction effect.

capacitance C_{Pore} of the pore volume (black) increases. For small contact areas, the constriction capacitance converges toward this pore capacitance ($C_{Cstr} \rightarrow C_{Pore}$ for $A_{contact} \rightarrow 0$). Consequently, the constriction capacitance can be used to roughly estimate the (average) depth of the pores.[20−22]

The constriction time constant ($\tau = R{\cdot}C$) increases for a decreasing contact area, i.e., for a growing single planar pore $A_{pore} = A_{electrode} - A_{contact}$ (see Figure 3e). This behavior can be attributed to the larger change in the increasing constriction resistance R_{Cstr} compared to the decreasing and converging constriction capacitance C_{Cstr}.

3.1.2. Understanding the Formation of the Constriction Signal in the Impedance. The formation of the constriction signal in the impedance spectrum for $A_{SE} = A_{electrode} > A_{contact}$ can be understood as follows. An impedance spectrum is measured over an extended frequency range. The conduction response of the individual transport processes in the material (e.g., bulk or GB transport) is frequency-dependent. This also holds for the contribution of the capacitor-like pore at the interface. At high frequencies, the dielectric conduction response starts to dominate, short-circuiting the pores at the interface. As a result, the component of the potential gradient perpendicular to the macroscopic transport direction vanishes. This leads to horizontal equipotential lines perpendicular to the transport direction across the entire sample ($A_{electrode,\ active} = A_{electrode}$). It corresponds to a quasi-1D transport between the WE and counter electrode (CE) across the electrode area at high frequencies (see arrows in Figure 4 (left)). This situation allows a determination of the bulk transport parameters (σ_{Bulk}, ε_{Bulk}) without pronounced errors based on the cell geometry.[20−25]

Upon frequency reduction in the impedance measurement, the conduction response of the individual transport processes changes from dielectric to electric conduction. Since the pores are insulating in this frequency range, the electrode area contributing to transport is reduced to the real contact area between the electrode and the SE ($A_{electrode,\ active} = A_{contact}$). Similar to the behavior of a conductor ($R \sim 1/A$), a smaller active electrode area leads to a larger resistance. Consequently, the frequency-dependent change of the active electrode area $A_{electrode,\ active}$ leads to the additional constriction contribution in the impedance spectrum.[20−25]

The reduction of the active electrode area $A_{electrode,\ active}$ to the real contact area $A_{contact}$ also affects the potential distribution in the SE and creates a certain SE volume fraction in which lower local current densities are observed (see arrows in Figure 4 (center)). Charge transport near the interface occurs in this case in 3D and not in quasi-1D. An approximate measure of this effect is the penetration depth, which corresponds to the distance from the electrode where the equipotential lines below the electrode within the SE become horizontal again. The corresponding volume ranging from the interface down to the penetration depth is referred to as the constriction region. Since the penetration depth depends on the applied frequency ν of the external exciting electric field (see arrows in Figure 4 (right)), the constriction effect is frequency-dependent.

The separation of the impedance into a bulk and a dynamic constriction contribution depends on the frequency, below which the pores at the interface cease to conduct dielectrically (cf. Figure 1c). If the pores are already insulating in the characteristic frequency range of the bulk transport, then both contributions cannot be separated from each other.[22] The situation is then comparable to the static constriction effect, in the sense that it leads to a scaling of the individual impedance contributions (cf. Figure 1b). Consequently, the actual specific transport parameters of the bulk process can no longer be determined correctly in this case.

In summary, the frequency-dependent change of the active electrode area $A_{electrode,\ active}$ and the associated change of the SE volume involved in the transport leads to additional impedance contributions in the spectrum. Thus, a semantic distinction between contact area $A_{contact}$ and electrode area $A_{electrode}$ is necessary to adequately describe the impedance behavior with respect to the dynamic constriction effect. The electrode area $A_{electrode} = E_x{\cdot}E_y$ describes the cross section of

https://doi.org/10.1021/acsami.2c07077
ACS Appl. Mater. Interfaces 2022, 14, 35545−35554

ACS Applied Materials & Interfaces www.acsami.org Research Article

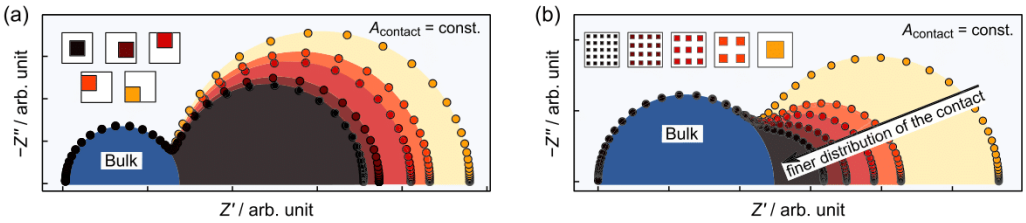

Figure 6. Dependence of the constriction resistance on the interface morphology. (a) The constriction effect, especially its resistance, depends strongly on the position of the contact spot in the interface layer. (b) A finer distribution of the contact area at the interface leads to a strong reduction of the constriction resistance.

the electrode to which a potential is applied. The contact area $A_{contact}$ describes the portion of the electrode area that is in physical contact with the SE. The contact area is often smaller than the electrode area ($A_{contact} \leq A_{electrode}$) due to the mechanic properties of both solids involved, i.e., not the entire solid electrolyte surface is in contact with the metal electrode unlike liquid electrolytes that mostly wet the entire electrode surface.

3.2. Dependence of the Constriction Characteristics on the Interface Morphology. The time constant τ_{Cstr} of the constriction contribution has a major influence on the shape of the impedance spectrum (cf. Figure 1c) and, consequently, on the conclusions about the experimentally or theoretically studied system drawn from the impedance analysis. Therefore, further investigations are required considering more realistic systems. In the following, we systematically vary the electrode geometry according to Figure 2c, the interface morphology according to Figure 2d, and the properties of the pores (depth δ_{Int}) or, more general, insulating inclusions (permittivity ε_{Int}) according to Figure 2e.

3.2.1. Impact of the Electrode Size on the Constriction Effect. First, we will study the impact of the electrode size on the transport behavior of the model system depicted in Figure 2c. Prior to analyzing the data, it should be noted that different electrode sizes $A_{electrode}$ can lead to different types of constriction effects. A larger surface area of the SE than the electrode area ($A_{SE} > A_{electrode} = A_{contact}$) will always lead to a static constriction since the available pathways through the structure are restricted at the interface. Solely dynamic constriction occurs in the system, when the electrode area is larger than the contact area between the SE and electrode ($A_{SE} = A_{electrode} > A_{contact}$). In this case, the transport paths are only constrained in a specific frequency range. A superposition of both static and dynamic constriction effects will occur when other relations between the three areas hold, e.g., $A_{SE} > A_{electrode} > A_{contact}$.

As can be seen in Figure 5a, many variations of the superimposed case (left) and the pure static (top right) and dynamic (bottom right) case can be anticipated. Thus, a semantic distinction between absolute contact area $A_{contact}$ and relative contact area $A_{contact}/A_{electrode}$ is beneficial but not mandatory when considering the two pure effects. The change in absolute contact area also results in a change in relative contact area in the case of the dynamic effect, while the relative contact area is always maintained (= 1) in the static situation.

Figure 5b shows the impedance results for five different electrode sizes ($A_{SE} \geq A_{electrode}$) at constant absolute contact area $A_{contact}$. Each impedance spectrum is normalized to the same bulk contribution to minimize the impact of the surplus SE volume at the edges of the electrode, i.e., the scaling of the impedance due to the static constriction effect. The individual contributions to the normalized impedance due to dynamic constriction differ significantly for the five cases. Smaller electrodes with larger relative contact areas $A_{contact}/A_{electrode}$ result in a lower impedance due to a decrease in the penetration depth into the SE and the increase in the volume contributing to the transport.

Similarly, Figure 5c depicts the impedance results for five different electrode sizes $A_{electrode}$ at constant relative contact area $A_{contact}/A_{electrode}$. Again, all impedance spectra are normalized to the same bulk contribution to not include the quantitative scaling due to the static constriction effect. Also, in this situation, there are significant changes in the dynamic constriction contribution visible in the normalized impedance spectra. The increase in the electrode size $A_{electrode}$ and the accompanying increase in the absolute contact area $A_{contact}$ lead to a decrease in the normalized dynamic constriction contribution.

Both series of impedance spectra underline that neither the relative contact area $A_{contact}/A_{electrode}$ nor the absolute contact area $A_{contact}$ alone is sufficient as a descriptor for the constriction effect. Consequently, larger electrodes and also larger absolute contact areas do not necessarily reduce the area-specific constriction resistance. Similarly, equal relative contact areas do not necessarily lead to equal constriction contributions.

3.2.2. Effect of the Distribution of the Contact Area at the Interface. We will now turn to morphology effects, i.e., the effect of the distribution of the contact area at the interface $A_{contact}$, which is known to have a huge influence on the constriction effect.[14] Mapping the real interface morphology in experiments is challenging since it is hardly accessible. The methods commonly used for characterizing interfaces in all-solid state batteries are transmission electron microscopy or focused ion beam scanning electron microscopy. Both are destructive and cannot be employed in situ on realistic structures. Thus, they usually can only provide static snapshots of a local region of the interface and thus little statistical information.

Obviously, pores are usually distributed over the entire electrode surface and their shapes and sizes can vary locally. Such disorder and inhomogeneities significantly affect the potential distribution within the system and are therefore expected to influence the shape of the impedance contribution due to constriction. To study the influence of individual morphology effects in more detail and to restrict the number of geometric parameters describing the pore distribution, we will analyze two simplified model cases depicted as insets in Figure 6. Instead of one contact spot centered in the interface layer, we will study two effects:

https://doi.org/10.1021/acsami.2c07077
ACS Appl. Mater. Interfaces 2022, 14, 35545−35554

ACS Applied Materials & Interfaces www.acsami.org Research Article

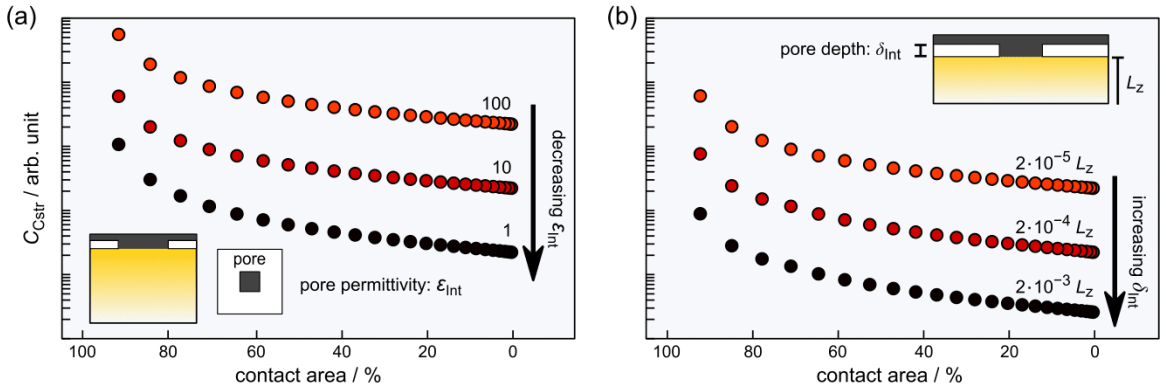

Figure 7. Impact of (a) the permittivity and (b) the thickness of the insulating layer on the constriction effect, i.e., pores in the considered model systems. The variations of the depth of the pores and their permittivity result in a change of the constriction capacity that is identical to that of a plate capacitor.

First, we will solely vary the position of the contact spot sandwiched between the electrode and the SE surface, while the contact area $A_{contact}$ is kept constant. Furthermore, we set $A_{SE} = A_{electrode}$, i.e., there is no static constriction effect that affects the computational results. The impedance spectra derived from the 3D electric network model (see Figure 6a) highlight that the larger the distance between the center of the contact spot and the center of the sample, the more pronounced is the dynamic constriction contribution to the impedance. The reason is that moving the single contact spot away from the central position leads to an increased penetration depth and a lower volume involved in the transport. Thus, a larger constriction resistance R_{Cstr} arises. The constriction capacitance C_{Cstr}, however, is almost unaffected. The combined behavior yields a longer time constant τ_{Cstr} when the distance of the contact spot from the sample center increases. When the contact spot is located at the sample center, all distances between the edges of the spot and the edges of the SE are minimized, the size of the constriction region is reduced, and the volume contributing to the transport at low frequencies is maximized. Therefore, the constriction resistance R_{Cstr} is minimal in the modeling.

Second, we divide up the contact spot into a number of regularly arranged smaller contacts of the same contact area $A_{contact}$. The impedance spectra in Figure 6b show that the dynamic constriction contribution to the impedance decreases with an increasing number of contact spots. The reason is that a finer distribution of the contact area $A_{contact}$ increases the contact surface to pore volume ratio at the interface and minimizes the distances between the centers of the contact spots and the centers of the pores. Thus, the penetration depth into the SE decreases leading to an increase in the volume contributing to the transport and a decrease in the constriction resistance R_{Cstr}.[24,25] The impact on the constriction capacitance C_{Cstr} is small as the capacitor-like pore area $A_{pore} = A_{SE} - A_{contact}$ is the same in all cases and the pores act, to a first approximation, as capacitors connected in parallel. Due to the reduction of the resistance R_{Cstr} with increasing fineness of the pore distribution, the time constant τ_{Cstr} shifts toward smaller relaxation times compared to the single contact case.

The discussion of the interface morphology highlights that a sole rearrangement of the contact spot(s) for a given contact area $A_{contact}$ will already yield a different dynamic constriction behavior. Therefore, it is challenging to derive any (simple) functional relationship between the constriction parameters (R_{Cstr} and C_{Cstr}) and the contact area $A_{contact}$.

3.2.3. Effect of the Pore Characteristics at the Interface. Finally, we address the impact of the pore properties or, more general, of insulating inclusions. The constriction effect in the case of lithium metal in contact with LLZO is caused by the formation of pores at the interface. Pores, however, are not necessarily required to cause dynamic current constriction. The continuous formation of a spatially heterogeneous insulating layer such as a highly resistive SEI at the interface can also lead to current constriction.[31] The same holds true for the time-dependent depletion of charge carriers at the interface due to the finite diffusion coefficient of the electrode material.[11,32,33] Hence, it is worth knowing how different (pore) permittivities ε_{Int} and pore depths δ_{Int} may affect the dynamic constriction phenomenon.

Both parameters do not influence the constriction resistance R_{Cstr}, but the constriction capacitance is proportional to the permittivity of the pores or inclusions ($C_{Cstr} \sim \varepsilon_{Int}$) and inversely proportional to the pore depths ($C_{Cstr} \sim 1/\delta_{Int}$). It should be emphasized that the quantitative changes are the same as those of a plate capacitor (see Figure 7). The time constant τ_{Cstr} shifts toward larger relaxation times for larger permittivity and toward smaller relaxation times for larger pore depth. It suggests that a local variation of the pore depth at the interface results in a distribution of time constants. Thus, a distortion of the low-frequency contribution of the impedance in the Nyquist representation is expected.[20,22] As a consequence, the shape of the impedance spectrum provides first indications about the homogeneity of the interface.

The discussed dependence of the constriction impedance on the pore characteristics shows that certain pore depths cannot be resolved experimentally with IS. Deep pores have a small time constant, which may well be in the range of bulk transport, leading to a transport behavior comparable to static constriction and a quantitative scaling of individual impedance signals. Thus, the impact of constriction is not separable from the individual impedance contributions of the transport signals. In contrast, shallow pores show large relaxation times, which may correspond to characteristic frequencies outside the typical frequency range of IS, i.e., these pores remain dielectrically conductive in the measurement range between MHz and several Hz. Therefore, it is possible that the IS data will not significantly differ from an ideal contact, if the

https://doi.org/10.1021/acsami.2c07077
ACS Appl. Mater. Interfaces 2022, 14, 35545−35554

constriction impedance is not within the chosen frequency interval. Unfortunately, it is not possible to give a universal value for the lower detection limit of pores since constriction as a geometric phenomenon also depends on various other parameters such as the interface morphology or the sample dimensions.

4. SUMMARY AND CONCLUSIONS

The following recommendations for the analysis of experimental impedance results can be derived from the 3D modeling of metal anodes with constriction effect:

- The interface contribution to the impedance is, in general, composed of a (true) charge transfer and a dynamic constriction contribution. Current constriction is not a self-contained type of migration process in the strict sense, i.e., it is not comparable to electric grain boundary or bulk transport. Rather, the dynamic constriction contribution in the impedance is related to the frequency-dependent change of the electrode area actively contributing to the transport (electrode area ↔ contact area), representing the frequency-dependent role of dielectric charge transfer across purely capacitive regions (e.g., pores or insulating interlayer patches) at the interface. It is a geometric effect that must be expected at different length scales.
- The constriction phenomenon is mainly affected by the SE volume near the interface (constriction region). The distance from the interface to the compensation of the constriction (penetration depth) is, in general, a function of the frequency.
- The spatial distribution of the contact area at the interface has a significant impact on the penetration depth into the SE. This is accompanied by a change of the fraction of the SE volume that contributes to the transport at low frequencies. A larger SE volume contributing leads to a lower constriction resistance R_{Cstr}. Consequently, it is challenging to derive a simple relationship between constriction resistance and contact area.
- The constriction capacity is influenced by the morphology of the interface, e.g., the shape of the pores and the distribution of the contact area. Its behavior is identical to that of a plate capacitor ($C_{Cstr} \sim \varepsilon_{Int}/\delta_{Int}$) when the depth of the pore(s) and its permittivity change. The constriction capacitance converges against the geometric capacitance of the macroscopic pore at the interface when the contact area $A_{contact}$ goes to zero.

The 3D electric network model presented allows the systematic study of morphology changes at the electrode/sample interface and their influence on the impedance response of the system. The constriction contribution in the impedance results from, e.g., pores or inclusions at the interface, whose conductive behavior changes from dielectrically conductive to insulating with decreasing frequency of the external electric field. The dynamic constriction phenomenon is solely a geometric effect, and its impact (e.g., size of the constriction region or even the effective contact area) is not constant but depends on the excitation frequency. The phenomenon may have its origin on various length scales of the system ranging from mesoscopic to macroscopic. Thus, the "interface impedance" in the case of many solid/solid interfaces is more than a pure charge transfer step as it is often assumed in the literature. Therefore, the term interface impedance should be avoided; instead, it is better to classify the interface contribution to the impedance spectrum according to its origin as charge transfer contribution or constriction contribution.

Overall, the network model used is a powerful tool to gain a better understanding of experimental impedance data. It may provide valuable insight into the microscopic processes occurring within the considered electrochemical cell, e.g., at the WE/SE interface. Making full use of the strength of the modeling requires reliable structural information of the interfaces and layers comprising the sample. Thus, a careful structural analysis of the specimens studied is essential and must accompany the theoretical analysis of the impedance data. Theory alone can only point out qualitative trends arising from changes of material parameters or specific morphological changes, whereas the combined analysis will yield more valuable information, e.g., on the correlation between pore formation and dynamics at the metal anode interface of all-solid-state batteries. Such an approach may have the potential for the targeted monitoring of hidden morphological changes at the metal/SE interface at the mesoscopic level and, thus, for a kind of "state-of-health" control system in applications. However, this vision requires more systematic combined experimental and theoretical studies on model systems with a high degree of control over the interfacial morphology.

AUTHOR INFORMATION

Corresponding Author

Janis K. Eckhardt − *Institute for Theoretical Physics and Center for Materials Research (ZfM), Justus Liebig University, D-35392 Giessen, Germany;* orcid.org/0000-0002-2799-0599; Email: janis.k.eckhardt@theo.physik.uni-giessen.de

Authors

Peter J. Klar − *Center for Materials Research (ZfM) and Institute of Experimental Physics I, Justus Liebig University, D-35392 Giessen, Germany;* orcid.org/0000-0002-4513-0330

Jürgen Janek − *Center for Materials Research (ZfM), Justus Liebig University, D-35392 Giessen, Germany; Institute of Physical Chemistry, Justus Liebig University, D-35392 Giessen, Germany;* orcid.org/0000-0002-9221-4756

Christian Heiliger − *Institute for Theoretical Physics and Center for Materials Research (ZfM), Justus Liebig University, D-35392 Giessen, Germany*

Complete contact information is available at: https://pubs.acs.org/10.1021/acsami.2c07077

Notes

The authors declare no competing financial interest.

ACKNOWLEDGMENTS

We greatly appreciate helpful discussions with Till Fuchs and Simon Burkhardt. We acknowledge computational resources provided by the HPC Core Facility and the HRZ of the Justus-Liebig-University Giessen. We would like to thank MSc. Philipp Risius and Dr. Marcel Giar of HPC-Hessen, funded by the State Ministry of Higher Education, Research, and the Arts (HMWK), for programming advice. Financial support is provided by the DFG via the GRK (Research Training

https://doi.org/10.1021/acsami.2c07077
ACS Appl. Mater. Interfaces 2022, 14, 35545−35554

Group) 2204 "Substitute Materials for Sustainable Energy Technologies".

REFERENCES

(1) Takeda, Y.; Yamamoto, O.; Imanishi, N. Lithium Dendrite Formation on a Lithium Metal Anode from Liquid, Polymer and Solid Electrolytes. *Electrochemistry* **2016**, *84*, 210−218.

(2) Tarascon, J. M.; Armand, M., Issues and challenges facing rechargeable lithium batteries. In *Materials for Sustainable Energy*; Co-Published with Macmillan Publishers Ltd: UK: 2010; pp. 171−179.

(3) Xu, K. Nonaqueous Liquid Electrolytes for Lithium-Based Rechargeable Batteries. *Chem. Rev.* **2004**, *104*, 4303−4418.

(4) Janek, J.; Majoni, S. Investigation of Charge Transport Across the AglAgI-interface: (I) Occurrence of Periodic Phenomena During Anodic Dissolution of Silver. *Ber. Bunsenges. Phys. Chem.* **1995**, *99*, 14−20.

(5) Schmalzried, H.; Janek, J. Chemical kinetics of phase boundaries in solids. *Ber. Bunsenges. Phys. Chem.* **1998**, *102*, 127−143.

(6) Murugan, R.; Thangadurai, V.; Weppner, W. Fast Lithium Ion Conduction in Garnet-Type $Li_7La_3Zr_2O_{12}$. *Angew. Chem., Int. Ed.* **2007**, *46*, 7778−7781.

(7) Zhu, Y.; Connell, J. G.; Tepavcevic, S.; Zapol, P.; Garcia-Mendez, R.; Taylor, N. J.; Sakamoto, J.; Ingram, B. J.; Curtiss, L. A.; Freeland, J. W.; Fong, D. D.; Markovic, N. M. Dopant-Dependent Stability of Garnet Solid Electrolyte Interfaces with Lithium Metal. *Adv. Energy Mater.* **2019**, *9*, 1803440.

(8) Connell, J. G.; Fuchs, T.; Hartmann, H.; Krauskopf, T.; Zhu, Y.; Sann, J.; Garcia-Mendez, R.; Sakamoto, J.; Tepavcevic, S.; Janek, J. Kinetic versus Thermodynamic Stability of LLZO in Contact with Lithium Metal. *Chem. Mater.* **2020**, *32*, 10207−10215.

(9) Zhu, Y.; He, X.; Mo, Y. Origin of Outstanding Stability in the Lithium Solid Electrolyte Materials: Insights from Thermodynamic Analyses Based on First-Principles Calculations. *ACS Appl. Mater. Interfaces* **2015**, *7*, 23685−23693.

(10) Eckhardt, J. K.; Burkhardt, S.; Zahnow, J.; Elm, M. T.; Janek, J.; Klar, P. J.; Heiliger, C. Understanding the Impact of Microstructure on Charge Transport in Polycrystalline Materials Through Impedance Modelling. *J. Electrochem. Soc.* **2021**, *168*, No. 090516.

(11) Krauskopf, T.; Hartmann, H.; Zeier, W. G.; Janek, J. Toward a Fundamental Understanding of the Lithium Metal Anode in Solid-State Batteries—An Electrochemo-Mechanical Study on the Garnet-Type Solid Electrolyte $Li_{6.25}Al_{0.25}La_3Zr_2O_{12}$. *ACS Appl. Mater. Interfaces* **2019**, *11*, 14463−14477.

(12) Sharafi, A.; Kazyak, E.; Davis, A. L.; Yu, S.; Thompson, T.; Siegel, D. J.; Dasgupta, N. P.; Sakamoto, J. Surface Chemistry Mechanism of Ultra-Low Interfacial Resistance in the Solid-State Electrolyte $Li_7La_3Zr_2O_{12}$. *Chem. Mater.* **2017**, *29*, 7961−7968.

(13) Gao, J.; Guo, X.; Li, Y.; Ma, Z.; Guo, X.; Li, H.; Zhu, Y.; Zhou, W. The Ab Initio Calculations on the Areal Specific Resistance of Li-Metal/$Li_7La_3Zr_2O_{12}$ Interphase. *Adv. Theory Simul.* **2019**, *2*, 1900028.

(14) Holm, R., *Electric Contacts: Theory and Application.*; Springer Verlag: 1967; p 484, DOI: 10.1007/978-3-662-06688-1_88.

(15) Slade, P. G., *Electrical contacts: principles and applications.*; CRC press: 2017; p 1311, DOI: 10.1201/b15640.

(16) Denhoff, M. W. An accurate calculation of spreading resistance. *J. Phys. D: Appl. Phys.* **2006**, *39*, 1761−1765.

(17) Kennedy, D. P. Spreading Resistance in Cylindrical Semiconductor Devices. *J. Appl. Phys.* **1960**, *31*, 1490−1497.

(18) Mazur, R. G.; Dickey, D. H. A Spreading Resistance Technique for Resistivity Measurements on Silicon. *J. Electrochem. Soc.* **1966**, *113*, 255.

(19) Zhang, P.; Lau, Y. Y.; Timsit, R. S. On the Spreading Resistance of Thin-Film Contacts. *IEEE Trans. Electron Devices* **2012**, *59*, 1936−1940.

(20) Fleig, J.; Maier, J. Finite element calculations of impedance effects at point contacts. *Electrochim. Acta* **1996**, *41*, 1003−1009.

(21) Fleig, J.; Maier, J. Point contacts in solid state ionics: finite element calculations and local conductivity measurements. *Solid State Ionics* **1996**, *86-88*, 1351−1356.

(22) Fleig, J.; Maier, J. The Influence of Laterally Inhomogeneous Contacts on the Impedance of Solid Materials: A Three-Dimensional Finite-Element Study. *J. Electroceram.* **1997**, *1*, 73−89.

(23) Fleig, J.; Maier, J. Rough electrodes in solid and liquid electrochemistry: impact of morphology on the impedance. *Solid State Ionics* **1997**, *94*, 199−207.

(24) Fleig, J.; Maier, J. The Influence of Current Constriction on the Impedance of Polarizable Electrodes: Application to Fuel Cell Electrodes. *J. Electrochem. Soc.* **1997**, *144*, L302−L305.

(25) Fleig, J.; Maier, J. Finite-Element Calculations on the Impedance of Electroceramics with Highly Resistive Grain Boundaries: I, Laterally Inhomogeneous Grain Boundaries. *J. Am. Ceram. Soc.* **1999**, *82*, 3485−3493.

(26) Rettenwander, D.; Welzl, A.; Cheng, L.; Fleig, J.; Musso, M.; Suard, E.; Doeff, M. M.; Redhammer, G. J.; Amthauer, G. Synthesis, Crystal Chemistry, and Electrochemical Properties of $Li_{7-2x}La_3Zr_{2-x}Mo_xO_{12}$ (x = 0.1−0.4): Stabilization of the Cubic Garnet Polymorph via Substitution of Zr^{4+} by Mo^{6+}. *Inorg. Chem.* **2015**, *54*, 10440−10449.

(27) Loho, C.; Djenadic, R.; Bruns, M.; Clemens, O.; Hahn, H. Garnet-Type $Li_7La_3Zr_2O_{12}$ Solid Electrolyte Thin Films Grown by CO_2-Laser Assisted CVD for All-Solid-State Batteries. *J. Electrochem. Soc.* **2017**, *164*, A6131.

(28) Boukamp, B. Electrochemical impedance spectroscopy in solid state ionics: recent advances. *Solid State Ionics* **2004**, *169*, 65−73.

(29) Wan, T. H.; Saccoccio, M.; Chen, C.; Ciucci, F. Influence of the Discretization Methods on the Distribution of Relaxation Times Deconvolution: Implementing Radial Basis Functions with DRTtools. *Electrochim. Acta* **2015**, *184*, 483−499.

(30) Ivers-Tiffée, E.; Weber, A. Evaluation of electrochemical impedance spectra by the distribution of relaxation times. *J. Ceram. Soc. Jpn.* **2017**, *125*, 193−201.

(31) Otto, S.-K.; Fuchs, T.; Moryson, Y.; Lerch, C.; Mogwitz, B.; Sann, J.; Janek, J.; Henss, A. Storage of Lithium Metal: The Role of the Native Passivation Layer for the Anode Interface Resistance in Solid State Batteries. *ACS Appl. Energy Mater.* **2021**, *4*, 12798−12807.

(32) Krauskopf, T.; Mogwitz, B.; Rosenbach, C.; Zeier, W. G.; Janek, J. Diffusion Limitation of Lithium Metal and Li−Mg Alloy Anodes on LLZO Type Solid Electrolytes as a Function of Temperature and Pressure. *Adv. Energy Mater.* **2019**, *9*, 1902568.

(33) Krauskopf, T.; Richter, F. H.; Zeier, W. G.; Janek, J. Physicochemical Concepts of the Lithium Metal Anode in Solid-State Batteries. *Chem. Rev.* **2020**, *120*, 7745−7794.

https://doi.org/10.1021/acsami.2c07077
ACS Appl. Mater. Interfaces 2022, 14, 35545−35554

2.5 Incompatibility of Pore Formation with Physical-Based 1D Circuit Models

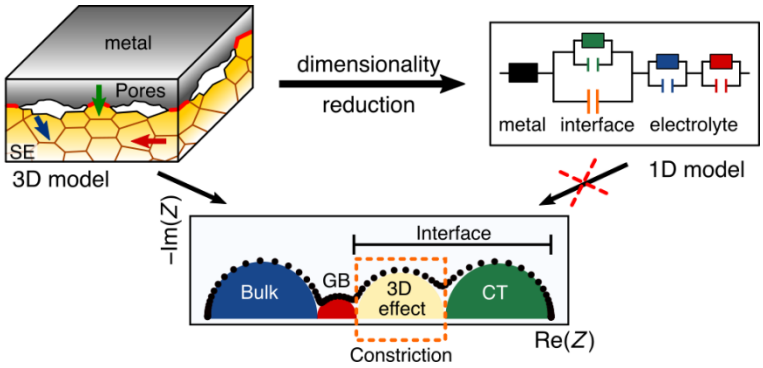

Abstract

A non-ideal contact at the electrode/solid electrolyte interface of a solid-state battery arising due to pores (voids) or inclusions results in a geometric constriction effect that severely deteriorates the electric transport properties of the battery cell. The lack of understanding of this phenomenon hinders the optimization process of novel components, such as reversible and high-rate metal anodes. Deeper insight into the constriction phenomenon is necessary to correctly monitor interface degradation and to accelerate the successful use of metal anodes in solid-state batteries. Here, we use a 3D electric network model to study the fundamentals of the constriction effect. Our findings suggest that dynamic constriction as a non-local effect cannot be captured by conventional 1D equivalent circuit models and that its electric behavior is not ad hoc predictable. It strongly depends on the interplay of the geometry of the interface causing the constriction and the microscopic transport processes in the adjacent phases. In the presence of constriction, the contribution from the non-ideal electrode/solid electrolyte interface to the impedance spectrum may exhibit two signals that cannot be explained when the porous interface is described by a physical-based (effective medium theory) 1D equivalent circuit model. In consequence, the widespread assumption of a single interface contribution to the experimental impedance spectrum may be entirely misleading and can cause serious misinterpretation.

Reference

3D Impedance Modelling of Metal Anodes in Solid-State Batteries – Incompatibility of Pore Formation and Constriction Effect in Physical-Based 1D Circuit Models. Janis K. Eckhardt, Till Fuchs, Simon Burkhardt, Peter J. Klar, Jürgen Janek, and Christian Heiliger *ACS Appl. Mater. Interfaces* **2022**, 14, 37, 42757-42769. (DOI: 10.1021/acsami.2c12991)

Reproduced with permission

ACS APPLIED MATERIALS & INTERFACES

www.acsami.org Research Article

3D Impedance Modeling of Metal Anodes in Solid-State Batteries—Incompatibility of Pore Formation and Constriction Effect in Physical-Based 1D Circuit Models

Janis K. Eckhardt,* Till Fuchs, Simon Burkhardt, Peter J. Klar, Jürgen Janek, and Christian Heiliger

Cite This: ACS Appl. Mater. Interfaces 2022, 14, 42757−42769 Read Online

ACCESS | Metrics & More | Article Recommendations | Supporting Information

ABSTRACT: A non-ideal contact at the electrode/solid electrolyte interface of a solid-state battery arising due to pores (voids) or inclusions results in a geometric constriction effect that severely deteriorates the electric transport properties of the battery cell. The lack of understanding of this phenomenon hinders the optimization process of novel components, such as reversible and high-rate metal anodes. Deeper insight into the constriction phenomenon is necessary to correctly monitor interface degradation and to accelerate the successful use of metal anodes in solid-state batteries. Here, we use a 3D electric network model to study the fundamentals of the constriction effect. Our findings suggest that dynamic constriction as a non-local effect cannot be captured by conventional 1D equivalent circuit models and that its electric behavior is not ad hoc predictable. It strongly depends on the interplay of the geometry of the interface causing the constriction and the microscopic transport processes in the adjacent phases. In the presence of constriction, the contribution from the non-ideal electrode/solid electrolyte interface to the impedance spectrum may exhibit two signals that cannot be explained when the porous interface is described by a physical-based (effective medium theory) 1D equivalent circuit model. In consequence, the widespread assumption of a single interface contribution to the experimental impedance spectrum may be entirely misleading and can cause serious misinterpretation.

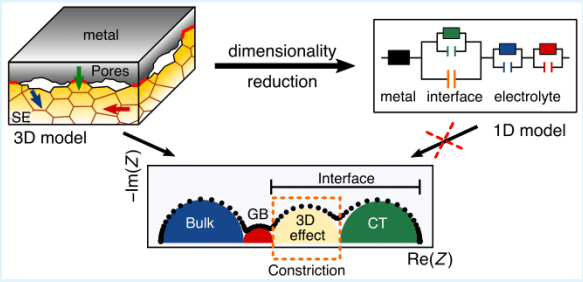

KEYWORDS: *reversible metal anode, interface morphology, pore formation, current constriction, impedance spectroscopy, solid-state battery, solid electrolyte, electric network model*

1. INTRODUCTION

Particularly in solid-state batteries (SSB), establishing and maintaining full electric contact between individual phases and components presents a severe challenge in addition to the chemical stability of the interfaces involved.[1−4] Pores naturally form during the mechanical assembly of the battery cell's layered architecture or may even form at interfaces under operation (e.g., during electrode stripping/dissolution at reversible metal anodes). Pore formation reduces the electrochemically active surface area and thus severely affects the electric transport properties of the cell.[5−8] Porous interfaces between a metal electrode and a solid electrolyte (SE) are often studied as a function of applied uniaxial pressure as the application of uniaxial pressure to the battery cell is a key process step during assembly of the different layers of solid-state batteries. Systematically increasing the applied pressure allows for continuous tuning of the pore density and distribution and, thus, the interface morphology and effective contact area.[9] While high pressure may be well used during formation of a battery cell to optimize the local microstructure, stack pressure during later battery operation should be low (on the order of about 1 MPa or lower) in order to meet the requirements for battery packs.

Impedance spectroscopy (IS), as a non-destructive method, is particularly suited for systematically studying the kinetics of solid/solid interfaces. When the frequency f of the exciting electric field in the IS measurement is swept over a wide range, different transport processes contributing to the overall electric response of the sample probed may be separated from each other, if their characteristic frequencies differ. IS data are usually analyzed by means of macroscopic physical-based 1D-equivalent circuit models, assuming that each component of the equivalent circuit represents a transport process at the microscopic level. Microstructural information, however, is typically not considered in the analysis, although it can have a

Received: July 20, 2022
Accepted: August 29, 2022
Published: September 8, 2022

https://doi.org/10.1021/acsami.2c12991
ACS Appl. Mater. Interfaces 2022, 14, 42757−42769

ACS Applied Materials & Interfaces www.acsami.org Research Article

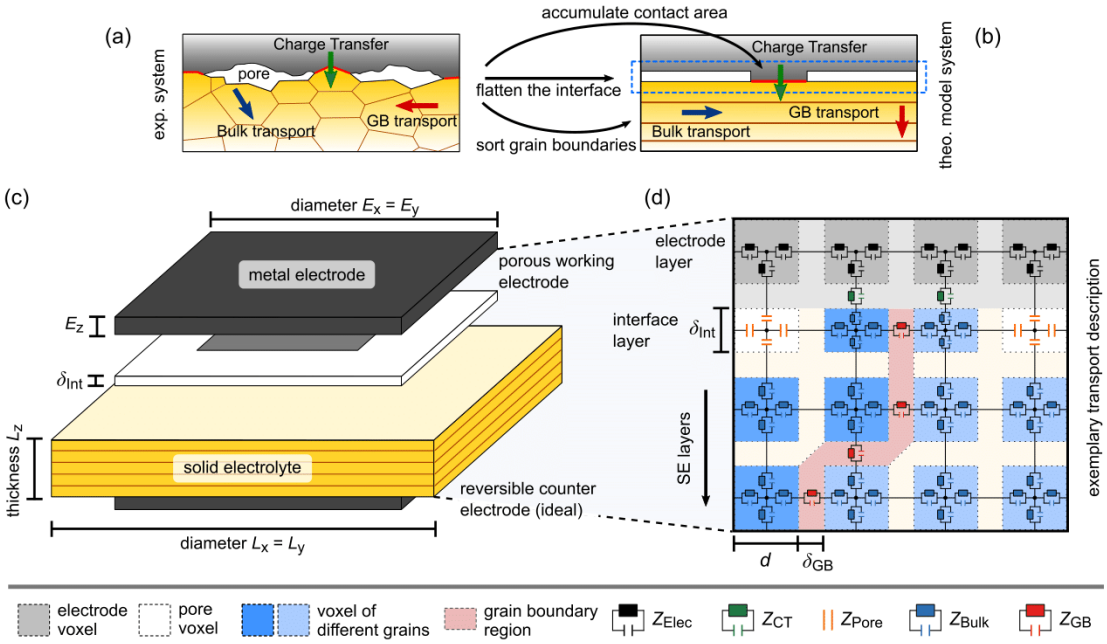

Figure 1. Overview of the computational model. (a)−(b) The real system is transformed into a simplified theoretical model system to enable systematic studies of individual model parameters. (c) The potential is applied between the porous working electrode (non-ideal) and the reversible counter electrode (ideal). Changes in the contact between working electrode and polycrystalline SE are described by the interface layer. (d) Charge transport processes are described by different *RC*-elements in the 3D electric network, while the pores at the interface are considered as capacitors.

major impact on the impedance, leading to further challenges in the interpretation of experimental data as will be demonstrated in this study.[10]

In the case of a reversible metal anode, the experimental system typically consists of a polycrystalline and cation-conducting solid electrolyte that is in contact with an alkali metal working electrode (WE), e.g., lithium metal in contact with a garnet-type SE such as variants of $Li_7La_3Zr_2O_{12}$ (LLZO) or sodium metal in contact with a NASICON-type SE such as $Na_{3.4}Zr_2Si_{2.4}P_{0.6}O_{12}$.[11−18] Usually, one would account for four different electric migration processes on the microscopic level, i.e., electronic transport in the metal electrode, electric charge transfer (CT) at the electrode/SE interface, and bulk as well as grain boundary (GB) ionic transport within the SE. Remaining pores at a non-ideal interface, surrounded by the metal WE on one side and the SE on another side, act as local capacitors. At varying voltage (e.g., in an IS measurement), their impedance strongly depends on the frequency f of the external electric field. At constant voltage (DC electric field, f = 0 Hz), the pores possess an infinitely large impedance. Thus, the active contact area between WE and SE is reduced by the pores, leading to (dynamic) current constriction at the interface. In our previous paper, we analyzed the constriction effect for a rather simple model case, i.e., pores on a homogeneous SE with zero polarization resistance.[19] Earlier work already considered this type of individual single crystal contacts, which is sufficient to study the origin of the constriction effect as such.[20−25] The equipotential lines in the SE region below the contact areas are not parallel to the interface as a consequence of current spreading within the SE. At high frequencies of the external electric field (AC, $f \rightarrow \infty$ Hz), the impedance of the pores even approaches zero and a high displacement current will flow, starting from the entire electrode. Altogether, the dynamic constriction effect cannot be considered as a local microscopic effect as it is determined by the morphology of the interface at least on a mesoscopic scale of nanometers to micrometers and can affect an almost macroscopic region below the contact.

The situation is more complicated in the case of (realistic) non-ideal contacts between a metal WE and a ceramic, polycrystalline SE exhibiting an inhomogeneous interface morphology. The reason is that the impact of the dynamic constriction effect on the electric properties of such an interface is far from local. The depth of the *constriction region*, i.e., the region where the equipotential lines are not parallel to the otherwise planar interface, varies with the frequency f of the externally applied electric field.[19−25] As a consequence, the constriction phenomenon also affects the macroscopic impedance response of the SE, i.e., the latter is not solely determined by the microscopic transport processes within the grains and across GBs.

In this study, we extend our previous approach and use a 3D electric network model to compute impedance data of realistic 3D model systems. The computational results are treated like experimental data in the standard impedance analysis procedure to illustrate the challenges and loss of information that occur when using 1D circuit models. We show that the interface impedance is determined by two contributions, that of the CT across the physical contact and that of the (dynamic) constriction effect. As both contributions generally exhibit a different frequency dependence, their interplay may yield one or two distinct semicircles in the Nyquist representation of the impedance spectrum. An analysis of the constriction effect with physical-based 1D circuit models is not straightforward, as such models cannot fully capture the effects of frequency-dependent current spreading caused by dynamic

https://doi.org/10.1021/acsami.2c12991
ACS Appl. Mater. Interfaces 2022, 14, 42757−42769

constriction. As a consequence, the usually successful approach of correlating macroscopic components of physical-based 1D equivalent circuit models with single microscopic transport processes fails. Additional degrees of freedom are necessary to describe the constriction phenomenon in 1D fit circuit models. Their dependencies on the real 3D system, e.g., the microscopic transport quantities of the SE or the interface are discussed.

2. COMPUTATIONAL DETAILS

2.1. Description of Model Structure. As described in the introduction, metal anode interfaces in SSB often suffer from local contact loss for several reasons. To study interface effects between a reversible metal anode and a SE in a SSB cell, it is therefore often sufficient to solely consider a theoretical or experimental model system consisting of a (porous) metal working electrode (WE), a ceramic SE and an ideal metal counter electrode (CE). The latter serves as a quasi-reference electrode (QRE) as it provides a stable, invariant and ideal contact to the SE ($A_{electrode} = A_{contact}$). Then, the impedance of the cell is dominated by the WE/SE interface, together with the properties of the bulk SE between the electrodes.[15] This avoids the use of traditional reference electrodes and the superposition of additional effects in the measurement. Figure 1a shows a 2D projection of a segment of such a 3D model structure in the vicinity of the WE/SE interface as it may be typically observed. The SE possesses a polycrystalline structure and pores (voids) at the WE/SE interface cause complex three-phase morphologies (metal, SE, pore space), making a systematic analysis of individual parameters challenging. Therefore, we deliberately simplify this system for studying the interplay between non-local current constriction and microscopic transport processes.

Without loss of generality, the number of geometric model parameters is reduced by increasing the symmetry of the system, e.g., for describing the microstructure of the SE or the interface morphology (see Figure 1b). The latter affects the magnitude of individual geometric impedance parameters (e.g., constriction resistance) quantitatively, but not qualitatively, as already discussed in the literature.[19,22] Here, all contact spots are combined to a single squared contact of area $A_{contact}$ in the center of the interface. The parallel gap of width δ_{Int} between WE and SE outside the contact mimics the pore system. The microstructure of the polycrystalline SE is rearranged into a stack of planar GBs separated by bulk-like SE layers with a spacing of 1/50 L_z, where L_z is the total thickness of the SE. The planar arrangement enables a straightforward translation of the model structure into a 1D equivalent circuit. Moreover, the WE, CE, and the SE are assumed to be of the same area ($A_{SE} = L_x \cdot L_y$).

Despite these simplifications, the 3D computational model structure pertains the key features of the real solid electrolyte, but it is less complex. It still grabs the important properties of the dynamic constriction effect, i.e., current spreading, curved equipotential lines, and frequency-dependent volume changes of the constriction region. This facilitates a systematic analysis of the impact of individual material parameters on the impedance.

2.2. Description of the 3D Impedance Network. A 3D impedance network model is used for the computation of impedance spectra $Z(f)$ of our model system depicted in Figure 1b. First, the structure is divided into individual voxels of edge length d that are assigned to either a grain within the SE (bluish), a pore at the WE/SE interface (white) or one of the metal electrodes (gray). The non-ideal interface morphology is modeled by a separate layer of voxels of constant thickness δ_{Int} that reflects the contact between WE and SE (see Figure 1c).

The transport processes at the microscopic level, i.e., between individual voxels of the discretized structure, are described by different local equivalent circuit elements, as depicted in Figure 1d. While bulk transport and transport across GBs within the SE as well as the CT step at the electrode/SE interface are considered by different *RC*-elements (Z_{Bulk}, Z_{Elec}, Z_{GB}, Z_{CT}), the pores at the interface are solely described as capacitors (Z_{Pore}). Microscopic bulk and GB transport are modeled by two ($2 \cdot Z_{Bulk}$) and three ($2 \cdot Z_{Bulk} + Z_{GB}$) *RC*-elements connected in series, respectively. The transport within the metal electrode is described by ($2 \cdot Z_{Elec}$) and the CT step at both interface by $Z_{Elec} + Z_{CT} + Z_{Bulk}$. Pore transport is considered either by the series connection of an *RC*-element with a capacitor ($Z_{Elec} + Z_{Pore}$, or $Z_{Bulk} + Z_{Pore}$) or by two capacitors ($2 \cdot Z_{Pore}$) connected in series, depending on the structural properties of the voxels involved. The local parameters ($R_{i,\,loc}$, $C_{i,\,loc}$) of the bulk, GB and pore circuit elements are calculated according to the rules for conductors and plate capacitors based on conductivities σ_i and permittivities ε_i. In contrast, the parameters of the local $R_{CT}C_{CT}$-element result from the polarization resistance R_{Pol} and the double-layer capacitance C_{DL} at the interface. Further details about setting up and solving the electric network model as well as computing an impedance spectrum are given in our previous work.[10]

2.3. Computational Parameters and Analysis of the Impedance Spectra. A cubic shape of the SE ($L_x = L_y = L_z$) corresponding to $(50\ \mu m)^3$ and a GB thickness of 10 nm (core region and adjacent space-charge region) is assumed. The results described in what follows, however, also apply to larger system sizes up to several millimeters or even larger. Table 1 summarizes the parameters of the geometric model and the transport quantities used in the computations (cf. computational results in Figure 2 to Figure 7). All microscopic transport parameters are in the range of, but not limited to, those of the solid electrolyte LLZO.[15] The transport within the (metal) electrode is assumed to be resistance-free. The pore depth δ_{Int} is given as a fraction of the transport length L_z and its value varies between the individual studies. In each series of

Table 1. Overview of the Transport Parameters Used in the Computations[a]

figure	L_z (δ_{Int})	σ_{GB} (μS/cm)	R_{Pol} ($\Omega \cdot cm^2$)	ε_{GB} (ε_0)	$\tilde{C}_{Pore}$ ($\mu F/cm^2$)	C_{DL} ($\mu F/cm^2$)
2	50 k	5.97	1	150	8.85	885
3a	50 k	5.97	–	150	88.5	–
3b	50 k	5.97	–	1.5 M	0.89	–
4	50 k	variable	–	150	88.5	–
5a	50 k	–	1	–	0.89	88.5
5b	50 k	–	1	–	885	88.5
6	50 k	–	variable	–	885	8.85
7	50 k	–	10	–	885	8.85

[a]These are in the range of, but not limited to, those of the solid electrolyte LLZO. The bulk conductivity and permittivity were fixed to σ_{Bulk} = 0.46 mS/cm and $\varepsilon_{Bulk} = 150 \cdot \varepsilon_0$, respectively.[15,28,29] The GB thickness (core region and adjacent space-charge region) is set to δ_{GB} = 10 nm.[15,30]

https://doi.org/10.1021/acsami.2c12991
ACS Appl. Mater. Interfaces 2022, 14, 42757−42769

ACS Applied Materials & Interfaces www.acsami.org Research Article

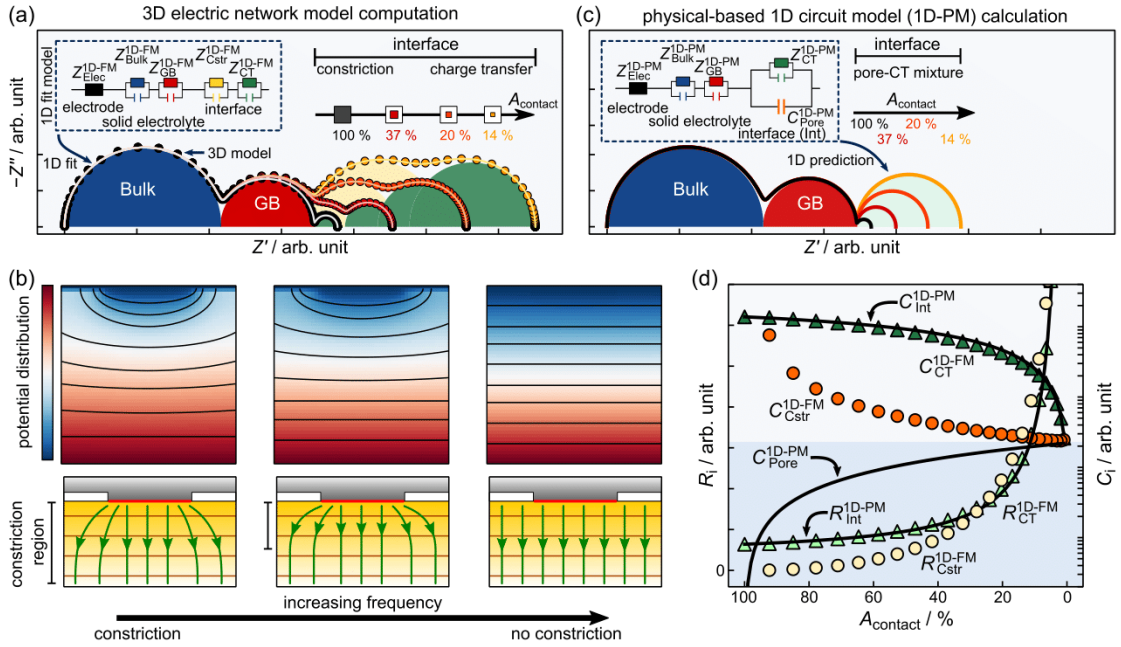

Figure 2. Non-local dynamic constriction effect and failure of the physical-based 1D equivalent circuit model in describing it. (a) Series of impedance spectra computed with the 3D electric network model (dots). A fourth constriction semicircle (yellow) arises resulting from the WE/SE interface, when the contact area is reduced ($A_{electrode} > A_{contact}$). (b) Potential distributions and current lines for three different excitation frequencies highlight the effect of dynamic constriction, i.e., frequency-dependent change of the active electrode area and variations in the size of the constriction region. (c) Transfer of the 3D model system depicted in Figure 1b into a physical-based 1D equivalent circuit (inset). Corresponding impedance spectra calculated or predicted for different contact areas $A_{contact}$ between WE and SE using the same transport parameters reveal three semicircles only. Constriction cannot be captured by the 1D-PM, but it can be fitted using the 1D-FM (inset in (a)). (d) Comparison of the predictions by the 1D-PM (solid lines) with the derived parameters ($R_i^{1D\text{-}FM}$, $C_i^{1D\text{-}FM}$) of the interface (circular and triangle symbols) based on the 1D fitting approach of the 3D network model computations.

impedance computations, the relative contact area $A_{contact}/A_{SE}$ of the single square-shaped contact spot is systematically varied in size from 100% (ideal contact, no pores) to 0% (no contact, capacitor-like arrangement of WE and SE).

Note that individual transport parameters in the computations may be chosen to vary in a wider range than expected in experiment. This is related to our approach of exclusively changing the contact area (at constant pore depth δ_{Int}) throughout a computed impedance series ($0\% < A_{contact} \leq 100\%$), which leads to an overestimation of $\Delta\tau_{Cstr}$, since both parameters have an opposite influence on τ_{Cstr}.[19] The aim of our study is, among others, the understanding of the time constant's τ_{Cstr} impact on the impedance spectrum and the derived macroscopic transport parameters. For this purpose, we discuss limiting cases distinguished by the arrangement of the time constants involved, i.e., τ_{Bulk}, τ_{GB}, τ_{CT}, and τ_{Cstr}. To ensure that a specific order of time constants is preserved during a computational series, we sometimes artificially lower or increase individual time constants τ_i by choosing "unrealistic" material parameters. For example, we modified the pore capacitance $\tilde{C}_{Pore}$ in case of the constriction signal or the permittivity ε_{GB} in case of the GB signal. However, this does not affect the qualitative results in these studies as the capacitance $\tilde{C}_{Pore}$ influences exclusively the constriction impedance. Similarly, the permittivity ε_{GB} and double layer capacitance C_{DL} only affect the corresponding macroscopic transport contributions and not that of geometric constriction.

The analysis of the computed impedance spectra derived by the 3D electric network model is based on a simplified 1D "*fit model circuit*" consisting of a resistor connected in series with four *RC*-elements as depicted as inset in Figure 2 a). The fitting was carried out using the commercial software *RelaxIS* 3 (version 3.0.18.15, rhd instruments GmbH & Co. KG). The Kramers–Kronig test of the impedances computed by the 3D electric network model yields residuals in the order of 10^{-6} %.[26] Thus, the computed impedances are almost free of noise signals, and it is valid to consider all data records (f, Z) in the 1D analysis approach.[27]

3. RESULTS

3.1. Grabbing Non-Locality of Current Constriction in 1D Equivalent Circuit Modeling. The fundamentals of current constriction and its dependence on the interfacial morphology (e.g., pore depth or distribution of the contact area) have already been discussed in detail in our previous work[19] and also in early studies by Maier and Fleig.[20−25] Here, we compare the results of two different 1D equivalent circuit models with the impedance $Z(f)$ of our 3D model structure (see Figure 1b) derived by the electric network model. The results help to underline the non-locality of dynamic constriction and its consequences. In what follows, the impedance $Z(f)$ derived by the electric network model takes the place of a measured impedance spectrum and serves as input for 1D modeling approaches, commonly used for analyzing experimental impedance data. This helps to understand the loss of information, when "real" experimental data are analyzed only within a 1D impedance circuit model.

https://doi.org/10.1021/acsami.2c12991
ACS Appl. Mater. Interfaces 2022, 14, 42757−42769

Figure 2b shows the potential distribution in the central cross section of the 3D model structure for various frequencies f of an applied electric AC field. The evolution of the potential distribution with f illustrates the key features of dynamic current constriction as a non-local effect, i.e., the effect of spatial focusing of the current paths at the contact spot and the corresponding bending of the equipotential lines. These are a consequence of the capacitor structure surrounding the contact area at the WE/SE interface. The capacitor structure has an infinitely large resistance in the DC case (f = 0 Hz) and becomes highly conductive in case of large modulation frequencies f of the AC field. Thus, the depth of the constriction region where the current paths are not parallel to each other and the equipotential lines are not parallel to the interface varies. As a result, the impact of the constriction effect is not local, but affects several layers of the macroscopic sample structure. This was already pointed out by Maier and Fleig in their work.[20−25]

The inset in Figure 2c shows an intuitive and straightforward translation of the 3D model structure into a physical-based 1D equivalent circuit model. For the sake of clarity, we assume a reversible and resistance-free CE. The model is referred to as "*physical model*" (1D-PM) in the following. It can be described by four building blocks connected in series. The first building block $Z_{\mathrm{Elec}}^{\mathrm{1D\text{-}PM}} = R_{\mathrm{Elec}}$ describes the transport within the metal electrodes as purely ohmic, i.e., $C_{\mathrm{Elec}}^{\mathrm{1D\text{-}PM}} = 0$. The second $Z_{\mathrm{Bulk}}^{\mathrm{1D\text{-}PM}}$ and third $Z_{\mathrm{GB}}^{\mathrm{1D\text{-}PM}}$ building blocks are modeled as *RC*-elements, respectively. They represent the microscopic transport processes within grains and across GBs in the SE.[31−33] The fourth element describes the non-ideal WE/SE interface as a parallel connection of the capacitance of the pore $C_{\mathrm{Pore}}^{\mathrm{1D\text{-}PM}}$ and an $R_{\mathrm{CT}}^{\mathrm{1D\text{-}PM}}C_{\mathrm{CT}}^{\mathrm{1D\text{-}PM}}$-element representing the CT at the physical contact. The interface description can be transformed into a single *RC*-element $Z_{\mathrm{interface}}^{\mathrm{1D\text{-}PM}}$ only where the capacitor $C_{\mathrm{interface}}^{\mathrm{1D\text{-}PM}}$ is the sum of the capacities $C_{\mathrm{CT}}^{\mathrm{1D\text{-}PM}}$ and $C_{\mathrm{Pore}}^{\mathrm{1D\text{-}PM}}$. The three quantities $C_{\mathrm{Pore}}^{\mathrm{1D\text{-}PM}}$, $R_{\mathrm{CT}}^{\mathrm{1D\text{-}PM}}$, and $C_{\mathrm{CT}}^{\mathrm{1D\text{-}PM}}$ are derived by weighting with the corresponding contact areas.

$$R_{\mathrm{interface}}^{\mathrm{1D\text{-}PM}} = R_{\mathrm{CT}}^{\mathrm{1D\text{-}PM}} = R_{\mathrm{Pol}}A_{\mathrm{contact}} \tag{1}$$

$$\begin{aligned} C_{\mathrm{interface}}^{\mathrm{1D\text{-}PM}} &= C_{\mathrm{CT}}^{\mathrm{1D\text{-}PM}} + C_{\mathrm{Pore}}^{\mathrm{1D\text{-}PM}} \\ &= C_{\mathrm{DL}}A_{\mathrm{contact}} + \tilde{C}_{\mathrm{Pore}}(1 - A_{\mathrm{contact}}) \end{aligned} \tag{2}$$

As a result, the 1D-PM can be represented as one resistor $Z_{\mathrm{Elec}}^{\mathrm{1D\text{-}PM}}$ plus three *RC*-elements $Z_{\mathrm{interface}}^{\mathrm{1D\text{-}PM}}$, $Z_{\mathrm{Bulk}}^{\mathrm{1D\text{-}PM}}$, and $Z_{\mathrm{GB}}^{\mathrm{1D\text{-}PM}}$ in a serial configuration.

Figure 2a, c show a series of impedance spectra in Nyquist representation for different contact areas A_{contact} computed by the 3D network model based on the realistic sample structure on the one hand and calculated or predicted by the 1D-PM on the other hand. The underlying microscopic transport parameters used in both sets of computations are the same and given in Table 1. The impedance series of the 1D-PM consist of three semicircles corresponding to the frequency-dependent signals of $Z_{\mathrm{Bulk}}^{\mathrm{1D\text{-}PM}}$ (blue), $Z_{\mathrm{GB}}^{\mathrm{1D\text{-}PM}}$ (red), and $Z_{\mathrm{interface}}^{\mathrm{1D\text{-}PM}}$ (light green). The comparison with the 3D network model computations, however, reveals some significant discrepancies. In particular, the 1D-PM cannot grasp the evolution of a fourth dynamic constriction contribution to the impedance of the model system (yellow), which increases with decreasing contact area.

Since the 1D physical (prediction) model fails in fully describing the realistic 3D model system, we define a "*fit model*" (1D-FM) circuit depicted in the inset of Figure 2a. It is a serial connection of five circuit elements and, thus, exhibits more degrees of freedom than the original (physical) 1D-PM. Again, we assume a resistance $Z_{\mathrm{Elec}}^{\mathrm{1D\text{-}FM}} = R_{\mathrm{Elec}}$ for the transport within the metal WE and *RC*-elements $Z_{\mathrm{Bulk}}^{\mathrm{1D\text{-}FM}}$ and $Z_{\mathrm{GB}}^{\mathrm{1D\text{-}FM}}$ for describing the transport within the SE. The non-ideal WE/SE interface is now described by two independent *RC*-elements in series resulting from charge transfer $Z_{\mathrm{CT}}^{\mathrm{1D\text{-}FM}}$ and dynamic constriction $Z_{\mathrm{Cstr}}^{\mathrm{1D\text{-}FM}}$.

It turns out that this model with its four *RC*-elements possesses enough degrees of freedom for adequately fitting all impedance spectra derived with the 3D network model for the highly symmetric model system. However, the interpretation of the 1D model parameters ($R_i^{\mathrm{1D\text{-}FM}}$, $C_i^{\mathrm{1D\text{-}FM}}$), in particular for i = CT or Cstr, derived by fitting the 3D computations is not straightforward, as the independent treatment of charge transfer and dynamic constriction at the interface in 1D-FM is not intuitive. This becomes apparent when comparing the predictions of the 1D-PM with the 3D network model results and its derived macroscopic transport quantities ($R_i^{\mathrm{1D\text{-}FM}}$, $C_i^{\mathrm{1D\text{-}FM}}$) based on fitting with the 1D-FM. While the contributions corresponding to bulk and GB transport within the SE are similar, i.e., $Z_{\mathrm{Bulk}}^{\mathrm{1D\text{-}FM}} \approx Z_{\mathrm{Bulk}}^{\mathrm{1D\text{-}PM}}$ and $Z_{\mathrm{GB}}^{\mathrm{1D\text{-}FM}} \approx Z_{\mathrm{GB}}^{\mathrm{1D\text{-}PM}}$, this does not hold for the parameters of the interface.

Figure 2d shows the constriction parameters $R_{\mathrm{Cstr}}^{\mathrm{1D\text{-}FM}}$ and $C_{\mathrm{Cstr}}^{\mathrm{1D\text{-}FM}}$ as circular symbols, that of the charge transfer $R_{\mathrm{CT}}^{\mathrm{1D\text{-}FM}}$ and $C_{\mathrm{CT}}^{\mathrm{1D\text{-}FM}}$ as triangular symbols and the 1D-PM predictions calculated according to eqs 1 and 2 as solid lines. The qualitative behavior of $R_{\mathrm{CT}}^{\mathrm{1D\text{-}FM}}$ and $R_{\mathrm{Cstr}}^{\mathrm{1D\text{-}FM}}$ is very similar and their dependence on A_{contact} resembles that of $R_{\mathrm{Int}}^{\mathrm{1D\text{-}PM}}$, i.e., in the case of $R_{\mathrm{CT}}^{\mathrm{1D\text{-}FM}}$ it even matches that of $R_{\mathrm{Int}}^{\mathrm{1D\text{-}PM}}$. The trends of the two capacitances $C_{\mathrm{CT}}^{\mathrm{1D\text{-}FM}}$ and $C_{\mathrm{Cstr}}^{\mathrm{1D\text{-}FM}}$ as a function of A_{contact} differ significantly in values and curvature. The behavior of $C_{\mathrm{CT}}^{\mathrm{1D\text{-}FM}}$ agrees with $C_{\mathrm{Int}}^{\mathrm{1D\text{-}PM}}$, but none of the fitted capacitances agree with $C_{\mathrm{Pore}}^{\mathrm{1D\text{-}PM}}$ as a function of A_{contact}. Thus, only the functional dependence of $R_{\mathrm{CT}}^{\mathrm{1D\text{-}FM}}$ and approximately that of $C_{\mathrm{CT}}^{\mathrm{1D\text{-}FM}}$ follow the dependence on contact area given by 1D-PM. Note that the predicted functional behavior is not universal, it depends on the order of the involved characteristic time constants as will be discussed in the next section.

Only in the limiting case where $Z_{\mathrm{Cstr}}^{\mathrm{1D\text{-}FM}}$ is zero, i.e., $A_{\mathrm{contact}} = A_{\mathrm{SE}}$, the impedance computed with the 3D electric network model is identical to that of the 1D-PM. The treatment of dynamic constriction and CT effect in 1D-FM as independent *RC*-elements leads to relaxation times $\tau_{\mathrm{Cstr}}^{\mathrm{1D\text{-}FM}} = R_{\mathrm{Cstr}}^{\mathrm{1D\text{-}FM}} \cdot C_{\mathrm{Cstr}}^{\mathrm{1D\text{-}FM}}$ and $\tau_{\mathrm{CT}}^{\mathrm{1D\text{-}FM}} = R_{\mathrm{CT}}^{\mathrm{1D\text{-}FM}} \cdot C_{\mathrm{CT}}^{\mathrm{1D\text{-}FM}}$ that depend on the contact area. Their time response, however, does not follow the prediction of the 1D-PM which describes the effect of the porous interface solely as a local effect. Therefore, dynamic constriction cannot be correlated with a local electric migration process in the system, as usually done in macroscopic physical-based 1D equivalent circuit models. Consequently, the underlying assumption that every contribution in the impedance corresponds to a microscopic electric migration process in the system does not hold.[10,34]

3.2. Dependence of the Constriction Characteristics on other Sample Parameters. We will now discuss how the non-locality and the frequency dependence of the dynamic constriction effect influences the impedance response. The focus is on the SE, its microstructure, and the microscopic transport processes inside, and also on the electrode/SE interfacial properties. For this purpose, we compute series of impedance spectra based on the 3D model structure depicted

https://doi.org/10.1021/acsami.2c12991
ACS Appl. Mater. Interfaces 2022, 14, 42757−42769

ACS Applied Materials & Interfaces www.acsami.org Research Article

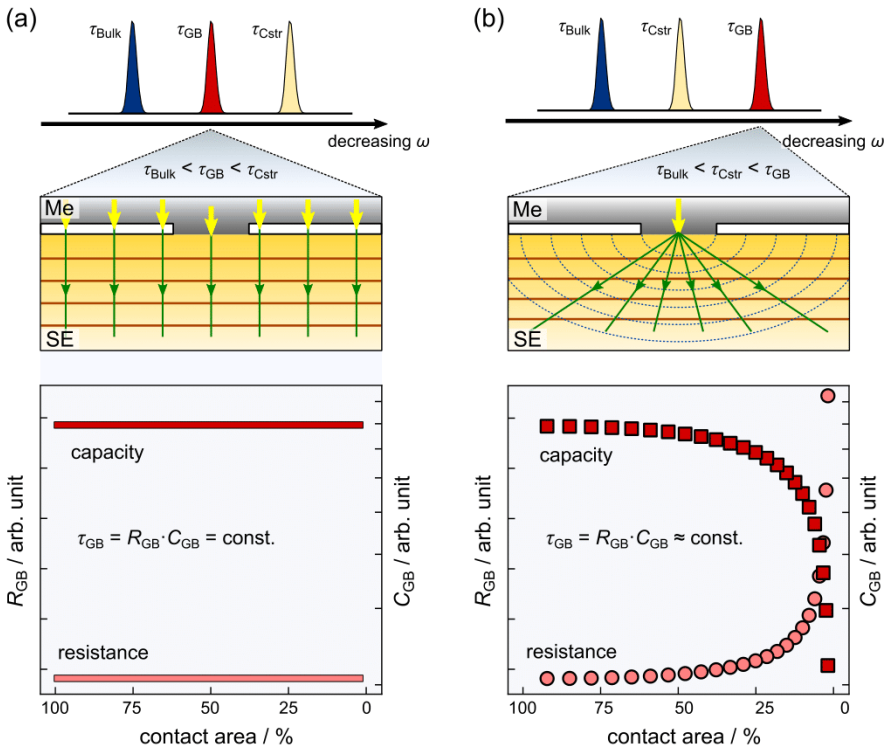

Figure 3. Interplay of dynamic constriction with GB transport in the SE. Constriction at the interface influences all impedance contributions with lower characteristic frequencies than its own. (a) Pores at the interface have no impact on the macroscopic impedance contribution of GBs (R_{GB}, C_{GB}). In the frequency range around $1/\tau_{GB}$, the transport paths through the system (green arrows) are independent of the pore fraction at the interface. (b) Transport paths through the structure, the GB volume contributing to the transport, and thus the transport parameters (R_{GB}, C_{GB}) depend on the contact area between electrode and SE, if constriction occurs at higher characteristic frequencies than GB transport.

in Figure 1b. Throughout such a series, specific model parameters are varied systematically, e.g., contact area or the materials parameters. All impedance spectra were subsequently fitted based on the 1D-FM. The corresponding macroscopic transport quantities ($R_i^{1D\text{-}FM}$, $C_i^{1D\text{-}FM}$) and the characteristic time constants $\tau_i^{1D\text{-}FM}$ assigned to the various transport processes are then analyzed. We will omit the superscript "1D-FM" for all these transport quantities in the remainder of this section.

To ensure in the following that the computational results on the interplay of dynamic constriction with microscopic transport processes are comprehensible, the origin of the corresponding time constants $\tau_i = R_i \cdot C_i$ (or characteristic frequencies $\omega_i = 1/\tau_i$) has to be clarified first. A microscopic electric migration process is usually described by an *RC*-element in a macroscopic 1D circuit model. At its characteristic frequency, the conduction response of the transport process changes from electric to dielectric (rule of thumb) with increasing frequency f of the exciting external electric field. Although dynamic constriction can also be described by an *RC*-element in a macroscopic 1D fit circuit model, it is not directly related to a microscopic electric migration process. Its time constant τ_{Cstr} corresponds to a characteristic frequency below which pores at the interface are electrically insulating and above which the pores are dielectrically conductive. This frequency-dependent switching of the active contact area $A_{electrode,\ active}$ opens up additional transport paths through the SE for externally applied frequencies above $1/\tau_{Cstr}$ (cf. Figure 2b)). These additional transport paths influence the macroscopic transport parameters (R_i, C_i) derived from fitting the impedance spectra and may also affect the relaxation times deduced for other transport processes. This "switching" of apparently electrically inactive pore areas from insulating to dielectrically conducting as the key ingredient of the constriction effect, has so far been mostly overlooked in the literature.

3.2.1. Effects of the Solid Electrolyte Characteristics on the Constriction Effect. First, we will solely focus on the interplay of the SE properties and the constriction effect. We assume that the CT step at both electrode/SE interfaces is resistance-free for the sake of simplicity and without loss of generality. We start considering the effect of the order of the time scales on the macroscopic transport characteristics (R_i, C_i) of the SE (i = Bulk and GB) derived by the 1D fitting approach and then discuss the effects of different microscopic transport parameters (σ_i, ε_i) of the SE on the constriction parameters. The latter is related to the fact that constriction as a geometric effect is relevant to all metal ion-conducting SEs with parent metal electrodes.[35−39]

3.2.1.1. Effect of the Time Scale on the Interplay of Constriction and Grain Boundary Characteristics. We start studying the influence of the interplay of the time scales of various microscopic or mesoscopic transport processes on the macroscopic impedance response of the system. For this purpose, two case studies were performed that differ in the material parameters of the pores and the grain boundaries ($\tilde{C}_{Pore}$ and ε_{GB}, see Table 1) to ensure that the order of the time constants is either $\tau_{Bulk} < \tau_{GB} < \tau_{Cstr}$ (case 1) or $\tau_{Bulk} <$

https://doi.org/10.1021/acsami.2c12991
ACS Appl. Mater. Interfaces 2022, 14, 42757−42769

ACS Applied Materials & Interfaces www.acsami.org Research Article

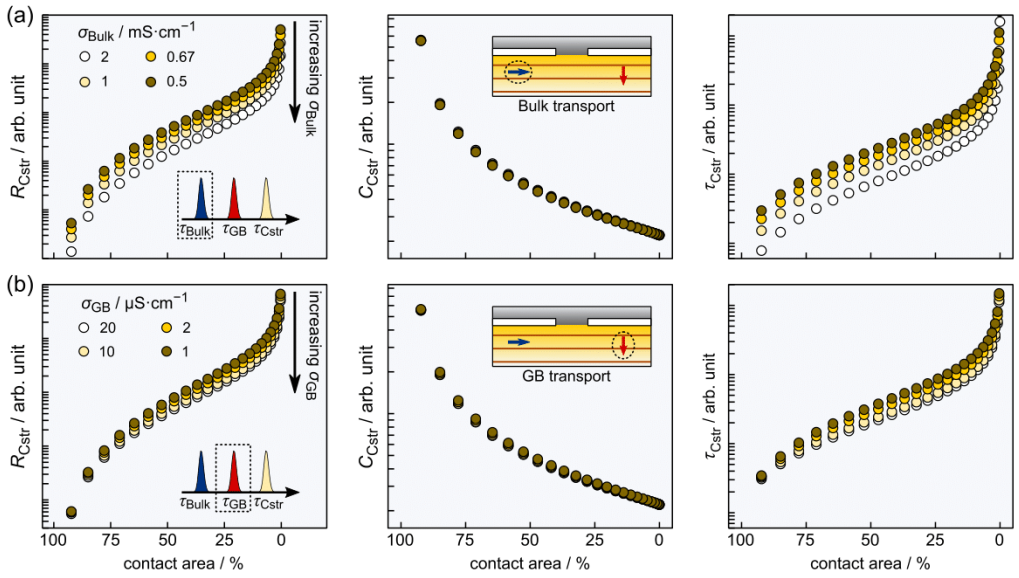

Figure 4. Dependence of the constriction behavior (R_{Cstr}, C_{Cstr}, τ_{Cstr}) on the conductivity of (a) bulk transport and (b) transport across GBs within the SE. The constriction resistance R_{Cstr} is only affected by transport processes with smaller time constants than its own ($\tau_i < \tau_{Cstr}$), since these are electrically conductive in the frequency range around $1/\tau_{Cstr}$ and thus influence the potential distribution and the size of the constriction region within the system. The constriction capacitance C_{Cstr} is unaffected in each case.

$\tau_{Cstr} < \tau_{GB}$ (case 2) independent of the contact area $A_{contact}$. As a result, Figure 3 a) and b) depict the macroscopic grain boundary fit parameters R_{GB} and C_{GB} as a function of relative contact area, respectively.

The order of the time constants in case 1 ($\tau_{Bulk} < \tau_{GB} < \tau_{Cstr}$) indicates that the pores at the interface are dielectrically conductive for frequencies around $1/\tau_{GB}$. In this frequency range, the electrode area actively contributing to the transport is the full SE surface area A_{SE}, i.e., there is no constriction present at the WE/SE interface. Thus, the current paths through the SE are quasi-1D and all the volume of the SE contributes to the transport as indicated by the green arrows in the upper part of Figure 3 a). This holds true regardless of the pore fraction at the interface. Therefore, the macroscopic transport quantities R_{GB} and C_{GB} are independent of the contact area $A_{contact}$ as depicted in the lower part of Figure 3 a). Such a behavior is observed experimentally, e.g., during the dissolution (stripping) or deposition (plating) of the lithium metal anode with LLZO as SE.[15,40,41]

The transport behavior is different when the order of the time constants of constriction and GB is reversed in case 2, i.e., $\tau_{Cstr} < \tau_{GB}$, as can be seen in Figure 3b). In this case, the GB signal lies in a frequency range where dynamic constriction is present at the interface, i.e., the pores are insulating. As a consequence, the sample volume of the SE pervaded by the current lines strongly depends on the contact area. In particular, only the grain boundary volume (i.e., area and thickness or transport length) pervaded by the current lines is reflected in the macroscopic parameters R_{GB} and C_{GB}. The resistance R_{GB} increases with decreasing contact area, as the volume of the SE effectively contributing to the transport is reduced in the constriction region. Similarly, the capacitance C_{GB} decreases with $A_{contact}$, since the effective area of the grain boundaries contributing to the transport is reduced, as shown in the upper part of Figure 3b. In this context, it is important to note that the variation of the macroscopic GB parameters (R_{GB}, C_{GB}) with $A_{contact}$ is due to the variation of the transport geometry and not associated with a change of the underlying microscopic transport quantities (σ_{GB}, ε_{GB}), which were kept constant in the corresponding computations.

Interestingly, the time constants derived from the (constant/varying) macroscopic fit parameters $\tau_{GB} = R_{GB} \cdot C_{GB}$ are (almost) preserved in both series of computations. This finding is related to the fact that the transport through the SE can be approximately regarded as a parallel connection of different serial transport paths. All those have in common that they contain shares of bulk and GB transport from both a local and macroscopic perspective. In this case, the initial phase information on the individual microscopic transport processes can be deconvoluted from the total impedance $Z(f)$ as demonstrated in eq S5 in the Supporting Information. This only applies to a symmetric arrangement where bulk and GB transport occur in each path (i.e., at least one grain boundary has to be crossed along each transport path). The theoretical consideration also highlights the presence of structural impedance contributions with mixed phase information. Apparently, the neglect of these contributions in 1D equivalent circuit analyses influences the derived macroscopic transport quantities (R_i, C_i) and thus the derived time constants τ_i.[10] This is the reason for the slight deviations of the calculated τ_{GB} from the microscopic parameter in the computations depicted in Figure 3b.

3.2.1.2. Effect of the Microscopic Transport Parameters on the Constriction Characteristics. We will now turn to the effect of variations of microscopic bulk or GB transport quantities (σ_i, ε_i) on the derived constriction parameters (R_{Cstr}, C_{Cstr}) extracted from the computed impedance spectra with the help of the 1D-FM. For this purpose, we analyzed series of 3D computations in which we systematically varied the contact area at the WE/SE interface. In each series, we deliberately changed only one of the four microscopic transport parameters

https://doi.org/10.1021/acsami.2c12991
ACS Appl. Mater. Interfaces 2022, 14, 42757−42769

ACS Applied Materials & Interfaces www.acsami.org Research Article

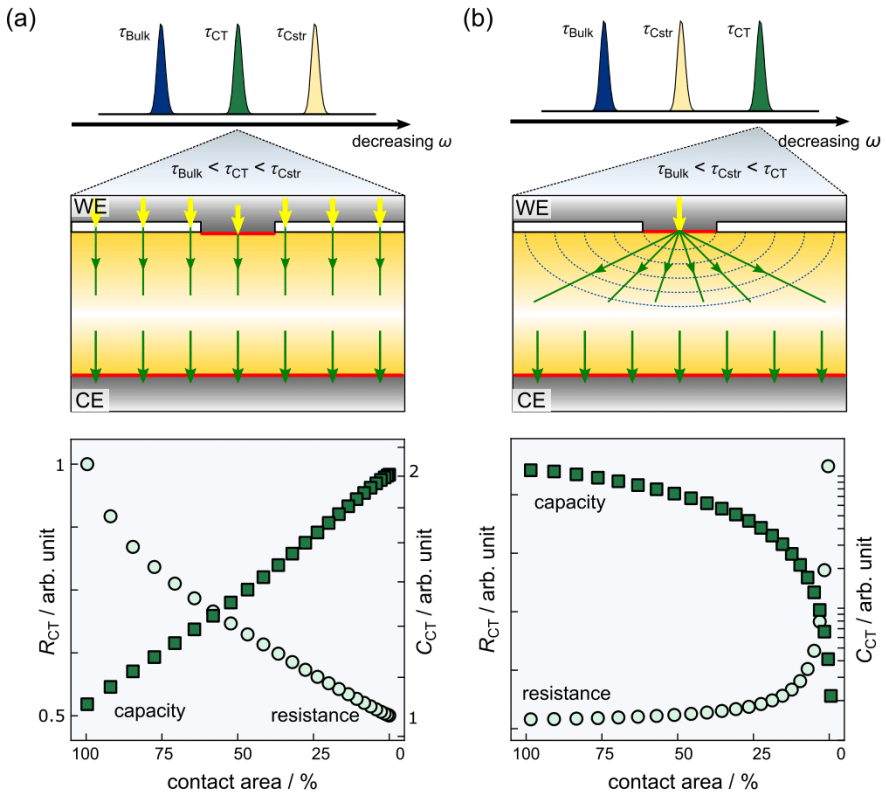

Figure 5. Interplay of dynamic constriction with charge transfer at the non-ideal WE/SE and ideal CE/SE interface. (a) Dielectrically shorted pores at the WE/SE interface ideally lead to quasi-1D pathways through the system (green arrows) in the frequency range around $1/\tau_{CT}$, regardless of the pore fraction at the interface. Thus, the macroscopic parameters (R_{CT}, C_{CT}) changes almost linearly with $A_{contact}$. (b) Electrically insulating pores in the frequency range around $1/\tau_{CT}$ lead to current spreading near the WE/SE interface, which results in a strong dependence of (R_{CT}, C_{CT}) on the contact area between WE and SE.

of the SE to study its qualitative effect on the impedance spectra.

Figure 4 shows the dependence of the constriction characteristics on the conductivities σ_i of (a) bulk and (b) GB transport. The overlapping symbols in the central graphs indicate that the constriction capacitance C_{Cstr} is not affected by a variation of the two SE related conductivities. In contrast, the constriction resistance R_{Cstr} increases for smaller conductivities σ_i. This is related to the non-local origin of this resistance. The potential distribution within the SE, the penetration depth into the SE and the size of the constriction region are functions of the conductivities σ_i. Therefore, the resistance R_{Cstr} can be considered a weighted linear combination of the individual microscopic transport processes in the system, i.e., $R_{Cstr} = \Sigma_i \alpha_i \cdot 1/\sigma_i$. Here, the weighting factors α_i depend on the potential distribution within the SE. This in turn is affected by the interface morphology, the structural composition of the constriction region (e.g., the number of grain boundaries near the interface, the effective contact area, the distribution of pores, etc.) and the characteristic time scales of individual transport processes occurring in the sample. The latter dependence is related to the fact that transport processes with a larger time constant than that of constriction are dielectrically shorted in the vicinity of $1/\tau_{Cstr}$, and thus, have no (major) impact on the potential distribution and the size of the constriction region in the system.

The spatially weighted averaging of the different microscopic transport processes at the WE/SE interface and within the SE contributing to the macroscopic quantities R_{Cstr} and C_{Cstr} derived by fitting with 1D-FM are also the cause of the dependence of τ_{Cstr} on contact area. The variation of $A_{contact}$ affects the weights assigned to the contributing microscopic processes which typically exhibit different characteristic frequencies. Another interesting implication of the non-locality of the constriction effect is that the activation energy $E_{a,\,Cstr}$ of the constriction resistance is an average of the activation energies $E_{a,\,i}$ of the microscopic transport processes involved.

In contrast to the conductivities, the permittivities ε_i of bulk and GB transport processes within the SE neither affect the constriction resistance R_{Cstr} nor the constriction capacitance C_{Cstr} (not graphically depicted). This finding is independent of the order of time constants in the system. The independence of the constriction capacitance from the microscopic SE transport parameters is somewhat expected, since C_{Cstr} is mainly related to the pore capacitance and therefore to the interfacial properties, e.g., morphology, pore depth distribution, and pore permittivity.[19]

3.2.2. Effect of the Interface Characteristics on the Constriction Effect. Finally, we focus on the impact of the interface properties on the impedance, i.e., those of the non-ideal WE/SE interface and those of the ideal CE. We initially assume that the additional CT step at the ideal CE can be captured by our 1D-FM, since the interfacial contribution at

https://doi.org/10.1021/acsami.2c12991
ACS Appl. Mater. Interfaces 2022, 14, 42757−42769

ACS Applied Materials & Interfaces www.acsami.org Research Article

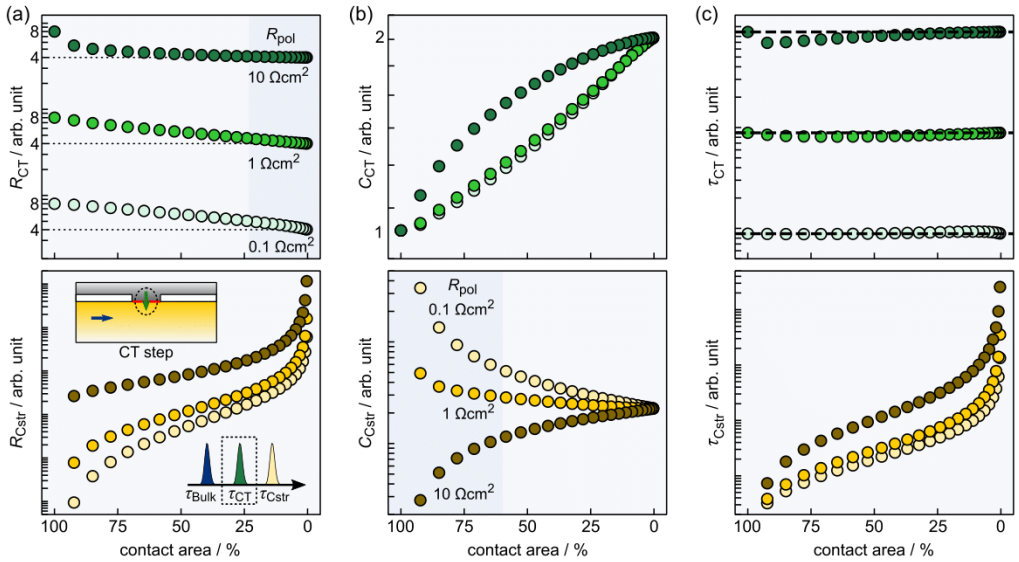

Figure 6. Dependence of the CT (top) and constriction (bottom) parameters, i.e., (a) resistance R_i, (b) capacitance C_i, and (c) time constant τ_i, on the polarization resistance R_{Pol} at both electrode/SE interfaces. The size of R_{Pol} affects the energetically preferred current path at the WE/SE interface, i.e., across the physical contact or through the pores, and thus the observed impedance behavior. The dashed horizontal lines in (c) indicate the microscopic (input) time constant of the CT step in the series of the 3D computations.

the non-ideal WE/SE contact was separated into a CT and a constriction part. For the sake of simplicity and without loss of generality, the GBs within the SE are assumed to be highly conductive (Z_{GB} = 0) in the following. Again, we will first consider the effect of the order of the characteristic time scales on the charge transfer characteristics (R_{CT}, C_{CT}) derived by 1D fitting approach and then discuss the impact of the variation of the microscopic interface transport parameters (R_{Pol}, C_{DL}) on the macroscopic constriction fitting parameters (R_{Cstr}, C_{Cstr}). The latter dependence is of particular interest, since many electrode/SE interfaces are not thermodynamically or kinetically stable, other than the Li/LLZO interface.[39,42−45]

3.2.2.1. Effect of the Time Scale on the Interplay of Constriction and Charge Transfer Characteristics. Again, two extreme cases are considered where the material parameters of the pores and the charge transfer ($\tilde{C}_{Pore}$ and C_{DL}, see Table 1) are chosen such that the order of time constants $\tau_{Bulk} < \tau_{CT} < \tau_{Cstr}$ (case 1) and $\tau_{Bulk} < \tau_{Cstr} < \tau_{CT}$ (case 2) is maintained independent of $A_{contact}$. Figure 5a and b show the derived macroscopic CT quantities R_{CT} and C_{CT} as a function of the contact area for case 1 and 2, respectively.

In case 1 ($\tau_{Bulk} < \tau_{CT} < \tau_{Cstr}$), the order of the time constants indicates that the CT steps at both interfaces, i.e., WE/SE and SE/CE interface, become electrically conductive in a frequency range where the pores at the WE/SE interface are dielectrically short-circuited. In an ideal scenario of negligible polarization resistance, the entire electrode area will actively contribute to the transport in the frequency range close to $1/\tau_{CT}$ forming almost quasi-1D current paths from the non-ideal WE across the SE into the ideal CE as indicated in the upper part of Figure 5a. The resistance R_{CT} will continuously decrease with decreasing contact area $A_{contact}$ (i.e., increasing pore area), while the capacitance C_{CT} will increase as somewhat anticipated. In the limiting case of complete contact loss at the WE ($A_{contact}$ = 0%), the resistance R_{CT} is half and the capacitance is twice the value compared to full contact ($A_{contact}$ = 100%) as the CT step will exclusively occur at the ideal CE. The slight deviations from a linear behavior in the lower graph of Figure 5a are related to the non-zero polarization resistance, as will be discussed in detail in the next section.

The transport behavior is different, when the order of the time constants of CT and constriction is reversed, i.e., $\tau_{Cstr} < \tau_{CT}$, as depicted in Figure 5b. The CT effect will occur in a frequency range where the pores are electrically insulating so that the active electrode area will correspond to the physical contact area only. As a consequence, current spreading will occur leading to non-linear changes of the CT quantities (R_{CT}, C_{CT}) as a function of the relative contact area $A_{contact}$ at the WE/SE interface. The functional behavior in terms of curvature depicted in the lower graph of Figure 5b and its origin are comparable to that observed in Figure 3b for the interplay of grain boundaries and geometric constriction.

3.2.2.2. Effect of the Microscopic Interface Parameters on the Constriction Characteristics. Now we turn to the impact of different microscopic interface transport quantities (R_{Pol}, C_{DL}) on the derived macroscopic constriction (R_{Cstr}, C_{Cstr}) and CT parameters (R_{CT}, C_{CT}) based on the fitting approach of the impedance spectra derived with the 3D network model with 1D-FM. For this purpose, we conducted a series of computations where we systematically varied the contact area at the WE/SE interface. We deliberately changed either the polarization resistance or the double-layer capacitance to identify corresponding trends.

The change of the double-layer capacitance C_{DL} does not affect the derived constriction parameters (R_{Cstr}, C_{Cstr}). This finding is similar to the variation of the bulk or GB permittivity ε_i within the SE. The results are not graphically depicted. The situation is different when varying R_{Pol}. Figure 6 shows the dependence of the CT and constriction impedance (R_i, C_i, τ_i) on the magnitude of the polarization resistance. We chose the parameters such that the characteristic frequency of the microscopic CT migration process is larger than that of constriction ($\tau_{CT} < \tau_{Cstr}$) independent of $A_{contact}$. Increasing the polarization resistance R_{Pol} leads to an increase in R_{CT} and

https://doi.org/10.1021/acsami.2c12991
ACS Appl. Mater. Interfaces 2022, 14, 42757−42769

ACS Applied Materials & Interfaces www.acsami.org Research Article

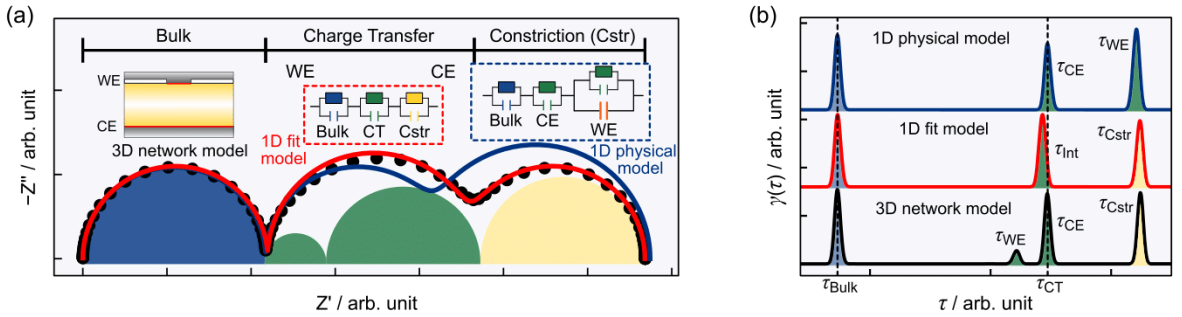

Figure 7. Comparison of the 3D electric network computation (black) with the simulated impedance of the 1D-FM (red) and with the calculated or predicted impedance of the modified 1D-PM (blue). Differences are clearly visible in both (a) the Nyquist plot and (b) the DRT representation of the individual impedances, especially with respect to the assignment of the single contributions. WE and CE must generally be considered separately when analyzing impedance data.

R_{Cstr}. Interestingly, the respective capacitances C_{CT} and C_{Cstr} also change, which was not the case when the conductivities within the SE were varied (see Figure 4). Larger polarization resistances lead to significant deviations from a linear relation of the CT parameters (R_{CT}, C_{CT}) in the intermediate $A_{contact}$ range (cf. the dark green dots in Figure 6a and b). Moreover, the slope and the sign of the curvature of the constriction capacitance C_{Cstr} vs $A_{contact}$ changes when R_{Pol} is varied, while its qualitative behavior is unaffected ($C_{Cstr} \rightarrow C_{Pore}^{1D\text{-}PM}$ for $A_{contact} \rightarrow 0$). The more resistive the interfaces at the physical contact become, the more the curvature of C_{Cstr} vs $A_{contact}$ approaches that of the macroscopic pore $C_{Pore}^{1D\text{-}PM}$ vs $A_{contact}$ (cf. Figure 2 d)).

The observed behavior is related to the current path evolving at the interface. The arrangement of the time constants ($\tau_{CT} < \tau_{Cstr}$) suggests that the CT steps at the interfaces become electrically conductive in a frequency range where the pores are dielectrically shortened. As a result, the ratio of the absolute values of pore impedance and the CT impedance (dominated by the polarization resistance) has a major effect on the amount of current flowing either across the physical WE/SE contact spots or across the pores as displacement current. The resulting spatial distribution of the total current dominates the overall impedance response of the system in this frequency range. The dependence of the current distribution at the interface and the associated transport across the SE on the polarization resistance is reflected, on the one hand, in the curvature of the CT fitting parameters (R_{CT}, C_{CT}) vs $A_{contact}$ and, on the other hand, in the convergence behavior of the constriction capacitance C_{Cstr} vs $A_{contact}$. A smaller fraction of current flowing across the physical contact spot leads to a smaller CT resistance and a larger CT capacitance. This coincides with the fact that the larger the fraction of displacement current across the pores to the total current in the frequency range below $1/\tau_{Cstr}$, the more the curvature of C_{Cstr} vs $A_{contact}$ approaches that of the macroscopic pore capacity $C_{Pore}^{1D\text{-}PM}$ vs $A_{contact}$. Thus, in the case of high polarization resistance R_{Pol}, larger pore areas (or smaller contact area) would lead to an increased constriction capacity whereas smaller constriction capacitance would arise in case of negligible polarization resistances.

The qualitative behavior of R_{Cstr} and τ_{Cstr} agrees with the conclusions drawn in the discussion of the impact of the microscopic transport quantities of the SE (see Figure 3). Both R_{Cstr} and τ_{Cstr} increase with increasing R_{Pol}. Interestingly, the time constant of the CT parameters $\tau_{CT} = R_{CT} \cdot C_{CT}$ that should be independent of the contact area deviates for some records $\tau_{CT}(A_{contact})$ from that of the microscopic (input) parameters as indicated by the dashed lines in Figure 6c.

To clarify this issue, we compare in Figure 7 the impedance spectrum of a 3D electric network computation (black dots) with that of the corresponding 1D-FM fitting (red curve) and with the impedance of the modified 1D-PM (blue curve), where an additional *RC*-element connected in series was added to represent the CE. We assumed a polarization resistance of 10 Ω·cm^2 and a contact area of 78% in this computation. For simplicity, the grain boundary impedance is set to zero and the SE is assumed to be bulk like. The Nyquist representation of the impedance spectra in Figure 7a visually consist of three well-separated semicircles. While the modified 1D-PM (blue) describes the bulk semicircle of the 3D electric network computation well, significant deviations occur for the interface impedances in the intermediate and low frequency range. Also, the fitted impedance curve according to 1D-FM cannot describe the impedance of the 3D computation in the intermediate frequency range.

To study these deviations in more detail, we transfer the impedance curves $Z(f)$ into the time domain by performing the individual DRT analyses, as shown in Figure 7b. The DRT of the 3D network computation (black) consists of four signals originating from bulk transport in the SE, the non-ideal WE, the CT at the ideal CE and the constriction effect. While the time constants of bulk transport in the SE and CT at the CE are identical to the corresponding microscopic parameters in the computations, the time constant at the WE shifted toward smaller relaxation times compared to the microscopic τ_{CT}. This is related to the multidimensional, non-serial transport behavior at the non-ideal WE/SE interface. The corresponding transport paths can be roughly regarded as the parallel connection of a pore capacitance and an $R_{CT}C_{CT}$-element. Since the two parallel paths are asymmetrical with respect to the transport processes involved (i.e., differ in terms of the microscopic transport mechanisms), the initial phase information on the microscopic CT step at the WE cannot be deconvolved from the total impedance $Z(f)$, as demonstrated in the Supporting Information. Thus, the assumed pure CT impedance originating from the WE is actually a mixed signal composed in parts from the CT step and the pores. In contrast, the ideal CE/SE interface can be approximated by a single $R_{CT}C_{CT}$-element, i.e., the time constant of the microscopic CT step is preserved. This underlines the need for a decoupled

https://doi.org/10.1021/acsami.2c12991
ACS Appl. Mater. Interfaces 2022, 14, 42757−42769

consideration of the WE/SE and CE/SE interface in a macroscopic 1D picture.

The modified 1D-PM (blue) describes the WE and CE separately. While the behavior of bulk and the transport at the CE fit the 3D computation, major differences appear in the description of the non-ideal WE/SE interface. Neither can the constriction contribution be reproduced by 1D-PM, nor is the quantitative and qualitative behavior of the mixed WE signal of the 3D computation properly described, i.e., the shift direction of τ_{WE} is incorrectly predicted and the amplitude and size of the shift are significantly overestimated. The 1D-FM (red), on the other hand, disregards a separate treatment of CT at the WE and CE. Both are described by the same single *RC*-element, leading to effective macroscopic transport parameters and a time constant different from the microscopic τ_{CT}. The constriction contribution, in contrast, seems to be adequately captured. This implies that the fit model does not have enough degrees of freedom and needs to be extended to consider both interfaces separately.

3.2.3. Effect of Partially Overlapping Signals on the Impedance Analysis. In the sections above, only limiting cases have been discussed, i.e., the number of microscopic transport processes occurring within the system was reduced and the time constants of the individual macroscopic impedance contributions were well separated. This facilitated the assignment of different impedance contributions to microscopic transport processes as well as the analysis of the derived macroscopic fit parameters (R_i, C_i). Obviously, such clear separation does not always occur in experimental systems, e.g., several transport processes may take place in a similar frequency range causing (partially) overlapping impedance contributions. This impedes the analysis and interpretation of the impedance results. In particular, several microscopic transport processes even out of different layers of the sample structure may contribute to multiple macroscopic impedance contributions of the 1D fit equivalent circuit. As a consequence, there is not necessarily a one-to-one correspondence between assignment of the macroscopic transport quantities (e.g., to grain boundary or bulk processes in the SE or CT at the WE/SE interface) and the actual microscopic transport processes in these regions.

However, the qualitative trends derived in the respective case studies can also be observed for more realistic values of the individual time constants (i.e., overlapping impedance contributions). Typical experimental impedance data of reversible metal anodes consists of three (well-) separated contributions.[15,41] These are usually assigned to bulk, GB and interface with decreasing frequency, respectively. The origin of "*the interface impedance*" is often not entirely clear in experiments. In the case of lithium metal in contact with LLZO, it is reasonable that it results from geometric constriction rather than electric charge transfer.[15,17] This indicates an ordering of time constants according to $\tau_{Bulk} < \tau_{GB} < \tau_{Cstr}$. In this sense, the qualitative results of the corresponding theoretical case study are comparable with the experimental observations, e.g., during the dissolution (stripping) or deposition (plating) of the lithium metal anode with LLZO as SE[15,40,41] The results for $\tau_{Bulk} < \tau_{Cstr} < \tau_{GB}$ are also of great relevance, since the constriction effect strongly depends on the interface morphology, especially on the pore depth (distribution). Here, the effect of deep pores can occur at quite high frequencies, which may lead to an influence on the macroscopic GB impedance contribution, e.g., due to an overlap of the corresponding impedance signals. In contrast, shallow pores cause a constriction at smaller frequencies similar to our computations.[19]

In many experimental situations, a clear ordering of the time constants cannot be given, in particular, when both interface processes, CT and constriction, are present. The reason is that their frequency-dependent behavior is usually quite similar. As a consequence, corresponding experimental impedance spectra only exhibit one distorted interface contribution, which impedes a clear assignment of individual processes. An interpretation of the experimental results in terms of the case studies presented here, considering a clear ordering of the time constants, is then not straightforward and a specific modeling is required.

4. SUMMARY AND CONCLUSIONS

The following conclusions for the analysis of experimental impedance results with porous metal electrodes can be drawn from the modeling of situations accounting for the constriction effect and CT effects at the interface between a metal electrode and a polycrystalline solid electrolyte. A few recommendations are formulated based on these conclusions:

- The impedance of the interface is generally composed of solid electrolyte interphase (SEI) and a CT contribution as well as a geometric constriction signal, when there is a non-ideal contact at the electrode/solid electrolyte interface. Dynamic constriction is a 3D effect that is related to the frequency-dependent change of the conduction behavior of pores or inclusions at interfaces. Its origin is on various length scales of the system ranging from mesoscopic to macroscopic.
- The time constant of the constriction signal τ_{Cstr} has a major impact on the shape of the impedance spectrum and therefore on the interpretation of experimental data. It is a descriptor for the change between dielectric and insulating behavior of the pores or inclusions at the interface. The interplay between constriction and microscopic transport processes depends on the relative position of the individual time constants. Dynamic current constriction will exclusively affect the impedance contributions with larger time constant τ_i than its own ($\tau_{Cstr} < \tau_i$). The constriction contribution itself is only influenced by the transport processes with smaller time constant τ_i than its own ($\tau_i < \tau_{Cstr}$). The constriction contribution in the impedance may also overlap with several transport signals, compromising the interpretation and analysis of IS data, e.g., the derivation of microscopic transport parameters (σ_i, ε_i).
- The geometric constriction resistance R_{Cstr} is of non-local origin and additionally increases the total resistance of a battery cell. It results from the frequency-dependent reduction of the SE volume contributing to the transport. It is composed of contributions of all transport processes that occur in the vicinity of the interface, i.e., the constriction region ($R_{Cstr} = \Sigma_i \alpha_i \cdot 1/\sigma_i$). The weights α_i of the individual contributions to R_{Cstr} depend severely on the interface morphology and the microstructure of the SE.
- The constriction capacitance C_{Cstr} is mainly affected by the pore characteristics at the interface and thus independent of the transport quantities of the SE. It is influenced by the morphology of the interface, e.g., the

https://doi.org/10.1021/acsami.2c12991
ACS Appl. Mater. Interfaces 2022, 14, 42757−42769

shape and depth of the pores as well as the distribution of the contact area, and the magnitude of the polarization resistance R_{Pol}.

On the one hand, our study of the (dynamic) constriction effect underlines the power of the IS method, e.g., for the investigation of pore formation and the dynamics at the metal anode interface of solid-state batteries. On the other hand, it also shows the high potential for misinterpretations. IS data is usually analyzed by means of a macroscopic physical-based 1D equivalent circuit model, each component representing a transport process at the microscopic level. The computations using a 3D electric network model demonstrate that a non-physical 1D (fit) circuit model may represent a measured impedance spectrum well in some circumstances, but then the interpretation of the derived model parameters (R_i, C_i) is challenging. Physical motivated 1D equivalent circuit models, in contrast, cannot fully capture phenomena in real systems such as the geometric constriction effect. It is a misconception that there is a one-to-one correlation between macroscopic impedance response and microscopic electric transport processes.

Consequently, the analysis and interpretation of impedance data is challenging without an explicit theoretical model, which takes into account structural properties on the mesoscopic scale. Thus, careful correlations with the actual sample structure need to be established in order to avoid misinterpretations of the impedance analysis. In a forthcoming study, we will compare experimental data with our detailed 3D electric circuit model and simplified 1D representations, to highlight the practical relevance of our work.

■ ASSOCIATED CONTENT

Supporting Information

The Supporting Information is available free of charge at https://pubs.acs.org/doi/10.1021/acsami.2c12991.

Analytical considerations on the transformability of individual electric circuits (PDF)

■ AUTHOR INFORMATION

Corresponding Author

Janis K. Eckhardt − *Institute for Theoretical Physics and Center for Materials Research (ZfM), Justus Liebig University, Giessen D-35392, Germany;* orcid.org/0000-0002-2799-0599; Email: janis.k.eckhardt@theo.physik.uni-giessen.de

Authors

Till Fuchs − *Center for Materials Research (ZfM), Justus Liebig University, Giessen D-35392, Germany; Institute of Physical Chemistry, Justus Liebig University, Giessen D-35392, Germany*

Simon Burkhardt − *Center for Materials Research (ZfM), Justus Liebig University, Giessen D-35392, Germany; Institute of Physical Chemistry, Justus Liebig University, Giessen D-35392, Germany*

Peter J. Klar − *Center for Materials Research (ZfM) and Institute of Experimental Physics I, Justus Liebig University, Giessen D-35392, Germany;* orcid.org/0000-0002-4513-0330

Jürgen Janek − *Center for Materials Research (ZfM), Justus Liebig University, Giessen D-35392, Germany; Institute of Physical Chemistry, Justus Liebig University, Giessen D-35392, Germany;* orcid.org/0000-0002-9221-4756

Christian Heiliger − *Institute for Theoretical Physics and Center for Materials Research (ZfM), Justus Liebig University, Giessen D-35392, Germany*

Complete contact information is available at: https://pubs.acs.org/10.1021/acsami.2c12991

Notes

The authors declare no competing financial interest.

The data that support the findings of this study are available from the corresponding author upon reasonable request.

■ ACKNOWLEDGMENTS

We acknowledge computational resources provided by the HPC Core Facility and the HRZ of the Justus-Liebig-University Giessen. We thank MSc. Philipp Risius and Dr. Marcel Giar of HPC-Hessen, funded by the State Ministry of Higher Education, Research, and the Arts (HMWK), for programming advice. Financial support is provided by the DFG via the GRK (Research Training Group) 2204 "Substitute Materials for sustainable Energy Technologies". J.J. and T.F. acknowledge funding by the German Federal Ministry of Education and Research (BMBF) of the LiSI project, grant identifier 03XP0224E. J.J. and S.B. acknowledge support by BMBF (Bundesministerium für Bildung und Forschung) within the Cluster of Competence FestBatt (projects 03XP0177A, 03XP0180, 03XP0433D).

■ REFERENCES

(1) Takeda, Y.; Yamamoto, O.; Imanishi, N. Lithium Dendrite Formation on a Lithium Metal Anode from Liquid, Polymer and Solid Electrolytes. *Electrochemistry* **2016**, *84* (4), 210−218.

(2) Tarascon, J. M.; Armand, M., Issues and challenges facing rechargeable lithium batteries. In *Materials for Sustainable Energy*; Macmillan Publishers Ltd, 2010; pp 171−179.

(3) Xu, K. Nonaqueous Liquid Electrolytes for Lithium-Based Rechargeable Batteries. *Chem. Rev.* **2004**, *104* (10), 4303−4418.

(4) McDowell, M. T.; Cortes, F. J. Q.; Thenuwara, A. C.; Lewis, J. A. Toward High-Capacity Battery Anode Materials: Chemistry and Mechanics Intertwined. *Chem. Mater.* **2020**, *32* (20), 8755−8771.

(5) Janek, J.; Majoni, S. Investigation of Charge Transport Across the AglAgI-interface: (I) Occurrence of Periodic Phenomena During Anodic Dissolution of Silver. *Berichte der Bunsengesellschaft für physikalische Chemie* **1995**, *99* (1), 14−20.

(6) Schmalzried, H.; Janek, J. Chemical kinetics of phase boundaries in solids. *Berichte der Bunsengesellschaft für physikalische Chemie* **1998**, *102* (2), 127−143.

(7) Lewis, J. A.; Cortes, F. J. Q.; Liu, Y.; Miers, J. C.; Verma, A.; Vishnugopi, B. S.; Tippens, J.; Prakash, D.; Marchese, T. S.; Han, S. Y.; Lee, C.; Shetty, P. P.; Lee, H. W.; Shevchenko, P.; De Carlo, F.; Saldana, C.; Mukherjee, P. P.; McDowell, M. T. Linking void and interphase evolution to electrochemistry in solid-state batteries using operando X-ray tomography. *Nat. Mater.* **2021**, *20* (4), 503−510.

(8) Vishnugopi, B. S.; Kazyak, E.; Lewis, J. A.; Nanda, J.; McDowell, M. T.; Dasgupta, N. P.; Mukherjee, P. P. Challenges and Opportunities for Fast Charging of Solid-State Lithium Metal Batteries. *ACS Energy Letters* **2021**, *6* (10), 3734−3749.

(9) Lee, C.; Han, S. Y.; Lewis, J. A.; Shetty, P. P.; Yeh, D.; Liu, Y.; Klein, E.; Lee, H.-W.; McDowell, M. T. Stack Pressure Measurements to Probe the Evolution of the Lithium−Solid-State Electrolyte Interface. *ACS Energy Letters* **2021**, *6* (9), 3261−3269.

(10) Eckhardt, J. K.; Burkhardt, S.; Zahnow, J.; Elm, M. T.; Janek, J.; Klar, P. J.; Heiliger, C. Understanding the Impact of Microstructure

on Charge Transport in Polycrystalline Materials Through Impedance Modelling. *J. Electrochem. Soc.* **2021**, *168* (9), No. 090516.
(11) Murugan, R.; Thangadurai, V.; Weppner, W. Fast Lithium Ion Conduction in Garnet-Type $Li_7La_3Zr_2O_{12}$. *Angew. Chem., Int. Ed.* **2007**, *46* (41), 7778−7781.
(12) Zhu, Y.; Connell, J. G.; Tepavcevic, S.; Zapol, P.; Garcia-Mendez, R.; Taylor, N. J.; Sakamoto, J.; Ingram, B. J.; Curtiss, L. A.; Freeland, J. W.; Fong, D. D.; Markovic, N. M. Dopant-Dependent Stability of Garnet Solid Electrolyte Interfaces with Lithium Metal. *Adv. Energy Mater.* **2019**, *9* (12), 1803440.
(13) Connell, J. G.; Fuchs, T.; Hartmann, H.; Krauskopf, T.; Zhu, Y.; Sann, J.; Garcia-Mendez, R.; Sakamoto, J.; Tepavcevic, S.; Janek, J. Kinetic versus Thermodynamic Stability of LLZO in Contact with Lithium Metal. *Chem. Mater.* **2020**, *32* (23), 10207−10215.
(14) Zhu, Y.; He, X.; Mo, Y. Origin of Outstanding Stability in the Lithium Solid Electrolyte Materials: Insights from Thermodynamic Analyses Based on First-Principles Calculations. *ACS Appl. Mater. Interfaces* **2015**, *7* (42), 23685−23693.
(15) Krauskopf, T.; Hartmann, H.; Zeier, W. G.; Janek, J. Toward a Fundamental Understanding of the Lithium Metal Anode in Solid-State Batteries—An Electrochemo-Mechanical Study on the Garnet-Type Solid Electrolyte $Li_{6.25}Al_{0.25}La_3Zr_2O_{12}$. *ACS Appl. Mater. Interfaces* **2019**, *11* (15), 14463−14477.
(16) Sharafi, A.; Kazyak, E.; Davis, A. L.; Yu, S.; Thompson, T.; Siegel, D. J.; Dasgupta, N. P.; Sakamoto, J. Surface Chemistry Mechanism of Ultra-Low Interfacial Resistance in the Solid-State Electrolyte $Li_7La_3Zr_2O_{12}$. *Chem. Mater.* **2017**, *29* (18), 7961−7968.
(17) Gao, J.; Guo, X.; Li, Y.; Ma, Z.; Guo, X.; Li, H.; Zhu, Y.; Zhou, W. The Ab Initio Calculations on the Areal Specific Resistance of Li-Metal/$Li_7La_3Zr_2O_{12}$ Interphase. *Advanced Theory and Simulations* **2019**, *2* (6), 1900028.
(18) Cortes, F. J. Q.; Lewis, J. A.; Tippens, J.; Marchese, T. S.; McDowell, M. T. How Metallic Protection Layers Extend the Lifetime of NASICON-Based Solid-State Lithium Batteries. *J. Electrochem. Soc.* **2020**, *167* (5), No. 050502.
(19) Eckhardt, J. K.; Klar, P. J.; Janek, J.; Heiliger, C. Interplay of Dynamic Constriction and Interface Morphology between Reversible Metal Anode and Solid Electrolyte in Solid State Batteries. *ACS Appl. Mater. Interfaces* **2022**, *14* (31), 35545−35554.
(20) Fleig, J.; Maier, J. Finite element calculations of impedance effects at point contacts. *Electrochim. Acta* **1996**, *41* (7), 1003−1009.
(21) Fleig, J.; Maier, J. Point contacts in solid state ionics: finite element calculations and local conductivity measurements. *Solid State Ionics* **1996**, *86*−*88*, 1351−1356.
(22) Fleig, J.; Maier, J. The Influence of Laterally Inhomogeneous Contacts on the Impedance of Solid Materials: A Three-Dimensional Finite-Element Study. *J. Electroceram.* **1997**, *1* (1), 73−89.
(23) Fleig, J.; Maier, J. Rough electrodes in solid and liquid electrochemistry: impact of morphology on the impedance. *Solid State Ionics* **1997**, *94* (1), 199−207.
(24) Fleig, J.; Maier, J. The Influence of Current Constriction on the Impedance of Polarizable Electrodes: Application to Fuel Cell Electrodes. *J. Electrochem. Soc.* **1997**, *144* (11), L302−L305.
(25) Fleig, J.; Maier, J. Finite-Element Calculations on the Impedance of Electroceramics with Highly Resistive Grain Boundaries: I, Laterally Inhomogeneous Grain Boundaries. *J. Am. Ceram. Soc.* **1999**, *82* (12), 3485−3493.
(26) Boukamp, B. Electrochemical impedance spectroscopy in solid state ionics: recent advances. *Solid State Ionics* **2004**, *169* (1−4), 65−73.
(27) Wan, T. H.; Saccoccio, M.; Chen, C.; Ciucci, F. Influence of the Discretization Methods on the Distribution of Relaxation Times Deconvolution: Implementing Radial Basis Functions with DRTtools. *Electrochim. Acta* **2015**, *184*, 483−499.
(28) Rettenwander, D.; Welzl, A.; Cheng, L.; Fleig, J.; Musso, M.; Suard, E.; Doeff, M. M.; Redhammer, G. J.; Amthauer, G. Synthesis, Crystal Chemistry, and Electrochemical Properties of $Li_{7-2x}La_3Zr_{2-x}Mo_xO_{12}$ (x = 0.1−0.4): Stabilization of the Cubic Garnet Polymorph via Substitution of Zr^{4+} by Mo^{6+}. *Inorg. Chem.* **2015**, *54* (21), 10440−10449.
(29) Loho, C.; Djenadic, R.; Bruns, M.; Clemens, O.; Hahn, H. Garnet-Type $Li_7La_3Zr_2O_{12}$ Solid Electrolyte Thin Films Grown by CO2-Laser Assisted CVD for All-Solid-State Batteries. *J. Electrochem. Soc.* **2017**, *164* (1), A6131−A6139.
(30) Tenhaeff, W. E.; Rangasamy, E.; Wang, Y.; Sokolov, A. P.; Wolfenstine, J.; Sakamoto, J.; Dudney, N. J. Resolving the Grain Boundary and Lattice Impedance of Hot-Pressed Li7La3Zr2O12 Garnet Electrolytes. *ChemElectroChem.* **2014**, *1* (2), 375−378.
(31) Beekmans, N. M.; Heyne, L. Correlation between impedance, microstructure and composition of calcia-stabilized zirconia. *Electrochim. Acta* **1976**, *21* (4), 303−310.
(32) van Dijk, T.; Burggraaf, A. J. Grain boundary effects on ionic conductivity in ceramic $Gd_xZr_{1-x}O_{2-(x/2)}$ solid solutions. *physica status solidi (a)* **1981**, *63* (1), 229−240.
(33) Verkerk, M. J.; Middelhuis, B. J.; Burggraaf, A. J. Effect of grain boundaries on the conductivity of high-purity ZrO_2−Y_2O_3 ceramics. *Solid State Ionics* **1982**, *6* (2), 159−170.
(34) Fleig, J. Impedance Spectroscopy on Solids: The Limits of Serial Equivalent Circuit Models. *J. Electroceram.* **2004**, *13* (1), 637−644.
(35) Zhang, Z.; Wenzel, S.; Zhu, Y.; Sann, J.; Shen, L.; Yang, J.; Yao, X.; Hu, Y.-S.; Wolverton, C.; Li, H.; Chen, L.; Janek, J. Na3Zr2Si2PO12: A Stable Na+-Ion Solid Electrolyte for Solid-State Batteries. *ACS Applied Energy Materials* **2020**, *3* (8), 7427−7437.
(36) Wang, C.; Gao, J.; Gao, X.; Zhao, Y. Stabilizing the Na/Na3Zr2Si2PO12 interface through intrinsic feature regulation of Na3Zr2Si2PO12. *Cell Reports Physical Science* **2021**, *2* (7), 100478.
(37) Krauskopf, T.; Richter, F. H.; Zeier, W. G.; Janek, J. Physicochemical Concepts of the Lithium Metal Anode in Solid-State Batteries. *Chem. Rev.* **2020**, *120* (15), 7745−7794.
(38) Krauskopf, T.; Mogwitz, B.; Hartmann, H.; Singh, D. K.; Zeier, W. G.; Janek, J. The Fast Charge Transfer Kinetics of the Lithium Metal Anode on the Garnet-Type Solid Electrolyte Li6.25Al0.25-La3Zr2O12. *Adv. Energy Mater.* **2020**, *10* (27), 2000945.
(39) Bay, M.-C.; Wang, M.; Grissa, R.; Heinz, M. V. F.; Sakamoto, J.; Battaglia, C. Sodium Plating from Na-β''-Alumina Ceramics at Room Temperature, Paving the Way for Fast-Charging All-Solid-State Batteries. *Adv. Energy Mater.* **2020**, *10* (3), 1902899.
(40) Wang, M. J.; Carmona, E.; Gupta, A.; Albertus, P.; Sakamoto, J. Enabling "lithium-free" manufacturing of pure lithium metal solid-state batteries through in situ plating. *Nat. Commun.* **2020**, *11* (1), 5201.
(41) Fuchs, T.; Haslam, C. G.; Moy, A. C.; Lerch, C.; Krauskopf, T.; Sakamoto, J.; Richter, F. H.; Janek, J. Increasing the Pressure-Free Stripping Capacity of the Lithium Metal Anode in Solid-State-Batteries by Carbon Nanotubes. *Adv. Energy Mater.* **2022**, *12* (26), 2201125.
(42) Kasemchainan, J.; Zekoll, S.; Spencer Jolly, D.; Ning, Z.; Hartley, G. O.; Marrow, J.; Bruce, P. G. Critical stripping current leads to dendrite formation on plating in lithium anode solid electrolyte cells. *Nat. Mater.* **2019**, *18* (10), 1105−1111.
(43) Schlenker, R.; Stępień, D.; Koch, P.; Hupfer, T.; Indris, S.; Roling, B.; Miß, V.; Fuchs, A.; Wilhelmi, M.; Ehrenberg, H. Understanding the Lifetime of Battery Cells Based on Solid-State Li6PS5Cl Electrolyte Paired with Lithium Metal Electrode. *ACS Appl. Mater. Interfaces* **2020**, *12* (17), 20012−20025.
(44) Spencer Jolly, D.; Ning, Z.; Hartley, G. O.; Liu, B.; Melvin, D. L. R.; Adamson, P.; Marrow, J.; Bruce, P. G. Temperature Dependence of Lithium Anode Voiding in Argyrodite Solid-State Batteries. *ACS Appl. Mater. Interfaces* **2021**, *13* (19), 22708−22716.
(45) Riegger, L. M.; Otto, S.-K.; Sadowski, M.; Jovanovic, S.; Kötz, O.; Harm, S.; Balzat, L. G.; Merz, S.; Burkhardt, S.; Richter, F. H.; Sann, J.; Eichel, R.-A.; Lotsch, B. V.; Granwehr, J.; Albe, K.; Janek, J. Instability of the Li7SiPS8 Solid Electrolyte at the Lithium Metal Anode and Interphase Formation. *Chem. Mater.* **2022**, *34* (8), 3659−3669.

https://doi.org/10.1021/acsami.2c12991
ACS Appl. Mater. Interfaces 2022, 14, 42757−42769

2.6 Guidelines for Impedance Analysis of Parent Metal Anodes

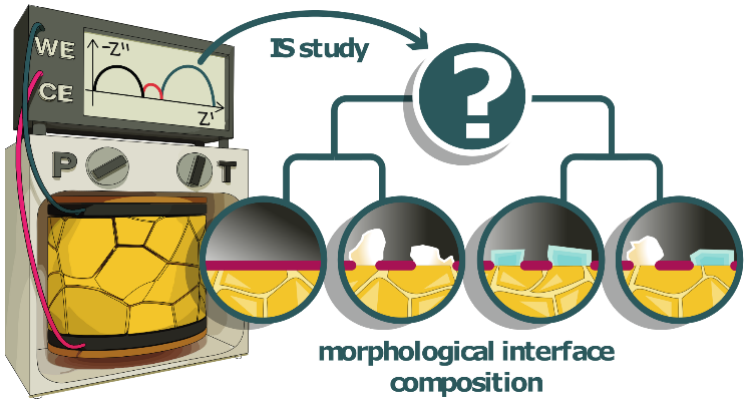

Abstract

Impedance spectroscopy is widely used in operando studies of solid-state batteries for characterizing charge transport and correlating it with structural features. A typical impedance spectrum reveals, in addition to transport signals of the solid electrolyte, one or more contributions due to processes taking place at the electrode interfaces. The focus of this study is on reversible (parent) metal anodes and a 3D electric network model is used to analyze the variation of their impedance as a function of pressure, temperature, or aging during cycling. This provides a recipe for experimentalists on how to identify impedance contributions arising from different interface effects, such as, charge transfer, dynamic current constriction, and solid electrolyte interphase formation. Rules are derived for assigning the different interface signals or identifying the dominant contribution in case of similar frequency dependence and a standard procedure for analysis is proposed. The suggested procedure is applied to experimental data of half cells where lithium metal is in contact with garnet-type $Li_{6.25}Al_{0.25}La_3Zr_2O_{12}$. This case study yields unambiguously that geometric current constriction due to morphological instabilities at the metal anode interface during cycling is the rate-limiting step for this type of metal anode, rather than the frequently assumed polarization resistance of the electric charge transfer migration process.

Reference

Guidelines for Impedance Analysis of Parent Metal Anodes in Solid-State Batteries and the Role of Current Constriction at Interface Voids, Heterogeneities and SEI. Janis K. Eckhardt, Till Fuchs, Simon Burkhardt, Peter J. Klar, Jürgen Janek, and Christian Heiliger *Adv. Mater. Interfaces* **2023**, 10, 8, 2202354-2202373. (DOI: 10.1002/admi.202202354)

Reproduced with permission

RESEARCH ARTICLE

ADVANCED MATERIALS INTERFACES
Open Access
www.advmatinterfaces.de

Guidelines for Impedance Analysis of Parent Metal Anodes in Solid-State Batteries and the Role of Current Constriction at Interface Voids, Heterogeneities, and SEI

Janis K. Eckhardt, Till Fuchs, Simon Burkhardt, Peter J. Klar, Jürgen Janek, and Christian Heiliger*

Impedance spectroscopy is widely used in operando studies of solid-state batteries for characterizing charge transport and correlating it with structural features. A typical impedance spectrum reveals, in addition to transport signals of the solid electrolyte, one or more contributions due to processes taking place at the electrode interfaces. The focus of this study is on reversible (parent) metal anodes and a 3D electric network model is used to analyze the variation of their impedance as a function of pressure, temperature, or aging during cycling. This provides a recipe for experimentalists on how to identify impedance contributions arising from different interface effects, such as, charge transfer, dynamic current constriction, and solid electrolyte interphase formation. Rules are derived for assigning the different interface signals or identifying the dominant contribution in case of similar frequency-dependence and a standard procedure for analysis is proposed. The suggested procedure is applied to experimental data of half cells where lithium metal is in contact with garnet-type $Li_{6.25}Al_{0.25}La_3Zr_2O_{12}$. This case study yields unambiguously that geometric current constriction due to morphological instabilities at the metal anode interface during cycling is the rate-limiting step for this type of metal anode, rather than the frequently assumed polarization resistance of the electric charge transfer migration process.

1. Introduction

Electrochemical energy storage devices become increasingly important in the view of the growing share of renewable energy sources in power generation. The successful implementation of the parent metal anode in secondary batteries can be considered a new milestone in the development of novel or improved battery technologies with higher energy densities and lifetimes.[1–3] By replacing graphite, the currently most widespread anode material, with lithium, the theoretical specific capacity on the anode side can be increased by approximately a factor of 10. However, the side reactions occurring due to the high reactivity of alkali metals in general result in severe challenges.[4–6] Dendrites can lead to short circuits and, together with liquid electrolytes, to fires.[7–9] A major research focus is on the substitution of the common liquid electrolyte by a solid electrolyte (SE) in order to suppress the growth of dendrites, on the one hand, and to reduce the flammability of the batteries, on the other hand. SEs are applied as both separators and catholyte components in all-solid state battery systems. However, the chemical, kinetic and thermodynamic stability of the metal anode|SE interface, in particular, poses a major challenge in the development process.

In this study, we focus on the separator SE that will be in direct contact with the alkali metal. Several inorganic SE ceramics are not chemically stable against the respective alkali metal, which can lead to the formation of a resistive solid electrolyte interphase (SEI) that strongly affects the electric transport properties of the battery cell. For example, the

J. K. Eckhardt, C. Heiliger
Institute for Theoretical Physics
Justus Liebig University
Heinrich-Buff-Ring 16, D-35392 Giessen, Germany
E-mail: janis.k.eckhardt@theo.physik.uni-giessen.de

The ORCID identification number(s) for the author(s) of this article can be found under https://doi.org/10.1002/admi.202202354.

DOI: 10.1002/admi.202202354

J. K. Eckhardt, T. Fuchs, S. Burkhardt, P. J. Klar, J. Janek, C. Heiliger
Center for Materials Research (ZfM)
Justus Liebig University
Heinrich-Buff-Ring 16, D-35392 Giessen, Germany

T. Fuchs, S. Burkhardt, J. Janek
Institute of Physical Chemistry
Justus Liebig University
Heinrich-Buff-Ring 17, D-35392 Giessen, Germany

P. J. Klar
Institute of Experimental Physics I
Justus Liebig University
Heinrich-Buff-Ring 16, D-35392 Giessen, Germany

ADVANCED SCIENCE NEWS
www.advancedsciencenews.com

ADVANCED MATERIALS INTERFACES
Open Access
www.advmatinterfaces.de

phenomenon of SEI formation plays a major role in argyrodite-type SEs versus lithium metal or sulfide-like variants of Na_3PS_4 versus sodium metal.[10–16] In addition, the mechanical properties of the solid materials involved have a major impact on the battery cells' performance. Unlike in the case of liquid electrolytes, a complicated interface morphology arises, when two solids come into mechanical contact. The contact formation depends, for example, on contact pressure, surface roughness, and the corresponding hardness of both materials. This can lead to the formation of pores of different shapes, sizes and depths at the interface. Similar interface morphologies occur upon plating or stripping of the metal electrode and the corresponding formation or annihilation of lattice defects, as originally suggested by Janek et al.[17–19]

Impedance spectroscopy (IS) is particularly suited for monitoring changes at the alkali metal|SE interface during operation due to comparably short measurement times. Individual contributions originating from microscopic transport processes within the SE (e.g., transport through the bulk of grains or across grain boundaries (GB)) may be separated from interface signals, if they differ in their characteristic time constants. The measured impedance data is mostly analyzed using 1D equivalent circuit models, although the actual transport through the real system is typically multidimensional and frequency-dependent.[20–22] As a result, this simplified analysis impedes a clear correlation between the macroscopic impedance response and microscopic transport processes, as mesoscopic phenomena such as dynamic current constriction (Cstr) due to the sample's morphology cannot be grabbed adequately.[23]

Nevertheless, experimental impedance data provide a powerful tool to correlate transport and structural properties and thus for operando monitoring of morphological changes, for example, at the interface between metal anode and solid electrolyte. Such impedance spectra exhibit one or more signals due to the interface. Recipes for experimentalists to assign the characteristics of these interface signals to the chemical and structural properties of the interface and the microscopic and mesoscopic transport processes across the interface are currently lacking. In the literature, the interface impedance is often simply attributed to an electric charge transfer (CT) process or SEI formation in the case of chemically unstable interfaces. Other processes that may become rate-limiting, such as diffusion of the reduced/oxidized species in the interface region, are only rarely considered.

Another important geometric effect that may affect the interface impedance is dynamic current constriction. In the case of reversible metal anodes under anodic current load (i.e., stripping), the accumulation of metal vacancies causes pore formation at the interface. This leads to a shrinkage of the electrochemically active surface area and an altering of the electrical and electrochemical properties.[24–28] Recent theoretical studies by Eckhardt et al.[29–30] and earlier work of Maier and Fleig[31–36] demonstrated that such pores lead to an additional geometric constriction resistance. Interestingly, the constriction effect can give rise to a separate semicircle in the Nyquist representation of the impedance data, resulting in a fingerprint that resembles a microscopic electric migration process. The corresponding impedance contribution, however, is not a microscopic transport process, but rather a global effect, which involves basically all the different microscopic transport processes occurring at the interface and adjacent regions.

The pore system is electrically insulating at low frequencies f of an exciting electric field, but it becomes dielectrically conductive at high frequencies. This change of conductivity with excitation frequency corresponds to a variation of the transport channels, where ions are injected into the SE. The whole electrode area and the entire SE volume can actively contribute to the transport through the system as long as pores at the interface are dielectrically conductive ($Z_{Pore} \approx 0\ \Omega$, displacement current). Insulating pores ($Z_{Pore} \rightarrow \infty\ \Omega$, electric current), however, lead to spatially focused (i.e., "constricted") ionic current lines at the remaining physical contact spots. The resulting constriction leads to a decrease of the active SE volume, which consequently causes a higher impedance.

SEI formation, CT between metal anode and SE or geometric current constriction, to name just a few possible reasons, are all effects related to the interface and contribute to the impedance response of the apparently reversible parent metal anode. In this study, we use a 3D electric network model to derive approaches, which allow experimentalists to analyze the interface impedance in terms of its origin and to identify the underlying microscopic process(es). For this purpose, the dependence of individual interface effects on stack pressure (i.e., contact area) and temperature are discussed. On this basis, we propose a novel approach and guideline for analyzing impedance data of electrode systems with chemically stable interfaces. This is validated by an experimental case study of a well-established system consisting of a lithium metal anode in contact with a garnet-type SE and corroborated by references to other published data. It reveals that current constriction due to morphological instabilities rather than the frequently assumed electric CT process is the rate-limiting step in the case of the system under study.

2. Computational Details

2.1. Description of the Model Structures

The 3D model systems considered comprise a dense polycrystalline solid electrolyte sandwiched between a metal working electrode (WE) and a metal counter electrode (CE) as shown in **Figure 1**a. The WE|SE interface is assumed to be non-ideal (e.g., porous), while an ideally-reversible and stable physical contact at the CE|SE interface is assumed serving as a quasi-reference electrode (QRE).[37] We assume a cubic shape of the SE ($L_x = L_y = L_z$) corresponding to a volume of $(100\ \mu m)^3$ and a thickness of 10 nm for the GBs including the adjacent space-charge region.[37–38] The non-ordered microstructure of the SE based on an average grain size of 10 µm is generated by using a Voronoi algorithm. We consider the same fixed typical microstructure of the SE in all series of simulations performed, where the relative physical contact area $A_{WE|SE} = A_{WE}/A_{SE}$ between WE and SE is varied. This enables a direct comparability of the computational results obtained for different materials parameters that can be assigned to interfaces, grains, and grain boundaries. It should be noted that the derived conclusions are general in nature and can also be applied to larger system sizes.

ADVANCED SCIENCE NEWS
www.advancedsciencenews.com

ADVANCED MATERIALS INTERFACES
Open Access
www.advmatinterfaces.de

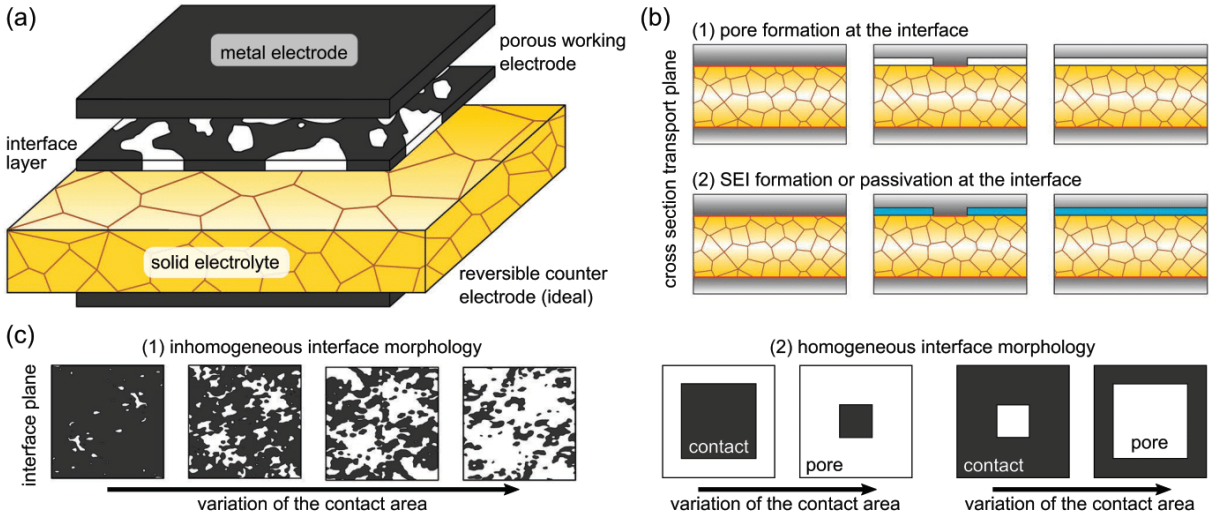

Figure 1. Schematic description of the 3D computational model systems. a) The cubic SE (yellow) is sandwiched between two metal electrodes (dark gray). The non-ideal WE|SE interface morphology is described by a separate quasi-2D layer of constant thickness. b) The effect of (1) pores and (2) an SEI or passivation is systematically studied using an impedance network model. Pores (white) are modeled as local capacitors, while the SEI or passivation (light blue) is described by local *RC*-elements with large resistivity. c) Overview of different (1) inhomogeneous and (2) homogeneous interface morphologies investigated. The former are derived from stress maps based on a multi-scale, time-dependent, 3D contact model reported by Zhang et al. Adapted with permission.[39] Copyright 2020, Elsevier.

The number of geometric model parameters for describing the WE|SE interface morphology is strongly reduced by focusing on a quasi-2D layer of constant thickness δ_{Int}. The latter is set to 10^{-4} of the transport length L_z and kept constant throughout all studies. The effect of this parameter on the impedance is discussed elsewhere.[29] In each series of computations, the relative physical contact area $A_{WE|SE}$ is systematically varied in size from 100% describing an ideal contact to 0% assuming a complete loss of contact. Such a loss or degradation of physical contact in real samples results either from pores or resistive inclusions (see Figure 1b). Experimental information on the explicit interface morphology at the mesoscale is difficult to access. Therefore, we consider four realistic inhomogeneous morphologies derived from lithium-surface-stress maps based on a multi-scale, time-dependent, 3D contact model published by Zhang et al.[39] The reported rectangular stress maps at various stack pressures were digitized, binarized, discretized, and extended via translation and rotation considerations to fit the geometry of our cubic 3D model system (see Figure 1c). In addition, we use two simplified interface geometries for comparison, whose ratio A_{WE}/A_{SE} can be continuously varied between ideal contact and no contact. One consists of a single square-shaped contact spot, and the second of a frame-like contact structure.

2.2. Description of the 3D Impedance Network and Choice of Materials Parameters

We use our 3D electric network model developed to describe the ion transport throughout the system.[29–30] *RC*-elements represent the electric transport processes within the SE (i.e., bulk and GB transport) in the nodal network. The redox reaction either oxidizing Me^0 or reducing Me^+ ions at the alkali metal|SE interfaces (i.e., the CT step) is also described by an *RC*-element based on a polarization resistance R_{Pol} and a double-layer capacitance C_{DL}. The notation of both microscopic parameters results from the Butler-Volmer description of the charge transfer across an interface. The pores and resistive inclusions or passivation reducing the physical contact area $A_{WE|SE}$ are mimicked by a capacitor and a *RC*-element with a large resistivity, respectively. It should be noted that we do not consider low-frequency diffusion processes in the system. The transport within the lithium metal electrode is assumed to be resistance-free. The same holds true, without loss of generality, for the CT step at the QRE. A detailed description about setting up the 3D electric network model and computing an impedance spectrum is given in our previous studies.[23,29–30]

We used the standard formulas for resistors and plate capacitors to calculate the values of the local circuit elements in the different layers of the sample. We chose as specific transport parameters values matching the garnet-type solid electrolyte $Li_{6.25}Al_{0.25}La_3Zr_2O_{12}$ (LLZO). The relative permittivity was set to $\varepsilon_{Bulk} = \varepsilon_{GB} = 150$.[37,40–41] The bulk ($\sigma_{Bulk} = 0.46$ mS cm^{-1}, $E_{a,Bulk} = 0.34$ eV) and GB ($\sigma_{GB} = 5.97$ µS cm^{-1}, $E_{a,GB} = 0.43$ eV) conductivities at room temperature were determined from temperature-dependent measurements.[37] The polarization resistance R_{Pol} describing the CT between metal electrode and SE was assumed to be 0.5 Ω cm^2 ($E_{a,CT} = 0.43$ eV). Three different parameter pairs for the double-layer capacitance C_{DL} and the pore capacitance $\tilde{C}_{Pore}$ were assumed to ensure a specific order of the characteristic time constants of CT and dynamic constriction, i.e., (1.77 F cm^{-2}, 885 µF cm^{-2}) for $\tau_{Cstr} < \tau_{CT}$, (1771 µF cm^{-2}, 443 µF cm^{-2}) for $\tau_{Cstr} \approx \tau_{CT}$, and (177 µF cm^{-2}, 4425 µF cm^{-2}) for $\tau_{CT} < \tau_{Cstr}$. The area-specific resistance $\tilde{R}_{SEI}$ and capacitance $\tilde{C}_{SEI}$ of the resistive SEI at the interface were assumed to be 100 Ω cm^2 and 88 µF cm^{-2}, respectively. Note that the single interface parameters are not necessarily related to the Li|LLZO interface.

ADVANCED SCIENCE NEWS
www.advancedsciencenews.com

ADVANCED MATERIALS INTERFACES
Open Access
www.advmatinterfaces.de

2.3. Analysis of the Experimental Impedance Data and the Computed Impedance Series

All impedance spectra, those derived by the 3D network modelling and those obtained experimentally for the case study, were analyzed in the frequency domain by fitting them with an 1D equivalent circuit model. It consists of four *RC*-elements connected in series representing bulk and GB transport within the SE, dynamic current constriction, and CT at the WE|SE interface. The resulting parameter pairs (R_i, C_i) with i = (Bulk, GB, Cstr, CT) represent the macroscopic quantities of the single transport effects. The theoretical and experimental impedance data were also evaluated in the time domain by performing a distribution of relaxation times (DRT) analysis. Both types of analyses were performed using the commercial software RelaxIS 3 (version 3.0.20.16, rhd instruments GmbH & Co. KG).

The computed series of impedance spectra based on the 3D electric network model are almost free of noise signals (see Figures 3–7). The Kramers–Kronig test yields negligible residuals in the order of 10^{-6}%.[42] Therefore, all data points originating from these simulations were considered in the impedance analysis process, and only a small regularization term was required in the calculation of each DRT.[43]

Frequency points below 200 Hz were excluded in the analysis of the experimental impedance data shown in Figure 9, since individual residuals, particularly of the imaginary part, were greater than 4% in the Kramers–Kronig test.[42] The same holds for frequency points above 0.2 MHz, since the high frequency impedance contribution is only partially recorded in the measurement range. The corresponding DRT were calculated using exclusively the real part of the impedance as the residuals are in the range of a few 0.1% only, indicating high quality of the data. No additional data points were generated by interpolation and the second derivative of the distribution function $\gamma(\tau)$ was used in the Tikhonov regularization problem.[43]

3. Results

3.1. Challenges in Interpreting Experimental Impedance Data

An experimental system for investigating reversible metal anodes consists at least of a three-layer stack comprising a parent metal electrode (e.g., Li, Na, Ag, etc.), a highly dense polycrystalline SE, and a counter electrode. Various transport processes are expected to occur in such systems, namely bulk transport and transport across GBs within the SE and, in addition, electric CT at the metal|SE interface. Furthermore, one must distinguish between electric CT at the metal|SEI|SE boundary and dielectric conduction across the metal|pore|SE interface. It is anticipated that several of these processes may be separated from each other by IS as they should possess a different dependence on frequency of the applied external electric field.[44] Bulk transport processes typically possess characteristic frequencies in the high frequency range (i.e., several MHz) and GB transport in the medium frequency range (i.e., several kHz) at room temperature. Interface contribution(s) are typically expected at lower frequencies.[44]

In general, the impedance response of all-solid systems is highly affected by the solid|solid interface geometry. **Figure 2** depicts a schematic decision tree, whose branches correlate different interface morphology scenarios with transport effects reflected in the impedance signal of the interface. It is meant as a guideline for identifying the process(es) that are likely to dominate the metal anode|SE interface impedance in a specific scenario. The effects accounted for are an electric CT step at the metal|SE interface, a resistive SEI or passivation, and geometric current constriction due to pores or inclusions. It should be noted that we do not consider other processes such as transport limitations within the metal electrode.

From top to bottom of the decision tree, we distinguish on the first level between chemically stable and unstable interfaces, on the second level between ideal ($A_{WE|SE}$ = 100%) and non-ideal physical contact ($A_{WE|SE}$ < 100%), and on the third level between morphologically stable and unstable interfaces at the mesoscopic scale. The anticipated interface effects for each branch of the decision tree are given at the bottom level. Apparently, only in a few cases one expects a single interface effect to be responsible for its impedance contribution (e.g., outer left branch). Additional constriction effects are frequently expected in the case of non-ideal physical contacts. In such situations, it is very important to identify the dominant interface process(es) that lead to an increase in impedance, since the strategies for improving the electric interface characteristics of a (battery) system depend on the dominant process.

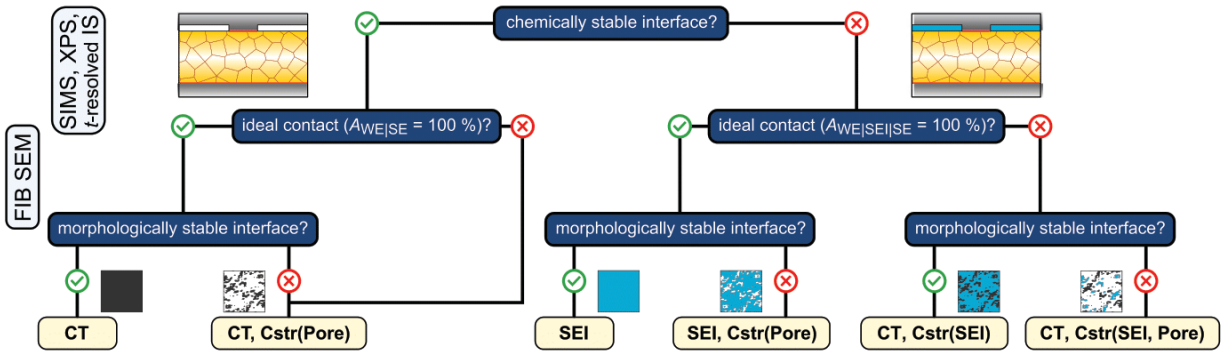

Figure 2. Effect of the geometric interface morphology on the impedance response of the system. The interface impedance in all-solid systems is often composed not only of electric migration processes, but also of additional geometric effects such as dynamic current constriction. Note that several other interface effects such as constriction due to transport limitations within the metal electrode are not considered in the decision tree.

ADVANCED SCIENCE NEWS
www.advancedsciencenews.com

ADVANCED MATERIALS INTERFACES
Open Access
www.advmatinterfaces.de

For this purpose, measuring a single impedance spectrum of a sample and fitting it with a 1D equivalent circuit model is not sufficient. It cannot fully resolve the significance of different interface effects, since it does not lead to individual characteristic impedance features. Moreover, often only one impedance signal assigned to the interface is experimentally observed, although several processes contribute. Therefore, establishing the relevance of different interface effects typically requires additional experimental input. This can be obtained, for example, by systematic variation of external parameters and monitoring of their impact on the sample's impedance response. This comprises in particular, experiments where the stack pressure is varied and the pristine interface with $A_{WE|SE} < 100\%$ due to porosity or inclusions becomes almost ideal. Although such experiments cause irreversible changes of the sample's morphology, they allow to "switch off" current constriction effects. Similarly, temperature-dependent measurements yield activation energies of the macroscopic resistances extracted from the impedances accounted for in the 1D equivalent circuit model used for fitting the experimental impedance spectra. This is helpful, as the constriction resistance arises from an averaging of different microscopic electric migration processes at the interface.

Such comprehensive impedance studies need to be complemented by direct investigations of the interface morphology. The chemical stability of an interface can be studied by time-resolved IS measurements complemented by well-established methods such as X-ray photoelectron spectroscopy (XPS) or secondary-ion mass spectrometry (SIMS).[45–47] The quality of the physical contact and its morphological stability under operation can be probed using focused ion beam scanning electron microscopy (FIB SEM).[48–50] Combining all these efforts allows experimentalists to correlate changes of impedance spectra during cycling with degradation of the cell caused by morphology changes at the metal anode|SE interface. Thus, such studies are essential for optimizing all-solid-state batteries employing metal anodes in a systematic fashion.

3.2. Signatures of Various Interface Processes on the Impedance Response of Battery Systems

The charge transfer at the metal|SE interface, the successive formation of an SEI, passivation or pores at the interface, they all affect the interface characteristics in their own specific manner. To highlight their individual signatures in the impedance response of the system, series of impedance spectra are computed using a 3D electric network model. Throughout each series, we systematically vary the interface morphology of the model system as depicted in Figure 1 for a given set of materials parameters. The computed impedance spectra were subsequently analyzed with a 1D equivalent circuit model consisting of four *RC*-elements connected in series to derive the macroscopic transport parameters (R_i, C_i) of bulk and GB transport within the SE as well as CT and geometric constriction effects due to pores or SEI formation at the interface. It should be noted that assuming a constant interface thickness δ_{Int} throughout an impedance series may lead to an overestimation of the fit parameter $\tau_{Cstr} = R_{Cstr} \cdot C_{Cstr}$ in the computations compared to experimental observation, as the simultaneous decrease in δ_{Int} somewhat compensates the effect of a decreasing $A_{WE|SE}$.[29] In this section, we first systematically investigate the branch of chemically stable interfaces within the decision tree, i.e., assuming no SEI formation or passivation, and then address chemically unstable interfaces with SEI formation.

3.2.1. Effect of Morphological Instabilities Due to Pore Formation at Chemically Stable Interfaces

We assume an interface that is free of a passivation or resistive SEI layer in this subsection. Such a situation is, for example, experimentally observed for lithium metal in contact with a garnet-type SE.[51–54] In the modelling, we keep the microstructure of the SE constant, whilst varying the pore distribution at the WE|SE interface. We compare the computational results of the four realistic interface morphologies based on the multi-scale contact model[39] with two simplified interface morphologies consisting of one square-shaped contact spot and one frame-like contact structure whose lateral extensions can be varied continuously in size, as shown in Figure 1c. The macroscopic transport parameters (R_i, C_i) extracted from the modelled impedance spectra by the 1D fitting approach are analyzed with respect to their dependence on interface morphology, contact area, and temperature. Thereby, we consider three different pairs of parameters for the double-layer and pore capacitance (see Section 2) to explore the order of constriction and CT relaxation time on the scale of time constants, since τ_{Cstr} has a significant effect on the shape of the impedance spectrum and thus the derived conclusions.

Influence of Inhomogeneous Interface Morphologies: Each of the graphs depicted in **Figure 3**a–c shows five impedance spectra in Nyquist representation based on the disordered interface morphologies between WE and SE depicted on their right. The three graphs correspond to different orders of interface time constants, i.e., $\tau_{Cstr} < \tau_{CT}$, $\tau_{Cstr} \approx \tau_{CT}$, and $\tau_{CT} < \tau_{Cstr}$, respectively. The relative contact area $A_{WE|SE}$ in each computation series varies between 100% (bottom) and 22% (top). Three semicircles can be visually observed, when considering an ideal physical contact ($A_{WE|SE} = 100\%$). These correspond to the two ion migration processes within the SE and the CT step at the interface. Bulk and GB impedances corresponding to the blue and red semicircles, respectively, remain unchanged when reducing the contact area by pore formation. Pore formation lead to dynamic current constriction that occurs as an additional geometric effect in the spectrum, which affects the interface impedance. As a general trend, the DC resistance of the whole electrode system increases with decreasing $A_{WE|SE}$, as indicated by the shift of the outer impedance semicircle to the right. However, the interface response differs in detail for the three cases of order of τ_{Cstr} and τ_{CT}.

The order of the time constants determines how the morphological changes at the interface are reflected in the impedance spectrum. For $\tau_{Cstr} < \tau_{CT}$ shown in Figure 3a, the change in impedance is related to the formation of an additional geometric constriction semicircle (yellow) between that of the GB (red) and the CT signal (green). In addition, the CT impedance contribution (green) at lower frequencies simultaneously

ADVANCED SCIENCE NEWS
www.advancedsciencenews.com

ADVANCED MATERIALS INTERFACES
Open Access
www.advmatinterfaces.de

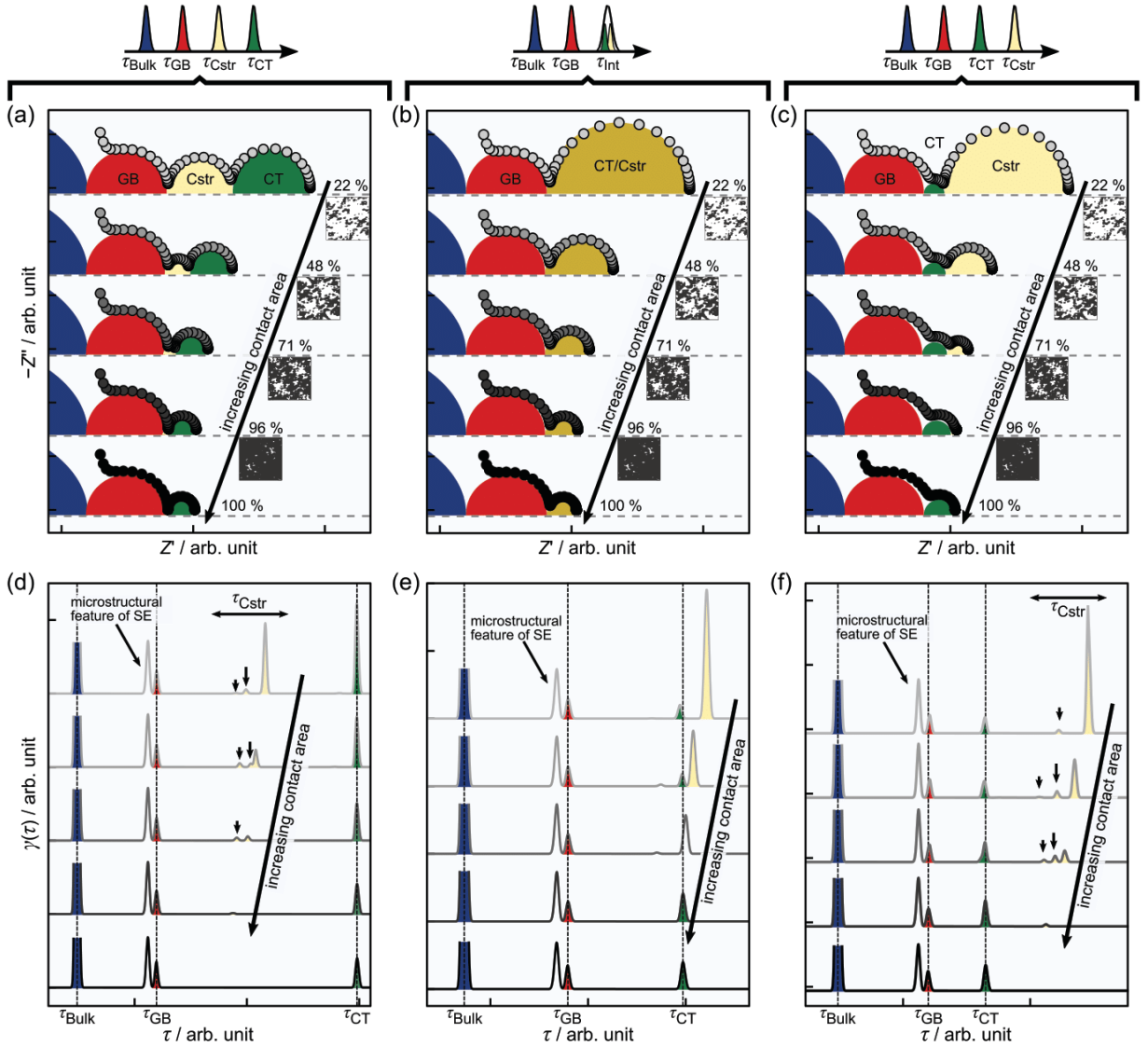

Figure 3. Computed series of impedance spectra in Nyquist representation and corresponding DRT analyses for various realistic WE|SE interface morphologies (inset) considering different orders of the time constants of CT and dynamic current constriction. The interface morphologies originate from simulated Li-surface-stress maps reported by Zhang et al. Adapted with permission.[39] Copyright 2020, Elsevier. Note that the bulk impedance (blue) is not fully displayed for clarity and low-frequency diffusion processes are not considered in the modeling. a–c) A porous interface leads to a constriction effect (yellow), which results in an increase in impedance with decreasing contact area $A_{WE|SE}$. The shape of the impedance and the changes of individual contributions depend on the order of the time constants of the interface processes involved. d–f) An inhomogeneous distribution of pores at the interface leads to additional DRT signals (black arrows) in the vicinity of the major constriction signal (yellow).

increases in size. In the case of similar time constants $\tau_{Cstr} \approx \tau_{CT}$ depicted in Figure 3b, only one effective interface semicircle (ochre) can be visually observed in the Nyquist representation of the impedance spectra that increases in size with decreasing $A_{WE|SE}$. In Figure 3c, where the order of time constants is reversed ($\tau_{CT} < \tau_{Cstr}$), an increasing geometric constriction semicircle (yellow) arises to the right of the CT signal (green) and dominates the interface impedance response with decreasing $A_{WE|SE}$, whilst the CT impedance decreases. It should be noted, however, that the DC resistance in the three cases is independent of the arrangement of the time constants for all $A_{WE|SE}$. This is not a universal effect, but is related to the modeling of the different order of time constants τ_i in the computations by adjusting the magnitude of the local capacitances in the 3D electric network, but not that of the local resistors. In the DC case ($f = 0$ Hz), the impedance of a local *RC*-element is solely given by its ohmic contribution. This is due to the fact that the capacitor is connected in parallel with a corresponding resistor and the absolute value of its impedance becomes infinity, i.e., $|Z_C(f = 0\ \text{Hz})| = \infty\ \Omega$.

ADVANCED SCIENCE NEWS
www.advancedsciencenews.com

ADVANCED MATERIALS INTERFACES
Open Access
www.advmatinterfaces.de

To investigate the effects of structural disorder and order of the time constants in more detail, we performed DRT analyses of the three series of impedance data as depicted in Figure 3d–f. Here, the amplitude of the leftmost signal (blue) corresponding to the bulk transport has been truncated in all DRT for a clearer data representation. The DRT corresponding to an ideal contact ($A_{WE|SE}$ = 100%) consist of four signals independent of the order of the time constants. The center positions of three signals match the (input) time constants of the microscopic electric transport processes in the system, i.e., bulk (blue) and GB (red) transport in the SE, and CT (green) at the WE|SE interface. The fourth signal in the vicinity of the GB time constant is related to the inhomogeneous synthetic microstructure of the SE and results from competing transport paths through the system which yield slightly different time constants. The occurrence of this effect in inhomogeneous samples can be analytically proven as demonstrated in our previous work.[23]

In the case of $\tau_{Cstr} < \tau_{CT}$ shown in Figure 3d, several additional signals form in the intermediate time range between GB and CT relaxation time, when the contact area $A_{WE|SE}$ is reduced. The strong dependence of the time constants (central position of these signals on the relaxation time axis) on $A_{WE|SE}$, especially of the main signal, is a characteristic feature of their geometric origin. In comparison, the time constant of a microscopic or local electric migration process does not depend on $A_{WE|SE}$. The dependence of these signals on $A_{WE|SE}$ reflects that dynamic constriction is a global effect, which varies with the interface morphology and averages over the time constants of the microscopic processes within the system. The smaller geometric signals (indicated by black arrows in the graphs) result from the inhomogeneous spatial distribution and the different sizes of the pores, since penetration depth and constriction region (i.e., the region in which equipotential lines are not parallel to the interface) increase with pore size. This implies that not only a pore depth distribution[29] leads to a (strongly) distorted constriction impedance, but also an inhomogeneous interface morphology with a broad pore size distribution. Similar results were recently also observed experimentally.[55–56] This finding is independent of the order of time constants. The signals related to the disorder (black arrows) shift with τ_{Cstr}. Thus, they are difficult to resolve in the case of $\tau_{Cstr} \approx \tau_{CT}$, but they can be easily observed again when $\tau_{CT} < \tau_{Cstr}$.

We continue our analysis of the model results by extracting the macroscopic transport parameters (R_i, C_i) from the computed impedance spectra by fitting them with a 1D equivalent circuit model. **Figure 4**a–c shows the evolution of the charge transfer (R_{CT}, C_{CT}, τ_{CT}), effective interface (R_{Int}, C_{Int}, τ_{Int}), and dynamic constriction parameters (R_{Cstr}, C_{Cstr}, τ_{Cstr}) as a function of $A_{WE|SE}$ for the three cases of order of time constants τ_{CT} and τ_{Cstr}. In the analysis, we also considered two simplified interface geometries, i.e., a single contact spot (blue triangles) and a frame-like contact spot (yellow squares), where $A_{WE|SE}$ can be tuned continuously, in addition to the five realistic interface morphologies (red circles). The macroscopic bulk (R_{Bulk}) and GB transport parameters (R_{GB}) are given as horizontal reference lines in green and orange, respectively, since both do not depend on the pore fraction at the two-phase boundary $A_{WE|SE}$. The reference line of the geometric pore capacitance C_{Pore} is displayed in black.

In the case of $\tau_{Cstr} < \tau_{CT}$ depicted in Figure 4a, the CT and constriction resistances (R_{Cstr}, R_{CT}) increase with decreasing $A_{WE|SE}$. The constriction capacitance C_{Cstr} approaches that of the pores C_{Pore} and the CT capacitance C_{CT} decreases with decreasing contact area $A_{WE|SE}$. The time constant of the CT electric migration process is preserved, while that of geometric current constriction changes by about three orders of magnitude. The reason is that R_{Cstr} tends to infinity and the capacitance C_{Cstr} tends toward C_{Pore} when $A_{WE|SE}$ goes to zero, i.e., for complete loss of physical contact. The CT transport parameters (R_{CT}, C_{CT}) are almost unaffected by the distribution of the contact area at the interface for constant $A_{WE|SE}$, in contrast to the geometric constriction parameters (R_{Cstr}, C_{Cstr}). Especially the resistance R_{Cstr} is strongly affected by the morphology of the interface. Its sensitivity on the distribution of the physical contact for fixed $A_{WE|SE}$ increases with decreasing $A_{WE|SE}$. The value of R_{Cstr} is the lower, the finer the distribution of the physical contact is at the interface. The constriction capacitance, on the other hand, is not affected by the distribution of contact. This behavior is known and discussed in more detail in our previous work and also by Maier and Fleig.[29,33]

In the case of $\tau_{Cstr} \approx \tau_{CT}$, only one interface signal can be visually observed in the modelled impedance spectra. The corresponding macroscopic transport parameters (R_{Int}, C_{Int}) extracted by fitting with the 1D equivalent circuit model reflect the superposition of CT and constriction effects, as shown in Figure 4b. The electric CT migration process dominates for an ideal physical contact, but the impact of geometric constriction becomes more prominent with decreasing contact area. The magnitude of the effective resistance R_{Int} depends significantly on the interface morphology for small $A_{WE|SE}$ similar to R_{Cstr} in case of $\tau_{Cstr} < \tau_{CT}$ shown in Figure 4a. The effective capacitance C_{Int} converges towards a certain value and the time constant τ_{Int} increases by about 1.5 orders of magnitude with decreasing $A_{WE|SE}$. These findings clearly indicate that the impact of geometric constriction in the case of a single interface impedance signal is not negligible, in particular, when $A_{WE|SE}$ is smaller than 50%.

The qualitative behavior of the macroscopic CT parameters (R_{CT}, C_{CT}) changes drastically, when the order of time constants is reversed, i.e., $\tau_{CT} < \tau_{Cstr}$, whereas that of dynamic constriction (R_{Cstr}, C_{Cstr}) is only quantitatively affected. Figure 4c highlights that the CT resistance R_{CT} decreases and the CT capacitance C_{CT} increases with decreasing contact area $A_{WE|SE}$. The trends of these two macroscopic parameters with $A_{WE|SE}$ are opposite to those of the two cases shown in Figure 4a,b. The behavior is somewhat surprising at first glance, but it is related to different evolving transport paths through the system for frequencies close to $1/\tau_{CT}$. All transport channels are nearly perpendicular to the interface and parallel to each other, i.e., not constricted anymore, since the pores are dielectrically conductive in this frequency range.[30] This is discussed in more detail in the next section.

Functional Dependence of Charge Transfer and Constriction Resistance on the Contact Area: The distinction between CT and constriction impedance is simplified if both contributions are well-separated in the spectrum. This is usually not the case in experimental data, which may explain why different functional relationships of what is summed up as *interface resistance*

ADVANCED SCIENCE NEWS
www.advancedsciencenews.com

ADVANCED MATERIALS INTERFACES
Open Access
www.advmatinterfaces.de

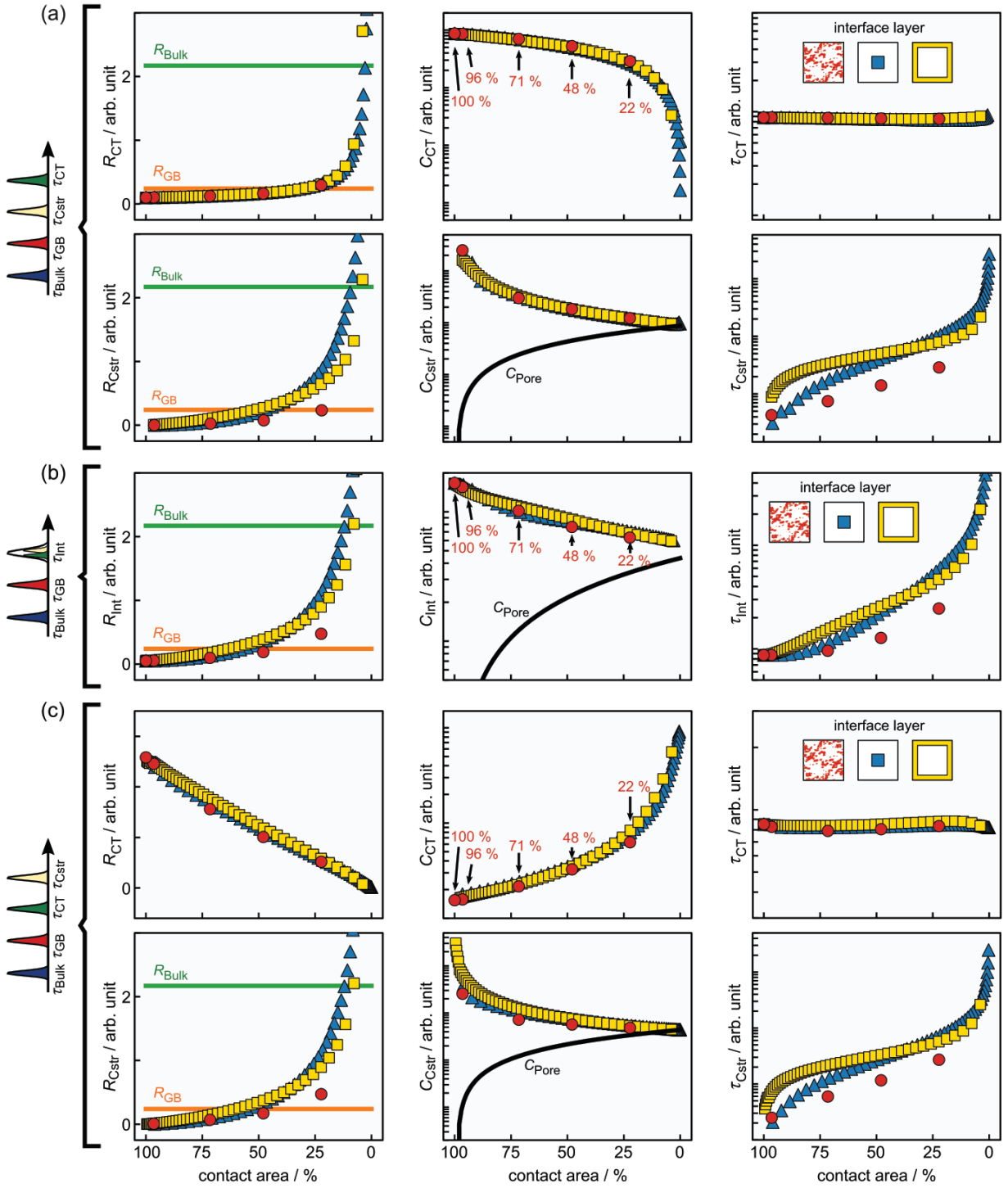

Figure 4. Evolution of the macroscopic transport parameters (R_i, C_i, τ_i) of the interface contributions, considering different orders of time constants, i.e., a) $\tau_{Cstr} < \tau_{CT}$, b) $\tau_{Cstr} \approx \tau_{CT}$, and c) $\tau_{CT} < \tau_{Cstr}$. The bulk (green) and GB (orange) parameters are independent of the pore fraction at the interface and shown as reference values. The CT parameters at constant contact area are nearly independent of the interface morphology but their qualitative behavior is not universal. It depends on the order of time constants. The constriction resistance, in contrast, depends on the distribution of the physical contact area at the interface.

ADVANCED SCIENCE NEWS
www.advancedsciencenews.com

ADVANCED MATERIALS INTERFACES
Open Access
www.advmatinterfaces.de

under force application are discussed in the literature.[37,39] It is frequently ignored that the interface impedance can have different origins and therefore a different dependence of the corresponding resistance R_i and capacitance values C_i on external parameters, such as stack pressure. This underlines the need for a theoretical in-depth analysis in order to evaluate how the constriction parameters (R_{Cstr}, C_{Cstr}) and the CT parameters (R_{CT}, C_{CT}) of the interface impedance behave, when the physical contact area $A_{WE|SE}$ is varied. For this purpose, the macroscopic transport parameters of the three computed impedance series shown in Figure 4 considering different orders of time constants τ_{Cstr} and τ_{CT} are further analyzed using a double logarithmic data representation, i.e., log R_i versus log $A_{WE|SE}$ and log C_i versus log $A_{WE|SE}$. This kind of data evaluation only holds, if the QRE does not affect the derived CT parameters, i.e., $Z_{QRE} = 0\ \Omega$. Otherwise, the offset due to the QRE needs to be subtracted from the CT parameters prior to calculating log R_i and log C_i.

The constriction resistance R_{Cstr} in **Figure 5**a,f is not proportional to $A_{WE|SE}^{-1}$, i.e., it does not exhibit a slope of –1 in the double-logarithmic data representation log R_{Cstr} versus log $A_{WE|SE}$. Once the constriction signal can be resolved in the impedance spectrum, R_{Cstr} increases by several orders of magnitude and may also become significantly larger than R_{CT}. Starting from a constriction resistance of zero for an ideal interface contact ($A_{WE|SE} = 100\%$), there is a sharp non-linear increase of log R_{Cstr} as log $A_{WE|SE}$ decreases, followed by an almost linear subregion with lower resistance increases at small contact areas. The general behavior, however, depends on the combination of the geometric interface morphology, the phases present at the interface and the corresponding materials parameters. Nonetheless, the qualitative trends are independent of the order of the time constants, but the increase in constriction resistance R_{Cstr} is somewhat more pronounced in the case of $\tau_{CT} < \tau_{Cstr}$.

The finding that R_{Cstr} is not proportional to $A_{WE|SE}^{-1}$ reflects the mesoscopic character of the constriction phenomenon. The impact of a variation of the physical contact area $A_{WE|SE}$ is not restricted to the interface layer itself, but globally affects the transport paths taken by the charge carriers through the system. Therefore, geometric parameters, such as the distribution of the pores or physical contact have a major effect on the magnitude of R_{Cstr}.[29,33] This indicates that performing the same experiment in the laboratory several times on nominally identical samples will lead to a distribution of resistances R_{Cstr} due to non-reproducible interface morphologies (i.e., geometric differences on the mesoscale). The impact of the variation of the interface morphology on R_{Cstr} is particularly pronounced at small physical contact areas. In consequence, a variance in the corresponding experimental data is not necessarily due to uncertainty in the measurement or in the fitting process with a 1D equivalent circuit model. Instead, the variance may reflect a change of the interface morphology and, thus, be at least partially of geometric origin. Therefore, the measure of the impedance in applications may be used for health monitoring of the interface. If the same sample is measured several times, for example, repeatedly during cycling, and the resistance R_{Cstr} changes, it is an indicator that the interface degrades. However, no simple functional or analytical relation between constriction resistance and contact area $A_{WE|SE}$ exists, but these considerations underline again the importance of the structural information about the interface morphology.

We applied the same procedure to evaluate the functional relationship of the CT resistance R_{CT} and the CT capacitance C_{CT}. The double logarithmic data representation in Figure 5b for $\tau_{Cstr} < \tau_{CT}$ shows a nearly linear relation between log R_{CT} and log $A_{WE|SE}$ that is almost independent of the interface morphology. Fitting the data with a linear function reveals slopes in the range of –1.03 and –1.08 for the three model systems considering different interface morphologies. Similar results are observed for the CT capacitance C_{CT}, as shown in Figure 5c. It also depends linearly on the contact area with slopes between 1.02 and 1.08. Interestingly, the functional relationships of R_{CT} and C_{CT} show a very different behavior in the case of the reversed order of the time constants ($\tau_{CT} < \tau_{Cstr}$) as shown in Figure 5g,h, respectively. The data representations of log R_{CT} versus log $A_{WE|SE}$ now exhibit slopes of approximately +1 and those of log C_{CT} versus log $A_{WE|SE}$ slopes of about –1. In other words, the sign of the slopes in the case of resistance and capacitance is reversed with the order of the time constants.

At first glance, this finding is unexpected because CT is a microscopic electric migration process and, therefore, its impact should remain restricted to the interface, other than in the case of the mesoscopic constriction effect. The macroscopic CT resistance and capacitance are expected to be proportional to the inverse of the active interface area ($R_{CT} \sim A_{WE|SE}^{-1}$) and proportional to the active interface area itself ($C_{CT} \sim A_{WE|SE}$), respectively. The deviating observations from this behavior are related to the evolving transport paths through the system. In the case of $\tau_{Cstr} < \tau_{CT}$, the pores at the interface are insulating for frequencies when the CT impedance signal arises. Therefore, the active fraction of the interface corresponds to $A_{WE|SE}$. This is why $R_{CT} \sim A_{WE|SE}^{-1}$ and $C_{CT} \sim A_{WE|SE}$ with slopes of –1 and +1 for log R_{CT} versus log $A_{WE|SE}$ and log C_{CT} versus log $A_{WE|SE}$, respectively. The transport situation is changed when considering the reversed order of time constants $\tau_{CT} < \tau_{Cstr}$. The pores at the interface are dielectrically conductive in the frequency range of the CT impedance signal. If the conduction contribution across the pores is comparable to that across the physical contact spots, the current is homogeneously distributed across the interface. In this situation, the CT resistance will linearly decrease $R_{CT} \sim A_{WE|SE}$ and CT capacitance will increase $C_{CT} \sim A_{WE|SE}^{-1}$ with decreasing $A_{WE|SE}$, i.e., increasing coverage of the interface with pores. Note that these two relationships only provide an estimate for the upper and lower bound of R_{CT} and C_{CT}, respectively, because heterogeneous current distributions at the interface with respect to $A_{WE|SE}$ and $A_{WE|Pore|SE}$ will lead to deviations. In particular, in the limiting case where conduction across the pores is orders of magnitude better than across the physical contacts, no significant CT contribution is expected in the impedance spectrum since the dominant current paths do not cross physical contact spots. The observed deviations of the absolute values of the slopes of the linear fitting curves from a value of 1 in Figure 5b,c,g,h are due to the contributions of the interface areas with the much higher impedance, which are connected in parallel to the fraction of the interface carrying most of the transport, i.e., the pores in case of $\tau_{CT} < \tau_{Cstr}$ and the physical contacts in case of $\tau_{CT} < \tau_{Cstr}$. This has been recently discussed in more detail in the literature.[30]

ADVANCED SCIENCE NEWS
www.advancedsciencenews.com

ADVANCED MATERIALS INTERFACES
Open Access
www.advmatinterfaces.de

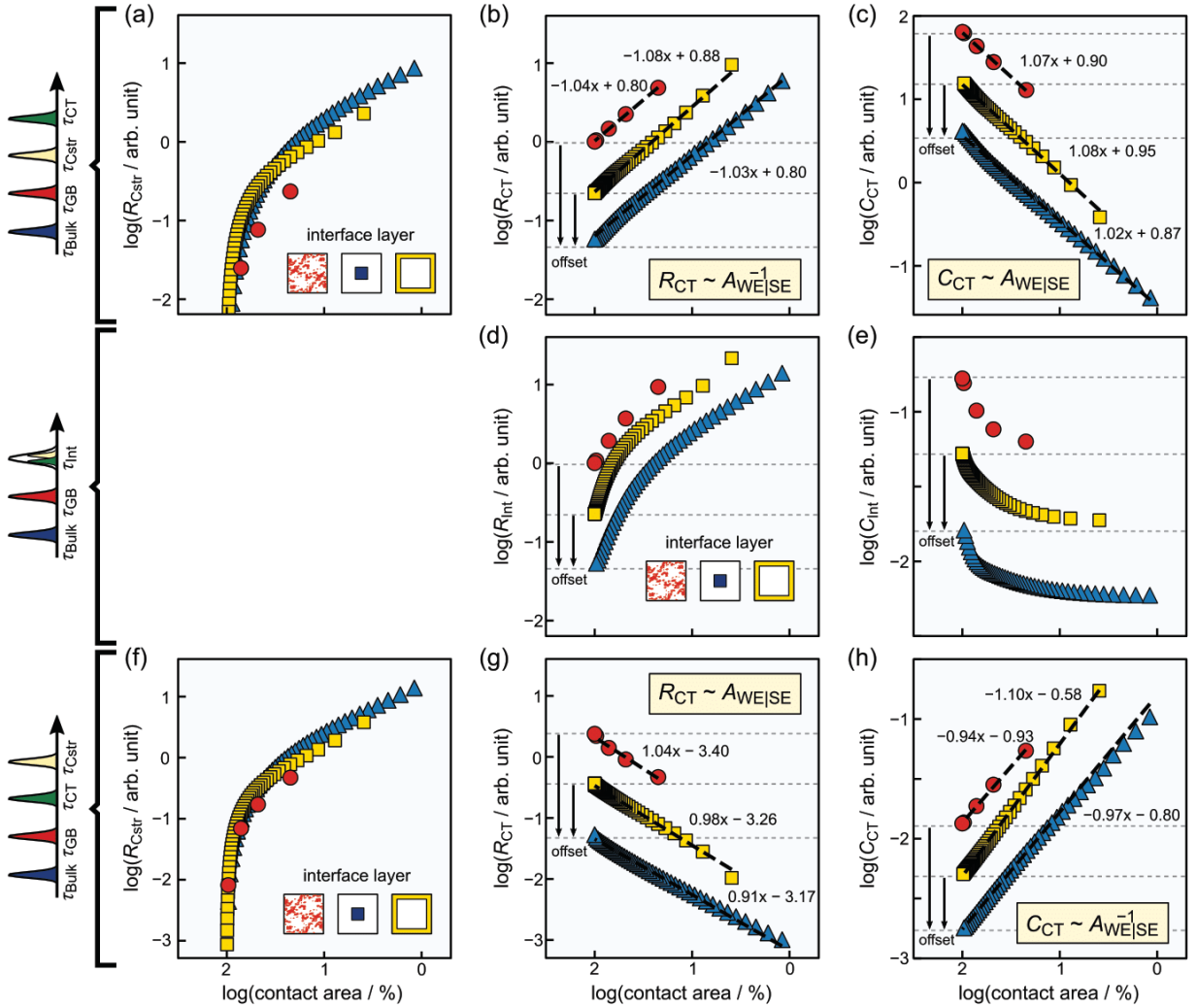

Figure 5. Functional dependence of interface contributions with the contact area $A_{WE|SE}$ considering different orders of time constants, i.e., a–c) $\tau_{Cstr} < \tau_{CT}$, d,e) $\tau_{Cstr} \approx \tau_{CT}$, and f–h) $\tau_{CT} < \tau_{Cstr}$. The dashed horizontal lines indicate an artificial offset along the *y*-axis for an improved comparability of the computational results. The non-linear behavior and strong dependence of R_{Cstr} on the interface morphology impedes the derivation of a universal functional relationship with the contact area. The CT resistance R_{CT} and capacitance C_{CT} are inversely proportional and proportional to the contact area, respectively, when $\tau_{Cstr} < \tau_{CT}$. The dependence of both parameters on the contact area is reversed in the case of $\tau_{CT} < \tau_{Cstr}$. The slight variations in the slop of the linear fits are due to the competing dielectric transport process through the pores at the interface.

The dependence of the effective interface parameters (R_{Int}, C_{Int}) on the physical contact area $A_{WE|SE}$ is shown in Figure 5d,e. These macroscopic transport quantities correspond to the situation in which only one interface impedance contribution can be observed, i.e., the intermediate case where $\tau_{Cstr} \approx \tau_{CT}$. As somewhat anticipated from the discussion above, no simple functional relationships are found between log R_{Int} versus log $A_{WE|SE}$ and log C_{Int} versus log $A_{WE|SE}$ because both, geometric constriction effect and CT contribute to one single signal. Starting from a minimum value at an ideal contact, the resistance log R_{Int} increases and the capacitance log C_{Int} decreases non-linearly with decreasing log $A_{WE|SE}$. The quantitative behavior observed depends on the interface morphology and the interplay of the materials parameters, as in the case of the pure constriction impedance. In particular, it is very sensitive to a variation of the polarization resistance describing the microscopic CT process.

So far, the following conclusions can be drawn from the discussion:

i) In the case of a porous interface, the geometric constriction effect disappears on the mesoscopic scale, when pressure is applied to the stack and the pores at the interface are closed due to plastic electrode deformation. In this limit and under the assumptions of chemical and thermodynamic stability of the interface, the interface impedance response is solely determined by the CT effect.

ADVANCED SCIENCE NEWS
www.advancedsciencenews.com

ADVANCED MATERIALS INTERFACES
Open Access
www.advmatinterfaces.de

ii) The macroscopic constriction parameters (R_{Cstr}, C_{Cstr}) may differ even at the same $A_{WE|SE}$, if the morphology of the interface on the microscopic and mesoscopic scale varies, i.e., the spatial distribution of the physical contact area across the interface changes. The impact of geometric constriction is not negligible over a wide range of relative physical contact areas $A_{WE|SE}$, in particular for $A_{WE|SE} < 50\%$. Charge-transfer-driven morphological instabilities of interfaces always lead to an increase of the DC resistance independent of the microscopic polarization resistance underlying the CT process. As a result, geometric current constriction will have a major effect, for example, on the cycling behavior of battery cells.

iii) The functional relationship between the macroscopic transport parameters (R_i, C_i) of electric migration processes like CT and the relative physical contact area $A_{WE|SE}$ is not universal. It depends on the order of the time constants of individual interface impedance contributions. The correlation $R_{CT} \sim A_{WE|SE}^{-1}$ only holds for estimating the magnitude of the CT resistance R_{CT}, if the condition $\tau_{Cstr} < \tau_{CT}$ is fulfilled. In the case of $\tau_{CT} < \tau_{Cstr}$, the resistance R_{CT} depends linearly on the contact area $R_{CT} \sim A_{WE|SE}$. Similarly, for the CT capacitance, it holds $C_{CT} \sim A_{WE|SE}$ for $\tau_{Cstr} < \tau_{CT}$ and $C_{CT} \sim A_{WE|SE}^{-1}$ for $\tau_{CT} < \tau_{Cstr}$.

Temperature Dependence of Charge Transfer and Constriction Resistance: Battery cells are exposed to different environmental conditions in applications. Thus, studies of the influence of the environment on the cell performance are essential. The temperature-dependence is of particular interest, since internal (e.g., heating) and external (e.g., ambient) temperature variations occur during operation in most applications and will lead to changes of all impedance contributions. The previous discussion of the dependence of the macroscopic parameters (R_{Cstr}, C_{Cstr}) and (R_{CT}, C_{CT}) on stack pressure (i.e., physical contact area) has already underlined that their behavior is very different. The former can be considered as geometric fit parameters in macroscopic 1D equivalent circuit models, whereas the later represent an electric transport process on the microscopic level. This implies that the resistance R_{Cstr} is not solely based on a conductivity or microscopic polarization resistance, but parameterizes the dynamic constriction effect. It is determined by contributions of all microscopic transport processes taking place close to the interface, and, in a sense, leads to a reduced active SE volume involved in the transport through the sample. In consequence, the temperature-dependence of the geometric parameter R_{Cstr} is not obvious and needs to be investigated as all the microscopic electric transport processes that contribute to it may have a different temperature-dependence, i.e., different action energies $E_{a,i}$.

For this purpose, we focus on one specific morphology of the 3D model system for which the physical contact area is $A_{WE|SE} = 22\%$ and the interface has the realistic disordered morphology depicted in Figure 1c. The temperature-dependence of the ionic migration processes, i.e., of bulk and GB transport within the SE as well as of CT at the interface, are described by an Arrhenius behavior, for example, $\sigma(T) \sim \sigma_0/T \cdot \exp[-E_a / (k_B \cdot T)]$. The values assumed for the activation energies $E_{a,i}$ of the microscopic transport processes are given in the Computational Details section. The permittivity values are considered to not dependent on temperature. We computed series of impedance spectra at temperatures between −40°C and 40°C and derived the macroscopic transport parameters (R_i, C_i) of the individual processes at each temperature by fitting the resulting spectra with the 1D equivalent circuit model. Variations of microscopic conductivities σ_i with temperature T are directly reflected in the macroscopic resistance values R_i derived by the fitting approach. Thus, the individual activation energies $E_{a,i}$ can be determined from the slopes of corresponding Arrhenius diagrams $\ln[T/(R \cdot A)]$ versus T^{-1}, using the macroscopic resistance parameters R_i.

Similar to the former discussion, we consider again the three cases of different orders of the time constants τ_{Cstr} and τ_{CT}. Here, we will not discuss the activation energies $E_{a,i}$ of the macroscopic resistances R_i corresponding to the microscopic electric migration processes, i.e., the CT at the interface, bulk, and GB transport. Their activation energies almost agree with those of the corresponding microscopic input parameters, i.e., that of the polarization resistance R_{Pol} and those of the bulk and GB conductivities σ_i. Instead, we will solely analyze the effective activation energy of the macroscopic resistance parameters R_{Cstr} used for the parameterization of the constriction phenomenon in the 1D equivalent circuit model and R_{Int}, in the case of $\tau_{Cstr} \approx \tau_{CT}$, which is also strongly affected by current constriction.

Figure 6a shows Arrhenius diagrams of the constriction resistance R_{Cstr} in the case of $\tau_{Cstr} < \tau_{CT}$. Five different sets of microscopic transport parameters (σ_i, ε_i) were considered in the computations. Starting with a reversible WE|SE interface and highly conducting GBs ($Z_{CT} = Z_{GB} = 0$, blue data points), the activation energy $E_{a,Cstr}$ of the constriction resistance R_{Cstr} is 0.34 eV and identical to that of the microscopic bulk transport $E_{a,Bulk}$. This agrees with the observations of Fleig and Maier who exclusively considered a homogenous SE and no CT step at the interface in their early theoretical studies.[31–33] The activation energy $E_{a,Cstr}$ increases slightly to 0.35 eV, when the GBs become resistive ($Z_{GB} \neq 0$, $Z_{CT} = 0$, red data points). The effect is only marginal for the sample configuration and transport parameters considered, although the activation energy assigned to microscopic GB transport with 0.43 eV is rather high compared to the bulk value of 0.34 eV. This is due to the fact that the electric transport properties of the entire system are dominated by bulk transport ($R_{Bulk} \approx 12 \cdot R_{GB}$). The effect of the additional electric GB transport on R_{Cstr} would be more pronounced for decreasing conductivity σ_{GB} or a more prominent GB microstructure (i.e., an increased GB volume fraction and more GBs to be crossed along the dominant transport path). Interestingly, assuming a non-zero microscopic polarization resistance at the interface ($Z_{GB} \neq 0$, $Z_{CT} \neq 0$, greenish data points) does not alter $E_{a,Cstr}$ despite the high value of $E_{a,CT}$ with 0.43 eV, even when R_{Pol} is varied by an order of magnitude ($R_{Pol} \rightarrow 10 \cdot R_{Pol}$). The reason is that in the case of $\tau_{Cstr} < \tau_{CT}$, the transport processes across the interface, i.e., across both the pores and the physical contact area, are predominantly dielectric in the frequency range close to $1/\tau_{Cstr}$. In consequence, R_{Cstr} and $E_{a,Cstr}$ are not affected by the electric transport step across the physical contact $A_{WE|SE}$ and thus by the polarization resistance.[30]

In Figure 6b, we consider the case of comparable relaxation times $\tau_{Cstr} \approx \tau_{CT}$ and study the activation energy $E_{a,Int}$

ADVANCED SCIENCE NEWS
www.advancedsciencenews.com

ADVANCED MATERIALS INTERFACES
Open Access
www.advmatinterfaces.de

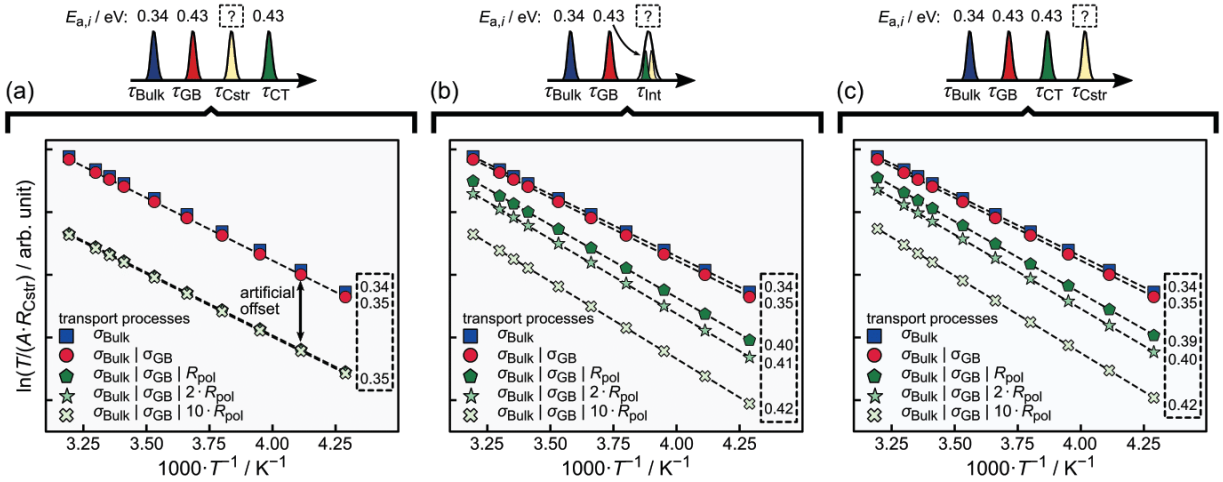

Figure 6. The constriction resistance R_{Cstr} is composed of contributions of all electric transport processes within the system. Its activation energy (numbers is dashed box) depends solely on the activation energy of the individual transport processes $E_{a,i}$. Only electric charge transport processes in the frequency range around $1/\tau_{Cstr}$ have an effect on the constriction resistance R_{Cstr}. Thus, a) the microscopic polarization resistance has no effect if $\tau_{CT} > \tau_{Cstr}$ and b,c) it affects $E_{a,Cstr}$ if $\tau_{CT} \leq \tau_{Cstr}$. The legend indicates the relative changes of the microscopic transport parameters in the computed impedance series. Note that the red and green points in (a) overlap and are only shifted along the *y*-axis for clarity.

of the single effective macroscopic interface resistance R_{Int}. In the frequency range of the interface impedance, pores are still almost dielectrically conductive while the transport across the physical contact takes place electrically. The transport situation resembles that for R_{Cstr} in the case of $\tau_{CT} < \tau_{Cstr}$, where the corresponding Arrhenius diagrams are displayed in Figure 6c. In both cases, the microscopic electric CT process at the interface is contributing to or even dominating the macroscopic resistances R_{Int} or R_{Cstr}, respectively. As a result of the frequency-dependent changes of the active SE volume for frequencies around $1/\tau_{Cstr}$, the averaging of the microscopic transport processes yielding R_{Int} and $E_{a,Int}$ or R_{Cstr} and $E_{a,Cstr}$ also changes.

The trends for the Arrhenius diagrams and the activation energies extracted are very similar, when looking at the five sets of microscopic transport parameters. The findings in the case of a reversible WE|SE interface considering highly conducting GBs ($Z_{CT} = Z_{GB} = 0$, blue data points) or resistive GBs ($Z_{GB} \neq 0$, $Z_{CT} = 0$, red data points) are similar to the results for $\tau_{Cstr} < \tau_{CT}$ shown in Figure 6a. The activation energy $E_{a,Int}$ or $E_{a,Cstr}$ equals that of the bulk process with 0.34 eV or increases only slightly to 0.35 eV due to the specific constellation and choice of materials parameters, respectively. Interestingly, the microscopic polarization resistance R_{Pol} now dominates the overall behavior of the macroscopic constriction resistance ($Z_{GB} \neq 0$, $Z_{CT} \neq 0$, greenish data points) for such an order of time constants. The activation energy $E_{a,Cstr}$ approaches that of the CT effect $E_{a,CT}$ with 0.43 eV, the more resistive the interface becomes, i.e., for increasing R_{Pol}. The activation energies of the effective interface resistance R_{Int} in Figure 6b tend to be slightly higher compared to those of pure constriction R_{Cstr} in Figure 6c. The reason is that R_{Int} includes a pure contribution of the macroscopic CT resistance R_{CT} based on the microscopic R_{Pol}, which typically has a higher activation energy than R_{Cstr} as originating from a microscopic migration process.

Altogether, the results on the temperature-dependence of R_{Cstr} and R_{Int} imply that the activation energies determined from Arrhenius diagrams reflect a weighting over all microscopic migration processes within the system. This indicates a relationship according to $R_{Cstr} = \Sigma_i\, \alpha_i \cdot 1/\sigma_i$ and a corresponding equation for R_{Int}. The weights α_i depend, for example, on the interface morphology, the contact area, the microstructure of the SE, the locations of GBs within the system and the order of the time constants of the individual transport processes. In particular, it holds that $\alpha_i \approx 0$, if $\tau_{Cstr} < \tau_i$.[30] The equation also implies that there is a range of values for $E_{a,Cstr}$ or $E_{a,Int}$ with boundaries given by the lowest and highest activation energies $E_{a,i}$ with $\alpha_i \neq 0$ of electric migration processes, i.e., $\min(E_{a,i}) \leq E_{a,Cstr} \leq \max(E_{a,i})$. This is due to the fact that $E_{a,Cstr}$ or $E_{a,Int}$ are a weighted average over the microscopic activation energies $E_{a,i}$ present in the system.

3.2.2. Effect of SEI Formation Due to Chemical Instabilities at Morphologically Stable Interfaces

Next, we turn to the right branch in the decision tree shown in Figure 2 and include the (electro)chemical instability of metal|SE interfaces. To our knowledge, there are only a few solid electrolytes that form an electrochemically and kinetically stable interface with alkali metals. Examples are the interfaces between lithium metal and garnets.[51–54] More common is the formation of an SEI (i.e., usually a multi-phase and nanoscale composite) at the interface, which usually exhibits less favorable charge transport properties, in particular a lower ionic conductivity than the SE itself. Here, the SEI is often continuously formed at the interface during operation, for example, when considering argyrodite-type SEs versus lithium metal.[10–14] The dynamic formation process corresponds to a transition from a WE|SE interface into a WE|SEI|SE layered interface over

ADVANCED SCIENCE NEWS
www.advancedsciencenews.com

ADVANCED MATERIALS INTERFACES
Open Access
www.advmatinterfaces.de

time – ignoring the many inner homo- and hetero-interfaces in the SEI itself. In the following we will therefore consider the SEI as a homogeneous phase for the sake of simplicity and as there is not enough knowledge on the composition of the SEI. At the end of this process, the SEI layer covers the entire interface and is morphologically stable. In consequence, the impedance response of the interface is exclusively determined by the SEI. This situation corresponds to the first leaf node in the right branch in the decision tree in Figure 2. The increasing thickness δ_{Int} of the SEI will lead to an increase of its resistance ($R_{SEI} \sim \delta_{Int}$) and a decrease of its capacitance ($C_{SEI} \sim 1/\delta_{Int}$). The transport behavior across the interface is more complex, when the interface is only partially covered by the SEI layer. This may be due to the presence of pores at the interface or ideal metal-SE contact areas. In such cases, the effect on the impedance response of the system is not clear and needs to be studied in detail on the basis of microstructural information of the corresponding samples.

Corresponding experimental interface morphologies are, for example, described in a recent study by Otto et al., when bringing lithium foil with a passivation layer on its surface (e.g., Li_2CO_3, LiOH or Li_2O) into contact with a garnet-type SE.[57] The surface roughness of the SE leads to local penetrations of the passivation layer, which leads to a distribution of energetically preferred $A_{WE|SE}$ contacts and less preferred $A_{WE|SEI|SE}$ contacts at the interface. The interface structure described represents the third leaf node in the right branch of the decision tree in Figure 2. Apparently, the interface morphology seems to show many similarities to the porous interfaces considered in the previous section. Thus, we only substitute the pores by a resistive SEI (or passivation) at the interface within the theoretical 3D model system, i.e., we assume that the aging of the interface is exclusively caused by an SEI. The adapted interface morphology consists of a single contact spot $A_{WE|SE}$ in the middle of the electrode surrounded by an SEI layer $A_{WE|SEI|SE}$ (see inset in **Figure 7**a).

Again, we perform a series of impedance computations mimicking that the microstructure of the SE is kept constant and a gradual degradation of the WE|SE occurs, this time due to the formation of an SEI layer. The capacitance $\tilde{C}_{SEI}$ and resistance $\tilde{R}_{SEI}$ of the SEI are set to 100 Ω cm^2 and 88 µF cm^{-2}, respectively. Without loss of generality, the microscopic polarization resistance R_{Pol} at the two-phase boundary $A_{WE|SE}$ is assumed to be negligible ($Z_{CT} = 0$), i.e., there is no macroscopic CT signal in the impedance spectra. It represents a limiting case, experimentally observed for the interface between lithium metal and LLZO.[37,58–59] This assumption significantly simplifies the data analysis. Otherwise, the impedance response will depend on the interplay of interface time constants τ_{CT} and τ_{SEI} in a similar way discussed in the previous section for the simultaneous presence of CT and pores at the interface.

Figure 7a shows the modelled impedance data for five different contact areas in the range between 100% and 4.3% in Nyquist representation. The respective interface morphologies are displayed on the right with the two-phase boundary contact as a gray square in the center of the interface area and the light blue three-phase layered contact surrounding it such, that $A_{WE|SE} + A_{WE|SEI|SE} = 100\%$. The impedance spectrum for an ideal contact without SEI ($A_{WE|SE} = 100\%$) consists of two well-separated semicircles representing bulk (blue) and GB (red) transport within the SE. An additional interface semicircle (yellow) is formed in the spectra, when $A_{WE|SE}$ decreases, i.e., an SEI forms. At first glance, the qualitative impedance behavior seems to be similar to the case of a porous interface discussed in the previous section. Bulk and GB impedance remain unchanged, while the interface impedance increases with decreasing $A_{WE|SE}$ (cf. Figure 3a). To study the frequency-dependence of the resulting interface signal, we performed a DRT analysis of all impedance spectra as shown in Figure 7b. The relaxation times of the bulk and GB signals are again independent of the SEI fraction at the interface. Interestingly, the time constant of the interface signal τ_{Int} does not match the time constant of the microscopic electric transport process across the SEI layer τ_{SEI}. Instead, it exhibits a relaxation time in the intermediate range between GB and SEI time constant ($\tau_{GB} < \tau_{Int} < \tau_{SEI}$).

To study the functional behavior of the interface time constant τ_{Int} in more detail, we consider the dependence of the macroscopic transport parameters (R_{Int}, C_{Int}), derived by the 1D fitting approach of the computed impedance spectra, on the contact area $A_{WE|SE}$ (see Figure 7c,d). The macroscopic transport quantities of the 1D fitting model, i.e., bulk (green) and GB (orange) resistances as well as the SEI resistance and capacitance (cyan), are given as reference values in the figures. As expected, the resistance R_{Int} increases and the capacitance C_{Int} decreases with decreasing $A_{WE|SE}$, but the quantitative changes do not fit those of an electric migration process. Both parameters converge towards the limiting case of a completely covered interface ($R_{Int} \to R_{SEI}$, $C_{Int} \to C_{SEI}$ for $A_{WE|SE} \to 0$), instead of being (inversely) proportional to changes of the contact area. The same holds for the variation of the time constant ($\tau_{Int} \to \tau_{SEI}$ for $A_{WE|SE} \to 0$) as shown in Figure 7e. Consequently, the observed interface impedance signal does not represent the pure characteristics of the SEI or passivation as typically assumed in the literature. Instead, the macroscopic parameters (R_{Int}, C_{Int}) are also affected by the bulk and GB conductivity within the SE as well as the microscopic polarization resistance at the interface. These parameters influence the amounts of current flowing across the two-phase boundary described by $A_{WE|SE}$ and the layered three-phase contact described by $A_{WE|SEI|SE}$ at frequencies close to $1/\tau_{Int}$. The influence of the SEI properties on (R_{Int}, C_{Int}) increases as $A_{WE|SE}$ decreases, since the fraction of current flowing through the SEI layer increases.

The transport situation at the interface will change, if also pores are present at the interface in addition to a non-uniform SEI layer. When there is no direct contact between the metal and the SE (i.e., $A_{WE|SE} = 0\%$), the interface impedance behaves similarly to the studies performed in the previous chapter. Herein, the SEI contact $A_{WE|SEI|SE}$ takes the role of the ideal $A_{WE|SE}$ areas. The morphology corresponds to that of the second leaf node in the right branch of the decision tree in Figure 2. Note that in this situation, the effects of the microscopic transport parameters of the SEI layer ($\tilde{R}_{SEI}$, $\tilde{C}_{SEI}$) on the interface impedance are comparable to those of the CT reaction (R_{Pol}, C_{DL}) in the former case.[30] Impedance data evaluation becomes even more complex when there are also ideal $A_{WE|SE}$ areas at the interface (see fourth leaf node in the right branch of the decision tree in Figure 2). In this case, there is not only an interplay between the transport across

ADVANCED SCIENCE NEWS
www.advancedsciencenews.com

ADVANCED MATERIALS INTERFACES
Open Access
www.advmatinterfaces.de

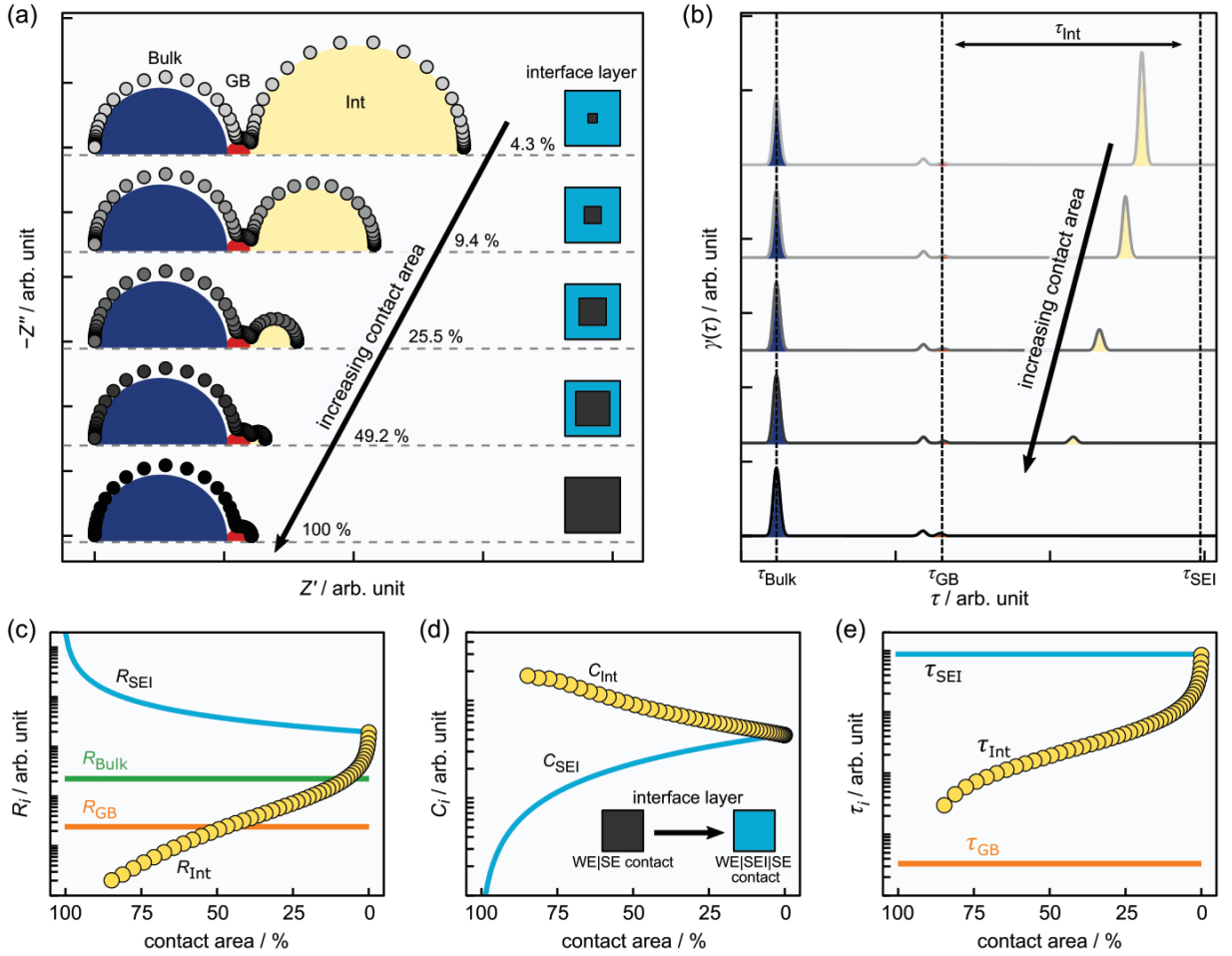

Figure 7. Impact of the successive evolution of an SEI layer (cyan) at the interface on the impedance response of the system. a) An additional interface contribution is formed in the impedance spectrum as the contact area $A_{WE|SE}$ decreases. Note that for simplicity, the CT step at $A_{WE|SE}$ was not considered in the modeling. b) The time constant of the interface signal does not match that of the microscopic transport through the SEI, if the interface is not fully covered. Evolution of the macroscopic transport parameters of the interface impedance, i.e., c) the resistance, d) the capacitance, and e) the time constant. Their qualitative behavior is similar to that of geometric constriction due to pore formation (cf. Figure 4). The macroscopic SEI (cyan), bulk (green), and GB (orange) parameters are given as reference values.

the $A_{WE|SE}$ and $A_{WE|SEI|SE}$ areas, but also across the $A_{WE|Pore|SE}$ contact. Basically, the active electrode area can then change with frequency between three levels: (1) the $A_{WE|SE}$ contact, (2) the $A_{WE|SE} + A_{WE|SEI|SE}$ contact, and (3) the entire electrode area. Therefore, three impedance contributions are generally expected in such a situation. Apparently, the exact form of the interaction and the evolution of the interface contribution depends on the morphology of the interface, the individual microscopic transport quantities, and the order of the individual time constants.

In summary, the impedance signal for partially covered interfaces $A_{WE|SE} > 0\%$ at different relative contact areas and temperatures behaves similarly to that in the presence of geometric constriction for porous interfaces (cf. Figure 4). The main difference is the slightly different convergence behavior for $A_{WE|SE} \to 0$, i.e., $R_{Int} \to R_{SEI}$ and $C_{Int} \to C_{SEI}$ in the case of SEI formation instead of $R_{Cstr} \to \infty$ and $C_{Cstr} \to \tilde{C}_{Pore}$ in the case of pores. Distinguishing between constriction due to SEI or pores gets more difficult, when the SEI resistivity increases. This leads to a similar frequency-dependence of the systems and especially a similar interface impedance behavior. It should be noted that the interface impedance reflects the pure SEI characteristics only, when the interface is fully covered.

3.3. Strategies for the Identification of Interfacial Processes

The identification of the rate-limiting process at the interface is an essential starting point for improving the overall characteristics of a solid-state battery cell with a metal anode. Only in rare cases, a single process determines the electric properties of an all-solid metal|SE interface as shown in the decision tree in Figure 2. Typically, several effects contribute to the impedance response of

ADVANCED SCIENCE NEWS
www.advancedsciencenews.com

ADVANCED MATERIALS INTERFACES
Open Access
www.advmatinterfaces.de

the interface. Examples from the microscopic to the mesoscopic level are the CT step at the two-phase boundary $A_{WE|SE}$, geometric constriction due to pores, or an SEI resulting in a layered three-phase contact $A_{WE|Pore|SE}$ or $A_{WE|SEI|SE}$. A macroscopic static constriction effect may occur, if the area at which the macroscopic WE is deposited on the SE surface is smaller than the latter, i.e., $A_{WE} < A_{SE}$.[29] However, this can be easily avoided by an appropriate contact preparation, for example, via sputter deposition. In what follows, we assume that the stacks are prepared such that all macroscopic layers have the same lateral dimensions.

The discussion in the previous sections has clearly shown that a careful analysis of the impedance data, in particular as a function of pressure, in the time or frequency domain allows the identification of the rate-limiting process at the interface in many cases. This holds especially for static situations, in which no SEI is dynamically formed or transformed during operation. It refers to systems with chemically stable interfaces and also to systems forming a kinetically stabilized interlayer (i.e., a uniform static secondary phase). Based on the derived criteria, we exemplarily define a strategy for experimentalists to follow in order to identify the origin of the interface impedance signals in recorded experimental spectra for symmetric Me|SE|Me arrangements, as described in Figure 1. In this situation, only CT and constriction effects determine the interface properties. The recipe for analyzing corresponding impedance data comprises several steps. The analysis is best performed in the time-domain according to the hierarchical scheme shown in **Figure 8**.

- Step 1: *Collection of impedance data at different stack pressures and performance of the corresponding DRT analyses.*

  Record an impedance spectrum of the pristine sample and perform a DRT analysis. The DRT will reveal either three or four main signals. The two signals at the shortest relaxation times τ usually correspond to transport processes within the SE, i.e., in the bulk of grains and across GBs. The remaining signals originate from the interface.

  i) If constriction and CT processes differ sufficiently in their characteristic time constants τ_i, two interface signals arise in the DRT (left branch).
  ii) If not, the signals due to the two interface processes overlap in the DRT (right branch).

- Step 2: *Behavior of the interface DRT signals under applied pressure.*

  Controlled application of stack pressure results in a continuous tuning of a porous interface morphology. Pores will gradually close with increasing pressure until an ideal and non-porous interface results at the highest pressures, i.e., $A_{WE|SE} \rightarrow 100\%$. This leads to a vanishing geometric constriction contribution. The DRT signal due to geometric constriction will exhibit a continuous change of the time constant (see black horizontal arrow in Figure 8) with the applied pressure and will vanish at the highest pressure at which the interface is ideal.

  i) In the case of two (separate) resolved interface signals, the one with decreasing amplitude and with changes in time constant as a function of pressure results from geometric current constriction. The time constant of the interface signal due to electric CT is independent of stack pressure, but its amplitude will also slightly change.
  ii) In the case of overlapping interface signals, the characteristic time constant of the single peak at the highest pressure will solely correspond to the CT effect. If no DRT signal can be resolved at the highest pressure, it is likely that dynamic constriction determines the overall interface properties of the system.

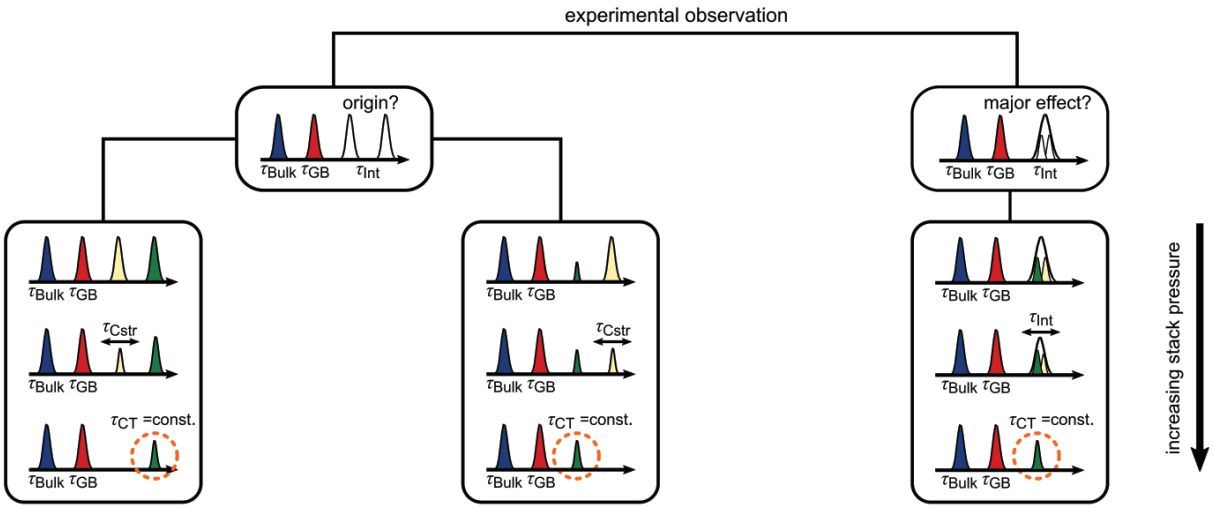

Figure 8. Guideline for assigning individual impedance signals to microscopic processes and estimating their magnitude on the systems interface properties in the case of chemically stable interfaces. The qualitative behavior for different stack pressures strongly depends on the order of time constants τ_i. In the limiting case of full physical contact $A_{WE|SE} = 100\%$, geometric current constriction signals vanish in the impedance spectrum.

ADVANCED SCIENCE NEWS
www.advancedsciencenews.com

ADVANCED MATERIALS INTERFACES
Open Access
www.advmatinterfaces.de

- Step 3: *Determination of the macroscopic transport parameters of the CT effect.*

  The remaining interface signal at the highest pressure is solely due to the CT effect. This means that the 1D equivalent circuit model used for fitting this experimental impedance spectrum in the frequency domain can be restricted to three *RC*-elements representing the two microscopic transport processes in the SE and that of the CT process at the interface. The macroscopic transport parameters for the CT effect based on the 1D fitting approach are given by the microscopic polarization resistance $R_{Int}(A_{WE|SE} = 100\%) = R_{CT}(A_{WE|SE}) = R_{Pol}$ and the double-layer capacitance $C_{Int}(A_{WE|SE} = 100\%) = C_{CT}(A_{WE|SE}) = C_{DL}$.

- Step 4: *Determination of the macroscopic transport parameters.*

  i) If two interface contributions are observed, the series of impedance spectra taken at different pressures can be fitted by a 1D equivalent circuit model consisting of four *RC*-elements, i.e., (R_{Bulk}, C_{Bulk}), (R_{GB}, C_{GB}), (R_{CT}, C_{CT}), and (R_{Cstr}, C_{Cstr}). This holds for $A_{WE|SE} < 100\%$, i.e., apart from the highest pressures applied where the impedance response does not vary anymore. Only (R_{Cstr}, C_{Cstr}) and (R_{CT}, C_{CT}) should vary as a function of pressure, the parameters corresponding to the SE should be independent of pressure as the pores are typically dielectrically shorted in this frequency range. It should be noted that the electrode area may change during the application of stack pressure, requiring a specific normalization of the impedance spectra, as described in the literature.[37,49]

  ii) If only one interface contribution is observed, the series of impedance spectra taken at different pressures can be fitted by a 1D equivalent circuit model consisting of three *RC*-elements, i.e., (R_{Bulk}, C_{Bulk}), (R_{GB}, C_{GB}), and (R_{Int}, C_{Int}). Here, only (R_{Int}, C_{Int}) should vary as a function of pressure.

- Step 5: *Order of the time constants of the interface processes.*

  The dependence of R_{CT} and C_{CT} on pressure correlates with their dependence on the physical contact area $A_{WE|SE}$ as it increases with increasing pressure. Although $A_{WE|SE}$ is not necessarily a linear function of pressure, the observed dependence of $R_{CT}(p)$ and $C_{CT}(p)$ can be compared to the relations for $R_{CT}(A_{WE|SE})$ and $C_{CT}(A_{WE|SE})$ given in **Table 1**. This helps to identify the order of the characteristic time constants τ_{CT} and τ_{Cstr}, in the case that both signals do not overlap. The assignment should agree with the order of τ_i derived from the DRT series in step 2, and thus serves as a validation.

  i) R_{CT} increases with pressure and C_{CT} decreases with pressure, then $\tau_{CT} < \tau_{Cstr}$.
  ii) R_{CT} decreases with pressure and C_{CT} increases with pressure, then $\tau_{CT} > \tau_{Cstr}$.

  In the case of overlapping interface signals, the relations for $R_{CT}(A_{WE|SE})$ and $C_{CT}(A_{WE|SE})$, together with R_{Pol} and C_{DL} derived in step 3, help to estimate the magnitude of the CT effect for different pressures or contact areas and thus to identify the dominant interface effect.

- Step 6: *Correlation with structural properties.*

  The dependence of $R_{CT}(p)$ and $C_{CT}(p)$ can be translated, based on the theoretical dependence of $R_{CT}(A_{WE|SE})$ and $C_{CT}(A_{WE|SE})$ given in Table 1, into a functional relationship $A_{WE|SE}(p)$. This can be correlated with the results of the structural analysis of the pore distribution (e.g., via FIB SEM) in

Table 1. Overview of the characteristics of transport signals compared to signals of geometric origin.

$\tau_{Bulk} < \tau_{GB} < \tau_{Cstr} < \tau_{CT}$		$\tau_{Bulk} < \tau_{GB} < \tau_{CT} < \tau_{Cstr}$	
constriction	charge transfer	constriction	charge transfer
$\tau_{Cstr}(A_{WE\|SE}) \neq$ const.	$\tau_{CT}(A_{WE\|SE}) =$ const.	$\tau_{Cstr}(A_{WE\|SE}) \neq$ const.	$\tau_{CT}(A_{WE\|SE}) =$ const.
$R_{Cstr}(A_{WE\|SE})$: non-linear	$R_{CT} \sim 1/A_{WE\|SE}$	$R_{Cstr}(A_{WE\|SE})$: non-linear	$R_{CT} \sim A_{WE\|SE}$
$R_{Cstr}(A_{WE\|SE} \to 100\ \%) \to 0$	$R_{CT}(A_{WE\|SE} \to 100\ \%) \to R_{Pol}$	$R_{Cstr}(A_{WE\|SE} \to 100\ \%) \to 0$	$R_{CT}(A_{WE\|SE} \to 100\ \%) \to R_{Pol}$
$R_{Cstr}(A_{WE\|SE} \to 0\ \%) \to \begin{cases} \infty \\ \tilde{R}_{SEI} \end{cases}$	$R_{CT}(A_{WE\|SE} \to 0\ \%) \to \infty$	$R_{Cstr}(A_{WE\|SE} \to 0\ \%) \to \begin{cases} \infty \\ \tilde{R}_{SEI} \end{cases}$	$R_{CT}(A_{WE\|SE} \to 0\ \%) \to 0$
$C_{Cstr}(A_{WE\|SE})$: non-linear	$C_{CT} \sim A_{WE\|SE}$	$C_{Cstr}(A_{WE\|SE})$: non-linear	$C_{CT} \sim 1/A_{WE\|SE}$
$C_{Cstr}(A_{WE\|SE} \to 100\ \%) \to \infty$	$C_{CT}(A_{WE\|SE} \to 100\ \%) \to C_{DL}$	$C_{Cstr}(A_{WE\|SE} \to 100\%) \to \begin{cases} \infty, R_{pol} \downarrow \\ 0, R_{pol} \uparrow \end{cases}$	$C_{CT}(A_{WE\|SE} \to 100\ \%) \to C_{DL}$
$C_{Cstr}(A_{WE\|SE} \to 0\ \%) \to \begin{cases} \tilde{C}_{Pore} \\ \tilde{C}_{SEI} \end{cases}$	$C_{CT}(A_{WE\|SE} \to 0\ \%) \to 0$	$C_{Cstr}(A_{WE\|SE} \to 0\ \%) \to \begin{cases} \tilde{C}_{Pore} \\ \tilde{C}_{SEI} \end{cases}$	$C_{CT}(A_{WE\|SE} \to 0\ \%) \to \infty$
$E_{a,Bulk} < E_{a,Cstr} \leq E_{a,GB}$	$E_{a,Bulk} < E_{a,GB} \leq E_{a,CT}$	$E_{a,Bulk} < E_{a,Cstr} \leq E_{a,CT}$	$E_{a,Bulk} < E_{a,GB} \leq E_{a,CT}$
$E_{a,Cstr}(A_{WE\|SE}) \neq$ const.	$E_{a,i}(A_{WE\|SE}) =$ const.	$E_{a,Cstr}(A_{WE\|SE}) \neq$ const.	$E_{a,i}(A_{WE\|SE}) =$ const.

ADVANCED SCIENCE NEWS
www.advancedsciencenews.com

ADVANCED MATERIALS INTERFACES
Open Access
www.advmatinterfaces.de

nominally equivalent samples treated at different pressures. Such comparisons serve as an additional validation of this data analysis approach.

- Step 7: *Correlation with temperature-dependent impedance measurements.*

  Temperature-dependent measurements allow to extract thermal activation energies for the observed macroscopic resistances R_i deduced by the 1D equivalent circuit fitting approach with four or three *RC*-elements connected in series. Typically, the activation energy of the metal ion migration in the bulk electrolyte is less than that of ion transport across a grain boundary in the SE and this in turn is less than or equal to that of charge transfer at the metal|SE interface ($E_{a,Bulk} < E_{a,GB} \leq E_{a,CT}$). This consideration is based on the assumption that charge transfer $Me = Me^+ + e'$ is the rate-limiting kinetic step in the system rather than ion migration in the electrolyte phase. In consequence, the activation energy of the 1D fit parameter R_{Cstr}, which represents an average of all microscopic electric transport processes in the system, lies somewhere between that of the bulk and that of the CT process, i.e., $\min(E_{a,i}) \leq E_{a,Cstr} \leq \max(E_{a,i})$. However, the value depends not only on the magnitude of the individual microscopic activation energies $E_{a,i}$ (i = Bulk, GB, CT), which are independent of geometry, but also on the global character of the constriction effect, which defines the macroscopic sample volume contributing to the transport and thus the weights in the averaging of the microscopic activation energies.

Table 1 summarizes the functional behavior of the macroscopic transport parameters describing CT and constriction effect when fitting with 1D equivalent circuit models in the case of different situations characterized by the order of the time constants τ_{CT} and τ_{Cstr}. The clear dependences should be helpful in the interpretation of experimental impedance spectra. However, a word of caution is essential here. The dependences derived, of course, are to some extent affected by the assumptions about the 3D sample morphology (see Figure 1). Minor deviations are anticipated, for example, if not only the contact area $A_{WE|SE}$ but also the thickness δ_{Int} of the electrically insulating layer at the interface is varied. In particular, this has a major superimposed effect on the macroscopic constriction capacitance as $C_{Cstr} \sim \varepsilon_{Int}/\delta_{Int}$, in contrast to the constriction resistance as $R_{Cstr} = \Sigma_i\, \alpha_i \cdot 1/\sigma_i + \Sigma_j\, \alpha_j \cdot R_{Pol,\,j}$.

Establishing similar hierarchical schemes for analyzing the interface impedance response in cases, in which an SEI layer is dynamically formed, is in principle also possible. However, this will require additional structural information and probably will depend significantly on the materials involved. For example, in the cases in which a non-uniform secondary phase takes the place of pores at the interface, the assumption that the interface morphology approaches a state under pressure where $A_{WE|SE}$ = 100% is not valid. In consequence, the constriction effect will not disappear at high pressures, and thus the derived hierarchical scheme is not applicable. Therefore, it is essential to know how the two phases at the interface behave under pressure in order to establish a corresponding scheme for such cases. The situation in the case of dynamic SEI formation is

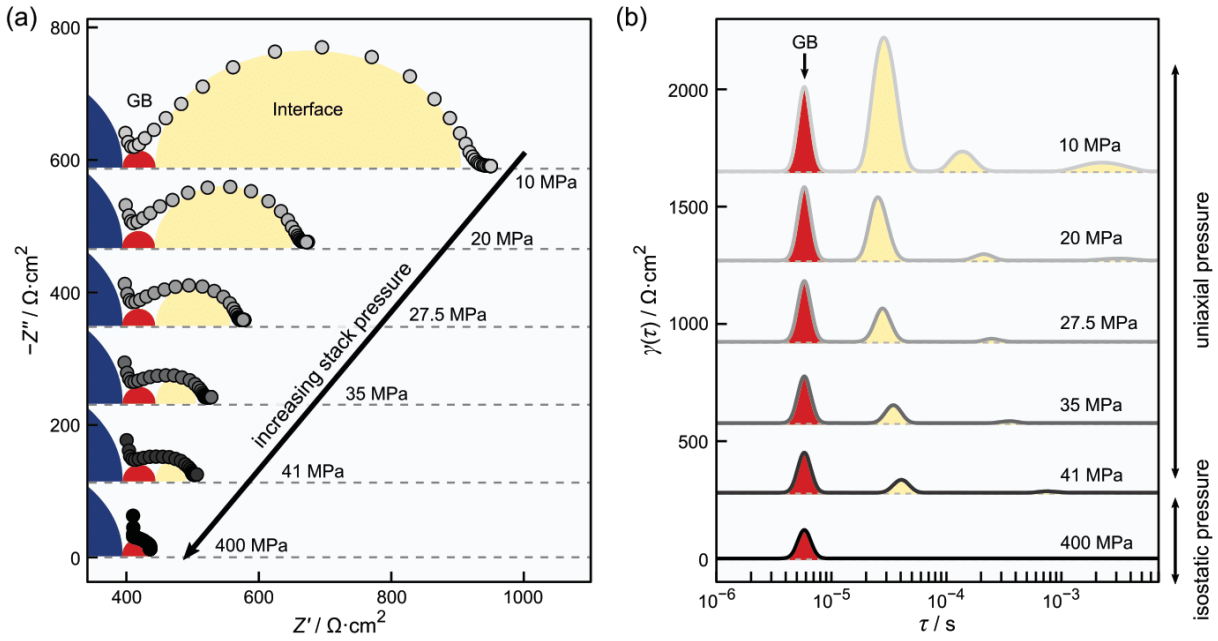

Figure 9. Experimental impedance data on the pressure-dependence of the interface impedance of a symmetric Li|LLZO|Li cell. The raw data originates from a recent study of Krauskopf et al. published in the literature. Adapted with permission.[37] Copyright 2019, American Chemical Society. The dashed lines indicate an artificial offset along the *y*-axis for visualization. a) The interface impedance (yellow) decreases with uniaxial pressure and vanishes after applying an isostatic pressure of 400 MPa. b) Even in the DRT analysis, there is no evidence for an interface signal at 400 MPa. Note that the bulk DRT signal could not be observed, since its impedance behavior is not fully captured in the measured frequency range.

ADVANCED SCIENCE NEWS
www.advancedsciencenews.com

ADVANCED MATERIALS INTERFACES
Open Access
www.advmatinterfaces.de

even more complex as the SEI changes continuously during operation. If its temporal evolution is known from a structural analysis, the corresponding variation of the impedance spectra during operation may be addressed and meaningful parameters may be extracted. For example, if a closed SEI layer at the interface is formed, its macroscopic transport parameters R_{SEI} and C_{SEI} will vary systematically with its thickness δ_{Int}, according to $R_{SEI} \sim \delta_{Int}$ and $C_{SEI} \sim 1/\delta_{Int}$. The analysis may be quite intricate, once the SEI itself is porous, which is a natural consequence of a negative reaction volume of SEI formation.[14,45]

3.4. Evaluating the Effect of Individual Interface Processes between Lithium and LLZO

Finally, we present an experimental case study to demonstrate the applicability of the hierarchical scheme discussed in the context of Figure 8. The data, which are analyzed here in more detail, are those of Krauskopf et al. They comprise an investigation of the effect of stack pressure on the impedance response of a symmetric Li|LLZO|Li cell arrangement.[37] Resistive SEI formation can be ruled out for this material combination, since the garnet-type solid electrolyte LLZO is one of the few Li-ion conductors that is kinetically stable against lithium.[51–54] Furthermore, Krauskopf et al. performed a microstructural analysis of the interface region and identified pores for stack pressures smaller than 400 MPa.[60–64] Both pieces of information demonstrate that the experimental results fulfill the assumption underlying the hierarchical scheme previously presented.

Figure 9a shows a series of impedance spectra in Nyquist representation taken at various external pressures. The initial spectrum at 10 MPa uniaxial stack pressure consists of three separated semicircles, i.e., two from bulk (blue, ≈1 MHz) and GB (red, ≈10 kHz) transport in the SE, and one from transport across the interface (yellow, <1 kHz). The continuous increase of uniaxial pressure resulted in a decrease of the single interface signal, i.e., an initial resistance R_{Int} of about 300 Ω cm^2 at 10 MPa decreased to 50 Ω cm^2 at 41 MPa. Furthermore, the semicircles of bulk and GB transport remained unchanged, i.e., they are not influenced by the applied pressure. In the frequency domain, it seems that only one interface contribution is present as only one impedance signal can be discerned. Interestingly, no interface signal could be resolved anymore (<0.1 Ω cm^2) after further increasing the external load to an isostatic pressure of 400 MPa, i.e., only the unchanged bulk and GB semicircles were observed.

We proceed now stepwise according to our hierarchical scheme:

As step 1, we perform a DRT analysis of the impedance data. The resulting series of DRT at various pressures is shown in Figure 9b. Frequency points below 200 Hz were excluded in the analysis, since individual residuals were greater than 4% in the Kramers–Kronig test. Similarly, frequency points above 0.2 MHz were neglected as most of the bulk contribution (blue) is not captured in the measured frequency range. As a result, parts of the GB impedance (red) were not reflected in the considered frequency range, which affects the magnitude of the corresponding DRT signal. Thus, the analysis conducted can only reveal qualitative trends in the data. Nevertheless, the DRT of the initial impedance at 10 MPa consists of four signals. The one at low relaxation times represents transport across GBs (red), while the three broad signals at higher relaxation times result from the WE|SE interface (yellow) as the CE was prepared as ideal QRE. The occurrence of more than two interface signals in the experimental data is due to competing transport paths through the sample.[23]

As step 2, we identify the interface DRT signals whose characteristic time constant depends on pressure and assign its origin to the constriction effect. The time constant of the GB signal around 10^{-5} s is independent of stack pressure as expected. The three other DRT signals from interface possesses with relaxation times between 10^{-5} s and 10^{-2} s, all strongly depend on external load. Their time constants shift and their amplitudes decrease and vanish with increasing uniaxial pressure. No contribution from the interface can be observed after an isostatic pressure of 400 MPa was applied. This suggests that all three signals arise from the constriction effect and the CT effect is negligible in case of the Li|LLZO interface.

Several other aspects support the conclusion that current constriction rather than CT is the rate-determining step at the Li|LLZO interface. First, the estimate of the upper limit of the macroscopic CT resistance at small contact areas according to step 5, which yields about 1 Ω cm^2, several orders of magnitude lower than the experimentally observed values for R_{Int}.[59] Second, the structural analysis (corresponding to step 6 of the hierarchical scheme) reveals pores at the interface. This is even more supported by a theoretical study of Zhang et al. who suggest that the physical contact $A_{WE|SE}$ roughly changes by a factor of five in the experiment of Krauskopf et al., from around 20% at 10 MPa to almost 100% at 400 MPa.[39] Third, temperature-dependent impedance measurements (corresponding to step 7 of the hierarchical scheme) yield a small activation energy for the interface signal $E_{a,Int}$ = 0.37 eV comparable to that of the bulk process $E_{a,Bulk}$ = 0.34 eV.

All listed observations agree very well with the computations performed and also with fundamental studies on the constriction effect published in the literature.[29–36] Thus, we conclude that the CT step at the Li|LLZO interface is negligible as current constriction effects clearly dominate the electric Li|LLZO interface properties in the samples studied by Krauskopf et al. This result is consistent with several other experimental observations, such as the evolution and the increase of an interfacial (i.e., constriction) impedance contribution due to pore formation during anodic dissolution.[50,63,65–68] Moreover, Ortmann et al. recently reported similar experimental findings for the interface between sodium and NASICON-type solid electrolyte $Na_{3.4}Zr_2Si_{2.4}P_{0.6}O_{12}$.[49] Their detailed analysis of the origin of the interface impedance reveals that the contribution of a naturally grown and kinetically stabilized interphase is negligible. Instead, pore formation leads to current constriction, which dominates the rate performance at the interface. This further emphasizes the important role of geometric constriction effects at alkali metal|SE interfaces on the way towards the successful implementation of reversible metal anodes in the market.

ADVANCED SCIENCE NEWS
www.advancedsciencenews.com

ADVANCED MATERIALS INTERFACES
Open Access
www.advmatinterfaces.de

4. Conclusions

Various processes, such as charge transfer, morphological and chemical instabilities due to pores or SEI formation, affect the interface properties of metal anodes in solid-state battery cells. Identifying the dominant interface effect(s) at metal|solid electrolyte interfaces is crucial, as the strategy for improving a solid-state battery depends on the rate-limiting process, which needs to be overcome. In this study, we use a 3D electric network model to investigate the interplay of these interface effects with the structural properties of a symmetric Me|SE|Me stack in order to assess their impact on the impedance data in the frequency and time domain.

We perform a thorough analysis of the dependence of the impedance data on the physical contact area $A_{WE|SE}$ and on temperature for different orders of the time constants of the underlying interface processes. Fitting the computed impedance data with 1D equivalent circuit models, in which different processes are represented by *RC*-elements, allows to translate the microscopic and mesoscopic transport properties into macroscopic transport parameters (R_i, C_i). This enables the development of universal recipes in the form of hierarchical schemes for analyzing experimental impedance data. We introduce such a scheme for systems with chemically stable interfaces, or with kinetically stabilized interlayer, for example, battery stacks with a porous WE|SE interface. The approach relies on the evolution of the impedance data when the porous interface morphology is continuously tuned under external pressure.

In principle, similar schemes can be developed for systems with other interface morphologies, e.g., interfaces with dynamic SEI formation. However, the impedance studies in such cases need to be accompanied by thorough structural investigations of the evolution of the interface morphology under operation or under external parameters like pressure. This is a necessity for extracting the functional relationship between the macroscopic transport parameters of the 1D equivalent circuit models and external control parameters tuned in the experiment. The approach sketched spans the bridge between 3D electric network modelling of impedance data and experimental measurements and corresponding analysis. It is widely employable and will help to speed up the optimization of solid-state batteries in the future.

This is successfully demonstrated considering experimental impedance data of a Li|LLZO|Li stack. We prove unambiguously that the Li|LLZO interface properties are dominated by geometric current constriction while the electric CT migration process plays only a negligible role. This also applies to recent experimental results on sodium in contact with a NASICON-type solid electrolyte. Consequently, charge-transfer driven morphological instabilities during cycling impedes the successful implementation of reversible metal anodes in the market. Thus, methods need to be developed to suppress pore formation at the WE|SE interface.

Acknowledgements

The authors greatly appreciate helpful discussions with Till Ortmann and Sascha Kremer. The authors thank Elisa Monte for the preparation of the graphical abstract. The authors acknowledge computational resources provided by the HPC Core Facility and the HRZ of the Justus-Liebig-University Giessen. The authors would like to thank MSc. Philipp Risius and Dr. Marcel Giar of HPC-Hessen, funded by the State Ministry of Higher Education, Research, and the Arts (HMWK), for programming advice. Financial support is provided by the DFG via the GRK (Research Training Group) 2204 "Substitute Materials for sustainable Energy Technologies". J.J. and S.B. acknowledge financial support by the German Federal Ministry of Education and Research within the cluster of competence FESTBATT (projects 03XP0177A and 03XP0180). J.J. and T.F. acknowledge funding by the German Federal Ministry of Education and Research (BMBF) of the LiSI and LiSI2 project, grant identifiers 03XP0224E and 03XP0509B.

Conflict of Interest

The authors declare no conflict of interest.

Data Availability Statement

The data that support the findings of this study are available from the corresponding author upon reasonable request.

Keywords

current constriction, interface impedance, lithium metal anodes, pore and SEI formation, solid-state batteries

Received: November 13, 2022
Revised: December 18, 2022
Published online:

[1] C. Niu, H. Lee, S. Chen, Q. Li, J. Du, W. Xu, J.-G. Zhang, M. S. Whittingham, J. Xiao, J. Liu, *Nat. Energy* **2019**, *4*, 551.
[2] H. Wang, D. Yu, C. Kuang, L. Cheng, W. Li, X. Feng, Z. Zhang, X. Zhang, Y. Zhang, *Chem* **2019**, *5*, 313.
[3] M. T. McDowell, F. J. Q. Cortes, A. C. Thenuwara, J. A. Lewis, *Chem. Mater.* **2020**, *32*, 8755.
[4] Y. Takeda, O. Yamamoto, N. Imanishi, *Electrochemistry* **2016**, *84*, 210.
[5] J. M. Tarascon, M. Armand, in *Materials for Sustainable Energy*, Macmillan Publishers Ltd, London **2010**, pp. 171–179.
[6] K. Xu, *Chem. Rev.* **2004**, *104*, 4303.
[7] K. Nishikawa, T. Mori, T. Nishida, Y. Fukunaka, M. Rosso, T. Homma, *J. Electrochem. Soc.* **2010**, *157*, A1212.
[8] H. E. Park, C. H. Hong, W. Y. Yoon, *J. Power Sources* **2008**, *178*, 765.
[9] M. Weiss, F. J. Simon, M. R. Busche, T. Nakamura, D. Schröder, F. H. Richter, J. Janek, *Electrochem. Energy Rev.* **2020**, *3*, 221.
[10] J. Kasemchainan, S. Zekoll, S. D. Jolly, Z. Ning, G. O. Hartley, J. Marrow, P. G. Bruce, *Nature Mater.* **2019**, *18*, 1105.
[11] M.-C. Bay, M. Wang, R. Grissa, M. V. F. Heinz, J. Sakamoto, C. Battaglia, *Adv. Energy Mater.* **2020**, *10*, 1902899.
[12] R. Schlenker, D. Stępień, P. Koch, T. Hupfer, S. Indris, B. Roling, V. Miß, A. Fuchs, M. Wilhelmi, H. Ehrenberg, *ACS Appl. Mater. Interfaces* **2020**, *12*, 20012.
[13] S. D. Jolly, Z. Ning, G. O. Hartley, B. Liu, D. L. R. Melvin, P. Adamson, J. Marrow, P. G. Bruce, *ACS Appl. Mater. Interfaces* **2021**, *13*, 22708.
[14] L. M. Riegger, S.-K. Otto, M. Sadowski, S. Jovanovic, O. Kötz, S. Harm, L. G. Balzat, S. Merz, S. Burkhardt, F. H. Richter, J. Sann,

ADVANCED SCIENCE NEWS
www.advancedsciencenews.com

ADVANCED MATERIALS INTERFACES
Open Access
www.advmatinterfaces.de

R.-A. Eichel, B. V. Lotsch, J. Granwehr, K. Albe, J. Janek, *Chem. Mater.* **2022**, *34*, 3659.
[15] V. Lacivita, Y. Wang, S.-H. Bo, G. Ceder, *J. Mater. Chem. A* **2019**, *7*, 8144.
[16] S. Wenzel, S. Randau, T. Leichtweiß, D. A. Weber, J. Sann, W. G. Zeier, J. Janek, *Chem. Mater.* **2016**, *28*, 2400.
[17] J. Janek, S. Majoni, *Ber. Bunsenges. Phys. Chem.* **1995**, *99*, 14.
[18] S. Majoni, J. Janek, *Ber. Bunsenges. Phys. Chem.* **1998**, *102*, 756.
[19] H. Schmalzried, J. Janek, *Ber. Bunsenges. Phys. Chem.* **1998**, *102*, 127.
[20] N. M. Beekmans, L. Heyne, *Electrochim. Acta* **1976**, *21*, 303.
[21] T. van Dijk, A. J. Burggraaf, *Phys. Status Solidi* **1981**, *63*, 229.
[22] M. J. Verkerk, B. J. Middelhuis, A. J. Burggraaf, *Solid State Ionics* **1982**, *6*, 159.
[23] J. K. Eckhardt, S. Burkhardt, J. Zahnow, M. T. Elm, J. Janek, P. J. Klar, C. Heiliger, *J. Electrochem. Soc.* **2021**, *168*, 090516.
[24] T. R. Jow, C. C. Liang, *J. Electrochem. Soc.* **1983**, *130*, 737.
[25] A. Schröder, J. Fleig, D. Gryaznov, J. Maier, W. Sitte, *J. Phys. Chem. B* **2006**, *110*, 12274.
[26] T. Krauskopf, B. Mogwitz, H. Hartmann, D. K. Singh, W. G. Zeier, J. Janek, *Adv. Energy Mater.* **2020**, *10*, 2000945.
[27] B. S. Vishnugopi, E. Kazyak, J. A. Lewis, J. Nanda, M. T. McDowell, N. P. Dasgupta, P. P. Mukherjee, *ACS Energy Lett.* **2021**, *6*, 3734.
[28] J. A. Lewis, F. J. Q. Cortes, Y. Liu, J. C. Miers, A. Verma, B. S. Vishnugopi, J. Tippens, D. Prakash, T. S. Marchese, S. Y. Han, C. Lee, P. P. Shetty, H. W. Lee, P. Shevchenko, F. De Carlo, C. Saldana, P. P. Mukherjee, M. T. McDowell, *Nat. Mater.* **2021**, *20*, 503.
[29] J. K. Eckhardt, P. J. Klar, J. Janek, C. Heiliger, *ACS Appl. Mater. Interfaces* **2022**, *14*, 35545.
[30] J. K. Eckhardt, T. Fuchs, S. Burkhardt, P. J. Klar, J. Janek, C. Heiliger, *ACS Appl. Mater. Interfaces* **2022**, *14*, 42757.
[31] J. Fleig, J. Maier, *Electrochim. Acta* **1996**, *41*, 1003.
[32] J. Fleig, J. Maier, *Solid State Ionics* **1996**, *86–88*, 1351.
[33] J. Fleig, J. Maier, *J. Electroceram.* **1997**, *1*, 73.
[34] J. Fleig, J. Maier, *Solid State Ionics* **1997**, *94*, 199.
[35] J. Fleig, J. Maier, *J. Electrochem. Soc.* **1997**, *144*, L302.
[36] J. Fleig, J. Maier, *J. Am. Ceram. Soc.* **1999**, *82*, 3485.
[37] T. Krauskopf, H. Hartmann, W. G. Zeier, J. Janek, *ACS Appl. Mater. Interfaces* **2019**, *11*, 14463.
[38] W. E. Tenhaeff, E. Rangasamy, Y. Wang, A. P. Sokolov, J. Wolfenstine, J. Sakamoto, N. J. Dudney, *ChemElectroChem* **2014**, *1*, 375.
[39] X. Zhang, Q. J. Wang, K. L. Harrison, S. A. Roberts, S. J. Harris, *Cell Rep. Phys. Sci.* **2020**, *1*, 100012.
[40] D. Rettenwander, A. Welzl, L. Cheng, J. Fleig, M. Musso, E. Suard, M. M. Doeff, G. J. Redhammer, G. Amthauer, *Lnorg. Chem.* **2015**, *54*, 10440.
[41] C. Loho, R. Djenadic, M. Bruns, O. Clemens, H. Hahn, *J. Electrochem. Soc.* **2016**, *164*, A6131.
[42] B. Boukamp, *Solid State Ionics* **2004**, *169*, 65.
[43] T. H. Wan, M. Saccoccio, C. Chen, F. Ciucci, *Electrochim. Acta* **2015**, *184*, 483.
[44] J. T. S. Irvine, D. C. Sinclair, A. R. West, *Adv. Mater.* **1990**, *2*, 132.
[45] S.-K. Otto, L. M. Riegger, T. Fuchs, S. Kayser, P. Schweitzer, S. Burkhardt, A. Henss, J. Janek, *Adv. Mater. Interfaces* **2022**, *9*, 2102387.
[46] A. Banerjee, X. Wang, C. Fang, E. A. Wu, Y. S. Meng, *Chem. Rev.* **2020**, *120*, 6878.
[47] K.-Y. Yang, C. Leu, K.-Z. Fung, M.-H. Hon, M.-C. Hsu, Y.-J. Hsiao, M.-C. Wang, *J. Mater. Res.* **2008**, *23*, 1813.
[48] X. Shen, Y. Li, T. Qian, J. Liu, J. Zhou, C. Yan, J. B. Goodenough, *Nat. Commun.* **2019**, *10*, 900.
[49] T. Ortmann, S. Burkhardt, J. K. Eckhardt, T. Fuchs, Z. Ding, J. Sann, M. Rohnke, Q. Ma, F. Tietz, D. Fattakhova-Rohlfing, C. Kübel, O. Guillon, C. Heiliger, J. Janek, *Adv. Energy Mater.* **2022**, https://doi.org/10.1002/aenm.202202712.
[50] M. J. Wang, E. Carmona, A. Gupta, P. Albertus, J. Sakamoto, *Nat. Commun.* **2020**, *11*, 5201.
[51] R. Murugan, V. Thangadurai, W. Weppner, *Angew. Chem., Int. Ed.* **2007**, *46*, 7778.
[52] Y. Zhu, J. G. Connell, S. Tepavcevic, P. Zapol, R. Garcia-Mendez, N. J. Taylor, J. Sakamoto, B. J. Ingram, L. A. Curtiss, J. W. Freeland, D. D. Fong, N. M. Markovic, *Adv. Energy Mater.* **2019**, *9*, 1803440.
[53] J. G. Connell, T. Fuchs, H. Hartmann, T. Krauskopf, Y. Zhu, J. Sann, G.-R. Mendez, J. Sakamoto, S. Tepavcevic, J. Janek, *Chem. Mater.* **2020**, *32*, 10207.
[54] Y. Zhu, X. He, Y. Mo, *ACS Appl. Mater. Interfaces* **2015**, *7*, 23685.
[55] T. Fuchs, C. G. Haslam, A. C. Moy, C. Lerch, T. Krauskopf, J. Sakamoto, F. H. Richter, J. Janek, *Adv. Energy Mater.* **2022**, 2201125.
[56] D. K. Singh, T. Fuchs, C. Krempaszky, B. Mogwitz, S. Burkhardt, F. H. Richter, J. Janek, *Adv. Funct. Mater.* **2023**, *33*, 2211067.
[57] S.-K. Otto, T. Fuchs, Y. Moryson, C. Lerch, B. Mogwitz, J. Sann, J. Janek, A. Henss, *ACS Appl. Energy Mater.* **2021**, *4*, 12798.
[58] A. Sharafi, E. Kazyak, A. L. Davis, S. Yu, T. Thompson, D. J. Siegel, N. P. Dasgupta, J. Sakamoto, *Chem. Mater.* **2017**, *29*, 7961.
[59] J. Gao, X. Guo, Y. Li, Z. Ma, X. Guo, H. Li, Y. Zhu, W. Zhou, *Adv. Theory Simul.* **2019**, *2*, 1900028.
[60] H. Koshikawa, S. Matsuda, K. Kamiya, M. Miyayama, Y. Kubo, K. Uosaki, K. Hashimoto, S. Nakanishi, *J. Power Sources* **2018**, *376*, 147.
[61] F. Yonemoto, A. Nishimura, M. Motoyama, N. Tsuchimine, S. Kobayashi, Y. Iriyama, *J. Power Sources* **2017**, *343*, 207.
[62] A. Badran, T. Clemenceau, N. Andriamady, D. Marshall, R. Raj, *MRS Commun.* **2021**, *11*, 283.
[63] T. Krauskopf, R. Dippel, H. Hartmann, K. Peppler, B. Mogwitz, F. H. Richter, W. G. Zeier, J. Janek, *Joule* **2019**, *3*, 2030.
[64] C. Lee, S. Y. Han, J. A. Lewis, P. P. Shetty, D. Yeh, Y. Liu, E. Klein, H.-W. Lee, M. T. McDowell, *ACS Energy Lett.* **2021**, *6*, 3261.
[65] K. Lee, E. Kazyak, M. J. Wang, N. P. Dasgupta, J. Sakamoto, *Joule* **2022**, *6*, 2547.
[66] F. Flatscher, M. Philipp, S. Ganschow, H. M. R. Wilkening, D. Rettenwander, *J. Mater. Chem. A* **2020**, *8*, 15782.
[67] T. Fuchs, J. Becker, C. G. Haslam, C. Lerch, J. Sakamoto, F. H. Richter, J. Janek, *Adv. Energy Mater.* **2022**, *13*, 2203174.
[68] T. Krauskopf, B. Mogwitz, C. Rosenbach, W. G. Zeier, J. Janek, *Adv. Energy Mater.* **2019**, *9*, 1902568.

2.7 Further (co-)Authored Publications

Charge transport in single NCM cathode active material particles for lithium-ion batteries studied under well-defined contact conditions. Simon Burkhardt, Markus S. Friedrich, Janis K. Eckhardt, Amalia C. Wagner, Nicole Bohn, Joachim R. Binder, Limei Chen, Matthias T. Elm, Jürgen Janek and Peter J. Klar *ACS Energy Lett.* **2019**, 4, 9, 2117-2123. (DOI: 10.1021/acsenergylett.9b01579)

Ab initio description of disorder effects in layered cathode active materials by the coherent potential approximation. Janis K. Eckhardt, Philipp E. Risius, Michael Czerner and Christian Heiliger *J. Phys.: Condens. Matter* **2022**, 34, 32, 325501-325509. (DOI: 10.1088/1361-648x/ac7502)

Kinetics and Pore Formation of the Sodium Metal Anode on NASICON-type $Na_{3.4}Zr_2Si_{2.4}P_{0.6}O_{12}$ for Sodium Solid-State Batteries. Till Ortmann, Simon Burkhardt, Janis K. Eckhardt, Till Fuchs, Ziming Ding, Joachim Sann, Marcus Rohnke, Qianli Ma, Frank Tietz, Dina Fattakhova-Rohlfing, Christian Kübel, Oliver Guillon, Christian Heiliger and Jürgen Janek *Adv. Energy Mater.* **2023**, 13, 5, 2202712-2202728. (DOI: 10.1002/aenm.202202712)

The Impact of Microstructure on Filament Growth at the Sodium Metal Anode in All-Solid-State Sodium Batteries. Ziming Ding, Yushu Tang, Till Ortmann, Janis K. Eckhardt, Marcus Rohnke, Georgian Melinte, Christian Heiliger, Jürgen Janek and Christian Kübel *Adv. Energy Mater.* **2023**, 2302322. (DOI: 10.1002/aenm.202302322)

Deposition of Sodium Metal at the Copper-NaSICON Interface for Reservoir-free Solid-State Sodium Batteries. Till Ortmann, Till Fuchs, Janis K. Eckhardt, Ziming Ding, Qianli Ma, Frank Tietz, Christian Kübel, Marcus Rohnke and Jürgen Janek *submitted to Advanced Energy Materials* **2023**.

3. Acknowledgements

More than half a century ago, Helen Keller (1880 – 1968) once said "*Alone we can do so little; together we can do so much*". Science is a collaborative effort, and the result is rarely due to the actions of individuals. I would like to take this opportunity to express my deepest gratitude to all the people who have supported me over the past years. It has been a pleasure to work in such a supportive environment alongside awesome mentors, inspiring role models, and great friends. My special thanks go to:

- **Prof. Dr. Christian Heiliger** for taking over the supervision of my doctoral thesis and for accepting me into his research group. I am particularly grateful for the constant support, and the great trust placed in me as well as the space to develop myself freely.
- **Prof. Dr. Peter J. Klar** for the constant support and promotion of all my projects, also during my studies. This work would not have been possible without your original idea to develop our own modeling framework. I would also like to thank you for always taking the time to discuss and improve the latest drafts of the manuscripts for our joint publications.
- **Prof. Dr. Jürgen Janek** for always showing great interest in my work and progress, for promoting all my projects and for the networking with other people and institutions in the same research field. I would also like to thank you for making the contact with BASF, which made it much easier for me to organize my three-month internship.
- **PD Dr. Matthias T. Elm** for the constant support and assistance with questions and problems that sometimes arose. I would also like to thank you for the great and entertaining time at conferences, the fruitful collaboration in our joint projects, and for proofreading this thesis.
- **Dr. Simon Burkhardt** for the excellent collaboration in all our joint projects – starting with the single-particle measurements during my bachelor time, through the master thesis and up to the doctorate. Our discussions, your perfectionism and your work ethic left their mark on me.
- **Markus S. Friedrich**, **Jan Luka Dornseifer**, **Sascha Kremer**, **Dr. Till Fuchs** and **Till Ortmann** for the rewarding collaboration in our joint projects and the great time at conferences. **Dr. Marcel Giar** and **Philipp E. Risius** for the maintenance of the high-performance computing clusters.
- **Joel Herbert** and **Sascha Kremer** for the pleasure of guiding you on your way to your Bachelor and Master degrees. Our professional exchange and the discussions on individual subjects were a pleasant break from the rest of the working day, but also the scientific debate on questions that seemed obvious also helped me to progress.
- The **Digitalization of Research & Development** department at **BASF**, which allowed me to do a three-month internship alongside my doctorate. Special thanks go to my supervisor **Dr. Robert M. Lee**, and team leader, **Dr. Maik Friedl**, who, despite the pandemic-related restrictions, tried to give me the best possible overview of daily work in an industrial company.
- **Dr. Alexander Fabian** for our weekly Thursday morning coffee break sessions, especially during the onset of the Covid pandemic, which made me feel less cloistered. **Nils Neugebauer**, **Dr. Mario Gies**, **Sebastian L. Benz** and **Jan M. Waack** for the always entertaining gossip. Although I spent most of my doctoral time in home office, I felt like I was always up to date on what was going on at university.

- **Elisa Monte** for the time and hard work you spent on preparing the awesome cover art and TOC figures for several publications. It has always been fascinating to witness the process from the development of the idea to the design of the final result.
- The **soccer team of AG Klar** – Dr. Marcel Weinhold ©, Markus S. Friedrich, Alexander G. Strack, Florian Eberheim, Paul Tuchecker and Maximilian von Roeder – with whom I was able to win the traditional JLU soccer tournament in 2019. #catenaccio
- **My family**, especially my parents Klaus and Sylke Eckhardt, for their constant support throughout my studies, in all further life decisions, and helping me keep my head up. I would also like to thank my sister Lena K. Eckhardt and my brother Dr. André K. Eckhardt for the welcome distractions from the sometimes overwhelming work.